Department of Pure and Applied Chemistry

The development of gold nanorod arrays in alumina as a substrate for multi-analyte SER(R)S sensing

Evelyn Caldwell

Degree of Doctor of Philosophy

May 2019

Declaration of Authorship

‘This thesis is the result of the author’s original research. It has been composed by the author and has not been previously submitted for examination which has led to the award of a degree.’

Signed:

Date:

Acknowledgements

I wish firstly, to sincerely thank my supervisor Dr Len Berlouis for having a door that is always open, the patience of a saint and counselling skills that are second to none. As well as my second supervisor Dr Alastair Wark, who…… let us just say deserves a medal.

Special thanks must also go to Professor Andrew Mills for initially allowing me this opportunity.

Thanks to the following people for their help and support throughout my time at Strathclyde; Dr Georgios Nikiforidis, Jim Morrow, Dr Paul Edwards, Dr Graham Skinner and Dr P L Tang of Agilent Technologies - UK, The University workshop and Neil Hodgson who, turned into reality my ideas from the scrappy drawings and wild gesticulations he was presented with. The final year students; Johnathan Mahoney, Anisa Muhammad, Marcus Ingram and Fraser Mole.

My family Mum (Rose), Dad (David), Iain, Mandy and Vicki for all their love and support throughout my many endeavours.

Finally John, Fiona, Claire and Graham for relentlessly bullying me, picking me up when I was down, mopping up my tears and making me laugh.

Abstract

Surface enhanced Raman spectroscopy (SERS) and the closely related surface enhanced resonance Raman spectroscopy (SERRS) play increasingly more important roles in both sensing and optical imaging applications. However, their widespread commercial use has been restricted in part by the lack of suitable substrates. Those currently available provide some but not all of the properties desirable in an ideal SERS substrate. Therefore, there is a need to provide a substrate with substantial signal enhancement with uniformity and repeatability of response over the entire surface. It is also advantageous for certain applications that the nanostructured substrate is also electrically conducting. The ideal substrate would also be capable of both single- and multi-analyte analysis, providing versatility through end user customisation to meet specific needs. In addition to robustness, ease of handling, surface regeneration and cost effectiveness are also desirable.

This work details the progress made towards developing such a SERS substrate. The main focus was the electrochemical production of ordered gold nanorod arrays (AuNR) in a porous anodised aluminium oxide (AAO) template that enabled good control of morphology, height, width and the spacing between vertically orientated rods. Optimisation work performed on the AAO template fabrication significantly reduced 'pore branching' that had previously occurred at the top of the AAO template. Comparison studies of electrodeposited AuNR that were formed in the pores to create SERS substrates were carried out. A controlled etching step was developed to partially expose the AuNR while maintaining electrical contact. SERS studies were initially performed using two well-established reporter molecules, one resonant (malachite green) and one non-resonant (4-mercaptobenzoic acid) with the excitation laser. The signal enhancement achieved with the AuNR was vastly superior to that obtained from a commercially available substrate (Klarite®), a monolayer of gold nanoparticles (NP) and a thin gold film. The signal was found to be uniform over the whole surface. A number of cleaning methods were also explored to enable repeat use and surface regeneration over several cycles.

An AuNR surface patterning method was also developed to multi-analyte detection on a single substrate. This comprised of AuNR 'dots', which can be individually functionalised. Finally, the application of the substrate for *in-situ* electrochemical studies was demonstrated in a specially designed flow-cell that allowed for controlled etching, cleaning and surface modification of the SERS substrate to be effected.

Abbreviations

AAO	Anodic Aluminium oxide
AgNP	Silver nanoparticles
AuNP	Gold nanoparticles
AuNR	Gold nanorod arrays
AAO	Anodic Aluminium oxide
ATR-IR	Attenuated total reflectance infrared spectroscopy
CE	Counter electrode
CVD	Chemical vapour deposition
CV	Cyclic voltammogram
DIW	Milli-Q deionised water (resistivity 18.2 MΩ cm)
DNA	Deoxyribonucleic acid
E	Potential
EF	Enhancement factor
EtOH	Ethanol
FTIR	Fourier transform infrared spectroscopy
Lm	Longitudinal mode
LSPR	Localised surface plasmon resonance
MBA	4-mercaptobenzoic acid
MeOH	Methanol
MG	Malachite green isothiocyanate
NA	Numerical aperture

NIR	Near infrared
NIR 797	NIR 797 isothiocyanate
NP	Nanoparticles
NQ	1,8-diaza-4,5-dithia-1,8-di(2-chloro-[1,4]-naphthoquinone-3-yl)octane
PEEK	Polyether ether ketone
PTFE	Polytetrafluoroethylene
RDE	Rotating disc electrode
RE	Reference electrode
rms	Root mean square
SC	Semiconductor
SCE	Saturated calomel electrode
SEF	Surface enhanced fluorescence
SERS	Surface enhanced Raman spectroscopy
SERRS	Surface enhanced resonance Raman spectroscopy
SHE	Standard hydrogen electrode
SPR	Surface plasmon resonance
TERS	Tip enhanced Raman spectroscopy
Tm	Transverse mode
UV	Ultra violet
Vis	Visible
V	Volt
WE	Working electrode

Table of Contents

"Happiness is a ball after which we run wherever it rolls,
and we push it with our feet when it stops"
Johann Wolfgang von Goethe

1. Introduction

1.1 Sensing and nanotechnology

Sensors have become invaluable and are now common place and a part of everyday life[1–3]. We are surrounded by them whether in the home, at work or at leisure, from heavily built up urban areas to the remotest rural environments. Increasingly sophisticated technology has been reduced in size and complexity in order to enable its use by persons with little or no scientific or technical knowledge of the processes involved in operating the devices satisfactorily. For example, hand held devices for home pregnancy testing[4], crop analysis[5], environmental analysis[6–9] the monitoring of insulin levels in diabetics[10] and in laboratories too, where space is of the essence.

From the development of the oxygen probe in 1956[11], the list of analytes able to be detected has expanded rapidly[12,13]. The principles and methods by which the detections occur fall within the areas of optical[1], thermal[14], mass and electrochemical[2]. This already wide range of detection methods coupled together with the emergence of nanotechnology in the 1980's[15] has seen the subsequent rapid increase and divergence in the areas of interest. Thus, research and development of sensors have resulted in a myriad of collaborations among scientists from the fields of chemistry, physics, computing and engineering.

Nanotechnology has come to the forefront of sensors research. It has been described as the practical application of scientific knowledge at the nanoscale[15] and is characterised by the production and/or use of materials where at least one dimension lies within the range of 1 – 100 nm (i.e. 10^{-9} m – 10^{-7} m). The concept was first postulated by Richard Feynman in 1959 who stated that "The problems of chemistry and biology can be greatly helped if our ability to see what we are doing, and to do things on an atomic level, is ultimately developed". However it was Norio Taniguchi who is credited with first introducing the term in 1974 and not until early in the following decade with the development of the scanning tunnelling microscope (STM) and the atomic force microscope (AFM) that it became a reality[13].

1.2 Metallic character and properties

The chemical properties associated with metals result from how readily metals lose their electrons to form positively charged ions, i.e. cations. The physical properties associated with metals include a lustrous shiny appearance, high density, good thermal and electrical conductivity. Most metals are solid and malleable with one notable exception being mercury which is liquid at room temperature[16].

1.2.1 Band theory of metals

The conductivity of metals is a result of atomic orbitals at similar energy levels combining to form a band. The outer valence band is either partially filled with electrons or overlaps with an unoccupied conduction band. As a result electrons can easily flow between the two under an applied electric field, resulting in the metal exhibiting high conductivity. The energy spread of this band is a result of the difference in energy between the most strongly bound "bonding orbital" and the highest energy "antibonding orbital". Electrons become delocalised i.e. detached from their original atom, moving freely within the molecular orbitals in the valence band. Strong forces of attraction exist between these delocalised electrons and the positive nuclei. Band theory derives these bands and band gaps by examining the allowed quantum mechanical wave functions for an electron in a large, periodic lattice of atoms or molecule[17–19].

An important factor in band theory is the Fermi energy; this refers to the energy associated with a particle in thermal equilibrium with a system of interest. The Fermi level is a hypothetical energy level of an electron, which at thermodynamic equilibrium has a one in two probability of being occupied at any given time. The Fermi level of a material expresses the energy required to add or remove an electron (μ). As such, the observed difference in voltage between two points, A and B, V_A-V_B in an electronic circuit is exactly related to the corresponding chemical potential difference, $\mu_A - \mu_B$, in the Fermi level[20,21] is given in Equation 1.1.

$$V_A - V_B = \frac{\mu_A - \mu_B}{-e} \qquad \textbf{Equation 1.1}$$

where e is the electron charge.

Electrons move from a body of high μ (low voltage) to low μ (high voltage) if a simple path is provided. This flow of electrons will cause the lower μ to increase (due to charging or other repulsion effects) and likewise cause the higher μ to decrease. Eventually, μ will settle down to the same value in both bodies, having reached the equilibrium (off) state of an electronic circuit[22].

The position of the Fermi level in relation to the band energy levels is a crucial factor in determining electrical properties. The Fermi level does not necessarily require the existence of a band structure or to relate to an actual energy level and is a precisely defined thermodynamic quantity. The bands and band gaps most relevant for electrical conductivity and optoelectronics are those with energies close to the Fermi level. A selection of elements Fermi energy levels are given in Table 1.1. Note that the Fermi energies of silver and gold are the lowest and iron and magnesium the highest[21].

Element	**Copper (Cu)**	**Silver (Ag)**	**Gold (Au)**	**Iron (Fe)**	**Manganese (Mn)**	**Zinc (Zn)**	**Cadmium (Cd)**	**Mercury (Hg)**	**Tin (Sn)**	**Lead (Pb)**
Fermi Energy (eV)	**7.00**	**5.49**	**5.53**	**11.1**	**10.9**	**9.47**	**7.47**	**7.13**	**10.2**	**9.47**

Table 1.1 *The Fermi energy levels of a number of elements. Silver and gold have the lowest values.*

In cases where the gap between the valence band and the conduction band is large, electrons are unable to jump from the valence band to the conduction band. Such compounds show little or no conductivity e.g. glass, polystyrene. When the gap between valence band and conduction band is small, some electrons may jump from the valence band to the conduction band and thus show some conductivity. Such materials are known as semiconductors e.g. silicon and germanium[23].

It is evident from looking at the band gap diagram in Figure 1.1 that in the case of a metal there is no separation between the bands. This helps the excited electrons move easily from one band to another and hence metals are good conductors of electricity. In the case of semi-conductors, there is only a small gap between the valence and conduction bands. As a result, only a small fraction of the electrons have enough energy to jump but it is possible to increase the conductivity of semiconductors by increasing the temperature or doping[20]. However,

with insulators the size of the gap between the valence band and conduction band is too great to allow any electrons to make the leap and therefore these materials exhibit no conductivity [19].

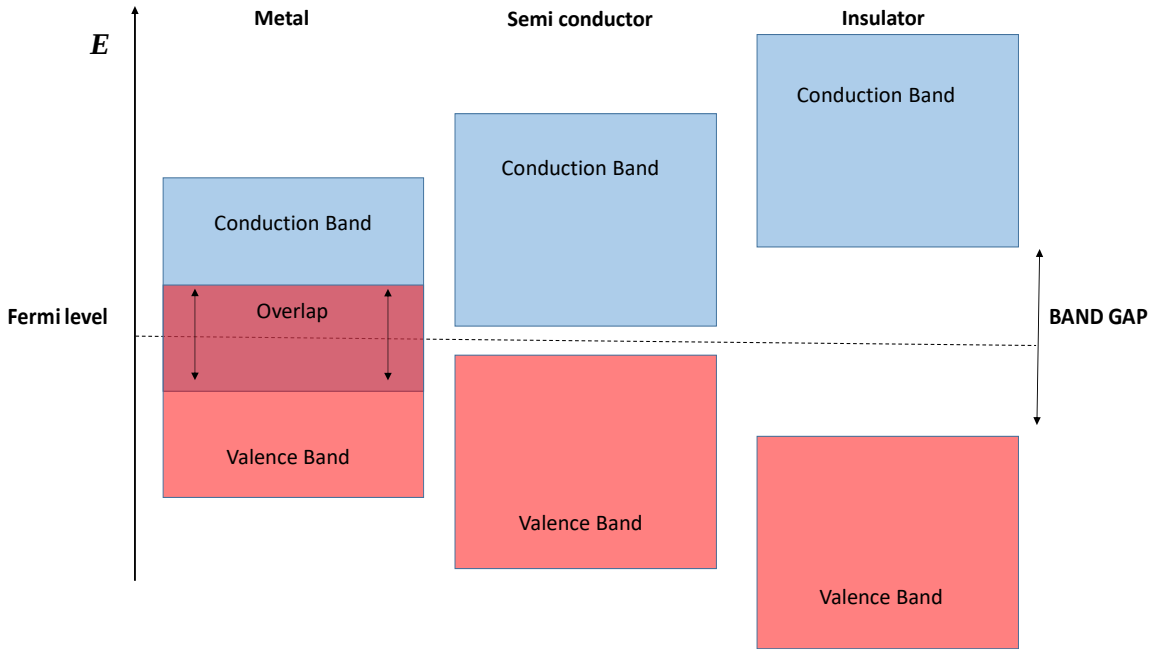

Figure 1.1 *Schematic representation of the band gap in metals, semi-conductors and insulators.*

1.2.2 Gold, silver and copper

Gold, silver and copper are often referred to as the coinage metals. These metals possess qualities, some similar and some different, that make them attractive in numerous applications[24]. As indicated in Table 1.2, they have the highest electrical and thermal conductivities of all metals, and are the most ductile and malleable. The most common oxidation state of 1+ occurs due to the loss of a single electron. However, a 2+ oxidation state is also common for copper and, to a lesser extent silver. This is due to the relatively low values of their second ionisation energies. While a 3+ oxidation state exists for gold due to its low third ionisation energy. Gold can also react with powerful reductants and solutions of the alkali metals in liquid ammonia to produce the gold anion Au^-.

All three elements have significant electron affinities due to half-filled orbitals in the neutral atoms.

Element	Symbol	Atomic number	Electron configuration	Electronegativity	Radius (pm)	Melting point (°C)	Density (g/m^3)
Copper	Cu	29	$4s^1 3d^{10}$	1.90	128	1085	8.96
Silver	Ag	47	$5s^1 4d^{10}$	1.93	144	962	10.50
Gold	Au	79	$6s^1 5d^{10} 4f^{14}$	2.40	144	1062	19.30

Table 1.2 *Properties of gold, silver and copper.*

Copper, silver and gold respectively are increasingly resistant to oxidation, with copper the most reactive and gold the least. Silver exhibits the greatest electrical and thermal conductivity of all the elements, as well as the least contact resistance.

1.2.3 Plasmonics

For centuries the unique optical properties of minute gold and silver particles was known to artists and craftsmen who utilised their vibrant colours for decorative purposes. However, it was not until the middle of the 19th century that the unique optical properties of gold and silver nanoparticles (NP) first aroused scientific interest[25,26]. This key property is linked to surface plasmon resonance[27] (SPR), which arises from the oscillation of free conduction band electrons at a metal/dielectric interface that have been excited by the absorption of incident electromagnetic radiation. They oscillate at a phase and amplitude matching that of the incident light and are associated with intense confined electric fields[12,28,29], as illustrated in Figure 1.2.

Electrons in the conduction band of metals move both freely and independently from the ionic background. It should be noted that the electron cloud of noble metals exhibit higher polarisability than other metals which shifts the plasmon resonance to lower frequencies within the visible spectrum[30]. Localised surface plasmon resonance (LSPR) occurs within a confined nanostructure and is associated with characteristic excitation wavelength ranges[31]. While the majority of metals exhibit plasmon resonance in the ultraviolet (UV) region, gold, silver, and copper exhibit LSPR at longer wavelengths in the visible-NIR region. For all three metals the position of the LSPR λ_{max} varies across the range depicted in Figure 1.3 and is also dependent on the nanoparticle size and shape[32,33].

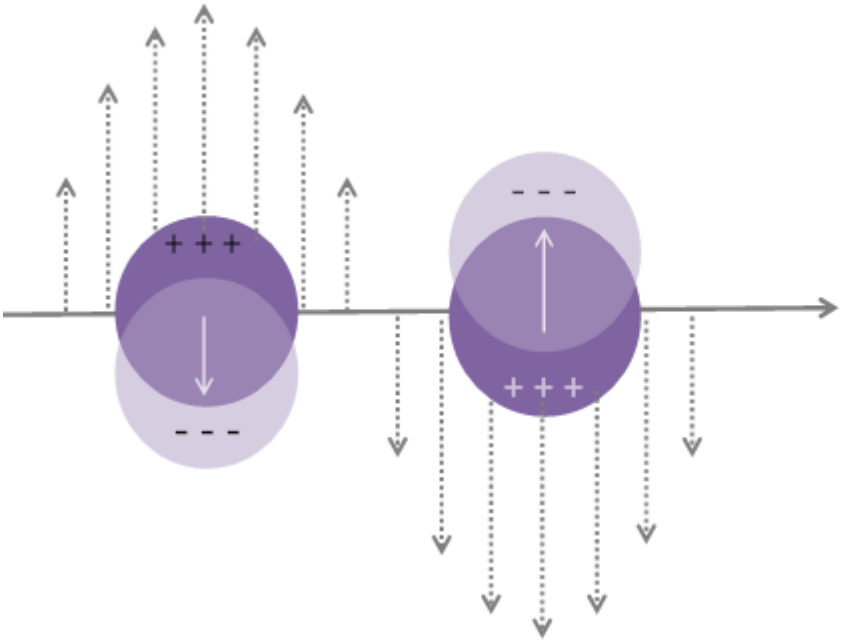

Figure 1.2 *Schematic depicting LSPR excitation within a gold nanoparticle in response to an applied electromagnetic field.*

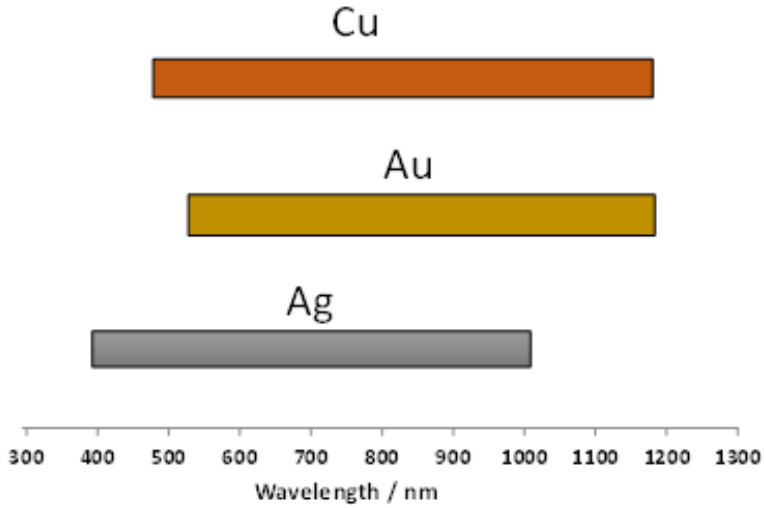

Figure 1.3 *Schematic representation of the LSPR excitation wavelength ranges associated copper, gold and silver. For all three metals, the LSPR λ_{max} varies across the range depending on the nanoparticle size and shape.*

In the case of thin noble metal films (~50 nm thick), the excitation of surface plasmon polaritons (SPP's) along the metal/dielectric interface (see Figure 1.4) results in plasmon propagation lengths that are significantly longer (i.e. micron scale) compared to that associated with LSPR in nanostructures. The SPP electric field is orientated perpendicular to the metal surface and propagate non-radiatively along the metal/dielectric interface and are sensitive to

the refractive index of the local dielectric environment. This allows their properties to be tailored using applied electric or magnetic fields in composite nanomaterials systems.

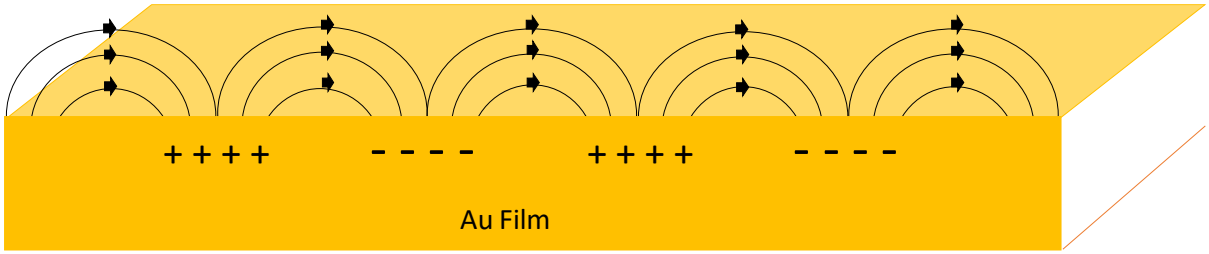

Figure 1.4 *Propagating SPP's on a thin gold film excited at the gold film/air* interface.

Other metals such as the alkali metals and gallium, indium, and rhodium, as well as metal alloys have all been explored as plasmonic substrates[17]. However, the reactivity of the alkali metals in air presents challenges and limitations for their effective use. Aluminium supported SPR falls within the UV region as do metal oxides such as titanium oxide[34].

1.2.4 Gold colloid

The unique health benefits of silver and gold have been known and utilised since ancient times, gold for its benign biocompatibility and silver for its antibacterial properties. The first purified colloidal gold solutions were produced in 1857 by Michael Faraday[25]. While in the 1930's, colloidal gold was used to prolong the lives and alleviate the suffering of terminally ill cancer patients reducing the quantities of opiates required to be prescribed[25].

Gold colloidal solutions are commonly produced using the Turkevich method[35] by boiling chloroauric acid ($HAuCl_4.3H_2O$) with a citrate reducing agent. In 2007 Haiss *et al*[36] used colloidal UV-vis spectra to correlate both size and concentration of gold nanoparticles within synthesised solutions containing nanoparticles between 5 and 100 nm in diameter with their corresponding LSPR λ_{max} falling between 520 nm and 580 nm. Figure 1.5 shows the extinction spectrum of a gold colloid ~20 nm in diameter.

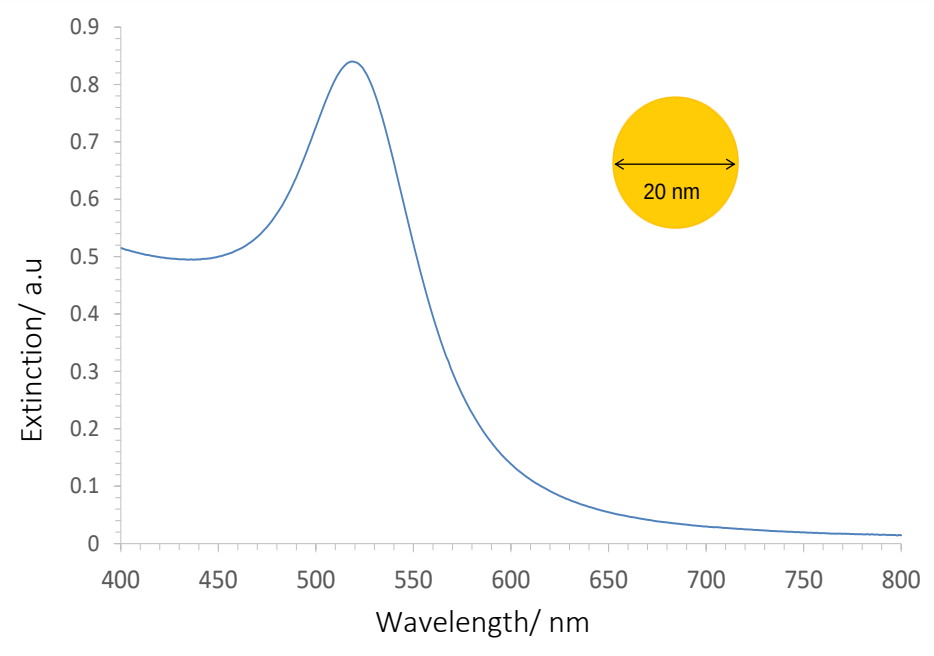

Figure 1.5 *Extinction spectrum for 20 nm gold nanospheres with λ_{max} at 520 nm produced using the Turkevich method. As the diameter of the sphere increases, the λ_{max} is increasingly shifted towards the NIR.*

For a metal colloid solution the size, shape and distance between particles, together with the dielectric function of the medium, have the greatest influence on the extinction bands of LSPR in the nanostructures[37,38]. The extinction cross section (σ_{ex}) is the sum of the absorption (σ_{abs}) and scattering (σ_{sc}) cross sections of a given nanoparticle[20,39], given in Equation 1.2.

$$\sigma_{ex} = \sigma_{abs} + \sigma_{sc} \qquad \textbf{Equation 1.2}$$

The shape of the LSPR profile depends strongly on the NP size. At low diameters (< 4 nm) the spectrum is dominated by interband electronic transitions. Between ~10 and 30 nm, the most dominant effect is that of excitation of plasmon dipole modes within the visible region. Above 30 nm in diameter, scattering effects (and other higher order plasmon modes) start to have an increased influence[25]. SPP's lose energy by depolarisation and the damping effect of electron scattering on their motion. As a result, the plasmon peak is wider, less intense and red-shifted with increasing diameter of the NP. At diameters greater than 100 nm scattering effects dominate the plasmonic response. El Sayed *et al*[40] have shown that the sum of all these effects caused a red shift on the λ_{max} of LSPR of about 0.7 nm for every 1 nm increase in particle radius (for diameter >25 nm). For particle sizes smaller than 25 nm, the λ_{max} is almost independent of particle size.

In the case of rod-like or ellipsoidal-shaped structures the extinction spectrum shows that the plasmon appears to have split into two modes corresponding to the oscillation along and perpendicular to the long axis of the particle[40] (Figure 1.6) as a result of being anisotropic. Nanorods (NR) can also be synthesised by a seed mediated growth mechanism[41]. The two extinction band maxima observed are associated with a transverse mode *(Tm*) across its diameter and a longitudinal mode (*Lm*) along the length of the rod. The position and intensity of the band maxima for each are strongly influenced by the aspect ratio (i.e. length/diameter), which in turn influences the optical properties and subsequent applications[42,43]. Typically, by increasing the aspect ratio, the LSPR of the longitudinal mode can be shifted from ~600 nm to > 1200 nm while the transverse mode will remain around ~520-550 nm[44,45].

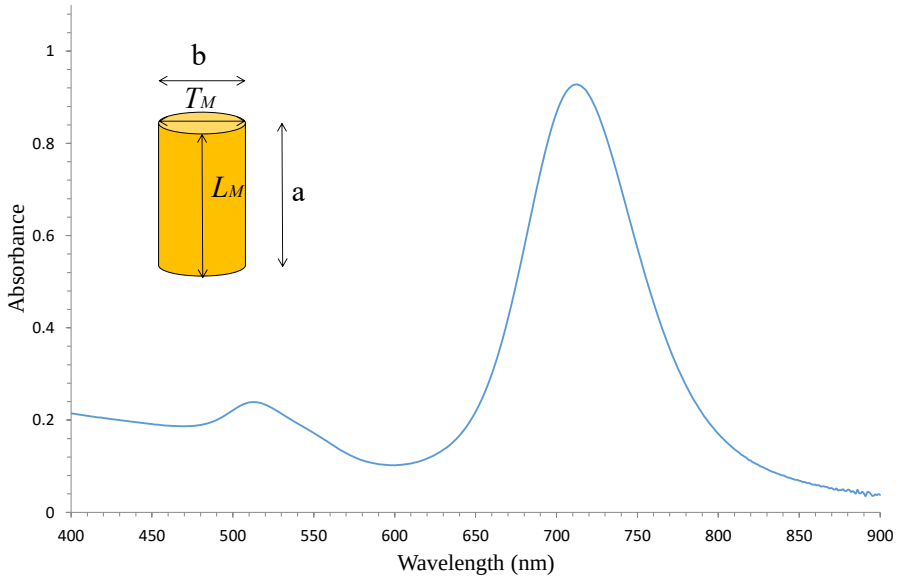

Figure 1.6. *Extinction spectrum of a gold nanorod colloid with an aspect ratio of ~4, width is ~15 nm. The λ_{max} of the Lm (along the length of the rod) is shown at 720 nm and a transverse mode Tm (across its diameter) at 520 nm.*

In general, other geometrical shapes of nanoparticles (e.g. triangle[38], cube[46], shell[47]) exhibit a red-shifted LSPR band compared to their spherical analogs[26]. *In vivo* applications require structural and compositional tuning of the nanoparticle, as tissue absorption in the near-infrared window (650–900 nm) is minimal[48]. The plasmon resonance wavelength of a metal nanoparticle is also affected by the presence of other NP in close proximity. When two or more NP are brought close together, their dipoles couple, and a shift in the LSPR mode takes place. An AuNP colloid containing AuNP ~15 nm in diameter shows a typical plasmon extinction maximum at 520 nm. However, if these particles agglomerate (induced by the addition of an

analyte or from a change in pH or increased ionic strength) a red-shift and widening in the extinction band is observed[30,]. This effect has been investigated both theoretically and experimentally for fixed and non-fixed distances[50]. The magnitude of the assembly-induced plasmon shift depends on the strength of the interparticle coupling which, in turn, depends on the distance between individual NP[51]. Therefore, the plasmon shift can give a measure of the distance between pairs of NP. El-Sayed and co-workers derived a method to estimate the interparticle separation from experimentally observed plasmon shifts *in vitro* or in biological systems[52].

1.3 Spontaneous Raman Spectroscopy

When light interacts with matter, a number of outcomes are possible[53]. The light may be absorbed, scattered, or may not interact with the material and may pass straight through it. However when monochromatic light interacts with a material, the vast majority of photons are scattered elastically i.e. with the same frequency/wavelength as that of the incident radiation which is referred to as Rayleigh scattering. However a tiny proportion of photons, *c.a.* 1×10^{-7}, are scattered inelastically i.e. with a different frequency/wavelength to that of the incident radiation[53], as illustrated in Figure 1.7.

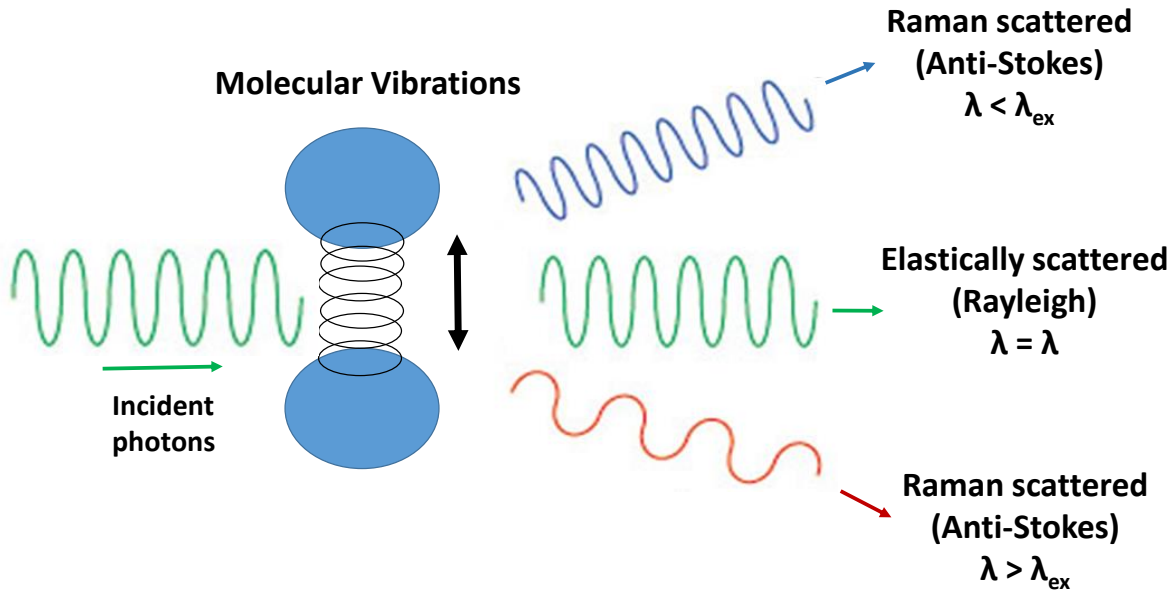

Figure 1.7 *Schematic representation of the Rayleigh and Raman light scattering.*

This phenomenon was first postulated by A. Schmekal in 1923[54] but was not discovered until much later in that decade. Two groups are credited with its discovery, but it is Sir CV Raman that is most closely associated with the phenomenon which was named after him[55–57].

A Jablonski diagram highlighting the different basic types of light scattering is given in Figure 1.8. Raman shifted photons can be of either a higher or lower energy (i.e. anti-Stokes or Stokes), depending on the initial vibrational state of the molecule[58]. The relative intensity of anti-Stokes Raman scattering is significantly less than that of Stokes Raman scattering due to the substantially fewer numbers of molecules that are initially in an excited vibrational state relative to that in the ground state. This energy difference between incident and scattered light corresponds to the difference between the two vibrational energy levels of the molecule as expressed by the Boltzmann population distribution[59], given in Equation 1.3. This states that the natural logarithm of the ratio of the number of particles in the upper state to the number in the lower state is equal to the negative of their energy separation divided by kT.

$$ln\left(\frac{N_1}{N_0}\right) = -\frac{(\varepsilon_1-\varepsilon_0)}{kT} = -\frac{\Delta\varepsilon}{kT} \qquad \textbf{Equation 1.3}$$

Where the lower energy state N_0 contains molecules at an energy of ε_0, and the upper state N_1 contains molecules at an energy of ε_1, k is the Boltzmann constant (1.38×10^{-23} J K^{-1}) and T is the absolute temperature in Kelvin.

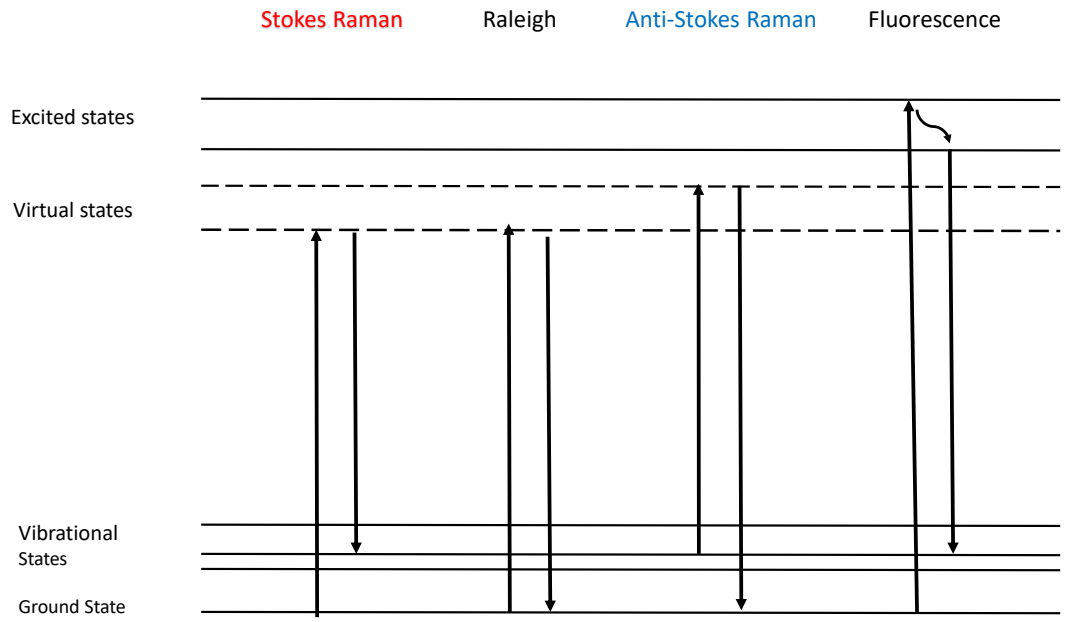

Figure 1.8 *Jablonski diagram for Raman spectroscopy illustrating that the wavelength shift of both Stokes and anti-Stokes Raman scattering either side of the Rayleigh line is the same.*

Raman and infrared (IR) spectroscopy are both forms of vibrational spectroscopy providing information from the interaction of light at a specific wavelength with a molecule. The resulting shift in wavelength of the scattered radiation is converted to a wavenumber ($1/\lambda$) and the difference between the shifted wavenumber with that of the incident light is calculated. In Raman spectroscopy this is referred to as Raman shift with the unit cm^{-1}. The spectrum produced consists of bands corresponding to the energy transitions resulting from specific molecular vibrational differences between the wavenumbers on the horizontal axis and the intensity of signal on the vertical axis. Thus, the horizontal axis relates to molecular vibration information, and the vertical axis relates to the strength of activity. This provides a unique fingerprint spectrum of the chemical and structural information of a molecule enabling its identification and quantification within a given sample. Where IR and Raman spectroscopy differ is that IR bands are the result of a change in the dipole moment of a molecule, whilst Raman bands result from a change in the polarisability of the molecule [60].

As Stokes-shifted Raman bands involve transitions from lower to higher energy vibrational levels these bands are more intense than anti-Stokes bands and hence are measured in conventional Raman spectroscopy while anti-Stokes bands are sometimes measured with fluorescing samples because fluorescence causes interference with Stokes bands. The magnitude of the shifts observed are independent of the excitation wavelength and are instead

dependent on the type of vibration responsible for the scattering. Since Raman scattering due to water is low, water is an ideal solvent for dissolving samples[61]. Raman measurements are typically performed using filters to block the incident light whilst passing the collected scattered light, followed by optical gratings to reflect specific Raman-shifted photons into a sensitive detector[59,63].

Raman spectroscopy is not normally capable of measuring samples with concentrations less than 1% w/v. For bulk samples, the benefits of Raman spectroscopy typically out-weigh its limited sensitivity, but when performing trace analysis spontaneous Raman generally cannot provide the required sensitivity[63].

1.3.1 Surface enhanced Raman spectroscopy

Surface enhanced Raman spectroscopy (SERS) is a means by which large increases in Raman scattering intensity can be obtained, and overcoming the traditional drawback of Raman scattering, *viz.* its inherent weakness[64,65]. With SERS, varying enhancement factors of the order of 10^4 to 10^8 times that of conventional Raman scattering have been observed for molecular species adsorbed on a range of different plasmonic substrate configurations[13]. SERS is of interest for trace material analysis, flow cytometry[66] and other applications where the current sensitivity/speed of a Raman measurement is insufficient. Enhancement takes place at the surface of a metal that has nanoscale roughness[67]. However, reducing the amount of variability in the SERS enhancement signal achieved across the entire surface area of many of the available substrates has still proven to be a major challenge[68].

The largest contributing factor to the enhancement observed is the distance of the adsorbed molecule from the plasmonic surface and its relative orientation[69]. Typically a distance range of 2–4 nm from the metal surface is required to produce the highest plasmonic electromagnetic field contribution to the Raman signal enhancement[67]. While a secondary contribution is thought to be due to a chemical effect involving the mixing of the orbitals of the adsorbed molecules with those of the metal atoms. The range of influence of this effect is much shorter at 1–5 Å[64] and it contributes less to the overall enhancement factor obtained. The SERS enhancement factor (*EF*) has been described by Le Ru and Etchegoin[70] as the ratio of SERS signal to Raman signal obtained for the same molecule in the absence of the SERS substrate

and with all other conditions being identical (Equation 1.4). However therein lies the greatest problem with using enhancement factors when trying to compare often vastly different topographies of SERS substrates. The density of molecules being probed within the incident laser beam focus is also often estimated. The *EF* can be defined as:

$$EF = \frac{I_{Raman}}{N_{Raman}} \times N_{Surf} \times I_{Surf} \qquad \textbf{Equation 1.4}$$

where the N_{Raman} and N_{surf} denote the number of probe molecules which contribute to the normal and SERS signals respectively, while I_{Raman} and I_{surf} denote the corresponding normal Raman and SERS intensities.

Another advantage of the SERS technique involving plasmonic substrates is that the fluorescence background signal can be significantly quenched[71]. This is important because fluorescence quantum efficiency is typically many orders of magnitude greater than that of Raman scattering. In the presence of fluorescence, the Raman signal is seen to sit on top of that of the much broader fluorescent background signal provided that the signal is not saturated.

1.3.2 Surface enhanced resonance Raman scattering

Surface enhanced resonance Raman Scattering (SERRS) was discovered around ~22 years ago[72] and adds the enhancement obtained from resonance Raman scattering to that obtained by SERS. This is achieved when the molecule under analysis contains a chromophore whose absorption maximum overlaps with the excitation wavelength of the laser used, giving rise to additional signal enhancements several orders of magnitude over that obtained from a non-resonant molecule. This phenomenon was first reported in 1997, where such enhancements were achieved through the adsorption of Rhodamine 6G (R6G) onto aggregated silver colloid films and is attributed to the random occurrence of "hot spots," at the films surface[75,76]. In this project malachite green isothiocyanate (MG) was used due to its compatibility with one of the excitation wavelengths used i.e. 633 nm and its low fluorescence[75].

1.4 SERS sensors application and challenges

The earliest SERS substrates involved the use of first silver and then gold electrodes[76, 77]. More recently, less interest has been directed towards the combination of electrode surfaces and plasmon–enhanced optical sensing[31] compared to the application of colloidal systems[78]. There are however clear advantages to be gained from the *in-situ* monitoring of plasmonic sensing surfaces and the changes induced due to electrochemical reactions. This is evident from work by groups in Switzerland[79] and South Korea[80] who have exploited the plasmonic properties of gold and silver nanoparticles and wires for label free in-situ analytical investigation and manipulation through the incorporation of flow cells.

In this section, an overview of different routes related to the preparation of SERS substrates and their applications is provided.

1.4.1 Fabrication of nanostructured materials

Ideal SERS substrates should be highly reproducible and provide optimal signal enhancement with the structure optimized for the largest enhancement[13,87]. The fabrication of nanostructured materials can essentially be split into two processes, that of "top–down" and "bottom–up" methods of creating nanoscale structures. Top–down approaches may be thought of as the creation of nanostructures through the erosion of a larger material from the surface down, either mechanically or chemically to, create nanostructures[68]. Bottom–up approaches involve creating complex nanoscale structures that have been built up from atoms or molecules to form directed/self-assemblies through complex mechanisms[12].

Top-down methods include film deposition[20] and laser[82] and mechanical[83] processing. Lithography is by far the most widely used top-down method employed industrially due to good reproducibility and large-scale fabrication[84]. Disadvantages related to top-down techniques include high cost, low throughput, low area density, and limited spatial resolution below a few nm. However, this has been largely overcome through the sequential deposition of a metal and a spacer[68].

1.4.1.1 Top-down assembly methods

Optical lithography has been used extensively in the manufacture of microelectronic chips manufacturing, with current short-wavelength lithography reaching dimensions just below 100 nm (the traditional threshold definition of the nanoscale[85]. However the use of extreme UV[93] and X-ray[88], are being developed to allow lithographic printing techniques to reach dimensions from 10–100 nm. Electro-beam lithography enables patterns down to about 20 nm. Here the pattern is written by sweeping a finely focused electron beam across the surface[89,90]. Focused ion beams[91] are also used for direct processing and patterning of wafers, although with somewhat less resolution than with electron-beam lithography. Even finer features can be obtained using scanning probes to deposit or remove thin layers.

Nanoscale mechanical printing techniques, such as stamping and moulding have produced substrates with features within the 20–40 nm range. Controlled patterning of a molecular monolayer on a surface has been achieved by stamping an ink of thiol functionalized organic molecules directly onto a gold-coated surface[92]. In another approach, a stamp mechanically presses a pattern into a thin layer of material. This surface layer is typically a polymeric material that has been made pliable for the moulding process by being heated during the stamping procedure[93]. Plasma etching can then be used to remove the thin layer of the masking material under the stamped regions. Thus, any residual polymer is removed and a nanoscale lithographic pattern is left on the surface[94]. Still another variation is to make a relief pattern on a silicon wafer using a photoresist, i.e. a light-sensitive material, typically a polymer, used to produce a patterned film coating on a surface[95] by optical or electron-beam lithography. A liquid precursor, e.g. polydimethylsiloxane[51], is poured over the pattern and then cured to produce a stamp that can then be covered in ink and capillary action ensuring the raised regions of the mask are fully covered and then cured in place. A benefit of this approach is that the stamp is flexible and can therefore be used to print nanoscale features on curved surfaces[96].

These nanoscale printing techniques offer several advantages beyond the ability to use a wider variety of materials with curved surfaces. In particular, such approaches can be carried out in ordinary laboratories with far-less-expensive equipment than that needed for conventional submicron lithography. The challenge for all top-down techniques is that, while they work well at the microscale, it becomes increasingly difficult to apply them at nanoscale dimensions. A second disadvantage is that they involve planar techniques, which means that structures are

created by the addition and subtraction of patterned layers (deposition and etching), so arbitrary three-dimensional objects are difficult to construct[83].

The manufacture and role of porous anodised alumina templates in the production of SERS substrates is discussed in depth later in Section 1.6.

1.4.1.2 Bottom up assembly

Bottom-up synthesis methods for nanoparticles involve creating larger systems from smaller units, including atoms, molecules, polymers, and/or nanoparticles[12]. Techniques used include chemical synthesis[32], laser printing[97], colloidal aggregation[98] and self-assembly[42,105]. Historically, the synthesis of chemically stable silver nanoparticles with high size and shape tunability, as well as monodispersity, has been more arduous than for gold. During the last few years, silver and gold nanoparticles have been prepared in very diverse shapes[12,46]. In addition to tuning the nanoparticle composition, size, and shape, bottom-up approaches also permit fine manipulation of the interparticle distance, making it easier to create hot spots (i.e., the intersection or close interaction of two or more plasmonic objects where the distance between objects is on the nm-scale)[100]. Hot spots are localised regions of highly concentrated, chemically driven assembly of nanostructures that often require linking molecules with specifically selected functional groups such as thiols[101] and amino-acids[102]. Silicon nanowires in a field–effect transistor (FET) arrangement have proved to be a popular choice in the development of optoelectric biosensors[103] as do carbon nanotubes[104] .

1.4.2 Plasmonic SERS nanosensors

Plasmonic nanosensors typically employ metallic nanostructures which support the excitation of SPR upon interaction with light[29,105]. Gold and silver colloidal solutions are by far the most commonly applied plasmonic sensing materials with the colloid either freely suspended having undergone controlled aggregation[98,106] or immobilised on or within a solid substrate[107,108]. These have been shown to support large enhancement factors (EFs) associated with SERS[109], where the weak Raman signals can by enhanced by as much as 10^6 to 10^{14}. There is now a wide variety of different substrate designs associated with attempts to optimise and reproduce the maximum possible SERS enhancement possible but this has continued to be challenging.

Noble metal nanostructures with sharp edges[110] and sharp, pointed tips[111,112] or nearly touching NP dimers[113,114] tend to exhibit some of the highest localised field enhancements.

There are two main approaches to SERS substrate design: (i) bulk solution measurements involving suspended metallic colloid which is often aggregated in a controlled fashion due to salt or the presence of a target[48,106], and (ii) the creation of planar substrates upon which metallic nanostructures are supported[115,116]. The latter option offers more opportunities for reproducibility and multiplexing than colloidal measurements as well as integrating into electrochemical systems. A summary of some of the different plasmonic substrates created on planar supports for SERS is given in Table 1.3.

Substrate	Description	Comments
Bulk metal colloid deposited on a planar substrate.	Nanospheres[117,118] Nanorods[42,119] Cylinders[104] Cubes[46] Pyramids[120] Flowers[37] Shells[121]	Assembled metal nanoparticles on glass slide, forming clusters. Originally only nanospheres, but over time, more shapes were developed. Hot spots can form in the spaces between particles but no uniformity across the surface. The sharp points on stars and pyramids result in a lightning rod effect further enhancing the effect.
Lithography-Based Methods	Electron beam lithography (EBL)[122]	Popular method used since 1990's producing substrates with good reproducibility and flexibility.
	Nanoimprinting lithography (NIL)[83,123]	Colloidal self-assembly and electrochemical deposition methods.
	Bead self-assembly[39] Nano hole templates[124]	Au or Ag nanoholes prepared using polystyrene ball to create nanoholes or covering silica template in a noble metal film.
	Klarite[125]	Gold deposited onto Si wafer structures. Once the industry standard.
	AAO templates[126,112,127]	Two-stage anodisation process. AAO templates can either be totally or partially removed after metal deposition.
Novel Methods	Deposition (no template) e.g. gold islands[128]	DNA scaffolding produced by folding DNA into random structures between islands.
	Oblique Angle Deposition [129]	A physical deposition technique used to produce Ag nanorods.
	Inkjet printing[130] 3D Printing[131]	Single use micro/nanofabricated substrate on disposable hydrophobic cellulose paper. Hotspot-Engineered 3D Multipetal Flower Assemblies
	Simleco[132]	Leaning Silicon Nanopillars covered in noble metals

Table 1.3 *Summary of various gold and silver SERS substrate designs created on a supporting surface.*

While SERS analysis is mostly confined within the visible to near infrared region, as this is where the majority of SERS substrates exhibit the strongest enhancements, tentative progress has been made towards using SERS in the ultraviolet frequency range[13,141,142]. UV SERS is highly desirable, especially in the detection of biological molecules such as protein residues and DNA bases with electronic resonance and SERS enhancement in the deep UV[123]. The challenges of achieving surface enhancement in the UV region include determining suitable substrate materials. Research has focused on the transition metals for this purpose such as gallium[103], cadmium[135] and titanium[136] nanowires which have attracted significant attention.

However, the enhancement factors achieved are many orders of magnitude less than those for silver and gold in the visible range. SERS enhancement in the deep UV has been achieved on Aluminium (Al) substrates[137] at excitation wavelengths of 244 nm and at 266 nm with aluminium tip coated silicon where an enhancement factor of ~210 was achieved[146, 147]. Another major challenge associated with SERS analysis in this region is that of photo degradation of samples[140].

Other metals such as the alkali metals[13] as well as metal alloys[141] have all been explored as plasmonic substrates. However, their reactivity in air presents challenges and limitations for their effective use. Aluminium SPR falls within the UV region as does titanium dioxide[142], and quantum dots. The electronic characteristics and band gap of quantum dots are closely related to their size and shape[143]. By increasing the size of quantum dots, the colour of emitted light shifts from blue to near-infrared, which allows their excitation and emission wavelengths to be highly adjustable, making them attractive for use in sensitive cellular imaging, photovoltaic devices, solar cells, and light emitting devices[144].

1.4.3 Surface functionalisation

From the earliest SERS experiments utilising pyridine, surface functionalisation of noble metal nanostructures has been used extensively in the development of applications for use in areas such as photonics[1], catalysis[145] and forensic[146], however it is their use in biolabelling and biochemical sensing where most interest has been focused. The surface modification of noble metal nanostructures can be modified by thiols[147], disulfides[148], amines[149], nitriles[150], carboxylic acids[151], and phosphine groups[152] with which they have an affinity to bond covalently.

In particular, the strong affinity between sulfur atoms and metal surfaces such as gold enables the immobilisation of thiol containing molecules on the surface of metals. This is underpinned by the relatively high chemisorption energy of 126 kJ/mol involved in facilitating the gold-sulfur (Au–S) bond. The formation of self-assembled monolayers (SAM's) onto the surface of gold substrates is the basis of many immobilisation and surface functionalisation chemistries[12,153,154]. The thiol-modified gold surface can be coupled to different biomolecules

including DNA and RNA sequences consisting of, for example, AuNP functionalised with thiol-modified DNA and incorporating a linker molecule[128].

Amines have also been employed in the functionalisation of silver nanoparticles with hexadecylamine resulting in an improved dispersion and stability of the particles[155]. However, the bond between amino groups and the metal surface is considerably weaker in comparison to that between the noble metal surface and a thiolate group. Both methods can be applied for the modification of AgNP by peptides through thiol or amines. Noble metal NP can be stabilised by the adsorption of tetraalkylammonium halides on the surface of the NP[156].

Typical SERS nanotags consist of a metal nanoparticle core, Raman reporter molecules such as a self-assembled monolayer of small molecules on the metal surface, and a biocompatible layer with targeting ligands[157]. The coating of SERS substrates with ligand molecules of specific terminal groups is extremely effective to boost the selectivity of the SERS substrate[158]. This functionalisation of SERS substrates is particularly useful in the case of complex molecules such as proteins or for molecules with low affinity to metal. The reporter molecules should possess the following qualities:

- High Raman scattering cross sections for high signal levels.
- Low numbers of atoms and/or high symmetry, resulting in a minimal number of Raman bands to facilitate multiplexing.
- Low or no photobleaching, for signal stability.
- Surface groups for binding the metal colloid surface with target molecules.

While, as previously stated, work with nanotags is predominantly within the visible spectrum range, a number of nanotags have been developed for NIR excitation. For example, recent work[159] developing reporters incorporating chalcogen atoms, which adsorbs strongly onto the surface of gold, resulted in exceptional SERS signals at excitation wavelengths of 1280 nm. This has seen picomolar (pM) limits of detection (LOD) with individual reporters identified by principal component analysis and classified according to their unique structure and SERS spectra.

1.4.4 Multiplex SERS analysis

SERS analysis has several advantages for use in molecular multiplexing[160,161]. Compared to absorbance and fluorescence techniques, SERS has narrower spectral widths allowing for the analysis of a greater number of species simultaneously. Low detection limits and good signal to noise ratios enable image applications and also real-time analysis such as high-throughput screening in flow-cytometry[66] or microfluidic systems[12]. In addition, as the SERS spectrum is a unique signature containing all the vibrational information of the target molecule[162], analysis can be carried out under biological conditions with little or no prior sample preparation.

The simultaneous analysis, identification and quantification of several different target molecules within a single sample provides time and cost saving benefits over conventional single analyte analysis[163]. The two general approaches to multiplexing are: (i) analysis of mixtures in the same sample where each target can be spectrally separated, and (ii) an array format where the specific measurement of each analyte is spatially separated on a surface substrate.

Multiplex SERS analysis of mixtures is proving to be an invaluable tool in cellular detection. As a result of real time analysis with the ability to both simultaneously detect and discriminate amongst individual proteins[164] and bacterial pathogens[165]. Noble metal colloidal solutions have been used to attach reporter molecules to strands of DNA that are then used to carry out studies within cells[48], as well as determining how cells respond to various toxins and environmental effects. Multiple analyte SERS detection from a single sample has been made possible using dyes of similar Raman cross sections and affinities for the surface of a metal substrate[166]. Successful multiplex analysis of tissue samples is helping increasingly earlier detection of cancer cell biomarkers[167,168]. At the University of Strathclyde, an example of this type of multiplexing is the application of silver colloidal solutions to monitor multiple dye-labelled DNA sequence strands in a sample[169]. However, one drawback with this approach is the overall SERS intensity of each analyte in the mixture is reduced in comparison to that obtained on a single analyte sample.

Nano-plasmonic materials have been used to support high-throughput screening and multiplexing due to the availability of a large surface area for receptor conjugation[158] or solid phase synthesis[99]. These provide improved accessibility of analytes to the entire sample volume for interaction with receptors and greater versatility in sample analysis and data acquisition

Work continues on improving the repeatability of dispersion of nanoparticles within metallic colloids[49], which may in future help to increase the number of analytes identifiable within a single sample and the signal strength achieved from each.

Noble metal arrays are also used for multiplex SERS analysis. These consist of organised periodic structures across a planar surface that can consist of a myriad of shapes such as rods[119], holes[131], triangles[126], cubes[47] and flowers[37]. While improved uniformity may be achieved, even slight variations in the size, shape and distribution of the component parts of a nanoarray may lead to a notable difference in the intensity of SERS signal across the entire surface area and so affect the reproducibility of the SERS signal under investigation. Often the EFs and the intensity of the SERS signal vary significantly with variation in size and morphology. Metallic nanowires consisting of two or more different materials have been produced by sequentially changing the electrolytic solution during the electrodeposition with the length of each segment controlled throughout the electrodeposition process[170]. These can then be used as platforms for multiplexed bioassays through utilisation of the differential reflectivity of the adjacent segments and the selective self-assembly of appropriate molecules on specific metal segments, enabling identification by conventional optical microscopes. Multisegmented nanowires have been utilised for developing nanogap devices[171]. Qin *et al*.[172] developed a generic approach to lithographically process 1D nanowires called on-wire lithography (OWL). This involves the selective removal of at least one of the segments of the multisegmented nanowire to create gaps, by wet-chemical etching of targeted segments and one side of the multi-segmented nanowires subjected to the deposition of a thin layer of insulting silicon dioxide. In this way nm sized gaps were created from as little as 5 nm up to several hundred nm in length on nanowires. Additionally, by means of dip-pen nanolithography nanoscopic conducting polymer were deposited within the created nanogaps to investigate the transport properties of nanogaps. Chen *et al*[173] demonstrated the use of heterometallic nanogaps for molecular transport junctions. Thiol terminated molecules were assembled into heterometallic nanogaps such as, platinum and gold molecules with a 2 nm gap between them, in order to observe the molecular diode behaviour.

1.4.4.1 Direct SERS detection

Direct detection requires spectroscopic signals from the target molecules to be complex enough to be different from one another. The absorption and emission signals from UV–vis–NIR and fluorescence are broad and lack fine structure making them unsuitable for the multiplex direct sensing of more than two or three molecules at a time[174]. SERS produces a complex vibrational pattern specific to each analyte that can be considered a vibrational fingerprint of that chemical entity. Direct SERS sensing requires the analyte to be as close as possible to the plasmonic surface of the substrate. These methods can only be applied to samples of moderate complexity unless using gold or silver substrates[175] in order to be able to be easily distinguished them from the background components in solution. Non-functionalised plasmonic particles have been employed for the simultaneous determination of textile fibres and dyes[166], thiols / amines in water, prions in plasma[11] and pharmaceuticals[177].

1.4.4.2 Indirect SERS detection

Indirect detection requires functionalisation of plasmonic surfaces with target-specific molecules[178]. This method has two main advantages over direct detection in that it can be used with substances that do not produce SERS signals or possess very small cross-sections, such as atomic ions or small inorganic molecules[179]. The second is in limiting the number of targets to interact with the plasmonic surface. Biomolecules tend to be the most common to be functionalised. The first biosensors were prepared by assembling antibodies (proteins) or nucleic acids onto the plasmonic surfaces[111,118]. Also, aptamers are becoming more popular [180] due to their simplicity of synthesis, in comparison with antibodies[164], and improved target specificity. However, due to the fact that most of the proteins and nucleic acids have a low to moderate SERS cross-section, SERS and fluorescent Raman reporters are used to identify specific biomolecules and their interactions. Recent advances in the fabrication of nanophotonic substates[181,173] has allowed the preparation of highly active SERS platforms[68], thus, paving the road for the label-free detection of the bio-interlayer and their interactions[184].

Again as with direct detection, problems arise due to vibrational overlapping of the modes of the different specific biomolecules. However, it is even more so here as indirect detection is dependent, on minute changes in the vibrational spectra of the free ligand as compared with the complexed one[185]. Thus, although this functionalisation usually works perfectly well for the selective determination of single analytical targets dispersed in complex fluids (i.e. blood,

plasma, urine) the multiplexing capability of this approach is not comparative with that of encoded particles.

Indirect SERS detection with encoded particles utilising nanoparticles, or hybrid microparticles[45], as SERS-active quantitation labels, has been employed. Externally labelled particles have been produced by adding dyes[186], photonic crystals[187], or quantum dots to silica[188] or polymer particles[143]. The chemical/physical nature of the particle such as shape, vapour permeability[189], spectroscopic properties have also been used as a codifying alternative. The use of SERS as labelling alternative is rapidly gaining relevance not only because of its unprecedented detection limits that dramatically decrease the detection times, but also owing to the practically unlimited number of fingerprints that can be used for simultaneous detection.

1.4.5 Reproducibility of SERS signals

Interest in SERS is predominantly fuelled by the high signal enhancement that can be achieved. However, SERS enhancement factors can vary substantially and not only from one sample to the next for a given substrate but also across the entire surface of each individual sample. Thus, consistent reproducibility of achieved results has proved to be somewhat elusive. Substrates made using colloids, where particle aggregation abounds, or roughened surfaces, suffer from an inability to control the uniformity and spacing between features[190]. As a result "hot-spots" i.e. areas exhibiting high enhancement are randomly interspersed amongst relatively large areas where little or no enhancement occurs. In this case identification of these hotspots, in order to maximise signal enhancement from a substrate, requires both time and a level of skill that precludes their use commercially[131].

Lithographic methods have facilitated the fabrication of well ordered, periodic noble metal nanoparticle arrays[79,191]. However there is a risk that the improved signal repeatability is at the expense of enhancement[68]. Noble metal arrays are organised periodic structures across a planar surface that can consist of a myriad of shapes such as rods[119], holes[131], cylinders[109], triangles[126], and cubes[47] and flowers[37]. While improved uniformity can be gained, Gopinath et al. found that even slight variations in the size, shape and distribution of the component parts of a nanoarray can lead to notable differences in the intensity of SERS signal and therefore the reproducibility of SERS signal that can be achieved[126].

The measured SERS signal is an average of the signal obtained across a given area. Therefore, random orientations of the reporter molecules can affect the repeatability of signal due to the uniformity of the orientations of all adsorbed molecules on a substrate. For the optical absorption process, the effective Raman cross-section of molecules is linked to their orientation and relates to the intensity and direction of incident light to that of the intensity of light scattered by the molecule[20,192]. The quality of the instruments constituent parts, such as the objective lens, laser frequency, incident power, temperature and integration time all play a part in the reproducibility of signal. Indeed Etchegoin *et al* observed that different laser powers induce different SERS EF's[193]. Variations in instrumental excitation, transmission and detection efficiency as well as variations in laser spot size will affect the reproducibility of the SERS signal achieved. Therefore, it is essential to keep the optical system used as stable as possible. However normalising the signal obtained can eliminate/reduce instrumental variations[194].

A significant motivation of this thesis is to create uniform SERS arrays of high reproducibility and signal enhancement with the SERS substrate manufactured via the use of porous AAO templates.

1.5 Anodised Aluminium Oxide

Aluminium is a soft and lightweight metal that is silver-white in appearance. It has a high thermal conductivity, excellent corrosion resistance and is both non-toxic and nonmagnetic. It is the second most malleable and the sixth most ductile metal and does not spark when struck[195]. Aluminium is a good electrical conductor, far superior to and cheaper than copper and is often used in electrical transmission lines[196]. Alloys made from aluminium with copper, manganese, magnesium and silicon are both lightweight and strong. When evaporated in a vacuum, aluminium forms a highly reflective coating for both light and heat. Unlike silver coatings, it does not deteriorate and thus aluminium coatings have many uses, including mirrors, films and decorative items[195].

While aluminium is one of the most abundant metals in the Earth's crust it is rarely found uncombined in nature due to being highly reactive. It reacts readily in an oxygen rich environment to form aluminium oxide (Al_2O_3), see Equation 1.5, commonly referred to as alumina, occurs naturally and is predominantly found in the mineral bauxite comprising of a

mixture of aluminium hydroxides and oxyhydroxides in addition to a number of impurities, mostly iron oxides and silicates[197,198].

$$2Al^{3+} + 3O^{2-} \rightarrow Al_2O_3$$ **Equation 1.5**

Campbell *et al*[199] found that a 4 nm thick oxide film formed on the surface of aluminium within 100 ps of the exposure of aluminium to oxygen. Conditions such as surface morphology and crystallography are found to have a significant effect on the surface film growth rate, composition, surface topography and crystallography. During prolonged heating to 500–600°C the oxide film grows to 100–400 nm. While at temperatures of 300°C and below the oxide takes the form of a continuous amorphous film, the thickness of which can be controlled by temperature. At higher temperatures oxide films comprising of both amorphous and crystalline oxides are formed, with the amorphous inner layer having a thickness of 1–1.5 nm[196]. The growth of the oxide film occurs by the outward diffusion of cations through the oxide film at low temperatures, and the inward migration of oxygen at high temperatures. The rate of film growth or thickening is temperature dependent and ultimate thickness is reached in about 20 hours[198].

Anodic oxidation (anodisation) of metals is an electrochemical process that enables the controlled formation of a surface oxide, thus changing the surface texture and nature of the film formed on the material. As previously stated aluminium when exposed to an oxygen rich atmosphere at ambient temperature self-passivates through the formation of a protective oxide layer between itself and its surrounding environment. Aluminium oxide is described as amphoteric[200], that is to say that while it primarily acts as a base it can also ionise to form a weak acid. Two anhydrous forms of aluminium oxide exist, α-$Al_2O_3$and γ-Al_2O_3, as well as two hydrated forms corresponding to the stoichiometries AlO.OH and Al(OH)[201].

Anodised aluminium is used in the manufacture of electronic components and capacitors, cookware, indoor and outdoor domestic products, medical equipment and devices, vehicles, architectural and construction materials, to name but a few. Increasing the thickness of the oxide layer provides a barrier to corrosion[195]. This was first used commercially in 1923 to protect parts of seaplanes from corrosion and known as, the now largely redundant, Bengough-Stuart Process[202] using a chromic acid based electrolyte solution. That year also saw the first use of oxalic acid with Gower and O'Brien popularising the use of sulfuric acid in 1927[203].

Phosphoric acid was introduced as an electrolyte in the anodisation process mid-century[204]. However, sulfuric acid remains to this day the most widely used[205]. In recent years, this long established process has been utilised in the field of nanotechnology. Whereby the novel structural features of porous AAO films that can, to a large extent, be tuned to each end users specific requirements has enabled their use in synthesizing a wide range of nanostructured materials[205, 206].

Two types of anodic oxide films can be grown on an aluminium surface, porous and non-porous[208]. Tartaric acid and sodium borate are examples of electrolytes used to produce non-porous alumina films[209]. Anodisation by acidic electrolytes such as phosphoric, sulfuric and oxalic acid form a porous alumina film on top of a non-porous barrier layer[210].

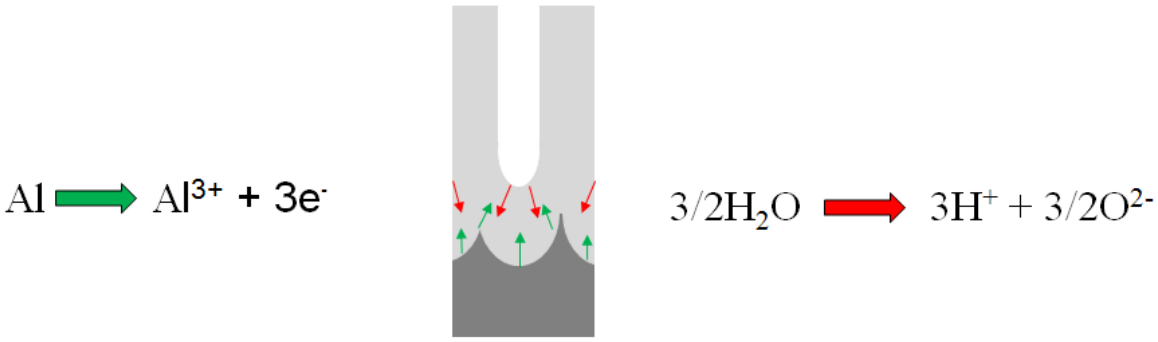

Figure 1.9 *Al^{3+} ions form at the aluminium/aluminium oxide interface and migrate into the oxide layer where they meet O^{2-} ions formed at the aluminium oxide/oxalic acid interface to form Al_2O_3.*

The hexagonal porous film formed consists of cylindrical pores that are perpendicular to the surface of straight non-intersecting channels with pore densities of up to $10^{11}/cm^2$. See Figure 1.9 The diameter of the pores are within the range of 5 – 100 nm and is a linear function dependent upon the anodisation voltage. In both cases, the film growth involves the migration of Al^{3+} ions and O^{2-} ions in the alumina by Brown and Mackintosh in 1973[211].

The choice of electrolyte too influences the pore size. The thickness of the porous film formed depends on the anodisation time whereas the thickness of the barrier layer is voltage dependent only[198]. Table 1.4 demonstrates the use of different acids and voltages can yield templates with different pore sizes and interpore spacings[212].

Electrolyte	Chemical Formula	Pore diameter (nm)	Inter pore spacing (nm)	Voltage (V)
Sulfuric acid	$H_2 SO_4$	30 – 55	60 - 70	25 – 27
Oxalic acid	$H_2C_2O_4$	40 -100	80 - 200	30 – 80
Phosphoric acid	H_3PO_4	130 -250	250 - 500	100 – 195

Table 1.4 *The expected pore diameter and interpore spacing produced in a hexagonally ordered porous alumina film that can be achieved across the optimum voltage range for each electrolyte.*

The porous film that forms on top of the non-porous barrier layer consists of an array of self-ordered hexagonal pores which form a honeycomb-like structure[213] as illustrated in Figure 1.10.

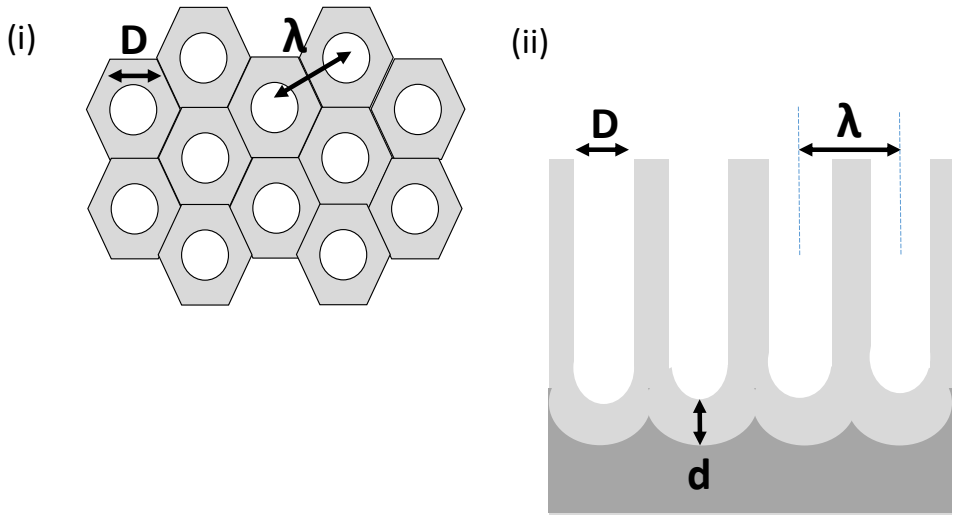

Figure 1.10 *Schematic illustration of (i) the honeycomb like pattern on the surface of a porous anodic aluminium oxide (AAO) film on top of aluminium base and (ii) cross-sectional view. D = pore diameter, λ = interpore spacing and d= barrier layer thickness.*

Porous AAO fabricated by the anodisation of aluminium in an acid electrolyte, can be carried out either under a constant potential[214] (i.e. potentiostatic) or a constant current[215] (i.e. galvanostatic) conditions. The potentiostatic anodisation method is the most widely employed for the fabrication of self-ordered porous AAO. There is a linear relationship between the applied potential and the structural parameters of the resulting AAO. In the case of galvanostatic anodisation the potential changes as a function of time. Under constant-current conditions, in accordance to Faraday's Law[16] the oxide growth rate should be proportional to the applied current density with a constant electric field required to sustain the applied constant

current resulting in the thickness of the growing barrier oxide increasing with increasing potential. However, in practice, the increase in potential is not linear with time. The various mechanisms involved, such as surface undulation/pore initiation during aluminium anodisation result in morphological instability during the transition from the formation of barrier layer oxide growth to that of porous oxide growth. Su *et al.*[216] has proposed the field-dependent nature of the heterolytic dissociation of water in the reaction have related the dissociation rate of water to the porosity of AAO.

The porous nature of AAO was initially used for aesthetic purposes. The pores were impregnated with dye and sealed, a technique widely used in the production of many household and decorative items in the 1950's and 1960's[195]. A variety of coloured effects was produced through the electrochemical deposition of dyes and metal salts into the pores. The exact mechanism of which was not known and indeed initially attributed to the formation of complex salts incorporating the metal oxides. However. this myth was subsequently dispelled through initially Keller's investigations into the morphology of porous alumina in the 1950's[204]. This was followed a decade later by the self-ordered growth mechanism proposed by research carried out in the 70's by O' Sullivan and Wood[201]. TEM analysis has also identified un-oxidised aluminium within the anodised film[217].

Work carried out in the early 1970's revealed, through the images obtained by electron microscopy from cross sectional analysis of porous anodic alumina films grown in both acid and alkaline electrolytes, smaller 'secondary' cells branching off from the main pores[218]. These branches were found to occur in both thick and thin films and were not affected by either sample pre-treatment or sub-grain structure. Recent work carried out at Imperial College has linked this phenomenon to the deployment of anodisation voltages greater than 24 V[219]. Branching at lower voltages either did not occur or was greatly reduced. This property has been utilised to help understand the ordered pore formation in a thin film of porous alumina on a polycrystalline sample of annealed aluminium.

Traditionally, during self-assembly porous alumina template formation, the ordered pore structure of the aluminium oxide is formed by 'mild anodisation' a two-stage anodisation process developed in 1995 by Masuda and Fukuda[220]. After the initial long anodisation stage, typically of duration of twenty hours and subsequent removal of the thick porous alumina film formed, an imprint in the underlying metal surface is revealed which can then be used as a

template with which to grow a thin highly ordered porous alumina film. Careful control of the operating conditions, such as voltage, electrolyte and temperature, enables control of morphology with the porous film thickness determined by the time of the second anodisation. The lengthy initial anodisation period is required due to the grain boundary breakdown of pore ordering within the grain domains. However this problem can be overcome by imprinting the sample surface with a silicon carbide template that yields a 'dimpled' surface, similar to that produced by the first anodisation process of AAO template production [221]. Studies have shown that this first anodisation period can be reduced substantially with no discernibly impact on the resultant template[222]. In addition, this process can be used to produce films with pores arranged in a square rather than hexagonal pattern[223]. Barrier layer thickness was widely thought to remain constant throughout the steady state growth due to a dynamic equilibrium between the rate of pore growth at the metal/oxide interface and that of field assisted dissolution at the oxide/electrolyte interface. However in recent years this mechanism has been disputed through tungsten tracer studies[224], which failed to detect any significant amount of the expected field assisted dissolution but instead found a flow of ions from pore base to cell suggesting the dissolution takes place via the ejection of Al^{3+} into the electrolyte with the oxide formation due to oxygen transportation.

1.6 Development of AAO nanomaterials

Porous alumina structures have played an important role in the development of nanomaterials with the pores providing tailor-made vessels to facilitate the production of nanorods [127] and wires[225] of specific length, width and morphology. The electrochemical templating method is especially useful for small areas in the mm^2 size and is therefore highly suitable for the fabrication of thin films suitable for nanorod formation and their subsequent charactersiation[226]. Research in this area has focused on producing films of between a few nm to several µm thick in addition to extending the range of surface area covered[227]. As well as altering the interpore spacing by increasing the voltage range of the existing techniques as well as the search for new electrolyte solutions[228].

1.6.1 Electroless deposition

Electroless deposition of the metal into the nanopore array has many benefits, not least allowing the subsequent formation of non-conducting compounds as well as deposition onto non-conducting substrates. In the case of porous alumina films, it allows the deposition of conducting materials without the need to first thin/remove the electrically insulating, non-porous barrier layer that separates the porous alumina film from the aluminium metal base [229,230] . Typically, once the desired structure has been formed the template is either partially or completely removed [231–234]. One of the simplest methods of production is that of sputter coating that can produce metal or silica arrays. Chemical vapour deposition[232, 233] (CVD) is used in the formation of carbon nanotubes, which can in turn be used as templates[28]. Intricate multi-walled carbon nanotubes are produced by predominantly the arc-discharge method or from the metal-catalysed decomposition of ethylene in a hydrogen environment.

Electroless deposition of metals into porous templates by Martin *et al* [237] initially concentrated on the electroless deposition of gold within the pores of track-etched polycarbonate membranes. The deposition process consisted of three stages:

1. Sensitisation: by immersing the porous template into an aqueous solution of $SnCl_2$ to deposit Sn^{2+} onto the surfaces of the membrane.
2. Activation by dipping the Sn^{2+}- sensitised template into a $AgNO_3$ solution, forming AgNP on the surface through.
3. Electroless deposition by immersing the template into a gold plating solution, in which the surface-bound AgNP act as catalyst for the reduction of Au^{+} to form AuNP on the template surface.

The AuNP act as autocatalysts for the reduction of Au^{+} to Au along the entire template surface and into the pores form nanotubes supported on a continuous gold film[227,234,235]. These have proved useful in selective ion-transport, biosensing[180], and electroanalysis[239]. However it has been noted that this type of electroless deposition method does not work in porous AAO templates because of insufficient binding sites[240] for the Sn^{2+} on the pore wall surfaces. This problem can be overcome by modifying the surface of the porous AAO template with 2-(succinic anhydride) propyl trimethoxysilane (SAPT), forming a covalent Al−O−Si bonds with functionalised OH on the oxide surfaces. Anhydride in the SAPT molecule hydrolyses to

dicarboxylic acid, which then chelates tin ions (Sn^{2+}) during the sensitisation process[221]. The incubated porous AAO membrane are treated with 35% hydrogen peroxide solution prior to Sn^{2+} sensitisation to increase the density of oxygen groups on the oxide surface[241].

The rate of electroless gold deposition increases with the pH of the plating bath[242]. At a high temperature, the porous AAO has been found to dissolve[243] and the pores of the AAO template become closed due to the higher rate of metal deposition relative to the rate of mass transfer of gold and formaldehyde down into the pores[240]. Yu *et al.*[244] reported that gold nanotubes formed by electroless deposition are characterised by a nanoclustered morphology, in which the size of the gold nanoclusters increases with the pH of the plating bath. They showed that the size of the gold nanoclusters determines the catalytic properties of gold nanotubes embedded in an AAO membrane.

1.6.2 Electrochemical deposition

Electrodeposition of metals into the pores requires either total or at least partial barrier layer removal[245–249]. The thinning of the barrier layer is essential to enable a current to pass though the effectively electronically insulating barrier film. Even with the thinner barrier layer, an a.c current of sufficient magnitude and frequency typically in the range of 10^1 to 10^2 Hz, is normally employed to force the current across the barrier layer, allowing for the deposition of metals into the pores during the cathodic part of the sinusoidal cycle[127]. The technique of electrochemical deposition of metals into a track-etched mica template to obtain 40- nm-thick and 15-μm-long Sn, In, and Zn nanowires was introduced by Possin[250]. Electrochemical deposition of materials into the pores of AAO template provides a number of advantages over other preparation methods of nanostructures, such as chemical vapour deposition[236] (CVD) atomic layer deposition[31] (ALD), and physical vapour deposition[129] (PVD). Electrochemical deposition into a porous template is simple and inexpensive, and can be performed without any specialist instrumentation[24 , 226, 246–248].

A common method of producing nanowires involves depositing a thin silver layer onto one face of an AAO membrane[255]. This silver layer then acts as the working electrode allowing the electrochemical deposition of a thin layer of sacrificial silver or nickel into the pores, to avoid the deposited nanowire spreading out at the pore mouth. The selected material is then

electrochemically deposited. The resultant nanowire/AAO composite sample produced is then is dipped into a nitric acid solution to remove both the silver working electrode layer and the silver or nickel sacrificial layer. The nanowires are subsequently collected by dissolving the AAO template in either a potassium hydroxide or phosphoric acid solution. The pore size of the porous AAO template determines the width of the nanostructure, while their length is proportional to the total amount of charge passed during the electrochemical deposition. Various metal nanowires (e.g. gold[42], silver[256], platinum[257], nickel[14], copper,[258] zinc oxide[259], and cobalt[257]) have been synthesised into porous AAO templates.

Pulsed electrochemical deposition[258, 259] has been used to produce multi-segmented nanowires with prescribed periodicity to fabricate gold/nickel, silver nickel and copper/nickel superlattice films[229,262,263] using a two component electrolytic solution containing salts of the nickel and either gold, silver or copper. Alternatively pulsing the cathodic potential between values above and below the reduction potential of the less noble metal component. As the less negative potential is pulsed, the more noble metal is exclusively deposited. However, on depositing a less noble metal, the more noble metal can be co-deposited. Therefore, it is necessary to ensure the concentration of the nobler metal ions is less than that of the less noble metal ions to allow the deposition of the nobler metal ions during pulsing of the more negative potential to be limited by ion diffusion.

Pulsed electrochemical deposition has been extended by other researchers to prepare multilayered films with alternating magnetic/nonmagnetic metals[264] Recently, Liu and coworkers[265] have demonstrated fabrication of tailor-made inorganic nanopeapods by pulsed electrochemical deposition of cobalt/platinum multilayers into porous AAO template, followed by a solid-state reaction between cobalt and aluminium oxide at a high temperature. Fabrication of multi-segmented metal nanotubes has also been demonstrated by Lee *et al*.[266] This method was based on the preferential electrochemical deposition of metal along the surface of pore walls decorated with metallic nanoparticles. Immobilised Ag nanoparticles (AgNP) were deposited on the pore wall surfaces of an AAO template by the spontaneous reduction of silver. The process for AgNP immobilisation is a slight variation of the well-established sensitisation-pre-activation protocol used with AAO and track-etched polycarbonate templates prior to the electroless deposition of metals[267]. Sn^{2+} ions are first chemisorbed on the pore wall surfaces by dipping the AAO membrane for two minutes into an aqueous solution of 0.02 M stannous chloride in 0.01 M hydrochloric acid. After thorough rinsing with water and drying, the

resulting AAO template was immersed into 0.02 M $AgNO_3$ solution. The cycle was repeated several times resulting in uniform deposition of AgNP on the oxide surfaces. These AgNP, immobilised on the AAO template facilitate the electrochemical formation of metallic nanotubes within the AAO pores. By periodically changing the electrolytic solution during electrochemical deposition to create nanotubes consisting of multiple metal segments.

1.6.3 Polymer nanostructures

In addition to metals semiconductors[267] and conducting polymers[141] are increasingly utilised in the development of nanostructures. Park and co-workers[51] found that two-component nanorods consisting of metal/conducting polymer layer can behave as mesoscopic amphiphiles. The synthesised segmented gold/polypyrrole nanorods were created by electrochemical deposition of gold into porous AAO template, followed by electrochemical polymerisation of pyrrole with the length of each segment controlled by the deposition time. These nanorods, once removed from the template, exhibited amphiphilic characteristics because of the hydrophilic gold segments and hydrophobic polypyrrole segments.

Electropolymerisation[268] is used in the synthesis of conducting polymer nanotubes within AAO pores as well as track-etched polycarbonate membranes. Electrically insulating polyacrylonitrile (PAN) nanotubes have been produced by dipping a porous template into a solution containing acrylonitrile and a polymerisation reagent[269]. While Steinhart *et al.*[270] developed a method based on the spontaneous spreading (or wetting) of a polymer melt or solution on a surface with high surface energy. The direct contact of porous inorganic templates (i.e. high-surface-energy materials) with polymer melts or solutions (i.e. low-surface-energy materials) results in the immediate wetting of pore wall surfaces with thin precursor film. They suggest that pore wall wetting is kinetically stable (but thermodynamically unstable), when the strong adhesive forces between the liquid and solid are neutralised upon complete surface wetting, due to the finite surface area of an individual pore of the template. To attain a thermodynamically stable state (i.e., complete pore filling), the cohesive force should dominate the viscous forces of the wetting liquid. Thus, pore wall wetting and complete filling occur on different time scales with the latter requiring several months or even several years of time. Complete pore filling was found to occur when the pore diameter of the porous template is smaller than the thickness of wetting layer (10−30 nm). The wetting layer thickness is thought

to be dependent on both the nature of the chosen polymer and the surface state of wetting solid as in the case of polystyrene melted into the pores of AAO results in arrays of polystyrene nanowires, rather than nanotubes they suggest that wetting of polymer melt or solution would occur through surface diffusion[271]. Therefore, individual polymer chains should align. Almost all polymer solutions with a low surface energy can be used to synthesize functional or composite nanotubes. Preparations of polymer nanotubes with high technical importance such as polyether ether ketone (PEEK) or polytetrafluoroethylene (PTFE), both of which are very difficult to process by conventional methods (e.g., extrusion or injection moulding of polymer), have been demonstrated by wetting of polymer melt impregnation into porous templates[272]. Multicomponent composite nanotubes[273] have also been utilised to prepare inorganic nanotubes, whereby the polymers are mixed with inorganic precursors that act as a carrier in the wetting process. Chemical transformation of the inorganic precursors within the composite nanotube walls yields inorganic nanotubes[274].

1.6.4 AAO mask techniques

Mask Techniques have been used to produce two-dimensional (2D) periodic arrays of nanostructures of metal[275], complex metal oxide[276] and semiconductor materials [277] to be used in applications such as electronic/optoelectronics, bio-sensing as well as high-density data storage. In 1996 Masuda *et al* reported the first fabrication of arrays of gold nanodots on a silicon substrate by using ultrathin AAO as a stencil mask for depositing gold. The group then added to these findings in 2000[278, 279]. Since then, thin AAO-based surface patterning has become increasingly popular due to offering quicker throughput time, reduced cost benefits, and good compatibility with high-temperature nanofabrication processes, in comparison to other surface nanopatterning techniques such as electron-beam direct writing (EBDW)[280], focused ion beam (FIB)[91], nanoimprinting lithography(NIL)[83], and scanning probe microscope (SPM)-based writing)[81]. Ultrathin AAO membranes can be transferred onto desired substrates by supporting AAO membranes with appropriate polymers (typically, poly(methyl methacrylate) (PMMA) or polystyrene (PS)[282]. A thin polymer layer is coated onto one face of an ultrathin porous AAO film, with both the barrier layer and aluminium substrate completely removed. The resulting AAO/polymer composite film is then transferred onto the required substrate where the polymer is removed by immersing the sample into an appropriate solvent or by oxygen plasma. However, this method is only suitable for use on a small scale as placing

largescale ultrathin AAO membranes onto a substrate often results in damage to the ultrathin AAO. Wafer-scale ultrathin AAO membranes (thickness = 200 nm) onto hydrophilised substrates by the selective etching of the aluminium base leaving an aluminium frame surrounding the AAO film which stabilised the ultrathin AAO film during transfer[283]. The ultra-thin AAO is first attached onto the wafer-scale substrate before removing the backside Al and alumina barrier layer. Ordered arrays of nanoholes[284] have been fabricated which because of their high regularity and density, have resulted in these nanostructures exhibiting many interesting properties that can be exploited in the development of effective antireflection structures[20], high performance electrodes [285] waveguides and photonic crystals[12] and optical devices[286]. Nanorings of gold[285] and bismuth ferrite (Bi FeO_3)[286] have been produced as well as nanopillars[289] whereby conducting polymer nanopillars of poly[3,4-ethylenedioxythiophene]:poly[styrene sulfonate] (PEDOT:PSS) were prepared for use in cell adhesion studies with cells fabricated using ultrathin AAO membranes masks. Nanodots can easily be produced by depositing a desired material through an ultrathin AAO membrane, in which the array pattern, size and inter space distance of the nanodots are defined by those of the ultrathin AAO mask[290]. Most physical vapour deposition (PVD) methods can be employed to create surface nanostructures, including e-beam evaporation[291], sputter deposition[292], and molecular beam epitaxy [293](MBE).

Fabrication of gold nanotube membranes through sputter deposition of thin gold film on the pore wall surfaces to produced nano-baskets. When followed by the electrochemical deposition of gold, to thicken the metal layer and subsequent removal of the AAO membrane by with a 30 wt % phosphoric acid solution produced a free-standing gold nanotube array membrane. This was then transferred onto the substrate of choice[294,295]. These were found to have a high degree of flexibility, enabling adhesion to curved surfaces. The inner diameter of the gold nanotubes is again controlled by deposition time. Thus smaller nanostructure smaller than the pore diameter of the starting AAO can be fabricated. Metal meshes have been utilised as stencil masks for patterning in the manufacture of transparent conductive electrodes[296], as well as metal-assisted chemical etching of silicon wafers used in the preparation of arrays of silicon nanowires in order to control size, surface morphology, and crystallographic [297]. However subsequent chemical vapour deposition (CVD) of materials into the pores of the AAO achieved uniform deposition of materials on the entire surface of the pore walls has proved to be a challenge. A fast rate of deposition may cause blockage of pores. The uniform deposition of carbon was first reported by Kyotani *et al.*[298] who performed the thermal decomposition of

propylene at 800 °C. Pyrolytic carbon deposition from propylene resulted in carbon tubes within the pores of AAO. Multiwalled carbon nanotubes (CNTs) embedded in porous AAO have also been obtained by CVD of a gaseous precursor, such as acetylene, in the temperature range of 550−650 °C in the presence of electrodeposited Co catalyst at the bottom of AAO pores[299]. The ordered arrays of CNTs have been utilised as field emitters[290], and platforms for intracellular delivery[300]. Porous AAO has also been utilised as a structure-guiding template in CVD growth of nanowires. It has been well established for the vapour-liquid-solid growth of silicon nanowires, that the nanowires grow preferentially along the ⟨111⟩, ⟨112⟩, or ⟨110⟩ directions depending on the diameter. While vertically aligned silicon nanowires on silicon substrate are popular for most practical applications in the current complementary-metal oxide-semiconductor technology[301]. Shimizu *et al.*[302] demonstrated homoepitaxial growth of silicon nanowires on a silicon substrate by utilising porous AAO as an orientation guiding template. This has been employed by Gorisse *et al*.[303] to prepare extended arrays of vertically aligned silicon nanaowires with tightly controlled diameters.

1.6.5 Novel AAO nanostructures

AAO templates are being increasingly used in the fabrication of novel nanostructures. A process pioneered by Martin *et al*. was used for the synthesis of a variety of semiconductor and insulator oxide nanostructures such as titanium dioxide[304], zinc peroxide[305], manganese dioxide[306], cobalt oxide[307], and silicon dioxide[308]. This method involves sol−gel deposition into the pores of an AAO template through the hydrolysis of precursor molecules, such as metal alkoxides in an organic media or inorganic salts in an aqueous media, in the preparation of a suspension of colloidal particles (sol) and their subsequent condensation to obtain a gel. Subsequent groups have produced inorganic nanotubes and wires by dipping the template directly into a solution containing sol particles for a set period of time[309]. These have been used extensively in the development of photovoltaics[310], gas sensing[311], ferromagnetic/electric[312], superconducting[313] and luminescence[314] properties.

Immersion of porous AAO template into a sol solution for prolonged periods of time produces nanowires[136], while immersion for short periods of times yields nanotubes[315]. The formation of these nanotubes indicates that the sol particles are adsorbed onto the pore wall surfaces due to electrostatic interaction between the negatively charged pore wall surfaces and the positively

charged sol particles. The formation of the nanotubes is heavily dependent on the temperature of the sol solution[316]. Short dipping times of less than 1 min produced 'bamboo-like' nanowires prepared from a sol solution at 50 °C. Whilst perfectly smooth walled nanotubes were synthesised from a solution at 5 °C. This showed that as the temperature of the sol solution decreased, the inside wall of silicon dioxide nanotube became smoother. Limmer *et al*. pointed out that filling of sol particles into oxide nanopores is mainly driven by the capillary force[114]. Heat treatment of sol-coated AAO templates often results in porous nanostructures or hollow tubes due to insufficient packing of sol particles with the oxide nanopores. An electrophoretic sol−gel process has resolved problems associated with low particle packing density[317] with utilisation of the electrophoretic motion of positively charged sol particles under an electric field. However, this method is not suitable for use with porous templates of small pore diameters.

Lipid bilayers[318] on porous AAO substrates have been found to be electrically insulating, and their ion-channel proteins, reconstituted in bilayer membranes, are fully functional. The optical transparency of porous AAO substrates enables fluorescent molecules deep inside its pores and lipid membranes at the surface of the pores to be examined by confocal laser scanning fluorescence microscopy[319]. This technique when combined with a label-free nanoporous optical waveguide sensor developed by Hotta *et al*.[320] enabled changes in reflection spectra of the AAO/aluminium layered films that were measured in the Kretschmann configuration[321], similar to the conventional surface plasmon resonance (SPR) sensor.

Semi-conductor quantum dots comprising of particles only a few nm in size have aroused much research interest. Their optical and electronic properties differ from that of larger light-emitting diodes (LEDs) that emit light when an electric charge passes through them, in that their band gap and electronic characteristics are closely related to their size and shape. Thus by increasing the size of the quantum dots, the colour of emitted light shifts from blue to near infrared, allowing the excitation and emission wavelengths to be highly adjustable[322]. This quality makes them ideal for use in sensitive cellular imaging, photovoltaic devices, solar cells, and light emitting devices[323]. The characteristic long-lived plasmonic excitations of semiconductor quantum dots, embedded in the pores of AAO film, in combination with the SPR of metallic nanostructures has proved beneficial in optical coupling at the nanoscale level[324].

1.7 Project Aims

This study aims to produce and utilise a porous anodic aluminium oxide (AAO) template and focuses on the optimisation of sample preparation, both template and gold nanorods, with the controlled etching back of the porous alumina to expose the gold nanorods. Indeed rather than removing the rods from the template, as is common practice, here the template remains in place and is instead etched back only as far as to expose the rods. Thus the template helps not only to support the deposited gold nanorods which are of several hundred nm in length, but also, by keeping the aluminium base in place, it enables electrochemical reactions to be performed on the gold nanorod arrays.

The central aim of this thesis was to produce and utilise porous anodic aluminium oxide (AAO) templates with which to develop electroactive SERS substrates by means of the following:

- The controlled anodisation of an electro-polished aluminium sample to create a porous alumina template with a defined pore size on an aluminium base.
- Develop a quick method to measure the alumina template film thickness.
- Develop a method for partial removal of the alumina barrier layer to enable electrochemical deposition of gold into the pores to create gold nanorod arrays (AuNR).
- Develop a method for the controlled etch-back of the alumina template to expose the vertically orientated AuNR whilst keeping the template in place;
- Characterisation of the substrate;
- Determine the effectiveness of the AuNR as a substrate with both resonant and non-resonant reporter molecules through comparison studies with known SERS substrates;
- Comparison of the signal strength of resonant and non-resonant reporter molecules at excitation wavelengths of 633 nm and 785 nm;
- Determine the robustness of signal and recyclability of the substrate;
- Design a flow cell to enable in-situ electrochemical polarisation experimentation;

- Devise a method to enable the selective electrodeposition of gold into the pores of the AAO template to create patterned surface to enable multiplex sensing on a single AuNR surface.

1.8 Thesis overview

Chapter 1 has introduced the concepts of sensors, properties of metals, plasmonics, SERS and AAO giving a brief overview of the history and background of the area of research in addition to literature pertinent to this thesis. It is in this chapter that the aims of this study are stated.

Chapter 2 examines the interaction of light with materials and lays out the underlying theory for light absorption, reflectance and ellipsometry. The fundamentals of electrochemistry are then explored leading to the electrodeposition of metal particles. The preparation of the anodised alumina templates is then described, starting from the basic electrochemical metal dissolution reaction to the formation of the barrier layer and under certain conditions, pores-size formation and control.

Chapter 3 states the materials, instrumentation and methods employed during this research work, listing the chemicals and giving the basic protocols used in the electrochemical measurements, Raman spectroscopy and Dark-field imaging.

Chapter 4 presents the procedures employed in the production of the alumina template from annealed high purity aluminium samples. The analysis of the ellipsometry data from *in-situ* monitoring of the film growth is presented and compared with that obtained by Fourier-transform infrared spectroscopy (FTIR) data on the film. This chapter's main focus is on the optimisation of sample preparation methods, both of the template and that of the gold nanorods. Controlled etch-back of the porous alumina is used to expose the gold nanorods. Thus the template helps not only to support the rods which are several hundred nm in length but also, by keeping the aluminium base in place, enables electrochemical reactions to be performed on the gold nanorod array. Having optimised the production of vertically orientated AuNR samples in the previous chapter, the focus of **Chapter 5** is to establish their effectiveness as a robust SERS substrate. Desirable qualities include such as ease of handling, good signal enhancement, signal uniformity across the sample surface as well as surface regeneration and

repeatability are investigated. Comparison of the signal enhancement obtained from the samples compared to that of a number of other available substrates were performed using both resonant and non-resonant Raman species. In addition, the deposition of electroactive species and nanoparticles onto the AuNR is also explored.

Chapter 6 introduces the concept and development of patterned samples to enable a means by which multiplex analysis of a wide variety of analytes on a single sample surface can be achieved. The challenges and eventual successes involved in this process are discussed. In addition, the spectra obtained for the attached reporter molecules at excitation wavelengths of 633 nm and 785 nm are compared. In effect, the essence of the work was to be able to produce reusable, multi analyte sensors with the capacity to be customised for specific and/or varied requirements in a very cost effective way.

Chapter 7 serves as a review of the main points established in the previous chapters to provide clarity, in addition to suggesting areas of further work to enable future advancement in the field.

2. Background theory

2.1 Light

Light[325,326] is electromagnetic radiation that is visible to the human eye at wavelengths of between approximately 400 nm – 800 nm[325]. Light is emitted and absorbed as photons which have wave – particle duality. That is to say they exhibit the properties of both particles and waves. Light transverse waves consist of both an electric (*E*) and a magnetic (*B*) field which oscillate perpendicular to the direction of travel and are orthogonal to one another. These waves oscillating in a multitude of directions are said to be unpolarised whereas polarised light waves oscillate in only one direction.

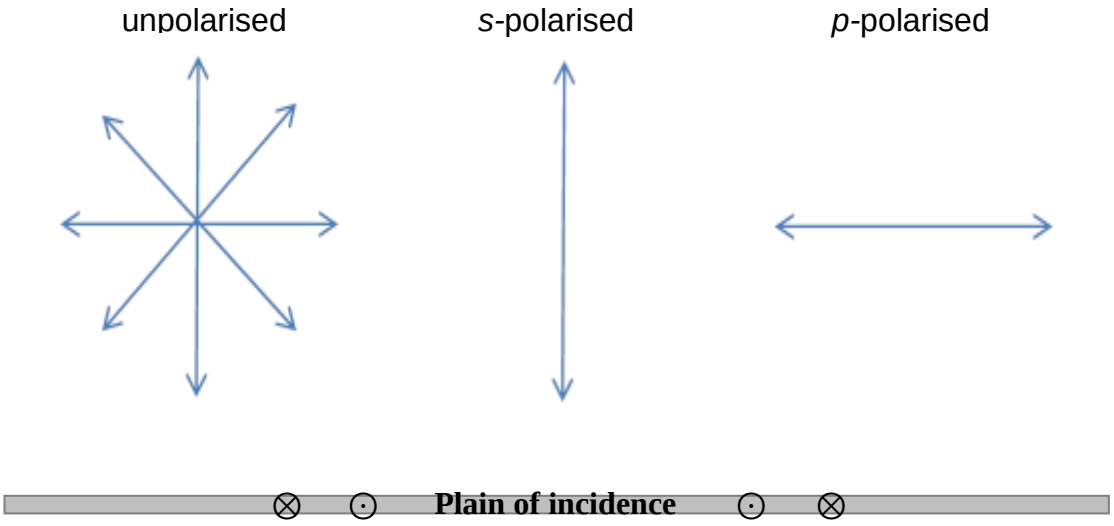

Figure 2.1 *Illustrates unpolarised, s polarised and p polarised light with respect to the plane of incidence.*

Polarised light can be described by resolving the electric vector into two orthogonal components (*p* and *s*) which are at right angles to each other and to the direction of propagation of the wave. As illustrated in Figure 2.1, light is said to be *p* - polarised if it is polarised parallel to the plane of incidence and *s* polarised if it is polarised perpendicular to the plane. These polarisations can be achieved by passing light through crystals which have different refractive indices for these two directions.

The p and s components of the incident wave are described respectively by the Equations 2,1 and Equation 2.2:

$$\boldsymbol{E_p = |E_p|\cos(\omega t + \delta_p)} \qquad \textbf{Equation 2.1}$$

$$\boldsymbol{E_s = |E_s|\cos(\omega t + \delta_s)} \qquad \textbf{Equation 2.2}$$

where $\omega = 2\pi f$, which is the angular frequency in time, and δ_p *and* δ_s are the respective phase shifts of the electric field parallel and normal to the plane.

2.1.1 Reflection of Light from a dielectric surface

The reflection of light from a dielectric surface is explained by the Fresnel Equations[325] which quantifies the fraction of incident light reflected by the surface as illustrated in Figure 2.2.

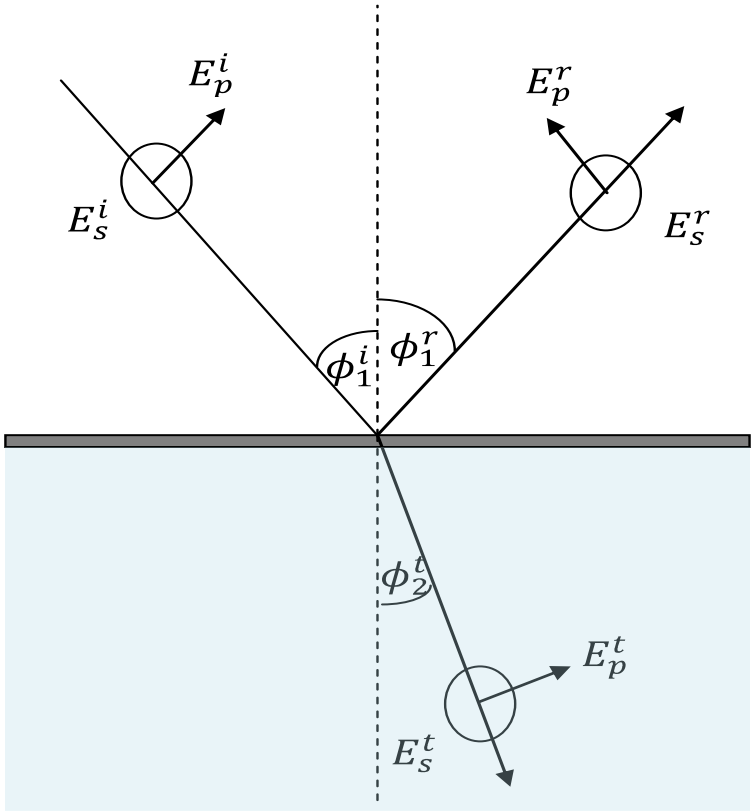

Figure 2.2 *Geometrical arrangements for reflection from a dielectric surface where i, r and t refer to incident, reflected and transmitted light respectively and where the refractive indices for the two media are* n_1*(unshaded region) and* n_2 *(shaded region).*

For a dielectric medium, the Fresnel's equations represent reflection and transmission coefficients of electromagnetic waves at an interface for both *p* and *s* polarised light. Fresnel's Equations can be stated in terms of the angles of incidence and transmission or more commonly, angle of refraction. The Fresnel reflection coefficients for *p* and *s* polarised light are derived from Maxwell's equations[327] regarding the electromagnetic theory of light and are given as:

$$r_p = \frac{E_p^r}{E_p^i} = \frac{n_2 \cos\phi_1 - n_1 \cos\phi_2}{n_2 \cos\phi_1 + n_1 \cos\phi_2} \qquad \textbf{Equation 2.3}$$

$$r_s = \frac{E_s^r}{E_s^i} = \frac{n_1 \cos\phi_1 - n_2 \cos\phi_2}{n_1 \cos\phi_1 + n_2 \cos\phi_2} \qquad \textbf{Equation 2.4}$$

Maxwell's equations state that light can be both reflected and refracted. While the angle of reflection ϕ_r is equal to the angle of incidence ϕ_i, the angle at which light is refracted can be derived from Snell's law (Equation 2.5). This relates to the refraction of light waves as they move from one optical medium to another and states that when light passes from one medium (1) to another (2) the ratio of the sine of the angle of incidence to that of the sine of the angle of refraction is equal to the inverse ratio of their refractive indices (*n*):

$$n_1 \sin(\phi_i) = n_2 \sin(\phi_r) \qquad \textbf{Equation 2.5}$$

when $n_2 > n_1$ it follows that $\phi_I > \phi_2$ therefore as can be seen from Equation 2.4, r_s is negative for all values of ϕ_I. This implies a phase shift of 180° between the incident and reflected waves. When ϕ_I=0 (i.e. normal incidence), r_p is positive but as ϕ_I increases, r_p decreases until it reaches zero at the point when $\phi_I + \phi_2 = 90^o$. This point is known as Brewster angle or the polarising angle, ϕ_B, and is the angle at which only s polarised light is reflected. While for all angles where $\phi_I > \phi_B$, r_p is negative.

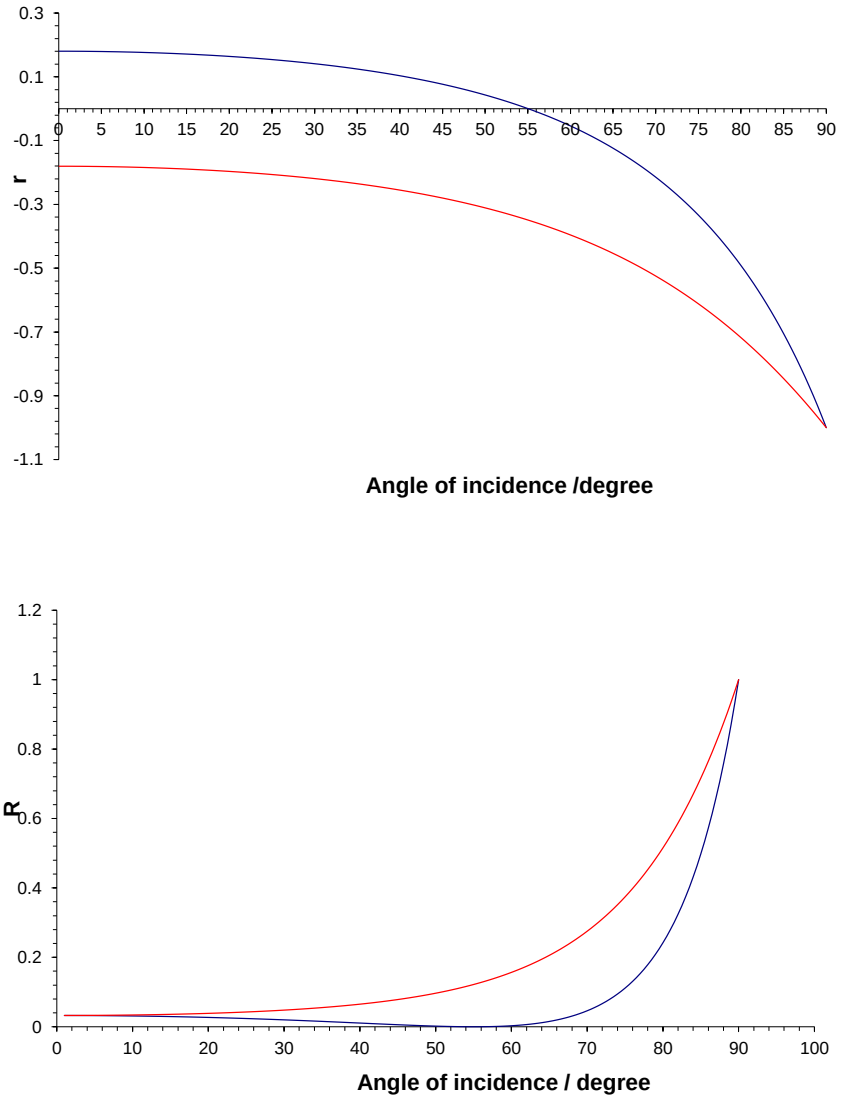

Figure 2.3 *Fresnel plots for s-polarised (red) and p-polarised (blue) light evaluated at an air aluminium interface for r, top, and R (r^2) bottom.*

The Fresnel plots evaluated at an air/aluminium interface showing the variation in *r* and *R* (*R* = r^2) as a function of angle of incidence are given in Figure 2.3. The *p* polarised light can be seen to exhibit lower intensity of reflectance than that of the *s* polarised light with zero reflectance for *p* polarised light at the Brewster angle.

2.1.2 Reflection from metal surfaces

Polished metallic objects reflect light particularly well, as such mirrors have been made from silver or aluminium coated glass. Metals contain large numbers of delocalised electrons which undergo oscillations by the electric field of an electromagnetic wave incident on the metal.

However not all of the light is necessarily reflected and it can also be partially absorbed and in certain cases transmitted, over a wide range of wavelengths through the surface of the metallic substrate. This is due to tightly packed energy levels in the conductance band and can be accounted for by defining the complex refractive index, $\tilde{n}$ as follows

$$\tilde{n} = n - ik \qquad \textbf{Equation 2.6}$$

where *n* is the refractive index and *k* is the extinction coefficient which is related to the normal absorption coefficient α, through:

$$\alpha = \frac{4\pi k}{\lambda} \qquad \textbf{Equation 2.7}$$

2.1.3 Reflection from a thin film surface

Measurement of reflection from thin films grown on substrates introduces a third phase and additional complications, as shown in Figure 2.4, which must be considered and accounted for. The thin film growth on top of a substrate introduces another phase with potentially different optical properties to that of the substrate. In addition, multiple internal reflections occur within the film itself.

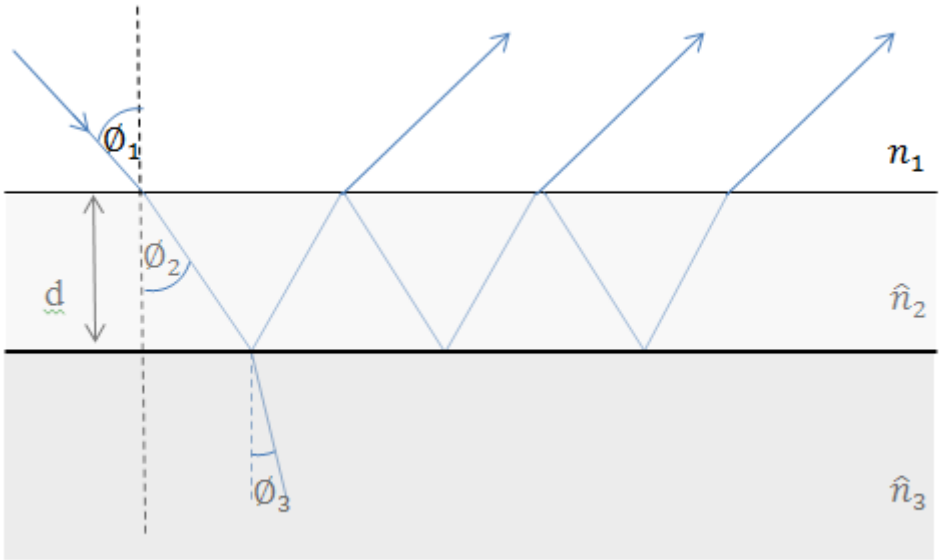

Figure 2.4 *Schematic representation of reflection from thin film covered surface.*

The ambient refractive index, in the analysis below, is assumed to be non- absorbing and therefore not considered complex. Therefore, for a semi-infinite parallel sided film of thickness *d* the multiple reflected and transmitted waves are given by:

$$\widehat{\boldsymbol{R}}_{\boldsymbol{p/s}} = \frac{\hat{\boldsymbol{r}}_{\boldsymbol{12}} + \hat{\boldsymbol{r}}_{\boldsymbol{12}}\ \boldsymbol{\exp(-2i\beta)}}{\boldsymbol{1} + \hat{\boldsymbol{r}}_{\boldsymbol{12}}\ \hat{\boldsymbol{r}}_{\boldsymbol{23}}\ \boldsymbol{\exp(-2i\beta)}} \qquad \textbf{Equation 2.8}$$

where $\hat{R}_{p/s}$ is the overall reflection coefficient and r_{12} and r_{23} refer to reflections from the ambient-film and film-substrate interfaces respectively for *p* and *s* polarised light. β represents the phase film thickness and corresponds to the phase introduced as a consequence of the light travelling through the film. It is defined as:

$$\boldsymbol{\beta = 2\pi\left(\frac{d}{\lambda}\right) n_1 cos\phi_2} \qquad \textbf{Equation 2.9}$$

The ratio between *s* and *p* polarised light is known as the ellipsometry equation and is given by:

$$\boldsymbol{\rho = \frac{\hat{R}_p}{\hat{R}_s} = \tan\Psi \exp(i\Delta)} \qquad \textbf{Equation 2.10}$$

where Δ = phase shift and ψ = amplitude ratio and is discussed in the following section.

2.2 Ellipsometry

Ellipsometry can be used to calculate film thickness and its refractive index[328, 329]. In order to understand the principals of the technique, consider two perpendicular polarised waves in phase. They will produce a single linearly polarised wave at 45° with respect to the plane of polarisation as seen in Figure 2.5. If they are polarised out of phase by 90° they will produce a circularly polarised wave. However these two are special cases and more generally, when two waves are out of phase by any other angle they produce an elliptically polarised wave as shown in Figure 2.5.

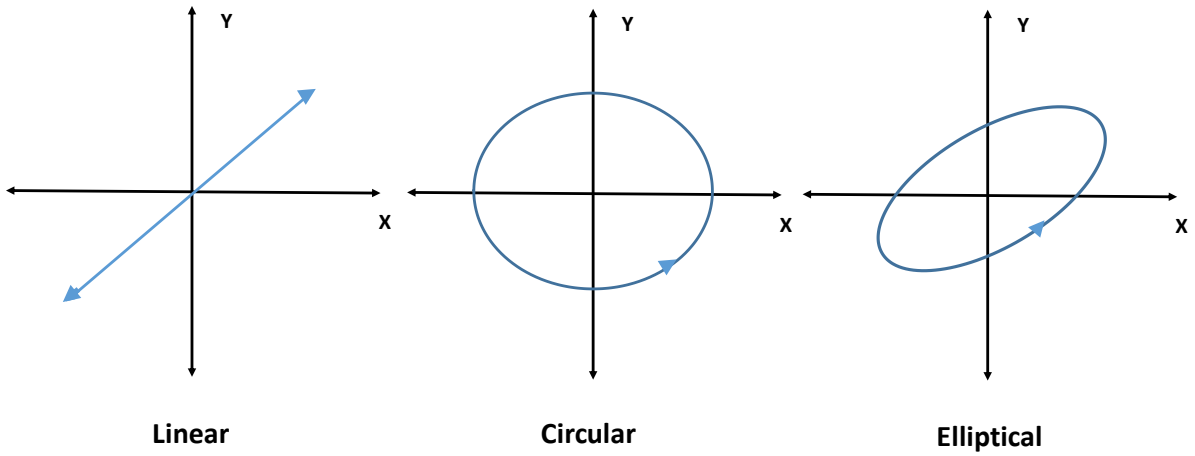

Figure 2.5 *Representation of, linearly polarised and circularly polarised light and elliptically polarised light.*

Ellipsometry measures the change in the polarisation state of light after reflection from the surface of a sample. The measured ellipsometry parameters are the angles Δ (phase shift) and ψ (amplitude ratio). These parameters are defined in Equation 2.11, which is reproduced below:

$$\frac{\hat{R}_p}{\hat{R}_s} = \tan \Psi \bullet e^{i\Delta}$$ **Equation 2.11**

2.3 UV-vis Spectroscopy

Ultraviolet and visible (UV-Vis) radiation interact with matter which cause electronic transitions (promotion of electrons from the ground state to a higher energy state)[238]. The ultraviolet region falls in the range between 190-380 nm and the visible region lies between 380 nm - 750 nm. Different molecules absorb radiation at different wavelengths. By recording the wavelengths and amount of absorption, this results in the creation of an individual molecule specific absorption spectrum consisting of absorption bands corresponding to the structural groups within the molecule. Moreover, the perceived colour of a substance is closely linked to its electronic structure. When radiation in the form of white light is fully reflected the perceived colour is white and when fully absorbed, black. However, when light of a specific wavelength is absorbed by a molecule it is the complementary colour created from the wavelengths of light not absorbed that is observed, as indicated in Table 2.1.

Absorption λ (nm)	Absorbed Colour	Observed Colour
400-435	Violet	Yellow-green
435-480	Blue	Yellow
480-490	Green-blue	Orange
490-500	Blue-green	Red
500-560	Green	Purple
560-580	Yellow-green	Violet
580-595	Yellow	Blue
595-605	Orange	Green-blue
605-750	Red	Blue-green

Table 2.1 *Table depicting the absorption wavelength of light, the associated colour and the resulting observed colour*

In addition, the amount of absorbance exhibited by any given sample is proportional to the number of absorbing molecules, i.e. the molar concentration, within the path of the source light beam. Therefore, it is necessary to correct the absorbance value for this. The corrected absorption value is known as "molar absorptivity", and is particularly useful in the comparison of the spectra and relative strength and concentration of the light absorbing components (chromophores). This is known as the Beer Lambert Law, given in Equation 2.12 that relates absorbance to solute concentration:

$$A = \varepsilon b c \qquad \textbf{Equation 2.12}$$

where A is absorbance, ε is the molar absorptivity (L mol^{-1} cm^{-1}), b is the path length (cm), c is the concentration (mol L^{-1}).

2.4 Dark-field microscopy

In dark-field microscopy directly dispersed light from a light source, within the ultraviolet to near infrared range, is removed with only scattered light directed at the specimen under investigation. This results in a cone of light which is observed as a ring on the surface of the sample under investigation within which the scattered light is diffracted, reflected and/or refracted off the object[330,331]. This facilitates investigation of specimens, such as those with refractive index values similar to that of the background, the features of which are unable to be distinguished using conventional microscopy.

In contrast to bright-field microscopy, in dark-field, the sample appears light and the background dark. This can be achieved through an adaptation of the conventional microscope set up by placing an opaque object below the sub-stage in order to block out any light shining from the base unit. The light source used is typically a tungsten-halogen lamp where the emitted light passes through a collector lens and then through the aperture and field diaphragms before striking the opaque stop in the opening port. The fitting of a dark-field condenser produces a hollow cone of light as the centre of the beam of light is blocked. Light passes around it and so only scattered light from the sample enters the objective lens that is located in the dark centre of the cone. The image observed is produced from the scattered light captured in the objective lens. This technique can be used to determine a sample's surface characteristics and morphology, such as depressions, ridges and boundaries in addition to defects such as cracks and scratches. In comparison to that obtained from bright-field the contrast amongst a sample's features is increased with some features only visible with dark-field microscopy. Reflectance dark-field microscopy has become a useful tool in nanotechnology by helping to facilitate the study of single metal nanoparticles, such as how size and shape affect LSPR and line width through predominantly Rayleigh scattering experiments as well as electron surface scattering experiments.

2.5 FTIR – Fourier Transform Infrared Spectroscopy

FTIR is a method of measuring molecular vibrational frequencies that lie in the IR region (typically 700 nm to 25 μm wavelength) of the electromagnetic spectrum[332, 333]. Light from a source across a range of frequencies is passed through a sample and the intensity of the transmitted light is measured at each frequency. When molecules absorb IR radiation, transitions occur from a ground vibrational state to an excited vibrational state. To be IR active, a change in dipole moment of the vibration of the species must occur when the IR radiation is absorbed.

The beam emitted from the source passes through a beam splitter, which splits it in two and sends each half in two directions at right angles to one another. While one beam is sent to a stationary mirror and then back to the beam splitter, the other is sent to a moving mirror and then back to the beam splitter. The motion of the moving mirror results in the two beams having different path lengths. As a result, when they recombine, the difference between the

two path lengths results in an interference fringe pattern *i.e.* an interferogram. The recombined beam is sent to the sample, which absorbs the specific wavelengths characteristic of its spectrum, subtracting specific wavelengths from the interferogram. The variation in energy levels for all wavelengths are plotted against time simultaneously. The mathematical function Fourier transform is then used to convert the intensity *vs*. time spectrum into an intensity *vs.* frequency spectrum.

2.6 Field emission scanning electron microscope

Field emission scanning electron microscopy (FE-SEM) produces images of a sample by scanning the surface with a focused beam of electrons. The electron beam, which typically has an energy ranging from 0.5 keV to 40 keV, is focused by one or two condenser lenses to a spot about 0.4 nm to 5 nm in diameter. The beam passes through pairs of scanning coils or pairs of deflector plates in the electron column, typically in the final lens, which deflect the beam in the *x* and *y* axes so that it scans in a raster fashion over a rectangular area of the sample surface[20, 291]. The SEM images in this work were produced using HITACHI SU-6600, a high resolution analytical variable pressure, field emission scanning electron microscope. This instrument is equipped with a variable pressure mode. This enables non-conductive samples such as alumina to be analysed without needing to be coated in gold coating.

As the primary electron beam interacts with the sample, the electrons lose energy by repeated random scattering and absorption within a teardrop-shaped volume of the specimen known as the interaction volume, which can extend from less than 100 nm to around 5 µm into the surface. The size of the interaction volume depends on the electron's landing energy, the atomic number of the specimen and the specimen's density. The energy exchange between the electron beam and the sample results in the reflection of high-energy electrons by elastic scattering, the emission of secondary electrons by inelastic scattering and the emission of x-rays. Specialised detectors can detect each of these secondary effects. The beam current absorbed by the specimen can also be detected and used to create images of the distribution of specimen current on the sample. Electronic amplifiers are used to amplify the signals which are displayed as variations in brightness. The raster scanning of the display is synchronised with that of the beam on the specimen in the microscope, and the resulting image is therefore a distribution map of the intensity of the signal being emitted from the scanned area of the specimen.

Field emission systems require an extremely high vacuum in which to operate. In this system, the source filament is not heated in order to emit electrons. Electrons are instead drawn from the field emission gun by subjecting the filament to a potential gradient, large enough that electrons are drawn out of the filament. Two anode plates are placed below the gun assembly. The first anode is responsible for the extraction voltage, typically 3-5 kilovolts, that draws the electrons out from their source. While a second anode produces a voltage that dictates the velocity at which the electrons travel down through the column. Both of these anodes act as electrostatic lenses, focusing the beam into a small initial crossover.

Magnification in a SEM can be controlled over a range of up to 6 orders of magnitude. Unlike optical and transmission electron microscopes, image magnification in the SEM is not a function of the power of the objective lens. The condenser and objective lenses focus the beam to a spot, but not to image the specimen. The resulting magnification is due to the ratio between the raster on the specimen and the raster on the display device. Increased magnification results from reducing the size of the raster on the specimen, and vice versa. Thus unlike conventional microscopy magnification is not controlled by the objective lens but by either the current supplied to the scanning coils or the voltage supplied to the deflector plates.

2.7 Electrochemical reactions

Electrochemical reactions are heterogeneous and usually involve the transfer of charge between a solid (electrode) and a species in solution (electrolyte)[334,335]. The direction of electron transfer is dependent on electrode potential with electrons moving from higher to lower energy level. Therefore, electrons will transfer from the electrode surface to the species in solution or from species in solution to electrode depending on whichever path leads to the occupation of a lower energy level. There are two basic types of electrochemical reactions, oxidation and reduction with oxidation of the species involving transfer of electrons from the electroactive species to the electrode and vice versa for reduction. For charge transfer to take place the electrodes need to be connected via an electrical circuit with an electrolyte that contains the electroactive species in close proximity to the electrode and oxidation at the anode must be balanced with reduction at the cathode[336], SEE Figure 2.6 .

$$\mathbf{O} + n\mathbf{e}^- \rightleftharpoons \mathbf{R} \qquad \textbf{Equation 2.13}$$

Consider the above reaction in Equation 2.13 occurring at an electrode surface. For the reaction to proceed O must be present at the electrode surface. As O is consumed, for the reaction to continue a mechanism to replenish O and remove R from the surface of the electrode is required. Thus the overall reaction scheme is as follows:

1. $O_{bulk} \longrightarrow O_{electrode}$ (Mass transport)
2. $O_{electrode} + e^- \longrightarrow R_{electrode}$ (Electrochemical reaction)
3. $R_{electrode} \longrightarrow R_{bulk}$ (Mass transport)

The rate at which the reaction proceeds is determined and limited by whichever one of these three reactions is the slowest and is referred to as the rate-limiting step.

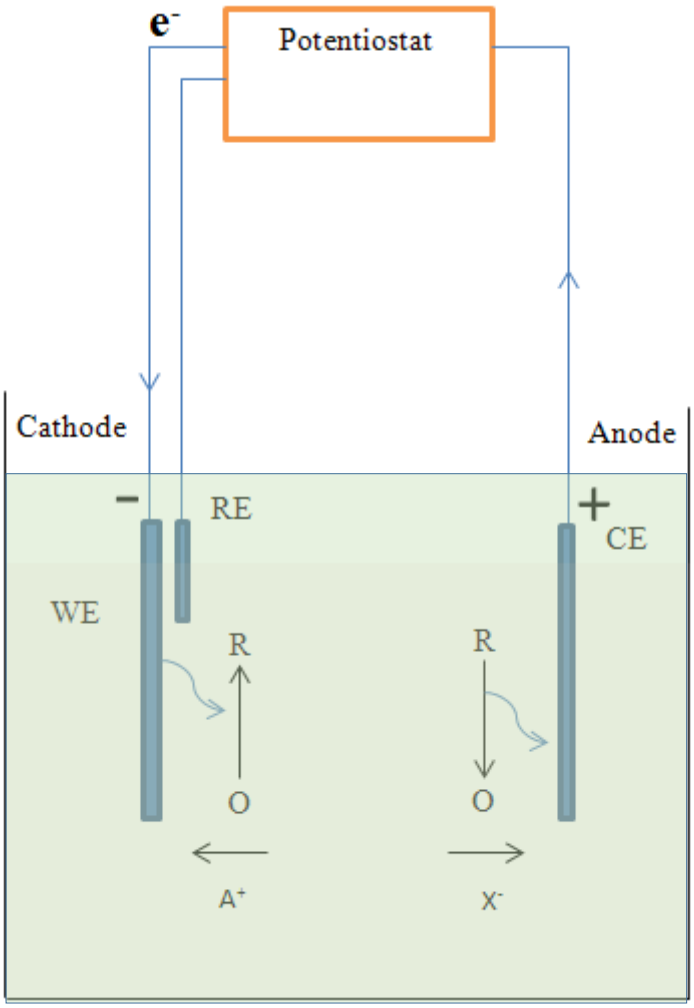

Figure 2.6 *A simple three electrode electrochemical cell comprising of a working electrode (WE) a reference electrode (RE) and a counter electrode (CE).*

As illustrated by the simple cell shown in Figure 2.6 where the electrolyte contains a dilute solution of the electroactive species O and R together with the inert electrolyte species A^+ and X^- which are present at much higher concentrations than the electroactive species. The reference electrode (RE) can be seen to be in close proximity to the working electrode (WE). This is where the reaction pertinent to the electrochemical study occurs. However, no current flows between the WE and RE. This is in order for the potential to be applied accurately across the electrode/solution interface while the counter electrode (CE) allows the current to flow through the circuit between CE and WE.

When no external power is applied, the system containing reactants O and R at the WE is in equilibrium resulting in a steady potential at the working electrode that is known as the reversible or equilibrium potential and this value can be calculated using the Nernst equation:

$$\boldsymbol{E^e = E^o + \frac{RT}{nF} ln \frac{C_O}{C_R}} \qquad \textbf{Equation 2.14}$$

where E^e is the equilibrium potential, E^o is the standard potential for O/R redox species, *R* is the gas constant, *T* is absolute temperature, *F* is the Faraday constant and c_R^∞ and c_O^∞ the bulk concentrations of R and O respectively. At the equilibrium potential, the net current (*i*) is zero.

$$\boldsymbol{i_0 = \overleftarrow{i} + \vec{i}} \qquad \textbf{Equation 2.15}$$

The exchange current density i_0 is equal to the partial anodic, $\overleftarrow{i}$, and cathodic, $\vec{i}$, current densities at the equilibrium potential, Equation 2.15.

On application of a potential, *E*, which is not equal to E^e, the resulting change from equilibrium conditions potential causes a net flow of electrons, i.e. a current. This potential, which is away from equilibrium, is known as the overpotential and is defined as:

$$\boldsymbol{\eta = E - E^e} \qquad \textbf{Equation 2.16}$$

The reactions involving electron transfer at the electrodes, Equation 2.17 and Equation 2.18, are assumed to follow first order kinetics:

Rate of reduction of O = $\boldsymbol{\vec{k}\, c_O^s}$ **Equation 2.17**

Rate of oxidation of R = $\boldsymbol{\overleftarrow{k}\, c_R^s}$ **Equation 2.18**

where c_O^s and c_R^s are the concentrations of electroactive species O and R respectively at the electrode surface.

The partial cathodic current density, Equation 2.19, and partial anodic current density, Equation 2.20, are then given as:

$$\vec{i} = -nF\vec{k}\, c_O^s \qquad \textbf{Equation 2.19}$$

$$\overleftarrow{i} = +nF\overleftarrow{k}\, c_R^s \qquad \textbf{Equation 2.20}$$

Here the convention is adopted that a reduction reaction gives a negative current and an oxidation reaction gives a positive one. The rate constants are dependent on the overpotential according to Equation 2.21 and 2.22.

$$\vec{k} = \vec{k}_0 \exp\left(\frac{-\alpha_C nFE}{RT}\right) \qquad \textbf{Equation 2.21}$$

$$\overleftarrow{k} = \overleftarrow{k}_0 \exp\left(\frac{\alpha_A nFE}{RT}\right) \qquad \textbf{Equation 2.22}$$

where $\vec{k}_0$ and $\overleftarrow{k}_0$ represent the rate constant when E = 0 and α_C and α_A the cathodic and anodic charge transfer coefficients which for simple systems sum to unity. Algebraic manipulation of the above equations leads to the Butler-Volmer equation, Equation 2.23, used to describe electrode kinetics:

$$i = i_0 \left[\exp\left(\frac{\alpha_A nF\eta}{RT}\right) \exp\left(\frac{-\alpha_C nF\eta}{RT}\right)\right] \qquad \textbf{Equation 2.23}$$

where i_0 is known as the exchange current density and represents the amount of current flowing in both directions at equilibrium. The Butler-Volmer equation has three limiting forms, *viz*, when η is small ($\leq$ 10 mV); large and negative or large and positive ($|\eta| \geq \frac{118}{n}$ mV). The latter two give rise to the cathodic, Equation 2.24, and anodic, Equation 2.25, Tafel equations:

$$log|I_C| = logI_o - \frac{\alpha_c nF\eta}{2.303RT} \qquad \textbf{Equation 2.24}$$

$$log|I_A| = logI_o + \frac{\alpha_A nF\eta}{2.303RT} \qquad \textbf{Equation 2.25}$$

This produces a plot as shown in Figure 2.7. These equations predict that as η is increased, current growth is exponential. However, this growth in current with respect to η is unsustainable and becomes limited by the speed of transportation of the species from solution to the surface of the electrode. As such, the system eventually becomes mass transport limited.

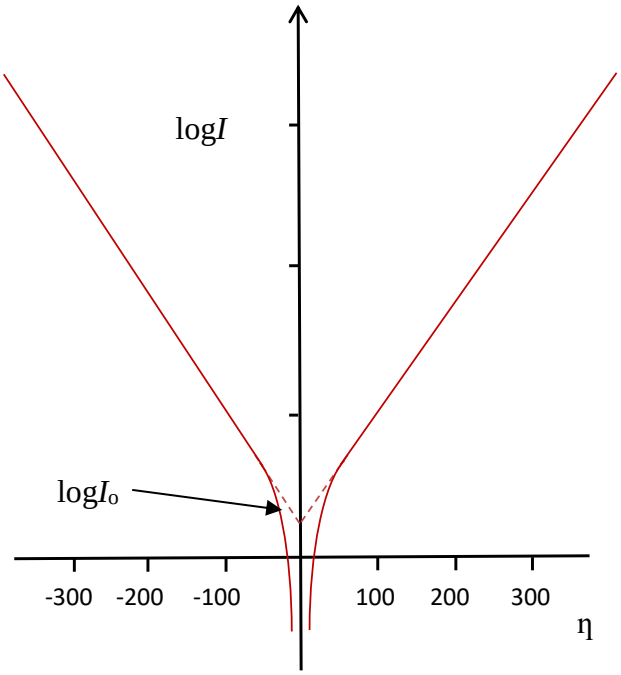

Figure 2.7 *Tafel plot logI vs η*

The three methods of mass transport are diffusion, migration and convection. Diffusion can be defined as the movement of a species due to a concentration gradient and occurs when there is a change in the concentration of the reacting species at the electrode surface during oxidation/reduction. This reaction converts the starting species to product (O → R). This creates a boundary layer close to the surface and up to 10^{-3} cm in thickness in which the concentrations of O and R vary as a function of distance from the electrode surface. The concentration of O is lower at the electrode surface (i.e.as it is consumed at the cathode) than in the bulk and the concentration of R is higher at the surface than in the bulk. It therefore follows that O will diffuse towards the electrode and R away from the electrode surface.

Natural convection occurs in all solutions and is due to small thermal or density differences that cause the solution to mix in a random and unpredictable manner. However, this effect can be overcome through forced convection where the solution is mixed by means of a spinning

bar, pump or by using a rotating disc electrode. In such circumstances the effects of natural convection are negligible and forced convection controls the amount of material arriving at the electrode surface.

Migration happens as a result of an electrostatic effect that occurs on the application of a voltage between the electrodes. In essence, this creates an electric field between the electrodes causing positive ions (cations) to move towards the negative electrode (cathode) and negative ions (anions) to move towards the positive one (anode).

2.7.1 Cyclic Voltammetry

Cyclic voltammetry is the technique most widely used to gather qualitative information from the initial studies into electrochemical reactions in order to characterise electron transfer reactions. Thus providing a means by which to locate the redox potentials of the electroactive species in solution or adsorbed at an electrode surface.

A three electrode system is normally used to obtain the most accurate results, comprising of a working electrode (e.g. gold, glassy carbon), a counter electrode (typically platinum) and a reference electrode such as a standard calomel electrode (SCE), silver/silver chloride (Ag/AgCl) or copper/copper sulphate (Cu/CuSO4). However cyclic voltammetry can also be carried out using a two electrode system employing a pseudo reference electrode. The open circuit potential (OCP) can be used as a guide in the initial selection of these values because at this potential no current will flow through the cell, The voltage is typically scanned between the OCP and one or more set values. The current response is plotted as a function of voltage and the resultant plot is referred to as a voltammogram. This shows that the current increases as the voltage is swept away from its initial value. The equilibrium position is shifted till eventually reaching a peak, denoting the reduction potential after which the cathodic current decreases as the concentration of reducible analyte is depleted. On reaching the voltage set as the upper limit the scan is reversed and the voltage swept back to either the initial OCP value or a third value. The scan rate v dictates the timescale over which the reaction occurs and is usually set between 0.5 mV s^{-1} and 1000 mVs^{-1}. In the forward reaction electrons flow from the electrode to the species in solution while the reverse reaction sees the current flow from the

solution species back to the electrode. If the reaction is reversible a peak, denoting the oxidation potential, will be seen in the reverse scan [337].

2.7.2 Rotating Disk Electrode

The Rotating disc electrode (RDE) is a hydrodynamic working electrode and comprises of a polished metal core surrounded by an insulation material e.g. platinum disk encased in epoxy or PTFE [338]. The disk's rotation is normally measured in cycles or rotations per unit time. The electrode's rotation induces a flux of the solution containing the electro-active species towards the electrode surface. As the disk rotates the resulting centrifugal force pushes the solution upwards and away from the electrode creating a hydrodynamic boundary layer at the electrode surface. The rate of flow, and thus the thickness of the boundary layer, is controlled by the electrode's angular velocity. Consequently mass transport is controlled by convective flow rather than being controlled or limited by the diffusion rate, as would be the case in cyclic voltammetry at stationary electrodes.

2.7.3 Electropolishing

Electro polishing of a metal surface is carried out in order to smooth and level out the flawed uneven surface of a metal. The initial process is known as macro smoothing and is achieved through the selective dissolution of at first µm-sized surface features, which is then followed by micro smoothing which involves the dissolution of surface features that are sub- micrometre in size. As a result of these selective dissolutions, the metal surface reflects light with a mirror-like finish, known as micro smoothing. Within the electrochemical cell the metal sample to be polished is the anode. The importance of electropolishing in preparing a smooth aluminium surface prior to anodisation to produce the ordered pores in the alumina layer cannot be understated. In the case of the two-stage anodisation process of aluminium, the resultant self-ordered arrangement of the pores is greatly influenced by firstly the purity of the aluminium sheet used (the purer the better) and secondly, the degree of sample surface smoothness achieved by electropolishing [339].

3. Experimental

All reagents used were of the highest grade available and the full list is given in the appendix. Milli-Q deionised water (DIW) with a resistivity 18.2 MΩ cm was used throughout. Prior to use all glassware used for nanoparticle work was soaked overnight in *aqua regia*, rinsed thoroughly in DIW then acetone and finally dried in a nitrogen stream. The glass electrochemical cell used for electropolishing and alumina film growth was also periodically cleaned with *aqua regia*.

3.1 Fabrication of an anodic alumina template

This section seeks to describe the steps involved in the production of a porous anodic alumina for use as a suitable template for the electrochemical production of gold nanorod arrays for use as a suitable SE(R)RS substrate.

3.1.1 Aluminium Substrate

A sheet of high purity aluminium (99.999%) was cut into 15 mm × 15 mm squares. Each aluminium sheet produced nine samples, which were annealed by heating in a nitrogen atmosphere. The heating rate employed was 20 °C/min, from ambient temperature to 600 °C. The temperature was then held at 600 °C for two hours and then allowed to cool to 30°C at a rate of 2 °C/minute. Annealing the aluminium provided the surface with large single crystalline grains that aid the growth of a self-assembled and highly ordered porous alumina matrix.

In order to get a smooth flat surface, the samples were individually mechanically polished using an E W Jackson & Sons LTD motorised polisher using initially 600 grade followed by 1200 grade emery paper and then finished with 1 μm and 0.3 μm alumina powder in conjunction with a wet polishing cloth. In order to avoid surface scratching and/or pitting the sample was kept wet throughout the polishing process. To degrease and remove any surface debris from the sample prior to the next step, the samples were rinsed thoroughly with deionised water (DIW), and then ultrasonicated in propan-2-ol for five minutes before being finally rinsed in ethanol and dried in a nitrogen stream.

3.1.2 Instrument set-up for the fabrication of AAO template

The dried aluminium sample was mounted onto the stainless steel base of the sample holder unit using silver conducting paint that provided an electrical contact in addition to a means of adhesion. After allowing fifteen minutes for the paint to dry, the sample holder's sheath was put on and screwed in place. The sample holder was then inserted into a glass cell surrounded by a water jacket and secured in place by a clip.

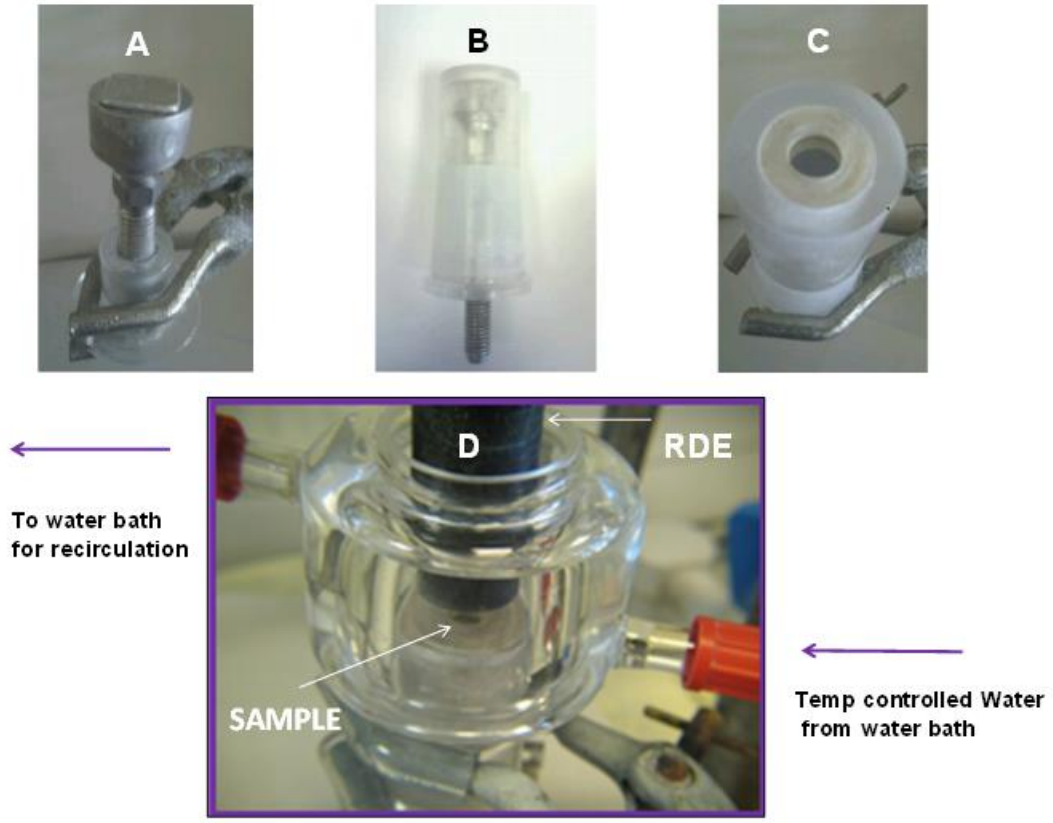

Figure 3.1 *The stages involved in assembling the cell for electropolishing in addition to first and second stage anodisation. A) Al sample mounted on sample holder base. B) Assembled sample holder (side view). C) Top view of sample in sample holder. D) Assembled cell.*

The sample therefore acted as the working electrode and while a rotating disc electrode consisting of a stainless steel core surrounded by an insulating epoxy resin was used as the counter electrode. The stainless steel electrode was polished prior to each use, see Figure 3.1. The voltage was supplied by a Hewlett Packard 6545A DC power supply. The electrolyte

temperature control was achieved by means of circulating water at the required temperature, controlled by a Gallenkamp Thermo Stirrer 85, through the outer jacket of the cell.

3.1.3 Electropolishing of aluminium sample

The electropolishing solution consisted of 40 vol% phosphoric acid, 38 vol% ethanol and 22 vol% DIW at a temperature of 45°C and was poured into the cell. The current was set to 275 mA which was calculated from the sample surface area, using the optimum current density of 350 mA/cm^2 [150]. The speed of rotation of the disc was initially set to 5 Hz, to reduce bubble adhesion to the surface and providing convection for the process. Starting from a voltage of zero, the cell voltage was increased gradually until a constant current of 275 mA was achieved at which point the voltage dropped back from a typical value of 122 V to *ca.* 36 V. The rotating disk's speed was then reduced to 0.35 Hz and the reaction allowed to continue for 5 minutes. Once used, the electropolishing solution was discarded and both cell and electrode were rinsed thoroughly with DIW. Electropolishing gave a mirror like finish to the surface of the aluminium.

3.1.4 Porous alumina film growth by two-stage anodisation

The porous alumina film growth was achieved by means of a two-stage anodisation process. The rinsed cell was filled with 0.3 M oxalic acid solution (Sigma Aldrich) at 30°C with the RDE set to rotate at 0.35 Hz. The voltage was set to 40 V and the current setting to the instrument maximum value of 1.53 A. This was done so that the applied voltage and not the current controlled the process. The actual current flowing during the anodisation process was very low, typically 0.65 mA. The first anodisation period lasted 20 hours and during this time, pore growth became increasingly more ordered at the metal/oxide interface. Over this period, a thin barrier layer (thickness = 80 nm) and a thick porous alumina film was formed on top of the aluminium substrate. The pores formed were ordered and parallel at the base but irregular and disordered at the surface (the initial region of pore formation). As in the electropolishing process, the solution was discarded on completion of this first anodisation and the sample and cell were rinsed with DIW.

The cell was dismantled and the sample removed, with all the residue of the silver conducting paint removed from the back of the sample with acetone on a cotton bud. The sample was then immersed in an etching solution of 1.8 wt% chromium trioxide and 6 wt% phosphoric acid at 70°C for 2 h. The subsequent removal of the thick film formed during the anodisation process left an imprint of the ordered pores, which was used as a template on which to grow the hexagonally ordered porous alumina film during the second anodisation process.

The 'oxide'-free sample was remounted onto the sample holder and inserted back into the anodisation cell. Both the set voltage and current were once again set to 40 V and 1.53 A respectively. Initially the duration of the second anodisation period was 30 minutes but this was subsequently reduced in accordance with the desired thickness of the film, which in turn determined the length of nanorods that could be formed in the pores. Anodisation durations of 10 minutes produced pores of ~2.8 μm in length, 5 minutes gave pores of ~1.4 μm in length and 2 minutes gave pores ~0.6 μm in length.

3.1.5 Barrier Layer Thinning

On completion of the second anodisation and without changing the oxalic acid solution, barrier layer thinning was immediately carried out. Initially, the current was set to that recorded at the end of the second anodisation period, typically 6.5 mA and the voltage was set to the maximum setting (122 V), as this process required to be under current control. The current was then gradually reduced in a step-wise manner, allowing the voltage to settle each time before reducing the current further. This was done until the cell voltage had reduced to 6.5 V. The solution was then removed and the sample and cell were washed thoroughly with DIW and sample holder removed. Care was taken to keep the sample surface wet throughout to avoid air getting into the pores and so preventing the gold plating electrolyte from accessing the pores. However, it was subsequently found that there continued substantial porous oxide growth during this period of barrier layer thinning. The method was subsequently altered with the voltage set to 122 V and the current set to 1.2 mA. When turned on the voltage dropped from 40 - 24 V within 30 seconds. The significance of the 24 V was that ellipsometry data had shown that there was little porous oxide growth at potentials lower than this.. The fall in voltage from 24 V to the 6.5 V limit in order to achieve barrier layer thinning was thus accomplished in about ten minutes.

3.1.6 Electro-deposition of gold into hexagonally ordered pores in alumina film

Gold was deposited into the hexagonally ordered alumina pores using a 0.1 M $KAu(CN)_2$ solution and an ac voltage of between 6.0 –7.0 V *rms* at 200 Hz. Again, here the sample itself acted as the working electrode with a looped platinum wire used as the pseudo reference/ counter electrode, shown in Figure 3.2.

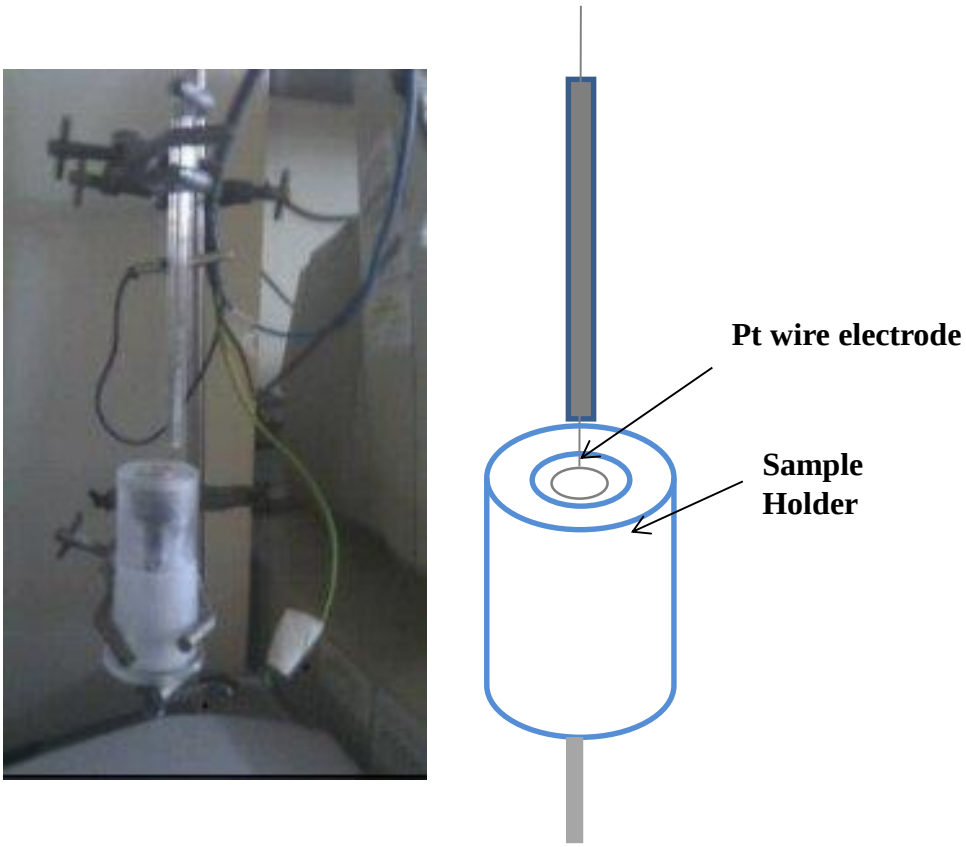

Figure 3.2 *Instrument set up for the deposition of gold into the alumina film pores. Gold was deposited into the samples hexagonally ordered alumina pores using a 0.1 M* $KAu(CN)_2$ *solution and an ac voltage of between 6.0 -7.0 V rms at 200 Hz.*

3.1.7 Etch-back of porous alumina film to expose the gold nanorod arrays

As the deposited gold did not entirely fill the full length of the pores, it was therefore necessary to etch-back the porous alumina film on top of the AuNR in order to expose them. The depth of the rods within the film was calculated from the fringe pattern observed in the specular reflectance measurements of the unetched sample using Equation 3.1:

$$\boldsymbol{d} = \frac{\boldsymbol{m}}{2\Delta\boldsymbol{\nu}\cdot\sqrt{(\boldsymbol{n}^2 - \boldsymbol{sin}^2\,\boldsymbol{\theta})}}$$ **Equation 3.1**

where $\boldsymbol{d}$ is the alumina film thickness above the AuNR, $\boldsymbol{m}$ is the number of fringes in wavenumber region used, $\boldsymbol{n}$ is the refractive index, $\boldsymbol{\theta}$ is the angle of incidence and $\Delta\boldsymbol{\nu}$ is the wavenumber region used (ν_1 - ν_2; cm^{-1}).

For the etch-back experiments, the sample was immersed into a 10 wt% phosphoric acid solution kept at a constant temp of 30 °C and placed in an ultrasonic bath. From these measurements the rate of alumina etch-back required to expose the AuNR was calculated to be *ca*, 10 min/1μm (0.1 μm/min). Specular reflectance and electrochemistry together with FE-SEM were used to monitor the exposure of the AuNR following the chemical etching process.

3.1.8 Summary and Schematic representation of Alumina film growth and gold deposition

- 1 mm thick aluminium sheet (99.999% purity) cut into 15 mm squares.
- Annealed (inert atmosphere, 600°C). [A]
- Mechanically polished. [B]
- Electro polished. [C]

A B C

- First anodisation; 20 hours in 0.3 M oxalic acid . [D]
- Removal of thick alumina film. . [E]
- Second anodisation; 2 min in 0.3M oxalic acid and barrier layer thinning (E_{cell} from 40 V to 6.5 V). [F]
- Gold is deposited into the hexagonally ordered . alumina pores from a 0.1 M $KAu(CN)_2$ solution using A.C. voltage of 6 V - 7 V rms at 200 Hz. . [G]
- Etch back of alumina film to exposed gold nanorods using 10% H_3PO_4. [H]
- Full surface coverage [I(i)] or patterned surface can be produced using a template during the deposition stage. [I(ii)] and [I(iii)]

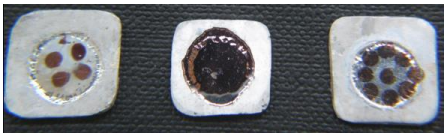

I(ii) I(i) I(iii)

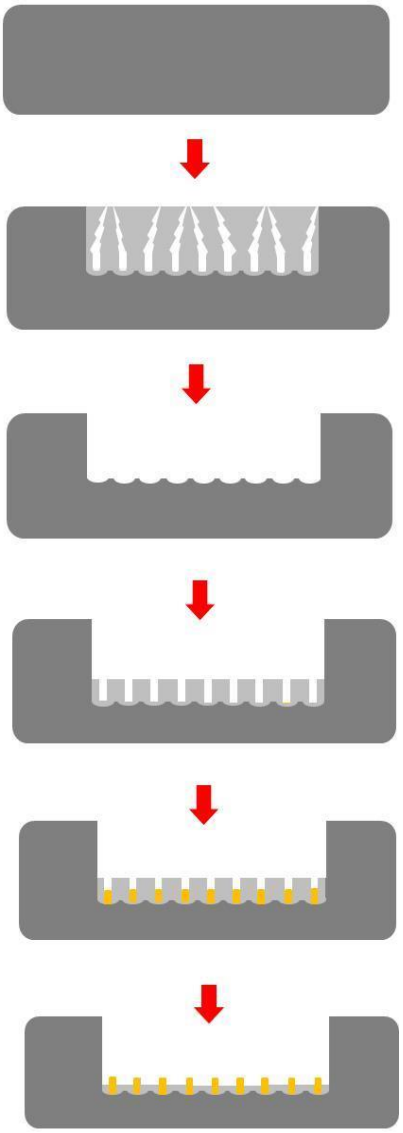

3.2 Specular Reflectance

These measurements were carried out to confirm the presence of AuNR and to determine the thickness of the alumina film above the AuNR. A polarised light beam was incident onto the surface of the sample and reflected at an angle equal to that of the incidence angle as shown in Figure 3.3.

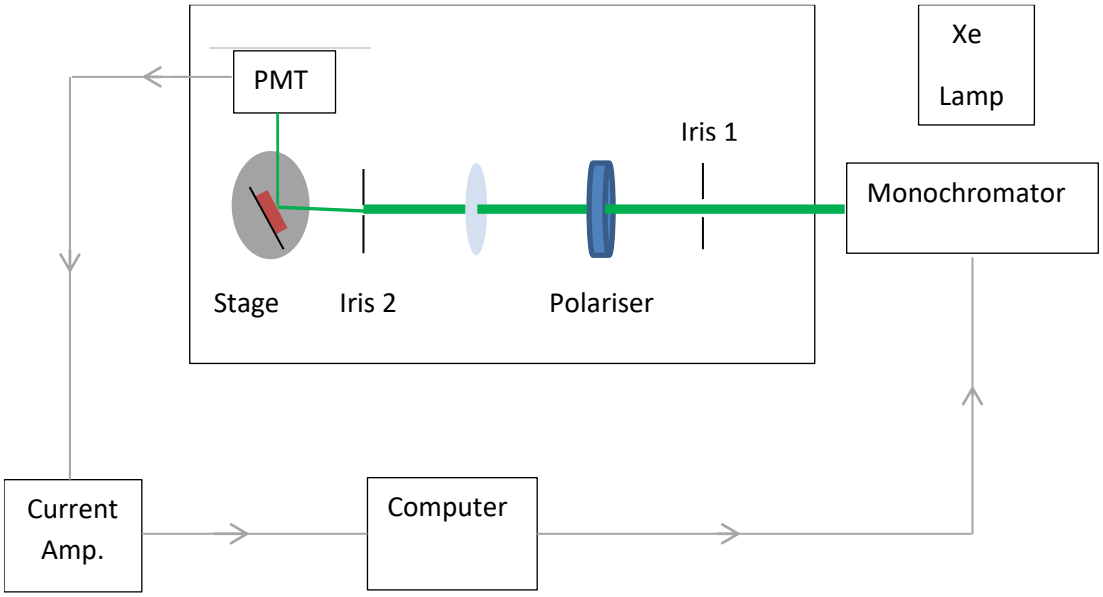

Figure 3.3 *shows the instrument set up used to gather spectral reflectance data from the alumina/gold samples.*

A computer controlled applied photophysics f/3.4 monochromator was used to select the light emitted from a xenon lamp into specific wavelength bands along a preselected range (i.e. 400 nm – 820 nm at 2 nm increments). The diameter of the beam was reduced by passing through an iris diaphragm and then polarised, either *s*- polarised (setting angle of 77° in holder) or *p*-polarised (setting angle of 374° in holder), before passing through a lens of focal length 10 cm. The beam was further reduced by passing through a second iris before reaching the sample surface. The reflected light was collected at the specular angle using a Photomultiplier tube (PMT) and the output signal was amplified using a Bentham Current Amplifier and recorded.

In order to obtain the lamp spectrum and so take into account any signal obtained due to the underlying aluminium substrate, all results were normalised against the signal obtained for a vacuum evaporated aluminium mirror, placed in the sample position on the optical stage.

3.3 Ellipsometry

The set up shown in Figure 3.4 was used for *in situ* monitoring of the alumina film growth during both the second anodisation and barrier layer thinning experiments. The experiments were conducted on a computer controlled Gaertner L116B Rotating Analyser Ellipsometer.

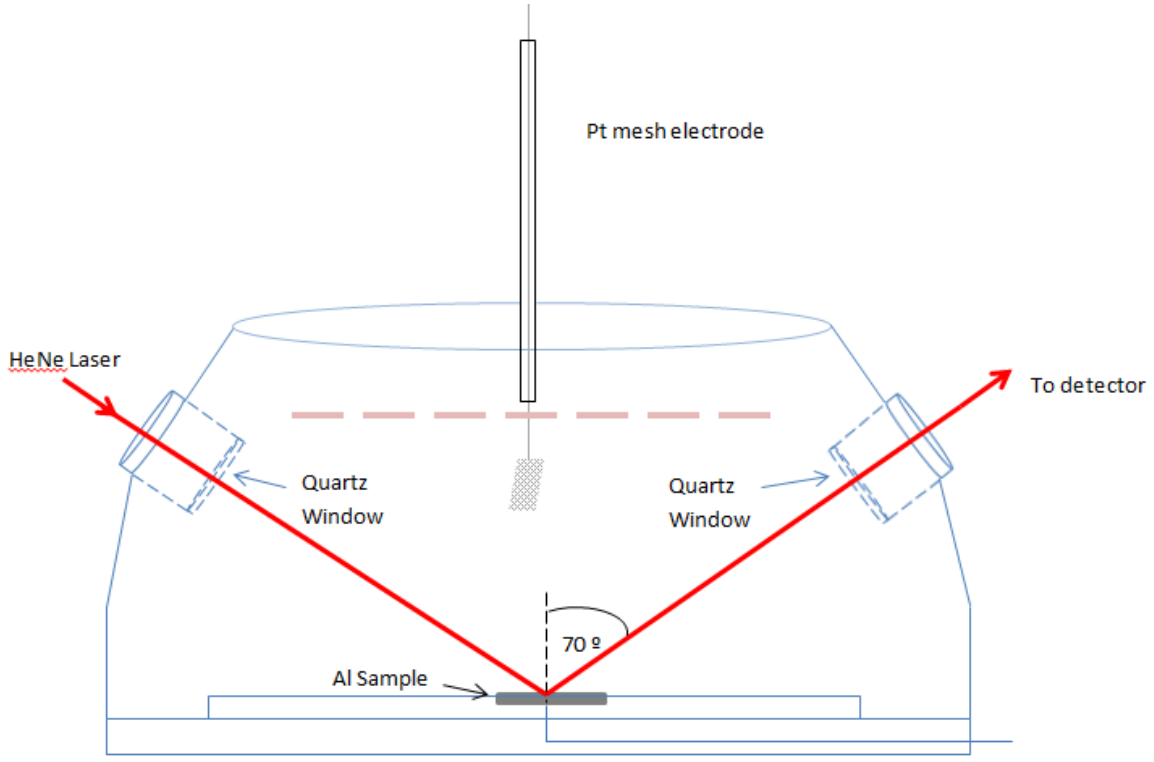

Figure 3.4 *Schematic representation of the ellipsometry cell set-up to gather ellipsometry data from Gaertner L116B Rotating Analyser Ellipsometer utilising a 1 mW He Ne (λ= 638.2 nm) at an angle of 70° incident to the sample.*

Prior to each *in situ* monitoring of the anodisation, the sample was electropolished as discussed above, in order to replicate normal sample preparation and ensure a clean smooth surface for alumina film growth. Fresh solution was used each time and discarded after use. The cell and platinum gauze electrode were thoroughly washed with DIW before adding the 0.3 M oxalic acid solution. The side chambers, by the quartz windows were checked and cleared of bubbles in order to allow the incident and reflected beams a clear passage. The program was set to record the ellipsometric angles (parameters) of Δ and Ψ every five seconds. Ten points were collected before the power from the HP 6564A power supply was switched on to start the anodisation process. At the end of the anodisation period, the power to the electrochemical cell was switched off. The same set-up and data acquisition were also employed for *in situ* monitoring of the barrier layer thinning process.

3.4 Fourier transform infrared spectroscopy

Fourier transform infrared spectroscopy (FTIR) specular reflectance spectra were obtained using a hand held Exoscan FTIR 4100 instrument mounted on a base unit and utilising a 45° specular reflectance probe with a gold mirror reference cap. The probe uses a patented Michelson interferometer design. Data was collected over the wavenumber range 5500 – 600 cm^{-1}. Prior to each sample run, a background check was carried out using the manufacturer supplied gold mirror reference cap that was clicked tightly into place to cover the head of the probe. The cap was then removed and the sample was laid face down flat onto the probe and held in place by hand to ensure a good contact between probe and sample.

Measurements were carried out on the porous film-covered aluminium surface in order to compare like-for-like results obtained by FTIR and ellipsometry and so enable a calibration chart for porous alumina film thickness using the Exoscan instrument to be produced. *In situ* electropolishing was carried out on the sample prior to monitoring of the second anodisation by the ellipsometer over a set time period. Immediately following this, the cell was dismantled and the sample was examined using the Exoscan FTIR. The sample was returned to the cell which was reassembled, the sample electropolished again with the whole process repeated until measurements for the second anodisation periods of three, four, six and seven minutes duration were obtained by both ellipsometer and Exoscan FTIR instruments.

3.5 Cyclic Voltammetry

All cyclic voltammetry experiments were first carried out using a three electrode system with a platinum wire mesh counter electrode, $Hg|Hg_2SO_4|K_2SO_{4\,(sat)}$ reference electrode (E = 0.64 V *vs* SHE) and a gold disc (7 mm diameter) as the working electrode. Electrochemical control was through an EG&G 362 scanning potentiostat with a scan rate of 50 mV s^{-1} and data acquisition was by a custom written LabVIEW 7.1 software. The cyclic voltammogram was then repeated replacing the Au disk electrode with the composite alumina-nanorod sample mounted in the same sample holder used during the sample preparation. Cyclic voltammograms with the AuNR used as the WE were carried out in a two electrode system, with the platinum counter electrode acting as a pseudo reference. Exposure of the rods and thus their ability to carry out electrochemistry was verified by cyclic voltammetry, using a 10 mM cupra ammonium nitrate ($[Cu^{II}(NH_3)_4]\ (NO_3)_2$) in a 1.0 M potassium nitrate solution. This solution

was prepared by adding an excess of concentrated ammonia (NH_3) to a solution of copper nitrate. Cyclic voltammetry was also used to grow a polythiophene layer on top of the gold nanorods embedded in the porous alumina matrix. A solution of 0.05 M thiophene in 0.1 M potassium sulphate in a 60% DIW/40% ethanol solution was used and the scan rate was set to 100 mV/s. The process of growing the polythiophene was repeated with the Au nanorod sample in a Flow cell. The sample here was first cleaned with oxygen plasma and was then left soaking overnight in the 0.05 M thiophene solution.

3.6 Reporter Molecules

The following reporter molecules were used in this study

- Malachite green isothiocyanate (MG) was chosen as a resonant Raman reporter molecule for SERRS due to its maximum absorbance strength (λmax = 630 nm) closely matching that of the laser excitation wavelength of 633 nm.

- 4-mercaptobenzoic acid (MBA) was chosen as a non-resonant reporter molecule.

- NIR 797 isothiocyanate (NIR) was chosen due to its maximum absorbance strength (max at 795 nm) closely matching that of the laser excitation wavelength of 785 nm

3.7 SERS Flow cell design and set up

A flow cell was designed to allow the AuNR to be exposed to different solutions *in situ* whilst mounted on the holder plate of the SERS instrumentation. The initial prototype is shown in Figure 3.5 with the final design, shown in schematic form in Figure 5.13 and in a photograph in Figure 6.13, which was arrived at after several iterations.

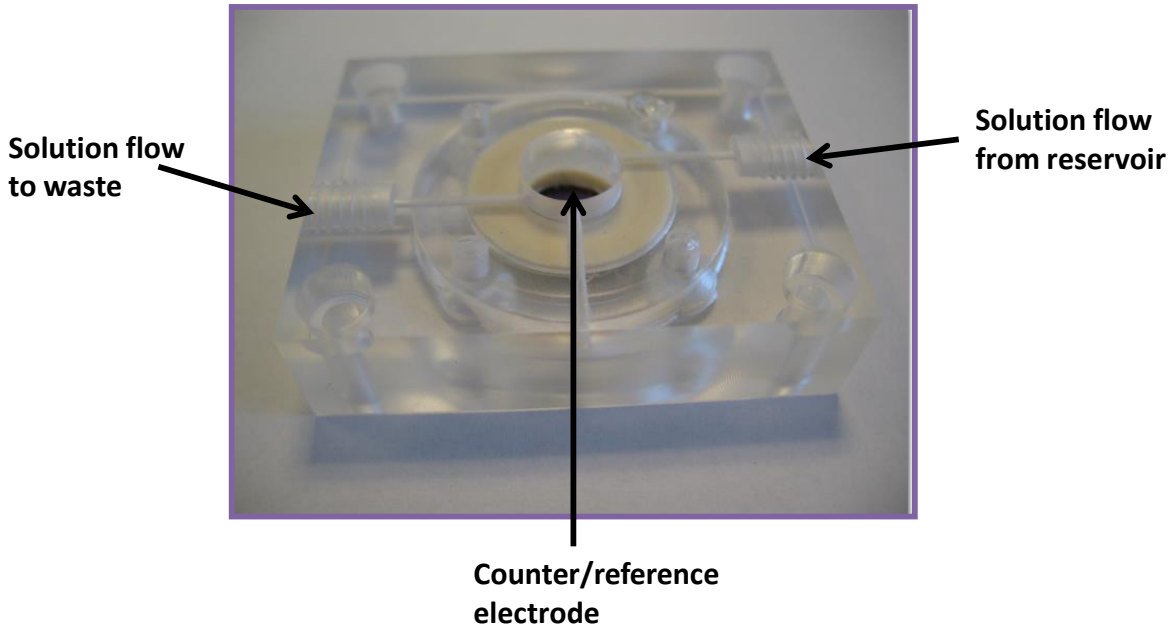

Figure.3.5 *The initial flow cell design, prototype made of perspex.*

The prototypes were made in perspex that had the advantage of making the flow cells inner workings visible. However once functionality had been optimised, PEEK was selected as the preferred material for the production of the finalised design. This was due to excellent and robust chemical resistivity of PEEK. Silver paint was used to attach the sample to the sample holder and provide an electrical connection to the potentiostat. A PTFE washer was used to provide a good seal between the edge of the sample and the flow cell so that electrolyte solution only had access to the central circular area of the sample containing the patterned AuNR spots.

The flow cell was designed in order to allow electrochemical control of the sample/solution interface to be maintained without compromising the SERS and dark-field signals from the sample. The dimensions of the cell were such that it could readily be incorporated into both the SE(R)RS and dark-field imaging set-up's. The electrolyte solution was pumped into the main body of the cell (volume 1 mL) using a peristaltic pump. Electrical connections to the AuNR working electrode and to the platinum wire counter/pseudo-reference electrode allowed electrochemical polarisation of the nanorods to be carried out during SE(R)RS measurements. The flow cell and tubing were cleaned prior to use by pumping through either a 10 vol% HNO_3 solution or 20 vol% *aqua regia* solution.

3.8 Gold nanorod array sample patterning

Initial production of AuNR samples involved gold deposited in all the pores. However this meant that the actual sample area was substantially larger in comparison to the area required for analysis. Therefore, in order to facilitate their use in multiplex analysis a method to selectively deposit gold only into predetermined areas was devised. This involved designing a PTFE mask that covered the sample surface during electrodeposition of gold into the alumina pores. This mask allowed gold electrodeposition only on selected parts of the anodised alumina sample surface not covered by the PTFE mask. This prevented the flow of current resulting in the areas of the sample under the template remaining gold free (see Figures 6.2 and 6.3 in Chapter 6).

3.9 Dark-field microscopy

The microscope used was a Nikon LU Plan ELWD with a 50× objective and a numerical aperture (NA) of 0.55 and a working distance of 9.8 mm and also a 20× objective with a NA of 0.4 and a working distance of 13 mm. The software used was Metamorph Photographs were taken on a Nikon Eclipse LV100 with a 50× objective and a Photometrics Scientific Coolsnap HQ camera. Samples were initially viewed without additional preparation by placing on the base plate. Samples prepared for SE(R)RS analysis (i.e. covered with a monolayer of MG) were also viewed in this way. However, in order to assess if it was possible to monitor the changes in the plasmonic properties of the Au NR arrays in response to an adsorption event. This was explored by the deposition of small 20 nm gold colloidal nanospheres onto an exposed AuNR. Coating the exposed AuNR on the sample with a monolayer of the nanospheres was achieved by, first cleaning the sample surface by oxygen plasma and then soaking the sample overnight in a solution of mercaptohexadecanoic acid in methanol, which was prepared by adding 4 mg of the acid to 15 ml of methanol. The sample was rinsed thoroughly in methanol and dried gently in nitrogen. It was then placed in a polydiallyldimethylammoniumchloride solution (PDADMAC) which was prepared by adding a 40 µl aliquot of PDADMAC into 1 mL of a 1 mM NaCl solution and left for 30 minutes. This was rinsed in DIW rinsed and gently dried in nitrogen stream. This procedure positively charges the sample surface, which helps the gold nanoparticles to attach to the surface [29]. Finally the sample surface was covered in the nanoparticles (T_m = 520 nm) and left for two hours before being gently washed and dried.

3.10 Surface Enhanced Raman Spectroscopy (SERS)/Surface Enhanced Resonance/Raman Spectroscopy (SERRS)

All SE(R)RS measurements were performed using a Renishaw Raman microscope system, both the 50 and 20 × working distance objective were utilised. The 50 × objective was used for samples in air whilst the 20 × was used for samples in an aqueous medium. Two excitation sources were employed at 633 nm and 785 nm. For direct comparison studies the acquired, sample spectra acquired at both wavelengths and at each of the available laser powers setting of 1%, 10%, 25%, 50% and 100% were normalised with respect to a silicon wafer reference standard thus enabling direct comparison of spectra obtained at different times and under varying conditions.

Typically, prior to SE(R)RS analysis, the AuNR samples were rinsed in methanol, dried in a nitrogen stream, cleaned in an oxygen plasma and then secured onto the base of the flow cell and left to set for ~5 min. A few drops of 1 mM malachite green isothiocyanate (MG) in methanol were added to the sample surface and left for 30 min, occasionally adding more drops of methanol when required to ensure the surface did not dry out. The sample was then rinsed thoroughly with methanol and dried in nitrogen to leave a monolayer of MG on the surface of the AuNR.

A similar procedure was employed for the investigation of the layer of polythiophene on the surface of the AuNR. The sample was first prepared as previously by rinsing in methanol, drying in nitrogen, oxygen plasma cleaning and soaking overnight in the 0.05 M thiophene solution. The polythiophene layer was grown by repeated potential cycling between preselected potential limits. The flow cell and system were set up with 0.1 M K_2SO_4 solution used as the electrolyte. The glass cover slip of the flow cell was cleaned with propan-2-ol rinsed in methanol and dried in nitrogen. Once both components were dry, the cell was assembled and a 0.1 M K_2SO_4 solution was pumped into the sample chamber using a peristaltic pump. The circuit was connected to a potentiostat and the open circuit potential of the system recorded. The system was switched on and starting from the open circuit, the potential was decreased in steps of 250 mV to -3000 mV and then increased back again in steps of 250 mV to 3000 mV

3.11 Substrate comparison study

As noted above, MG was chosen as a resonant Raman reporter molecule for SERRS due to its maximum absorbance strength (λ_{max} = 630 nm) closely matching that of the laser excitation of 633 nm. The non-resonant reporter molecule 4-mercaptobenzoic acid (MBA) was also selected. Solutions containing 1 mM of each of these compounds were made up in ethanol. For comparison, nanoparticle samples were prepared by first cleaning a glass slide in aqua regia which was then covered in a polydiallyldimethylammoniumchloride solution (PDADMAC) prepared by adding a 40 μL aliquot into 1 mL of a 5 mM NaCl solution to positively charge the surface. This was left for 30 min and then the surface washed and dried. The sample surface was then covered in the nanoparticles (T_m = 520 nm) and left for two hours before being gently washed and dried. The gold film samples were prepared by vapour deposition of gold (3 layers) onto a glass slide. The samples were cleaned, prior to use, using a plasma cleaner (Harrick Plasma Cleaner PDC-32G) at high power (18 W) for five minutes with a twenty minute vacuum step. An oxygen flow of 2 mL/min in the plasma chamber was maintained throughout the entire process.

All SE(R)RS measurements were obtained over a ten second collection time using a Renishaw Ramanscope system equipped with both 633nm HeNe (50 mW) and 785 nm (50 mW) lasers and a grating of 1200 l/mm. Measurements were performed using either a 50x (NA 0.6) dry or a long working distance 20x (NA 0.4) dry objective lens. The 20x LWD lens was required for *in-situ* measurements while both the 50x and 20x were employed *ex-situ* at various times throughout the thesis.

3.12 Field emission - scanning electron microscope

The field emission - scanning electron microscope FE-SEM used was a HITACHI SU-6600, a high-resolution analytical variable pressure, field emission scanning electron microscope. Variable pressure enables the analysis of no-conductive samples without the need to coat in gold. No pre-treatment of samples was required prior to analysis by FE-SEM. Up to a maximum of seven samples could be placed in the specimen chamber at a time. The samples were mounted onto a circular specimen stub and held in place by means of a double sided carbon tape to ensure the nanorod arrays were electrically conductive and grounded to prevent

an accumulation of electrostatic charge on the sample surface. For those samples with areas with low or no gold deposition, the back of the samples were coated in silver conducting paint prior to mounting on the specimen stub in order to aid charge dispersal. Images were taken looking directly down onto the sample which was at an angle of 30^{o}.

4. Development of gold nanorod arrays

The focus of this chapter is the preparation and optimisation of the experimental conditions required to create vertically orientated AuNR. This primarily involved the optimisation of the conditions employed for the preparation of the porous alumina template. Ellipsometry was used to monitor the growth of the porous films and its thickness. It was also employed in the development of a less time consuming method of measuring alumina film thickness by FTIR. A second anodisation process was also carried out in order to yield ordered hexagonally patterned pores with controlled diameter. Gold electrodeposition in the pores is then described followed by the spectroscopic evaluation of the composite gold/alumina layer. Controlled etch-back is used to expose the nanorods so that electroactive species could be reduced/oxidised on the composite surface. This chapter aims to show the benefits in the choice of an alumina template for the growth of nanorod arrays.

4.1 Cyclic voltammetry of non-porous and porous thin film alumina growth

Prior to examining the porous alumina film growth, the formation of a non-porous aluminium oxide barrier layer was studied. This was achieved using 0.3 M tartaric acid solution at 30°C for the electrolyte with the technique of cyclic voltammetry. The following experiments were performed using the same cell set up as was used for ellipsometry experiments, as shown in Figure 3.4. The mechanically polished sample acted as the working electrode with a platinum gauze counter/pseudo reference electrode. The data obtained is shown in Figure 4.1 for repeated cycles with the positive limit in each subsequent cycle increased by 0.5 V. As can be seen from the plot, initial oxidation of the aluminium sample occurred at −1.0 V ($Hg/Hg_2SO_{4(sat)}$) and a rapid rise in current was found as the aluminium underwent anodic dissolution, Equation 4.1.

$$Al \rightarrow Al^{3+} + 3e \qquad \textbf{Equation 4.1}$$

The initial rise in the current is due to Butler-Volmer kinetics resulting from an increase in the overpotential but this is then impeded by the formation of an aluminium oxide film on the aluminium surface. This film is formed as a result of a high Al^{3+} ion concentration building up

around the electrode surface and its subsequent reaction with the solvent to precipitate out as $Al(OH)_3$ and then to Al_2O_3, shown in Equation 4.2 and Equation 4.3 respectively

$$Al^{3+} + 3H_2O \rightarrow Al(OH)_3 + 3H^+ \qquad \textbf{Equation 4 2}$$

$$2Al(OH)_3 \rightarrow Al_2O_3 + 3H_2O \qquad \textbf{Equation 4.3}$$

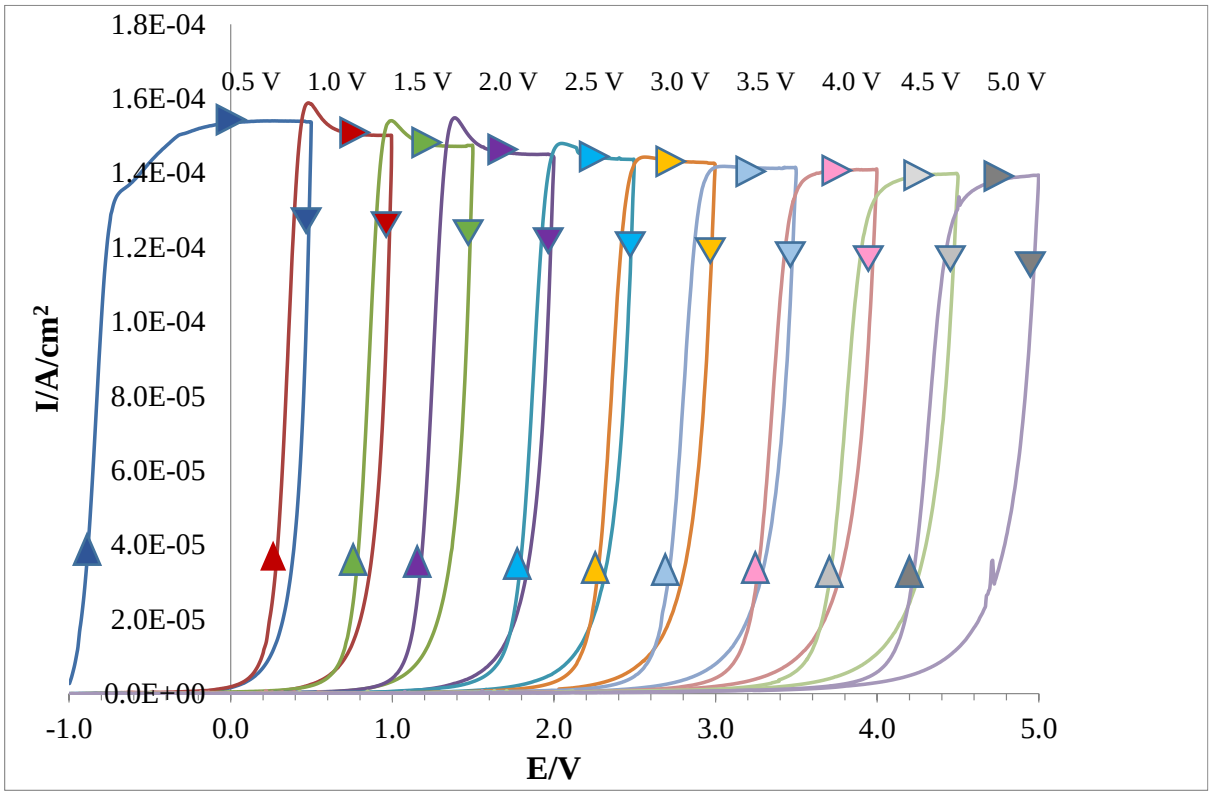

Figure 4.1 *Multiple cyclic voltammograms showing the growth of non-porous alumina, by repeat cycles of increasing positive limits from 0.5 V to 5 V, in 0.3 M tartaric acid, at a scan rate 50 mV/s.*

The solid alumina film formed an electronically insulating film that inhibited any further free dissolution of the aluminium, referred to as a barrier layer. In order for further growth to occur, ions (Al^{3+}, O^{2-}) had to be forced through the film. In order to achieve this a very high electric field was required (~ 10^6 V cm^{-1}). The continued growth of the film could only occur by increasing the voltage as this then maintained the constant electric field. Thus, as can be seen in the first cycle, the rate of film growth became constant with increasing voltage up to the limit, set at 0.5 V. At this point in the cyclic voltammogram, the voltage was reversed reducing the voltage and the electric field available for film growth. This reduced electric field was then

insufficient to allow the ions to move through the solid, resulting in the film growth becoming severely inhibited and so the flow of current dramatically falling to zero.

In the second cycle, the positive limit was set to 1.0 V with the same starting potential as before. It is immediately apparent that no film growth occurred until the applied voltage reached 0.5 V. At this point, the electric field was high enough to once again move ions through the film and film growth was restored, yielding a constant rate of growth. Again, when the limit of 1.0 V was reached and the voltage sweep was reversed, the current again dropped to zero. The same effect could be seen in all subsequent cycles with continued film growth only occurring beyond the limit of the last cycle once the voltage exceeded that limit. This is known as the high field growth mechanism[340] and is typically found for the growth of barrier films. This also means that the voltage applied to the system dictates the thickness of the film. Thus for a given voltage, a finite film thickness will be obtained.

The corresponding series of voltammograms in a system where in addition to a barrier layer a porous oxide film is formed on the aluminium surface is shown in Figure 4.2. The electrolyte used in this instance is 0.3 M oxalic acid. The form of the first cycle was similar to that observed in tartaric acid, i.e. onset for anodic dissolution of Al at −0.5 V with an initial rapid rise in current followed by a period of constant growth rate until the potential limit of 0.5 V is reached. Once again, on reversal of the voltage scan, the current dropped dramatically. However, with the next cycle film growth can be seen to start much earlier than the potential limit of the previous cycle, here at 0 V. This indicates that at this point, the film present on the surface was not a full barrier layer and indeed previous work[340] has shown that in oxalic acid a porous layer grows on top of the barrier layer. The porous film forms because of field induced chemical dissolution of the barrier layer with both porous film growth and barrier layer thickness maintained by the electric field. The growth process could be observed in all subsequent cycles, where barrier film growth and porous film formation occur prior to reaching the previous cycle's potential limit.

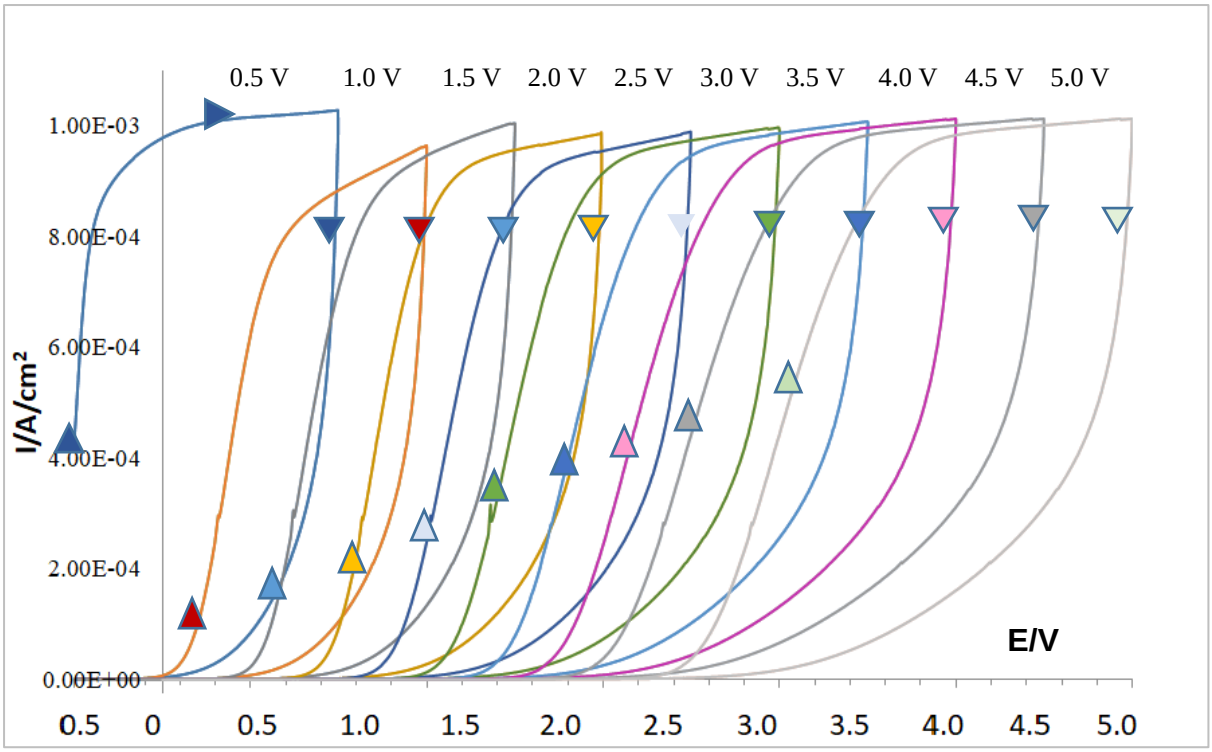

Figure 4.2 *Multiple cyclic voltammograms of aluminium, with increasing positive limits from 0.5 V to 5 V in 0.3 M oxalic acid, scan rate 50 mV/**s.***

4.2 Ellipsometric monitoring of alumina film growth

Alumina film growth in both tartaric acid and oxalic acid media was monitored using *in–situ* ellipsometry. Here the sample was placed in the specially designed electrochemical cell and sealed with araldite as shown previously in Figure 3.4. Electropolishing was carried out on the sample in the cell prior to anodic oxide growth. Figure 4.3 shows the data obtained for the barrier layer film growth in tartaric acid up to a final voltage of 110 V. The voltage was stepped up and held at each of the voltages indicated in Table 4.1 and the ellipsometric data at each step was recorded at intervals of five seconds. It can be seen in Figure 4.3 that on each occasion the voltage was increased a sudden spurt of film growth occurred which tailed off exponentially to give a grouping of points indicating that film growth at that voltage had terminated. Further growth only occurred on the next voltage increase, repeating the response discussed previously. The trend in the data is entirely in line with the cyclic voltammetry data. However, it was not possible to model the data obtained beyond 90 V as the roughness of the surface of the non-porous film from that point onwards did not fit the modelling criteria used, *viz,* parallel surface films interacting with the incident radiation.

Ellipsometry was used to monitor the growth and help determine the thickness of the thin film alumina produced during anodisation in a 0.3 M tartaric acid solution. The modelling of the ellipsometry data is also shown in Figure 4.3 and was carried out using a custom written software, ELLIPSE, with values for the refractive indices of the aluminium substrate, alumina barrier layer and electrolyte medium together with the alumina thickness at the various voltages are given in Table 4.1. Due to the high-field growth mechanism, an increase in voltage was required after a period of 30 s at each set voltage to facilitate further film growth. Data was recorded at intervals of 5 s. and is represented by markers in the figure. A multi-coloured smooth line represents the modelled data. Each coloured segment represents a different film, the properties of which were obtained by modelling of the data and are given in Table 4.1.

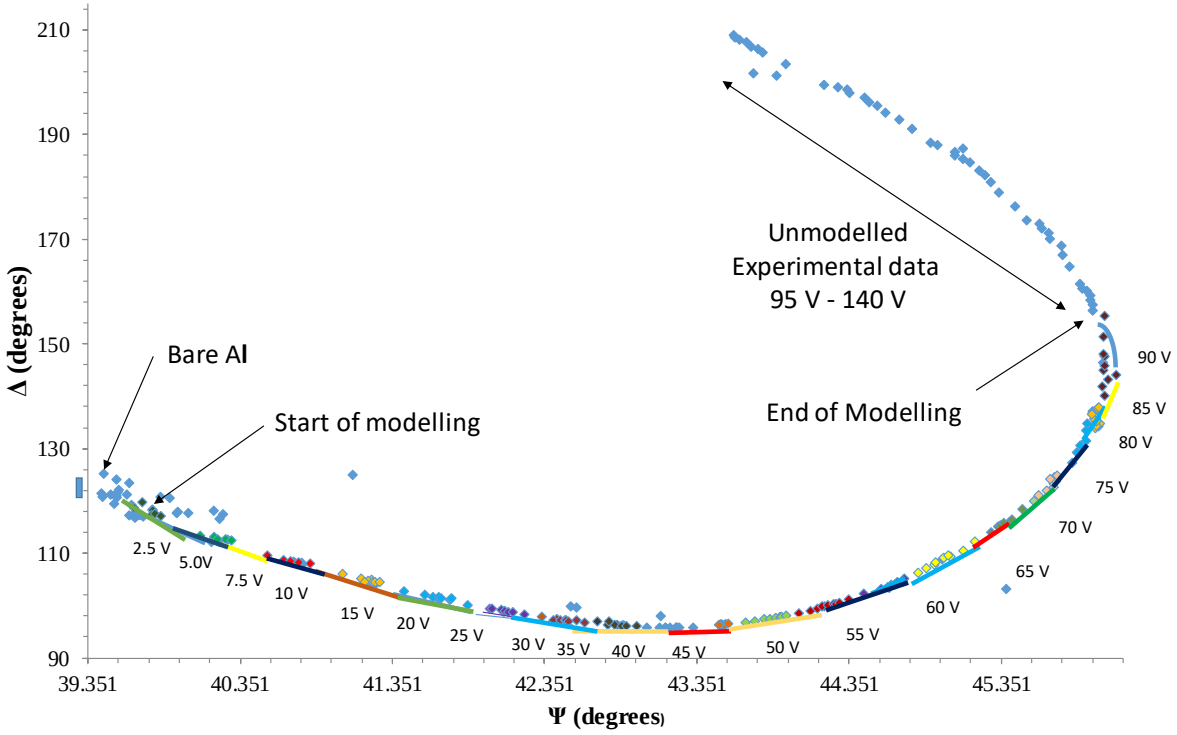

Figure 4.3 *Ellipsometry Δ-ψ plot for the modelling of non-porous alumina film grown on aluminium in 0.3 M tartaric acid by potential step from 0 V to 140 V. Experimental data was represented by markers and modelled data is represented by a multi-coloured smooth line. Each segment of which represents the growth at each voltage increase as given in Table 4.1. N.B It was not possible to model the data obtained from 95 V to 140 V due to the roughness of the non-porous film.*

Voltage (V)	Film Thickness (nm)	Refractive index *n*.
2.5	**11**	**1.5**
5.0	**15**	**1.5**
7.5	**16**	**1.5**
10.0	**18**	**1.5**
15.0	**25**	**1.5**
20.0	**31**	**1.5**
25.0	**38**	**1.5**
30.0	**47**	**1.5**
35.0	**53**	**1.5**
40.0	**59**	**1.5**
45.0	**65**	**1.5**
50.0	**70**	**1.5**
55.0	**79**	**1.5**
60.0	**87**	**1.63**
65.0	**94.5**	**1.63**
70.0	**104**	**1.63**
75.0	**110**	**1.63**
80.0	**122**	**1.63**
85.0	**128**	**1.63**
90.0	**137**	**1.63**

Table 4.1 *Film thickness and associated refractive index obtained from the modelled ellipsometry data in Figure 4.3 of non- porous alumina formed with an applied voltage by step increase over the range 2.5 V to 90 V in tartaric acid.*

The refractive indices evaluated for the barrier film at each voltage showed some variation with a step increase in film thickness. Initially *n* was 1.5 from 2.5 V – 55 V then increased to 1.63 from 60 V to 90 V. However it can be seen in Figure 4.4 that the barrier film thickness increases linearly with voltage. Furthermore, the inverse gradient of the line gives the required electric field for film growth with a value obtained here being 0.672 V nm^{-1} or 6.72×10^6 V cm^{-1}.

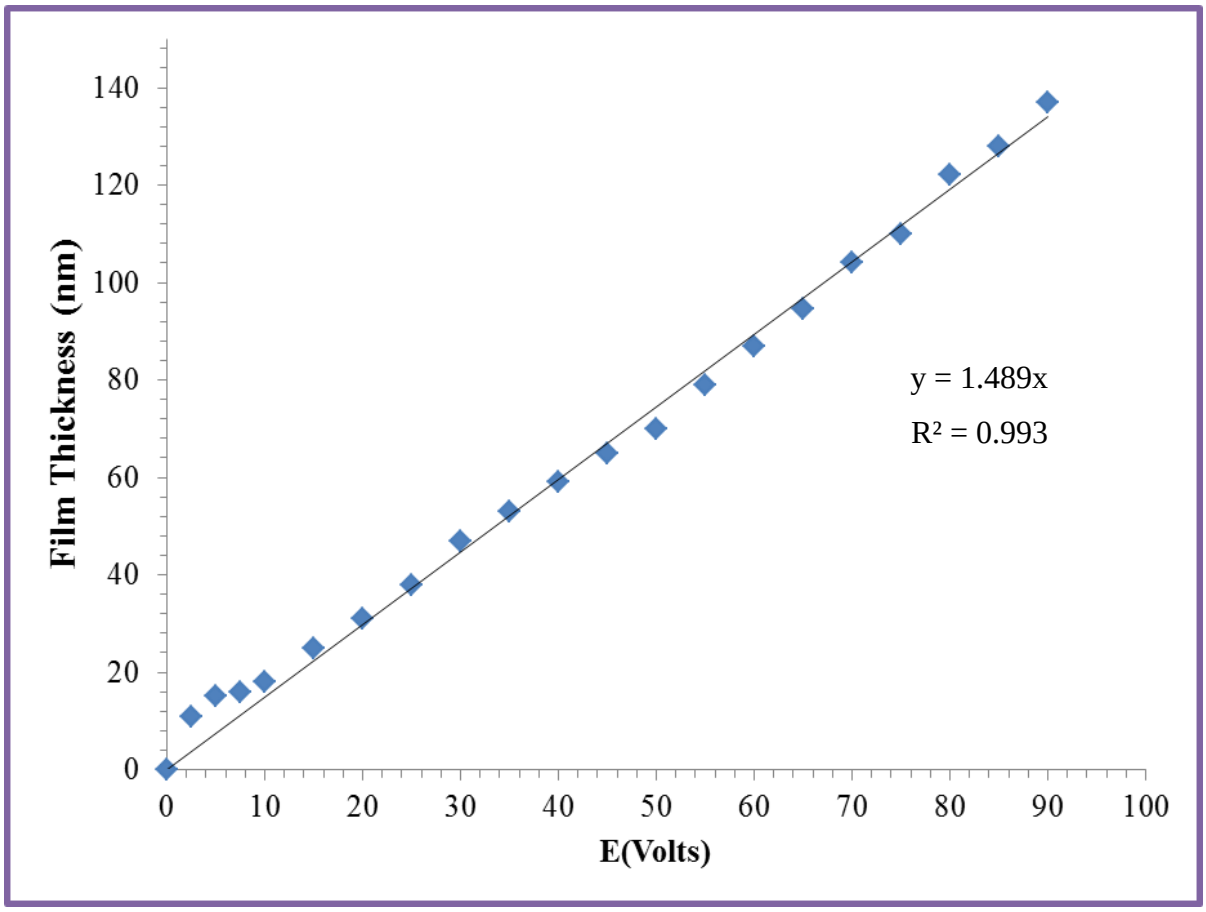

Figure 4.4 *The plot of barrier film thickness against voltage shows the relationship to be linear.*

In contrast to the results obtained with tartaric acid, film growth in an oxalic acid medium gave rise to a porous film on top of the barrier layer. From the ellipsometric data shown in Figure 4.5 it can be seen that on application of the constant 40 V potential across the aluminium/solution interface, there was a large initial shift in the Δ-Ψ signal from the start value, corresponding to the formation of the barrier film of 100 nm at that voltage. However, in this medium, film growth did not stop. The progression of the data points indicates the continuous growth of the porous layer on top of the barrier film.

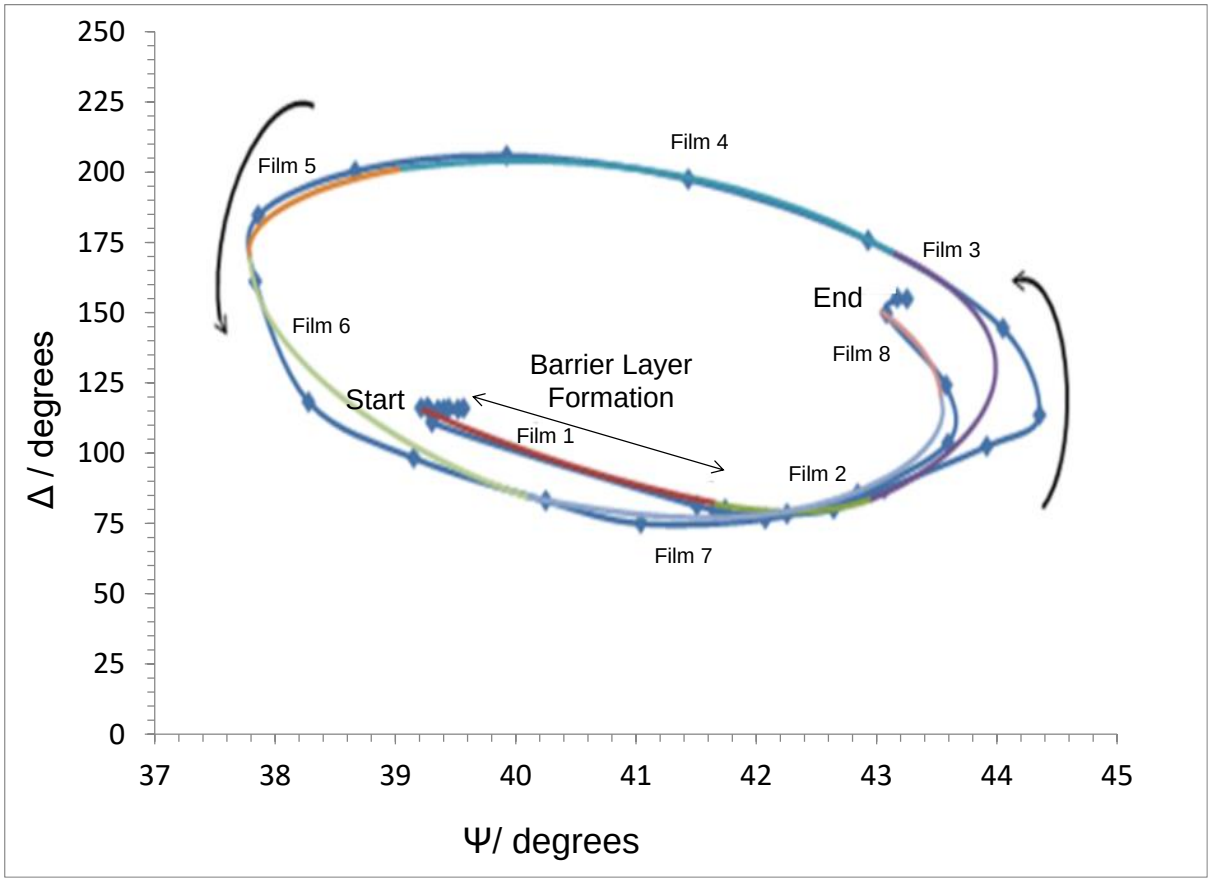

Figure 4.5 *Ellipsometric data for the growth of an alumina film on aluminium in oxalic acid at a constant voltage of 40 V, measured over a five-minute period. The experimental data represented by blue markers on a solid blue line with the modelled data represented by a multi-coloured smooth line each coloured segment of which represents one of Films 1 to 8.*

One complete loop in the Δ-Ψ curve, shown in Figure 4.5 corresponds to a film thickness of 248 nm calculated using Equation 2.10 which represents the thickness of films 2-5. Film 1 represents the barrier layer while films 6, 7 and 8 represent an incomplete second loop. The total film thickness is the sum of each of the eight film thicknesses and was calculated to be 563 nm. The data used in this calculation is given in Table 4.2. Again, this data confirms the observations and interpretation of the cyclic voltammetric data, in that the porous film growth can occur at voltages lower than that required to form the full barrier layer. This is because field assisted dissolution of the oxide layer occurs at random points on the surface [155]. This reduces the film thickness at those points and so growth can continue at the same applied voltage. It should be noted that growth occurs where the metal is oxidised at the aluminium/aluminium oxide interface.

Film	n	k	*d* (nm)
1	1.5	0.000	110
2	1.53	0.000	40
3	1.6	0.000	45
4	1.65	0.004	160
5	2.35	0.035	3
6	1.57	0.001	80
7	1.54	0.000	100
8	1.5	0.005	25

Table 4.2 *Ellipsometric data for the growth of the alumina film grown on aluminium in oxalic acid at a constant voltage of 40 V, measured over a 5 minute period, as shown in Figure 4.5 in which each of the eight films used in the calculation of the overall film thickness are represented by each successive coloured segment.*

As has been mentioned previously in Section 3.1.6, gold electrodeposition must take place inside the pores of the alumina film formed in the oxalic acid electrolyte in order to form the AuNR. However, at 40 V, the barrier layer thickness is quite substantial (~60 nm) and it would be impossible to electrodeposit the gold through this electronically insulating layer. For this reason, the barrier layer at the bottom of the porous alumina layer must be thinned or removed before any gold deposition can occur. To do this, the voltage was reduced step-wise from the 40 V growth voltage so that film-dissolution rather than growth dominated. This reduction in cell voltage was continued until a final voltage of 6.5 V remained across the film. This process of barrier layer thinning was also followed using *in-situ* ellipsometry.

However, ellipsometric monitoring during the barrier layer thinning showed that the porous alumina film continued to grow during most of the voltage-reduction process. This growth rate was found to be quite rapid whilst the voltage was in the range 40 V to 24 V but then slowed considerably for voltages between 24 V and 6.5 V. As is evident from the plot in Figure 4.6 this drastically affected the overall film thickness of the porous layer, doubling and even tripling the final film thickness obtained for second anodisation periods of two minutes and five minutes duration.

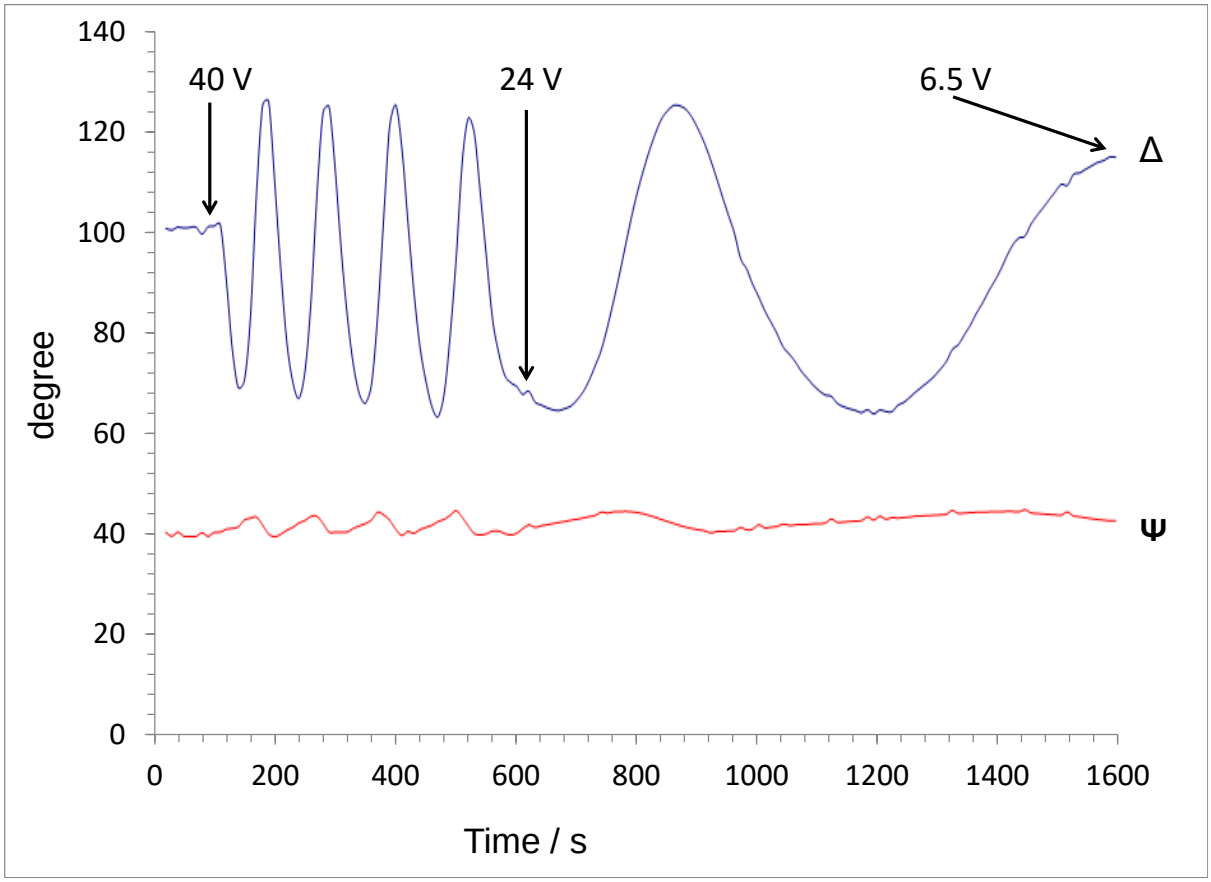

Figure 4.6 *Δ-Ψ signature obtained during the barrier layer thinning process. The growth rate was found to be quite rapid whilst the voltage was in the range 40 V to 24 V but then slowed considerably for voltages between 24 V and 6.5 V.*

It is apparent that during the period taken (~500 s) to reduce the voltage from 40 V to 24 V four complete cycles in the Δ-Ψ data occurred. Assuming a refractive index of the porous alumina as n = 1.5, this yields a phase film thickness of 316 nm and so, 4 × 316 nm = 1264 nm = 1.26 µm of further film growth occurred over that period.

Clearly, this procedure was not suitable for producing pores of the required length and diameter for subsequent gold deposition. An initial modification to this method involved a rapid decrease of the voltage from 40 V to 6.5 V in 60 s in order to prevent this continued porous film growth. However, this also prevented barrier layer thinning and therefore made any subsequent electrodeposition of the gold more difficult. A procedure was developed, whereby the voltage was set to 122 V and the current to 0.0012 A (1.2 mA). This saw the voltage fall to 24 V within 30 s and then slowly drop to 6.5 V. Providing the voltage drop from 24 V to 6.5 V took at least 10 minutes, the barrier layer was found to have thinned sufficiently to allow the subsequent

electrodeposition of the gold in the pores with minimal further porous film growth. This procedure was subsequently adopted for preparing the alumina template prior to gold electrodeposition throughout the remainder of the work.

Although ellipsometry gave an accurate measurement of pore depth, the set up was not amenable for use on the actual samples subsequently prepared for gold electrodeposition. Once mounted using epoxy resin, the sample could not be removed undamaged from the cell. It was felt that a more rapid and straightforward technique such as FTIR might be more useful in giving the required information on pore length, especially following the barrier thinning process.

4.3 Analysis of porous alumina samples by specular reflectance FTIR spectroscopy

The analysis of the porous alumina samples by specular reflectance FTIR was initially carried out in order to determine if it could be used as a means of detecting the longitudinal surface plasmon resonance of the AuNR in the IR region. This was in addition to establishing the amount of alumina required to be etched back in order for the gold nanorods to be exposed. This technique did not prove to be effective for these purposes. It did however show that there was a linear relationship between the reflectance intensity spectra for anodic film growth after different anodisation periods, as shown in Figure 4.7. There are several peaks in this spectra but the relevant one here is that of aluminium oxide at 955 cm^{-1}. This is due to the longitudinal mode of the Al-O bond stretching vibration[156]. The double peaks at 1475 $cm^{-1}$and 1570 cm^{-1} are due to adsorbed carbonate species[157]. It can be seen that the intensity of this feature increases with anodisation time and film thickness.

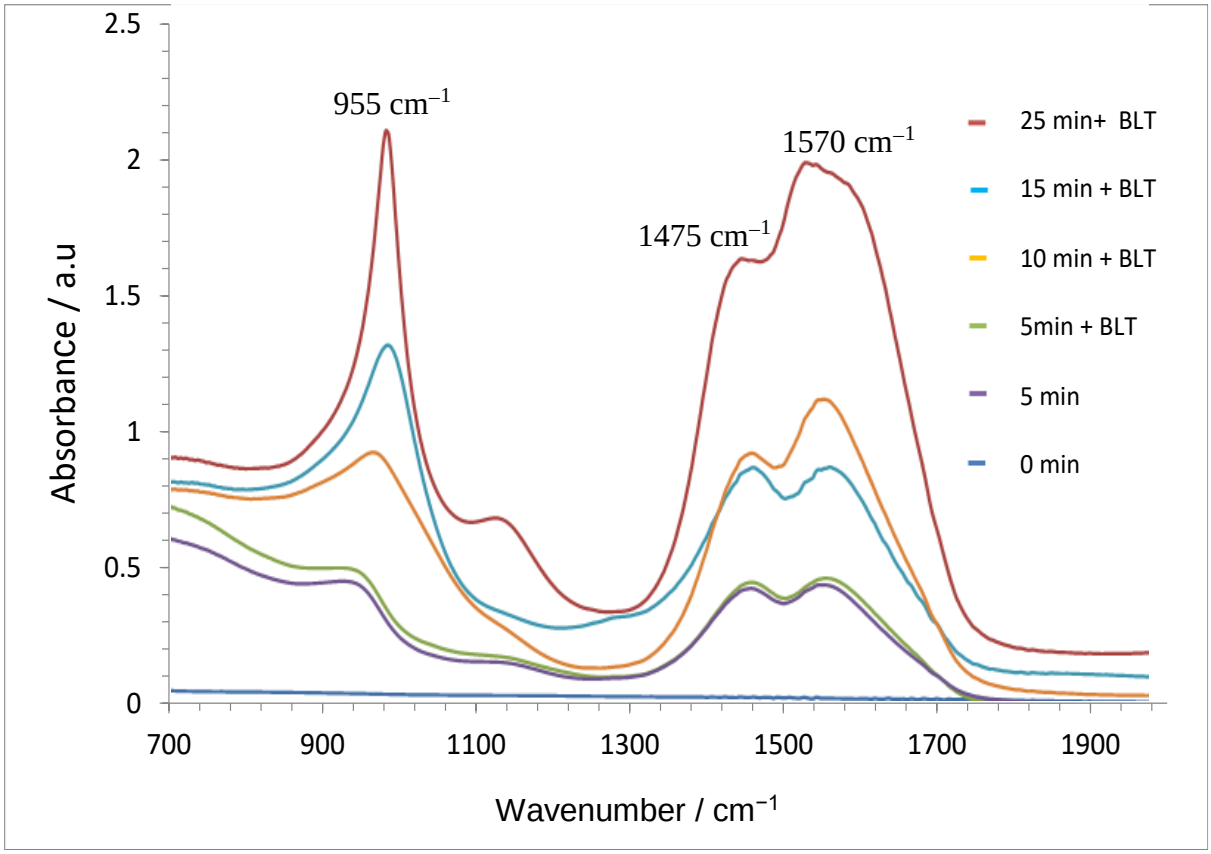

Figure 4.7 *Plot of absorbance against wavelength for alumina films grown using various second anodisation periods of 0, 5 minutes, 5 minutes with barrier layer thinning (BLT), 10 minutes with BLT, 15 minutes with BLT, 25 minutes with BLT in oxalic acid.*

For the peak at 955 cm^{-1}, the plotted data shows a linear relationship between the reflectance intensity and the duration of the second anodisation period, as shown in Figure 4.8.

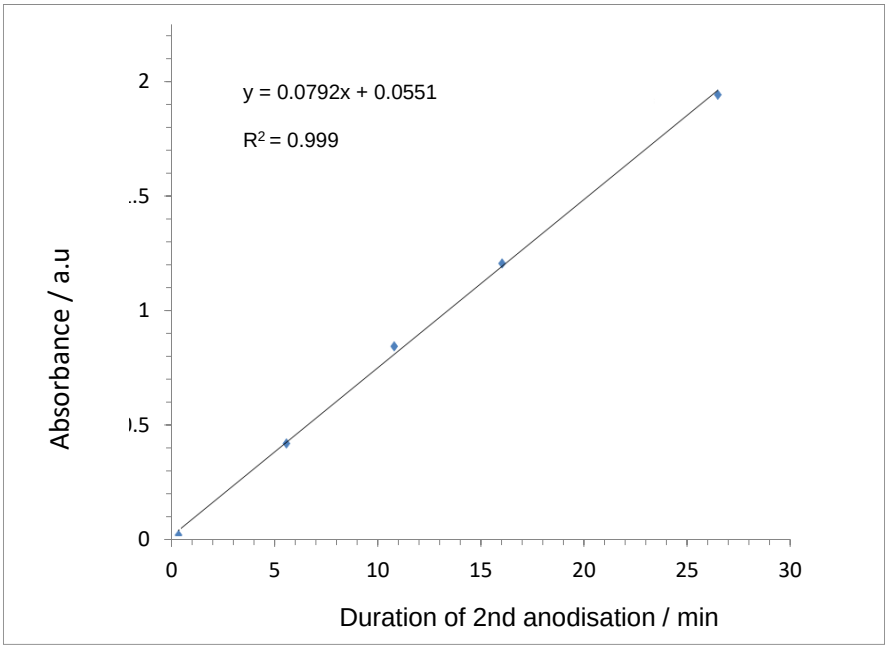

Figure 4.8 *Plot of absorbance at 955 cm^{-1} vs duration of second anodisation period (blank corrected) at 0, 5, 10, 15 and 25 minutes.*

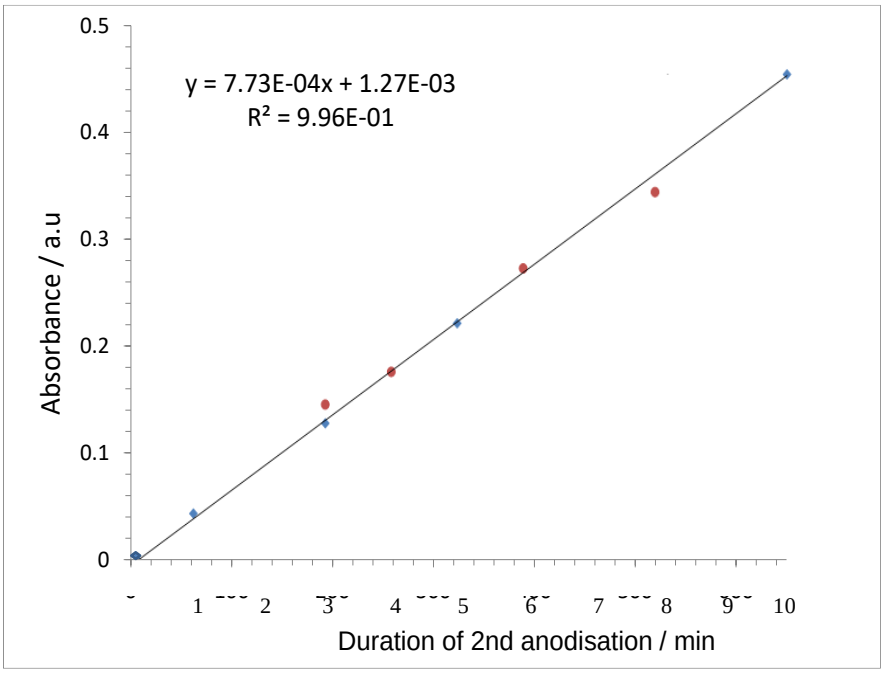

Figure 4.9 *Plot of absorbance at 955 cm^{-1} as a function of second anodisation time encompassing in-situ ellipsometry monitoring of film growth of samples anodised for periods of 1, 3, 5 and 10 minutes duration (blue dots) and 3, 4, 6 and 8 minutes (red dots).*

In order to verify the validity of this approach in determining the second anodisation porous film thickness, samples were anodised for periods of 1, 3, 5 and 10 minutes duration in oxalic acid. *In-situ* monitoring was performed during each anodisation to determine the film thicknesses by ellipsometry. Subsequently, the FTIR spectra of these samples were also measured. Figure 4.9 shows the FTIR intensity at 955 cm^{-1} as a function of second anodisation time measured by both ellipsometry and FTIR. This data was then produce the data used in Figure. 4.10 and shows the FTIR intensity at 955 cm^{-1} as a function of the film thickness. Thus this calibration plot was drawn from the data obtained from *in-situ* ellipsometry monitoring of film growth for the samples anodised for periods of 3, 4, 6 and 8 minutes (red dots). The excellent correlation between film thickness and the FTIR intensity was confirmed.

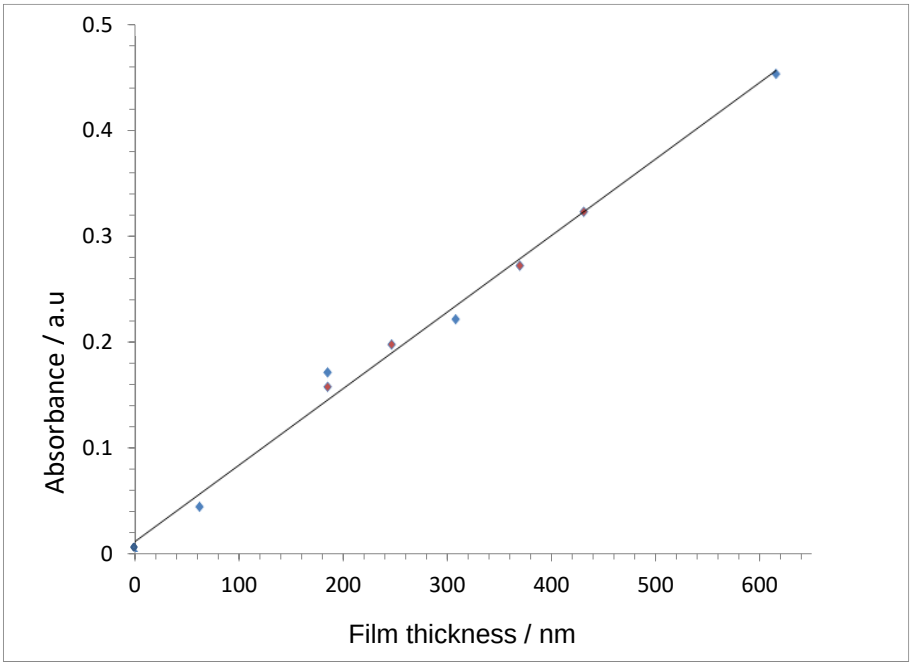

Figure. 4.10 *Plot of absorbance at 955 cm^{-1} vs film thickness, calculated from the data in Figure 4.9 as measured using FTIR (blue dots) and ellipsometry (red dots).*

These results show that the FTIR could be used as a quick method for determining film thickness from the duration of the second anodisation period. As far as has been determined, no similar work had been carried out at the time. However recent searches have found that 'in situ attenuated total reflectance infrared (ATR-IR) spectroscopy has been used to monitor the transformation of γ-Al_2O_3 into boehmite (AlO(OH)) under hydrothermal conditions[158].

4.4 Electrodeposition of gold into alumina pores

The electrodeposition of gold into the pores of the alumina film required the application of an ac voltage across the cell with the counter and reference electrode terminals connected together as a pseudo-reference electrode in the two-electrode cell configuration. The duration of the deposition as well as the final amplitude of the ac voltage determined the length of the nanorods obtained. It was necessary to use ac voltage for this purpose as a barrier layer of ~60 nm remained between the underlying aluminium and the porous oxide layer. Since the barrier layer thinning process was to be halted when the voltage across the alumina film reached 6.5 V, the initial ac voltage (*rms*) applied was set to this value. It was evident that gold deposition occurred immediately on application of the ac voltage from the instantaneous change in colour across the sample area from silvery-grey to purple, indicating the presence of AuNP within the pores. It should be noted that the electrodeposition of gold occurred only during the negative half cycle of the sinusoidal voltage. An annealing process of the etched anodic oxide film occurred on the positive half cycle, which eventually made it more difficult for further electrodeposition to take place.

Figure 4.11 shows two alumina samples prepared as described previously in section 3.1.8. As all conditions including the second anodisation time were identical for these two samples, the porous templates produced have the same pore width and depth.

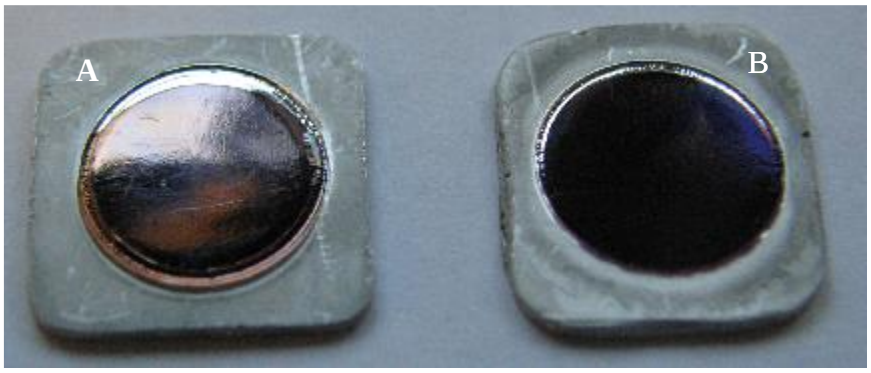

Figure 4.11 *Two samples A and B with the electrodeposition of gold into the pores of an alumina substrate (15 mm × 15 mm). Sample A (light pink colour achieved using a deposition time of 1 second at an ac voltage of 6.5 V_{rms}. Sample B (deep purple colour) achieved using a deposition time of 10 seconds at 6.5 V_{rms}) and 5 seconds at 7 V_{rms}.*

Sample A, which has a light pink colour was achieved using a deposition time of one second at an ac voltage of 6.5 V_{rms}. Sample B on the other hand is a deep purple colour achieved using a deposition time of ten seconds at 6.5 $V_{rms)}$ and five seconds at 7 V_{rms}.

4.5 Specular reflectance on gold nanorod arrays

Specular reflectance spectra using polarised light were obtained for the samples after gold deposition into the pores of the alumina template. In order to help determine the depth of the gold within the alumina film and so calculate the amount of alumina be removed in order to expose the AuNR. The spectra were all normalised using an aluminium mirror to remove the contribution to the signal obtained from the supporting aluminium substrate beneath the gold-alumina layer. Reflectance spectra of the bare alumina template (i.e. containing no AuNR) followed the same signature as that of the aluminium mirror but at a lower intensity.

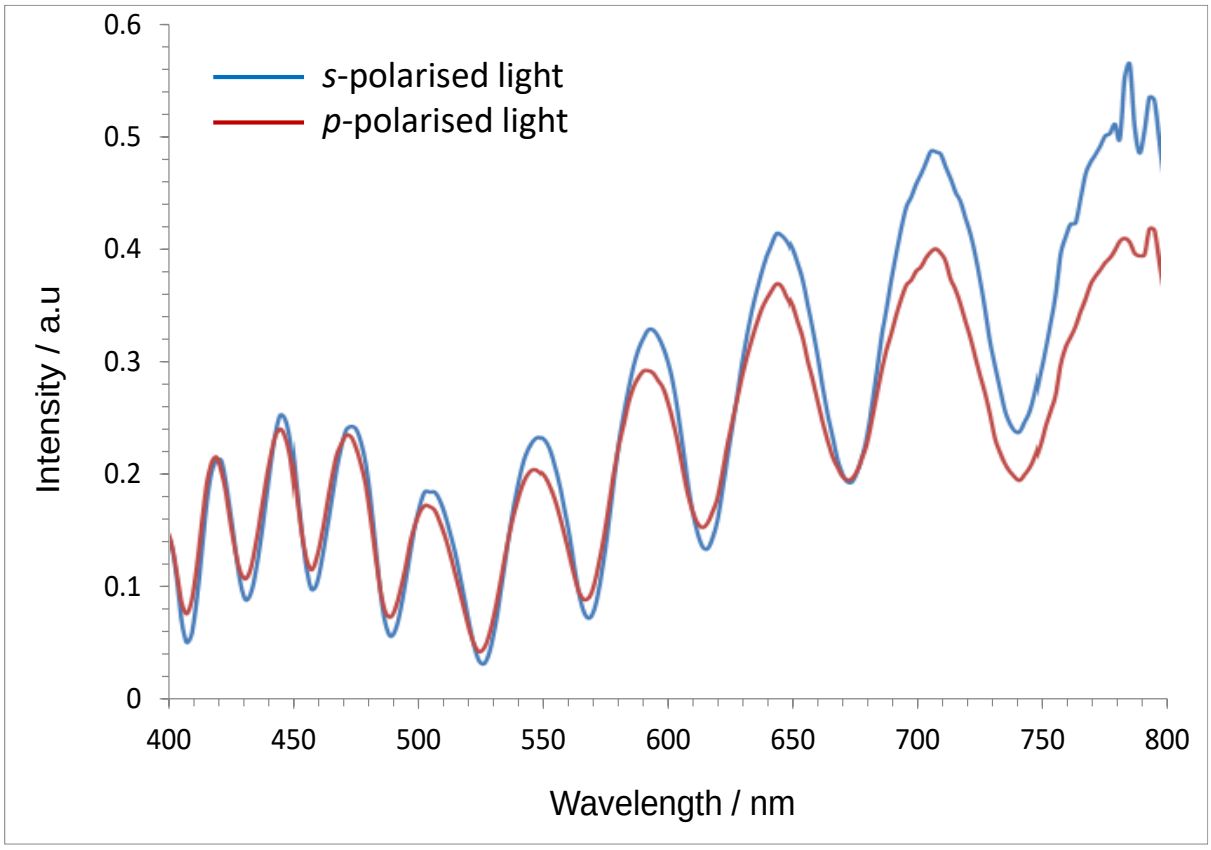

Figure 4.12 *Specular reflectance using s (blue) and p (red) polarised light at an angle of incidence of 36°showing the interference pattern arises as a result of the different distances travelled by the beams of light reflected from the oxide/air interface and the gold-alumina/alumina interface.*

In the case of the gold-alumina composite samples, the most distinctive feature of the spectra obtained was the interference pattern over the wavelength range 400 nm to 800 nm. This is shown in Figure 4.12 and arises as a result of the different distances travelled by the beams of light reflected from the oxide/air interface and the gold-alumina/alumina interface. Superimposed onto the pattern is a distinctive dip in the average intensity as a result of the transverse plasmon resonance at ~ 520 nm. This dip is clearly visible in the spectra obtained with both *s*- and *p*- polarised light. The spectrum obtained for *p* polarised light, as expected, showed less intensity in the reflected light detected. However, no real evidence of the longitudinal plasmon was found for this sample, which would have been attributed to the absorption band of the longitudinal plasmon. This must unfortunately lie out with the instrument's range in the NIR region.

The fringe pattern seen in the *s*-polarised light spectrum was used to calculate the depth of the pores down to the electrodeposited gold within the pores. The clarity and amplitude of the fringes are also an indication of the smoothness of the aluminium substrate and the uniformity in thickness of the porous oxide layer, i.e. the sharpness of the interfaces produced by the anodisation and gold electrodeposition. Poorly polished samples exhibited little if any interference fringes. The smoother the aluminium surface the more ordered and parallel the pores developed during anodic film growth.

Figure 4.13 compares the specular reflectance spectra obtained for two alumina samples with electrodeposited gold. Sample A was produced with a second anodisation period of two minutes whereas Sample B was produced with a second anodisation period of thirty minutes. Both Samples A and B were subjected to identical conditions for the deposition of gold into their pores at 6.5 V_{rms} for 6 s. The T_m plasmon at 520 nm is clearly visible in the spectra of both samples, indicating similar pore diameters of the alumina templates, the number and intensity of fringes present in each are considerably different. This shows the depth of the gold within the pores of the alumina matrix to be substantially greater in sample B than in sample A. Indeed the values obtained using Equation 3.1 (inset in Figure 4.13) were found to be 8.52 μm for sample B and 1.13 μm for sample A. It can also be seen that the reflected light from sample B was around 30 times less intense than that for sample A, indicating that the depth of the gold/alumina interface within the pores attenuated the reflected light.

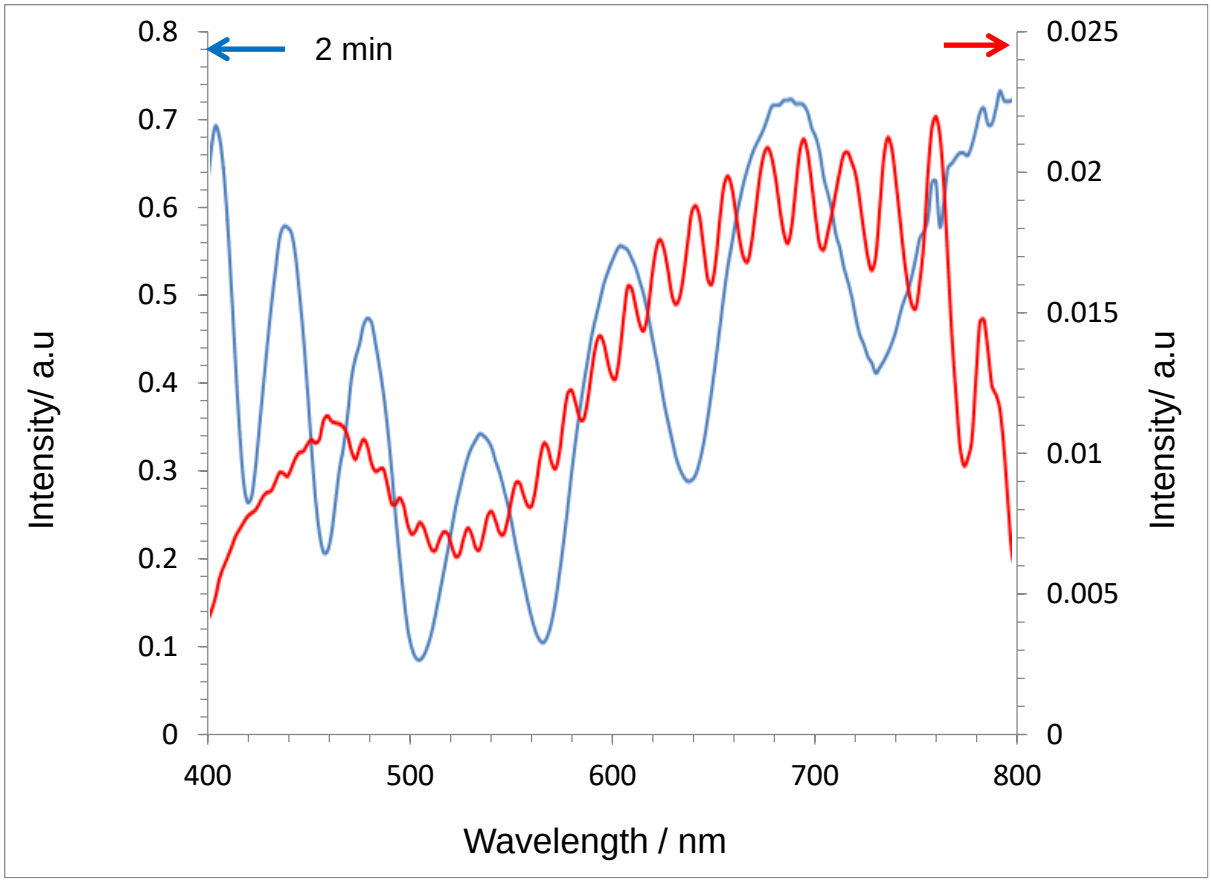

Figure 4.13 *Specular reflectance spectra of sample A (blue) prepared by 2 minute second anodisation period and sample B (red) by 30 minute second anodisation period.*

4.6 Etch-back of porous alumina to expose gold nanorods

The AAO pores provide an ideal template for the manufacture of nanorods and wires. As previously discussed, the most common methods of manufacture are sputter coating into the alumina template followed by the total dissolution of the template. Much less common is the partial exposure of the nanorods by controlled dissolution of the AAO film to create a robust and accessible nanorod array SERS substrate. This is in part due to the difficulty in controlling the etch-back process. Under-etching of the overlying alumina surface results in rods that are not exposed while over-etching results in the rods tilting or fusing together, collapsing or even ultimately, the removal from the template and the rods. In addition, the inconsistency and poor repeatability of results from sample to sample have hindered the widespread use of this technique. The reflectance measurements discussed in Section 4.5 can greatly aid this aim as it determines, through analysis of the specular reflectance fringe patterns obtained, the thickness of the alumina layer to be removed in order to achieve this.

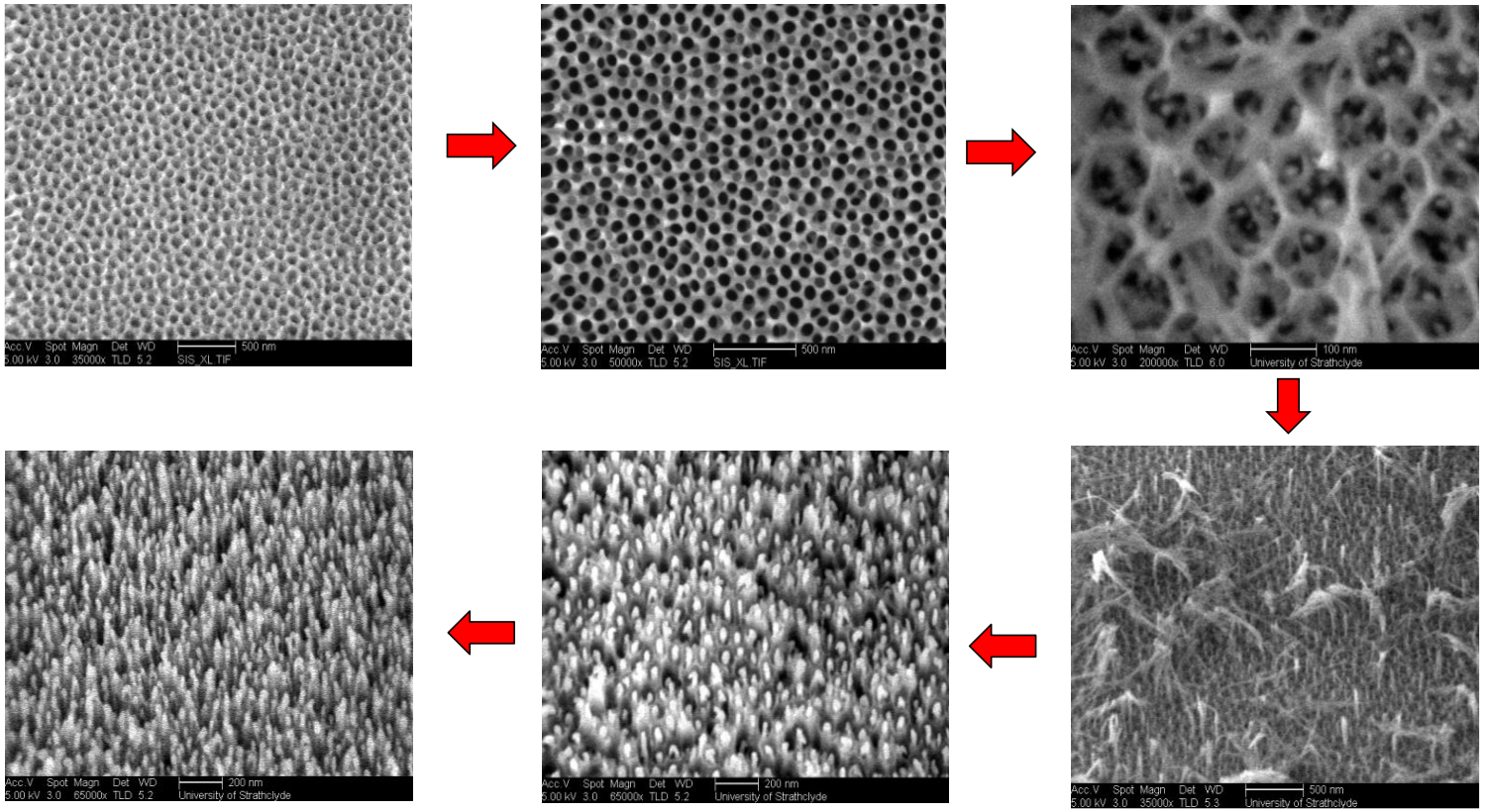

Figure 4.14 *FE-SEM depicting etch-back of the honeycomb like porous alumina structure to reveal the AuNR within. Following the red arrows clockwise, initially the gold is hidden from view deep within the pores. During the etch-back process, the pores widen as the pore walls reduce in thickness. Eventually the alumina falls away to reveal the rods, where the alumina forms a ghost like halo around the rods, and finally the rods are fully exposed. The rods are 20 nm in diameter with an interpore spacing of 40 nm.*

.

The greater the distance the light has to travel through the alumina to reach the gold/alumina composite layer, the greater the number of fringes obtained.

In order to expose the AuNR and so prepare the samples for use as SERS substrates, a 10 wt% phosphoric acid solution was used to etch-back the alumina film to expose the AuNR buried within. As shown in Figure 4.14 the etch-back process involved both a widening of the alumina pores and a gradual removal of the pore walls above the rods until the AuNR were exposed. This process was carried out in an ultrasonic bath to ensure that the resultant alumina debris did not fall back onto and adhere to the surface of the AuNR. The time required to expose the nanorods, without causing damage to them, corresponded to an etch rate of 0.1 µm/min. Also evident in Figure 4.14, the AuNR were found not to be as in a highly ordered hexagonal pattern as might have been expected. The surface of each rod appeared rough and with sharp edges. The width of the rods was found to be ~ 20 nm with a separation distance of around 40 nm.

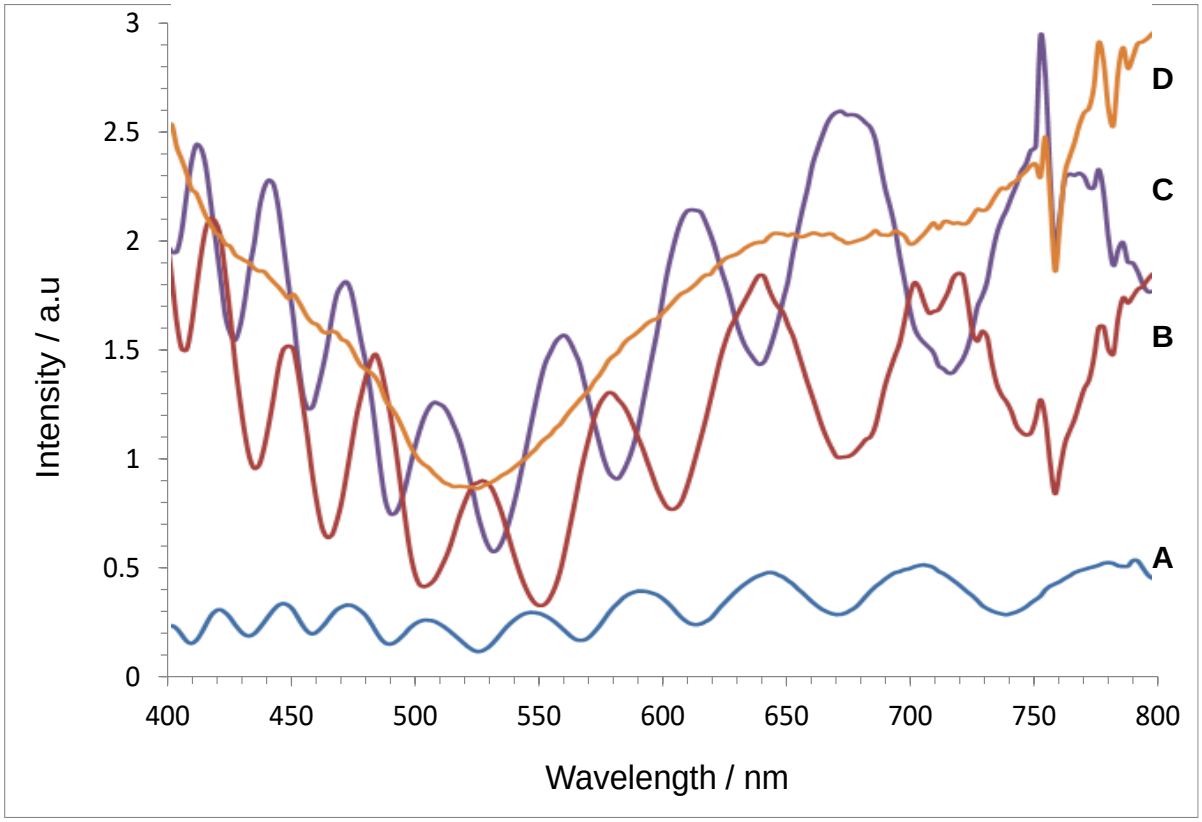

Figure 4.15 *Specular reflectance using p-polarised light following etch-back process of a sample from unetched sample (***A***), sample after 17 minutes of etching (***B***), after 20 minutes of etching (***C***) and 25 minutes of etching (***D***).*

Etch-back of the alumina film to reveal the nanorod arrays also resulted in an increase in the measured intensity of the reflectance as the pores reduced in length above the AuNR and widened. As expected, the specular reflectance spectra showed the number of fringes obtained reduced as the film was etched-back and disappearing entirely once the AuNR were exposed. This is illustrated in Figure 4.15, which shows the specular reflectance data with *p*-polarised light of the etch-back process of a sample in which the depth within the alumina pores of the AuNR was calculated to be 2.52 μm.

It can be seen that the fringes became more separated as the etch-back process occurred and disappeared altogether once the rods were exposed, as expected. Confirmation of their exposure was obtained from FE–SEM imaging. During the etch-back process, the sample surface became visibly more lustrous. Once the AuNR were exposed, a clear and marked difference between the spectrum obtained using *s*-polarised and that for *p*-polarised light was observed.

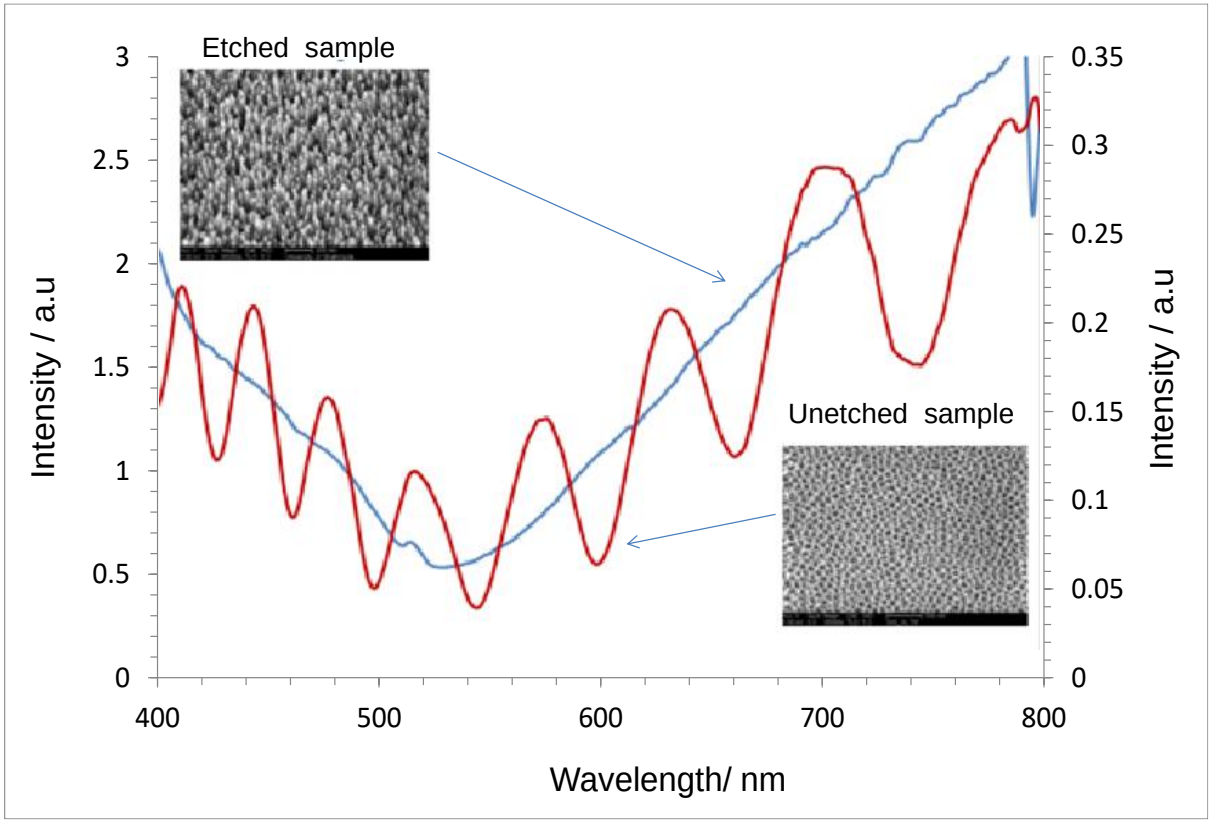

Figure 4.16 *Comparison of the specular reflectance spectra obtained for a sample prior to (secondary axis on the left) and after etching (primary axis on the right) to expose the AuNR. The fringe pattern visible before etching disappears once the AuNR are fully exposed.*

This is due to absorption in respect to the longitudinal plasmon. L_m only being present with *p*-polarised light. The spectra obtained for a sample before and after exposure of the AuNR are given in Figure 4.16. Equation 3.1 was used to calculate the etch-back time required to expose the rods and this was evaluated to be 25 minutes. It can again be seen that after this period of etch-back no fringes were observed, indicating that the nanorods had indeed been fully exposed, thus validating the calculated etch rate in the phosphoric acid solution. During the etch-back process the number of fringes in the reflectance spectrum reduced as the dissolution of the porous alumina film progressed. During this time, the pore walls thinned and progressively widened, falling away in long strands until the rods were fully exposed. Confirmation of the extent of exposure was obtained from FE - SEM imaging. During etch-back, the sample surface became visibly more lustrous. Once the gold rods were exposed, a clear and marked difference between the spectrum obtained using *s*-polarised and *p*-polarised light was evident as shown in Figure 4.17.

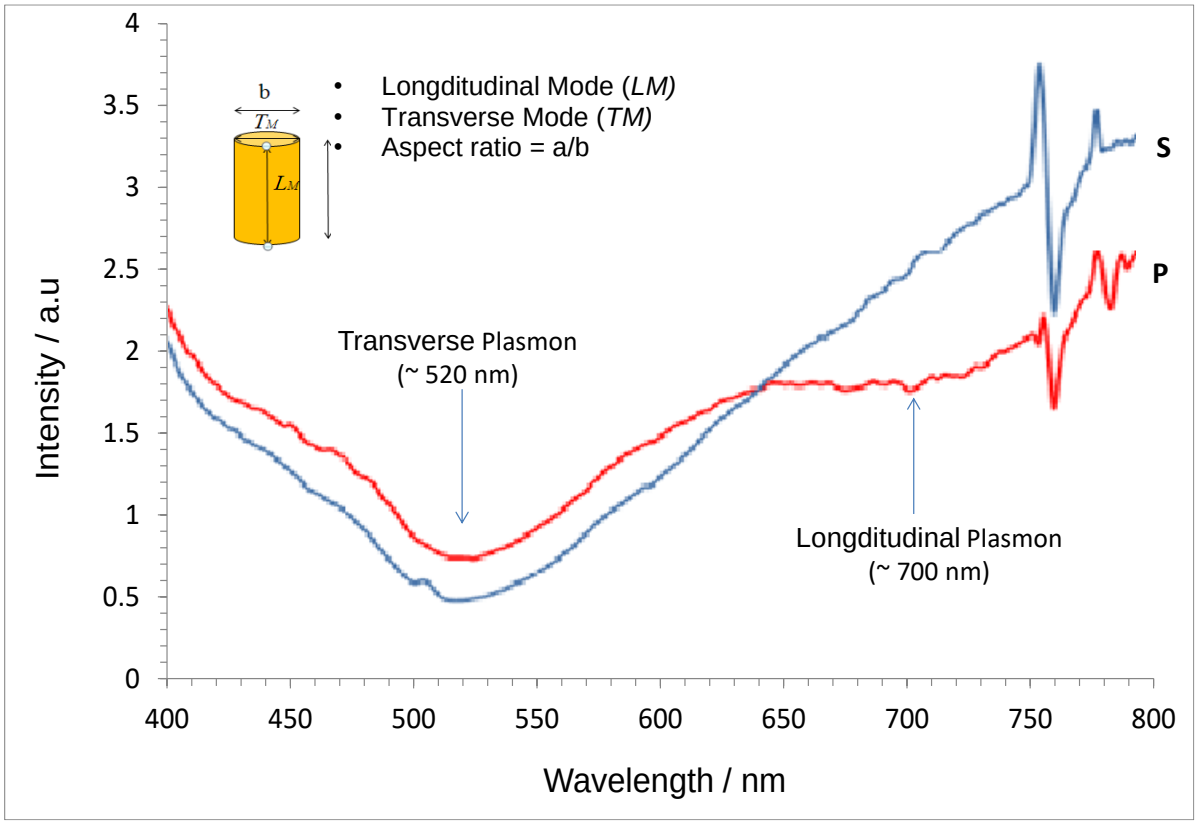

Figure 4.17 *Specular Reflectance of exposed AuNR-alumina composite using s- and p-polarised light at an angle of incidence of 36°. A longitudinal plasmon resonance can clearly be seen at ~700 nm with p polarised light only.*

As expected from the specular reflectance data obtained for the exposed nanorod-composite layer at an angle of incidence of 36° shown in Figure 4.17 only the transverse plasmon at 520 nm is observed with *s*-polarised light. With *p*-polarised light, both longitudinal and transverse modes are observed. The presence though of the L_m mode at ~700 nm is surprising as a plasmon at this wavelength would normally be attributed to gold rods with an aspect ratio of ~1.8[32,103]. Clearly, this is not the case in this instance as these AuNR consist of rods several hundreds of nm in length. It is therefore postulated that the effective medium of the L_m mode is mediated by the fact that the dielectric medium at the top of the rods is air with a relative dielectric constant $\varepsilon = 1$, whereas for the length of the rod that remains within the alumina template, $\varepsilon = 9.34$. As noted above, the plasmon frequency is very sensitive to the medium surrounding the nanoparticles.

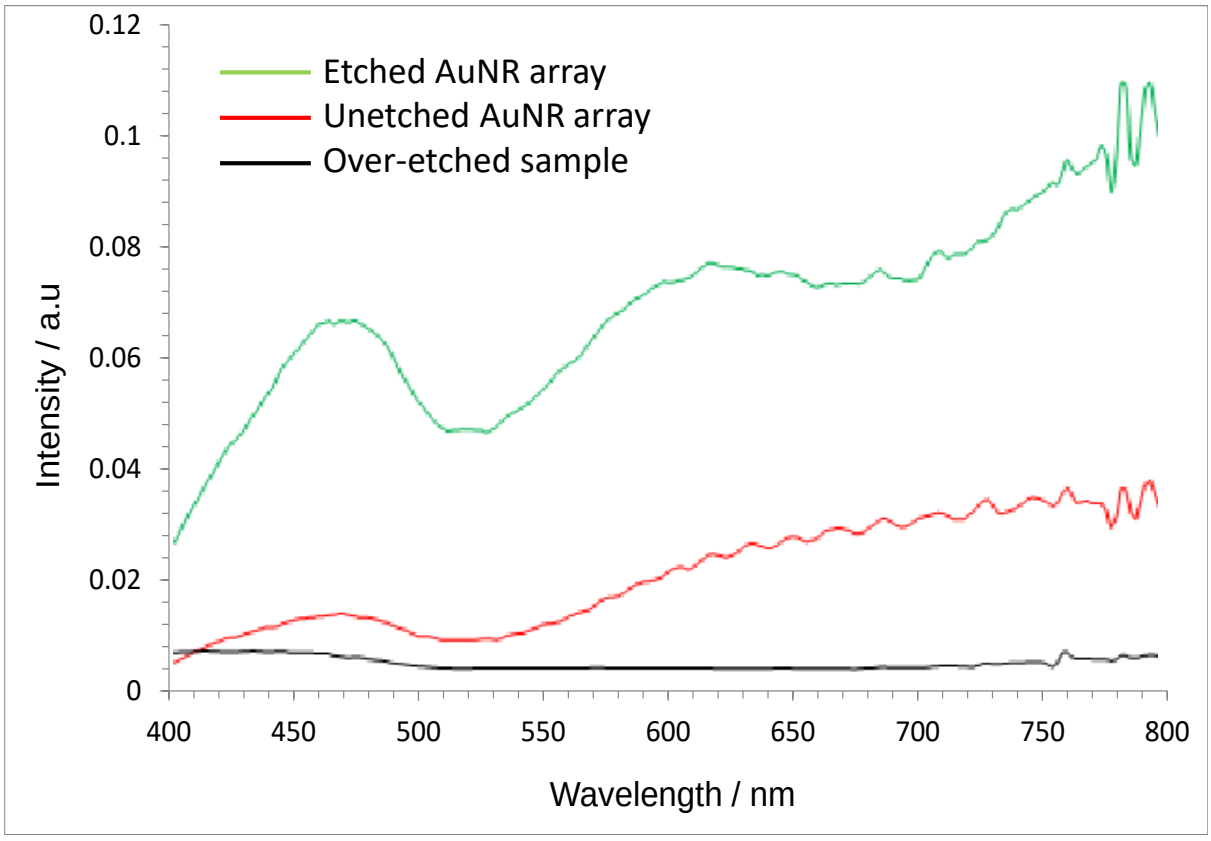

Figure 4.18 *Specular Reflectance using p polarised light showing the spectra obtained for an unetched sample (red curve); exposed AuNR (green curve) and over-etched sample (black line).*

Over-etched samples showed a marked reduction in the intensity of reflection and loss of the plasmon features (and obviously, no interference fringes), signifying a loss in the ordering of the AuNR.

Figure 4.18 shows the specular reflectance spectra obtained from a sample prior to etching (red), etched-back to reveal the AuNR (green) and finally once the sample had been over-etched (black). It is evident that the over-etched sample exhibits none of the desired optical properties and furthermore, the sample surface appeared dull and non-reflective to the naked eye.

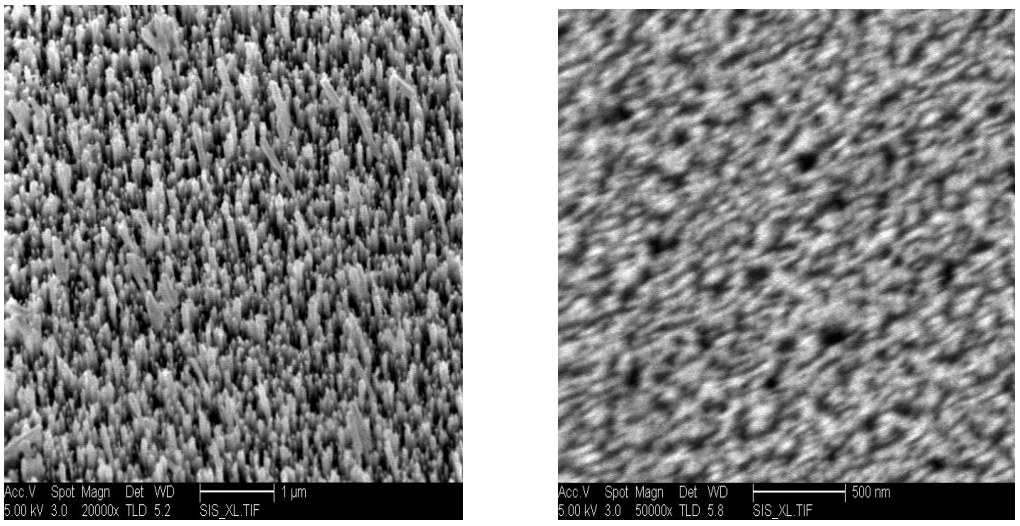

Figure 4.19 *FE-SEM images of an AuNR sample once etched on the right and on the image on the left shows the same sample after over etching.*

Comparison of the FE-SEM images in Figure 4.19 of the correctly etched sample with fully exposed nanorods to that of the image taken after the sample had gone on to be over-etched. This image clearly shows the amount of damage to the alignment of the nanorods.

More FE-SEM images of the consequences of over-etching of the AuNR samples can be seen in Figure 4.20. Over-etching occurs when the sample is left for too long in the etching solution causing the rods to tilt, bend, fuse together, collapse and ultimately break free from the aluminium substrate. To the naked eye, this caused the sample surface to lose both colour and lustre.

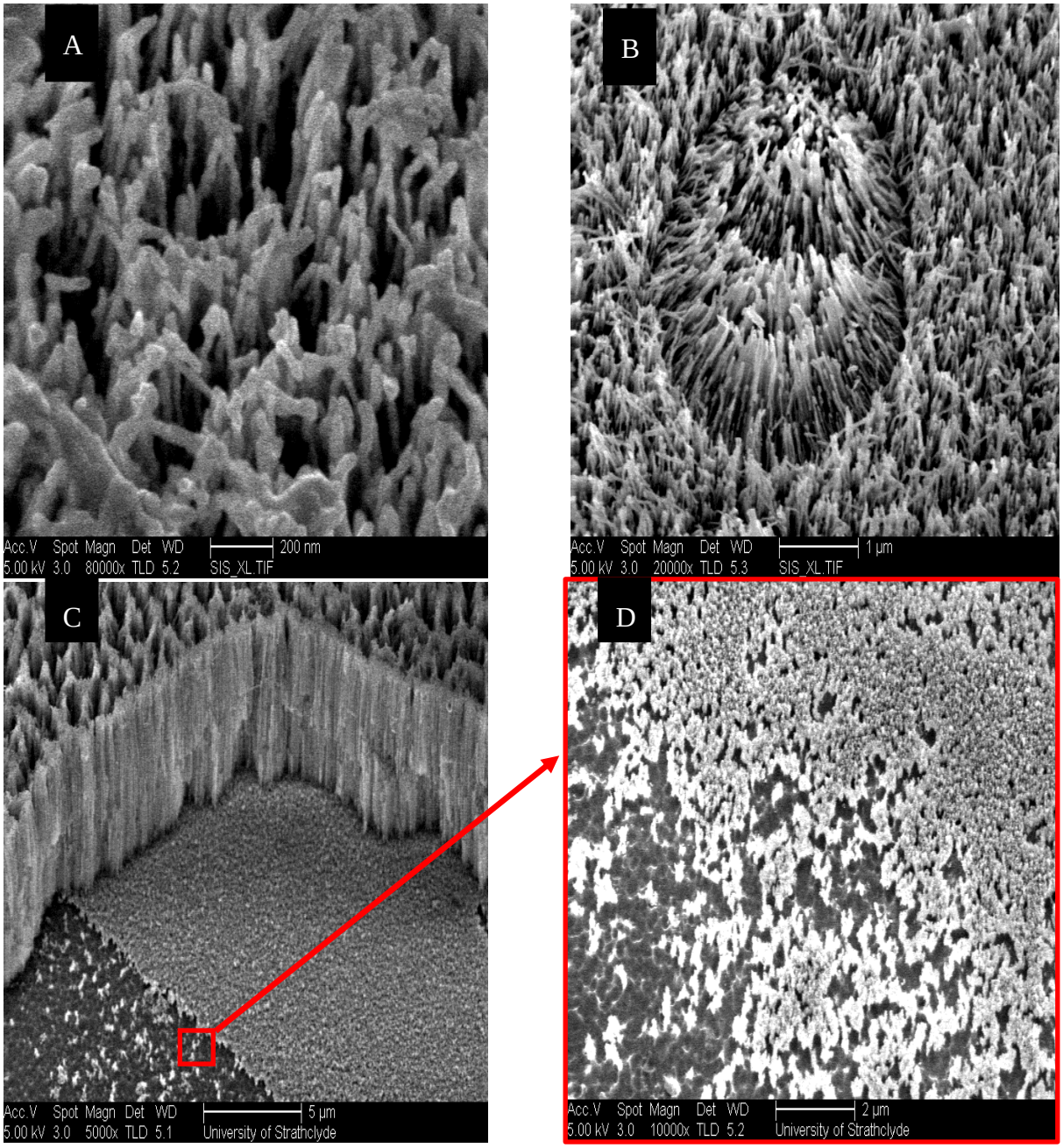

***Figure 4.20**. Examples of the effects of over-etching on AuNR samples. **A-** shows distorted and fused nanorods**. B-** shows partially collapsed nanorod. **C-** shows an area where a portion of the alumina template has broken off exposing the template structure lengthwise. **D-**is a close up image of the area highlighted with a red box in **C** and shows residual alumina and on the bottom left hand side of the image the surface pattern of the template has been exposed (sample stage set to 30°).*

4.7 Investigation of the electrochemical response of gold arrays

The electrochemical response from a gold disk electrode similar in area to that of the AuNR sample with a diameter of 7 mm was recorded. This was then compared to the electrochemical response obtained from the unetched sample. Finally the electrochemical response of the etched sample was recorded. The results of these three experiments are shown in Figure 4.21.

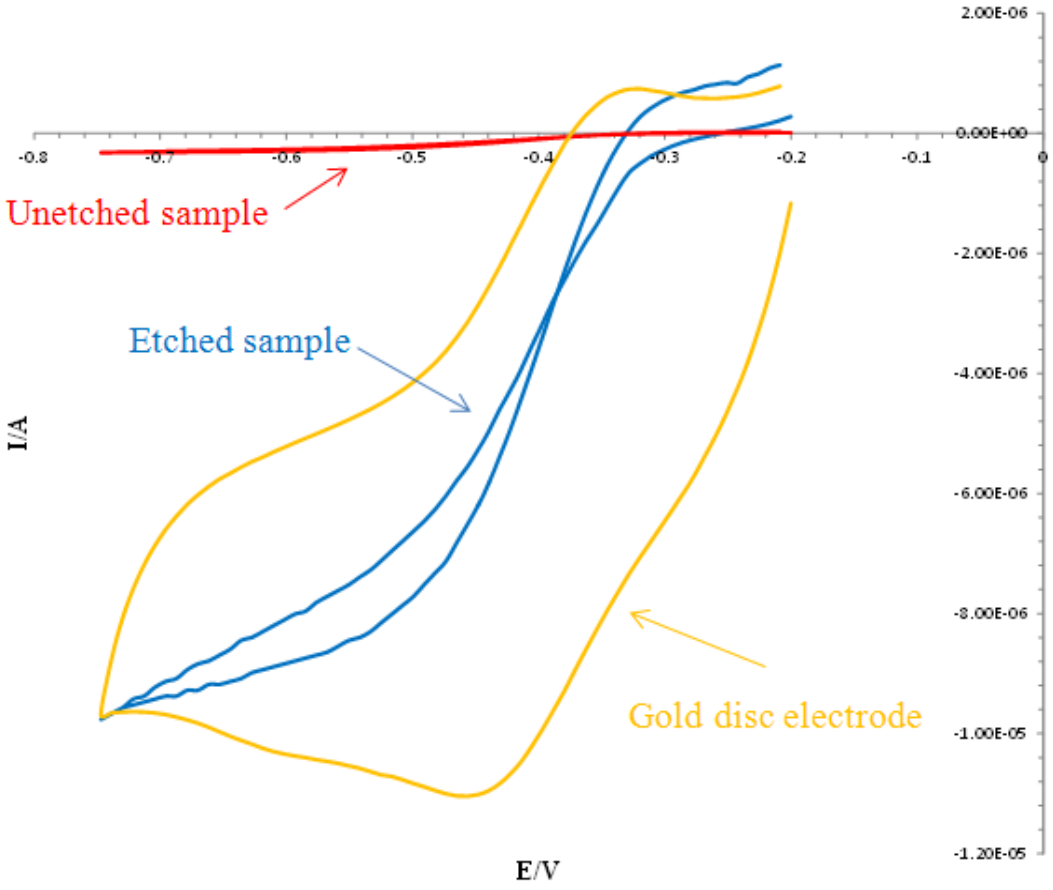

Figure 4.21 *CV of AuNR-alumina composite electrode in 10 mM* $[Cu^{II}(NH_3)_4]$ $(NO_3)_2$*/1 M* KNO_3 *of an unetched sample (red) and following 25 minutes etch-back to expose AuNR (blue). The CV from a gold disk electrode is shown for comparison (yellow). Scan rate = 50 mV/s; 298 K.*

This shows that the unetched composite material produces no *I-V* response as the gold nanorods are buried deep within the alumina template. However, during the etch-back process, the AuNR became gradually more exposed and the electrochemical response from the reduction of Cu^{II} → Cu^{I} then becomes very evident. For comparison, the current-voltage (*I-V*) response from an

gold disk electrode in the same solution is also shown and this gave the classic diffusion controlled peak for the reduction reaction. However, the S-shaped electrochemical response of the exposed nanorod arrays corresponds more to that of spherical diffusion to a microelectrode surface as opposed to that of semi-infinite linear diffusion exhibited at the surface of the gold-disc electrode.

4.8 Chapter 4 summary

This chapter has focused on the preparation of vertically aligned nanorod arrays, which were produced by *a.c* electrodeposition of gold into the pores of a hexagonally ordered alumina film grown on an aluminium substrate using a two-stage anodisation process in oxalic acid. Rather than removing the rods from the template[159], as is common practice, here the template remained in place and was instead etched-back in a controlled manner only as far as to expose the rods. Thus, the template itself helped to support the rods that were several hundred nm in length. Keeping the aluminium base in place allowed for ease of handling whilst affording a degree of protection to the sample. In addition, the aluminium base facilitates their use as an electrode in an aqueous environment and so enabling electrochemical reactions to be performed on the exposed AuNR surface.

In terms of the sample preparation, the use of a mechanical polisher helped produced flatter, smoother sample surfaces that in turn helped to encourage development of parallel pores during film growth. Bubble formation on the sample surface, which can result in pitting and hinder ordered pore formation, was reduced during the electropolishing procedure by initially setting the speed of the RDE to 5 Hz and so controlling convective flow to the electropolishing surface. Once the reaction had started and the electropolishing process had taken hold, the rotation speed was then reduced to 0.3 Hz to prevent surface scarring and groove formations from flow patterns. The freshness of the anodisation solution also greatly affected the rate of film growth. The older the anodizing solution, the slower was the rate of growth. Therefore, in order to standardise growth, a fresh solution was prepared for every sample. The porous alumina film thickness was determined by the length of the second anodisation period and this was verified by both ellipsometry and specular reflectance FTIR. Thus, film thickness could be accurately calculated by modelling the ellipsometric data from the second anodisation period. Whilst the

use of the specular reflectance FTIR instrumentation to find the longitudinal plasmon failed as the range was out with its limit, it was discovered that it could be used as a quick method to determine film thickness using the bayerite peak at 995 cm^{-1}.

The *in-situ* monitoring of the barrier layer thinning process revealed that film growth continued at a substantial rate even though the applied cell voltage was reduced from 40 V to 24 V. Below the latter voltage, film growth slowed dramatically with little further growth observed between 24 V and 6.5 V. SEM images showed the surface morphology of the AuNR to be rough and sharp edged which would make them hydrophilic unlike rods with a smooth and rounded morphology which tend to be more hydrophobic[160]. This should also prove beneficial in regards to increasing SERS enhancement. The width of the rods was found to be ~ 20 nm with the distance between each some ~40 nm. However, it was not possible to determine the length of the rods since they remained anchored to the bottom of the pores and consequently it was not possible to calculate the aspect ratio of the rods. However further utilisation of specular reflectance FTIR in this regard may prove to be beneficial.

5. Characterisation of gold nanorod arrays using SE(R)RS

Having optimised the production of vertically orientated AuNR samples in the previous chapter, the focus of Chapter 5 is to establish their effectiveness as a robust SERS substrate. Desirable qualities include ease of handling, good signal enhancement, signal uniformity across the sample surface as well as surface regeneration and repeatability. These studies were performed with selected Raman reporters (resonant and non-resonant with the incident laser excitation wavelength) to enable comparative measurements to be made. In addition, the deposition of electroactive species and nanoparticles onto the AuNR was explored. Initial studies concentrated on the resonant species in order to determine the maximum strength of signal enhancement that can be obtained compared to that of the bare AuNR surface. Uniformity of the signal strength across the sample surface is also investigated. Regeneration of the sample surface and repeat application of reporter molecules is also looked at along with electropolarisation studies of the SE(R)RS intensity.

5.1 Reporter molecules

In this chapter, Raman reporter molecules that were both resonant and non-resonant with the incident excitation laser were utilised. A number of molecules have proved to be efficient Raman reporters and have been used for this purpose over the preceding decades.[161] The work in this chapter focuses mostly on two Raman reporter molecules, namely malachite green isothiocyanate (MG) and 4-mercaptobenzoic acid (MBA). Both species are used extensively in nanotechnology and SE(R)RS and are frequently used with gold nanoparticles (rods, spheres, cubes) particularly in suspensions[35]. Both are attached to the AuNR through chemisorption as a result of the strong gold sulfur attraction producing stable sulfur-gold covalent bonds. In addition comparison of the signal enhancement obtained can be easily compared to that of other substrates. Additional Raman active species are discussed later in sections 5.6.2 (polythiophene), 5.6.3 (NQ) and in chapter 6 (NIR 797).

5.1.1 Malachite green isothiocyanate (MG)

This dye was selected as a resonant reporter molecule to be used in order to achieve the maximum signal enhancement possible when using a 633 nm helium-neon (HeNe) laser. As MG is a non-fluorescent dye, the high background contributions to SERS spectra typically associated with the fluorescence of common are not seen with this dye. In the presence of high fluorescence, the Raman signal may become swamped making detection difficult or in some cases impossible. Reducing laser power and sampling time can assist in reducing the background signal. However, the Raman signal is also reduced. In the case of a relatively weak Raman signal this may have the knock-on effect of decreasing the signal to noise ratio to unacceptable limits.[60] The structural formula of MG is given in Figure 5.1. Note the position of the sulfur atom which is associated with a strong chemisorption interaction between the reporter and a gold surface.

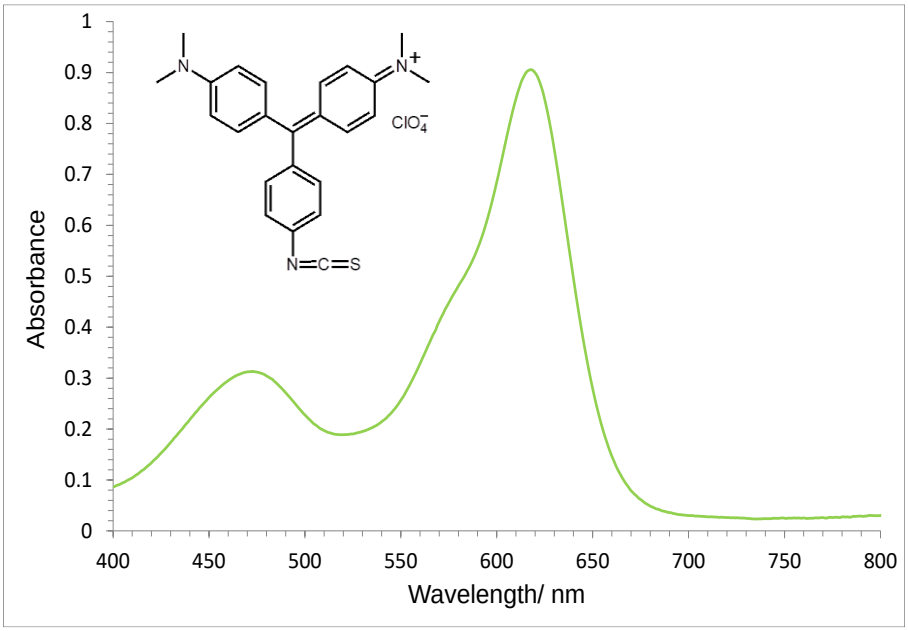

Figure 5.1 *Absorbance spectrum of MG 10 $^{-5}$ M in methanol. (λ_{max} at 630 nm).*

In addition the maximum absorbance strength of the dye molecule (λ_{max} = 630 nm) closely matches that of the laser excitation wavelength of 633 nm. This is predominantly due to de-localised π systems, which with increasing size require a lowering of which the energy at which the highest occupied molecular orbitals (HOMO) are occupied. This effect contributes to a large resonant enhancement of the Raman signal.

5.1.2 4-mercaptobenzoic acid

4-mercabtobenzoic acid is commonly selected as a non-resonant Raman reporter and is frequently used in benchmarking SERS signals[341,342]. This is due to the high affinity of the thiol group for metal surfaces and having a well-characterised Raman scattering cross-section. Its characteristic SERS spectrum within the region 600 cm^{-1} to 1800 cm^{-1} comprises of two sharp peaks at 1075 cm^{-1} and 1587 cm^{-1}.

The molecular structure for this molecule is shown in Figure 5.2. It was chosen as the non-resonant reporter molecule and it absorbs in the UV.

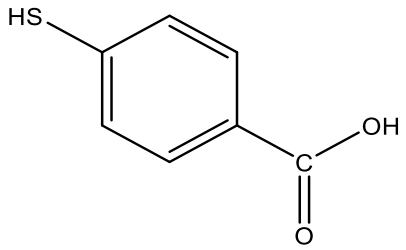

Figure 5.2 *Structural formula of 4-mercaptobenzoic acid.*

This aromatic non-fluorescent, non-resonant molecule, with its λ_{max} falling within the UV spectrum, was selected for a number of reasons. Firstly, the molecule is frequently used in benchmarking SERS signals due to the simplicity of the molecule. As it is non-resonant the enhancement of the signal is dominated by the plasmonic substrates rather than electronic properties of the reporter itself. The capacity for achieving a good monolayer coverage is another reason for using this as a reporter molecule. The molecule, as seen in Figure 5.2 has two bonding sites available to the gold: the thiol and COO^- groups. At lower concentrations the molecules preferably adsorb via the sulfur atom and align at an angle tilted towards the plane[154]. However, at MBA concentrations ($\geq 10^{-3}$) and/or at acidic pH, protonation of the carboxylic groups occurs and the molecules align themselves vertically to the plane.[19, 162]

5.2 Exploration of vertically aligned gold nanorod arrays as an effective SERRS substrate

Initial SE(R)RS experiments were carried out using a monolayer of the Raman reporter molecule malachite green isothiocyanate (MG) adsorbed onto the surface of the gold. The AuNR samples, as determined in Section 4.6, consisted of vertically aligned gold rods 20 nm in width and several μm long with an inter rod spacing of around 40 nm which equate to a

spacing of one rod per 40 nm. As each sample has a total surface area of ca. 1.96×10^{13} nm^2 it therefore follows that each AuNR sample contains approximately 4.9×10^{10} rods.

Prior to analysis, each sample was cleaned by rinsing with methanol, drying and then subjecting the sample to oxygen plasma. This was performed to remove any surface contaminants that may have adsorbed on the sample surface. Oxygen plasma is a strong oxidiser that can desorb and break down organic surface contaminants to volatile species such as CO and CO_2 whilst any inorganic contaminants are converted to highly oxidised compounds that are subsequently rinsed from the surface with a stream of deionised water (DIW). Failure to remove any surface contaminants may drastically inhibit or limit the bonding sites available on the individual rods within AuNR [163].

5.2.1 Gold nanorod arrays as a substrate for SERRS

The spectrum obtained for the bare (i.e. no attached dye molecules) AuNR is shown in Figure 5.3 showing a relatively weak and featureless signal was obtained. However, the background is still higher than expected which may be attributed to laser induced photoluminescence from the porous alumina film [164, 165].

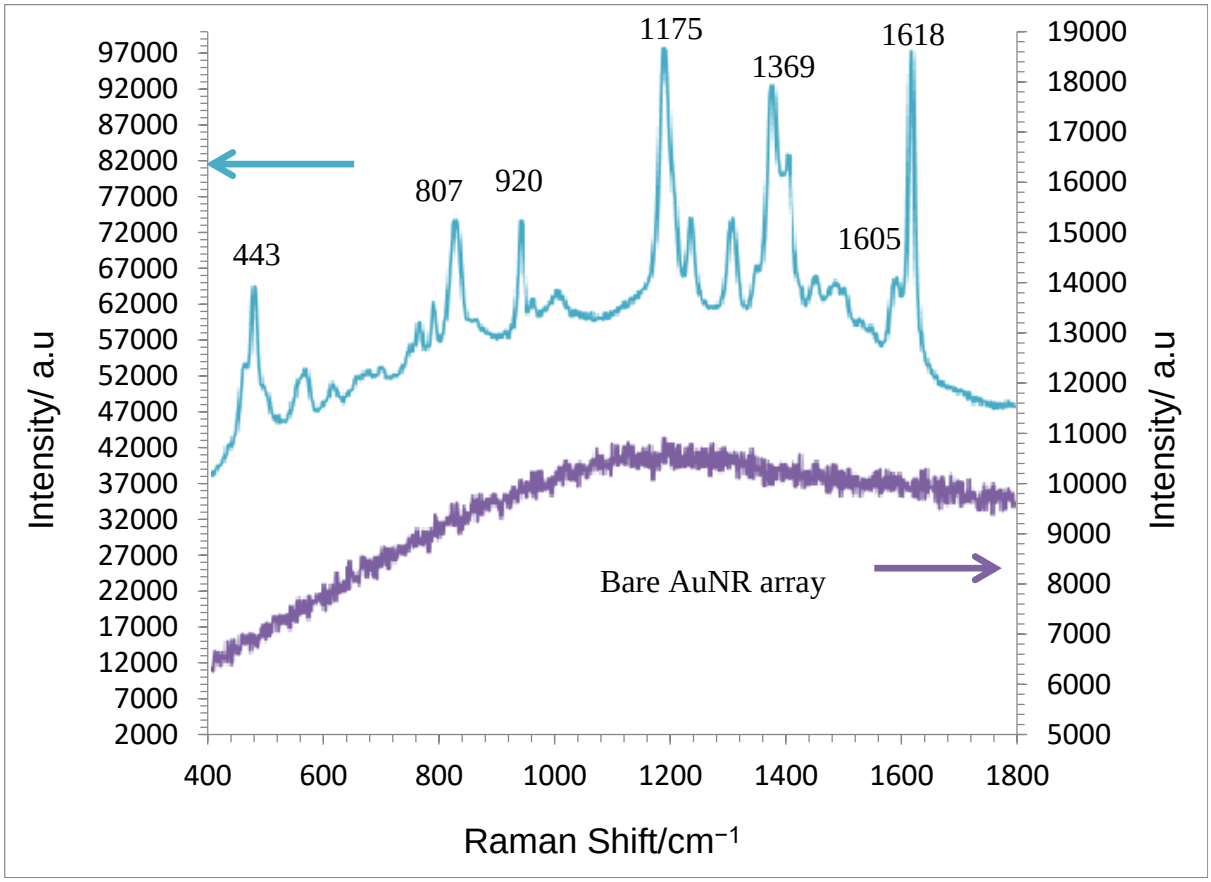

Figure 5.3 *Raman spectra obtained for bare exposed AuNR sample (purple). Prepared by a five minute second anodisation period with gold deposition carried out for 6 s at 6.5 V and 25 minutes etch-back to expose the nanorods* $_{rms}$*. The SERRS spectrum for the same AuNR sample covered in a monolayer of MG (blue) in air* λ_{ex}*= 633 nm at 1% laser power, with a 50× objective.*

A monolayer of MG was formed by exposing the AuNR sample to a 10^{-4} M MG solution in methanol overnight. Numerous peaks can be seen, corresponding to that of the established MG SERRS fingerprint [20, 60, 166] and the strong enhancement due to the SERRS effect of the dye on the AuNR shown in Figure 5.3. The laser intensity in these experiments was 1% of the total power available, equivalent to ~0.5 mW cm^2. The peak height at 1618 cm^{-1} was measured by the increase in intensity from the 1677 cm^{-1} position on the spectrum baseline and repeat measurements indicated a· % RSD of 5.1 across numerous samples (n =10). While this is greater than that seen on the single sample surface, the variation in the signal across the sample surface at a % RSD of 2.2 which is within the instrument variation calculated using a silicon wafer at 520 cm^{-1} that gave a % RSD of 3.3.

5.2.2 Effect of total nanorod length on SERS signal enhancement

The overall length of the nanorods is determined mostly by the magnitude of the applied ac voltage and the deposition time in the 0.1 M $KAu(CN)_2$ solution. While the actual length of the AuNR produced has yet to be fully determined, it is expected to be typically in the region of several hundreds of nm. Varying the applied ac voltage during gold deposition from 6 V_{rms} - 10 V_{rms} and deposition times from 1 s to 30 s however did not reveal any discernible difference in the intensity or position of the SERRS peaks obtained from AuNR samples after etch-back when the rods were exposed. In the previous chapter Figure 4.11 shows two such samples and while the colour seen is considerably lighter in colour sample A than in sample B the resultant SERRS spectra showed no discernible differences between the two samples. This was the case throughout the study in air with a 50× objective and 1 % laser power, with a mean intensity of ~30000 with a standard deviation of ~2000 and RSD of 5.9% suggests that most, if not all, enhancement in signal arises from the T_m plasmon, which is independent of the length of the rods, and hotspots created in the spaces between individual nanorods in the array. Indeed, Figure 5.4 shows the difference in the intensity of the signal obtained between a 'good' AuNR sample (blue) and one where the template has been over-etched (orange) and the rods have collapsed. The over-etched AuNR collapse transforming from straight vertical rods to disfigured ones, and fused clumps. To the naked eye the sample surface appears dull.

Here the difference in intensity of signal obtained between the spectra for the two samples is quite striking. The spectrum obtained with the 'good' AuNR sample was obtained at 1% laser power with the over-etched sample requiring 100% laser power. The spectrum of the over-etched sample appears noisy. This confirms that the vast majority of signal enhancement is supplied by hotspots created in the spaces between individual rods in the AuNR.

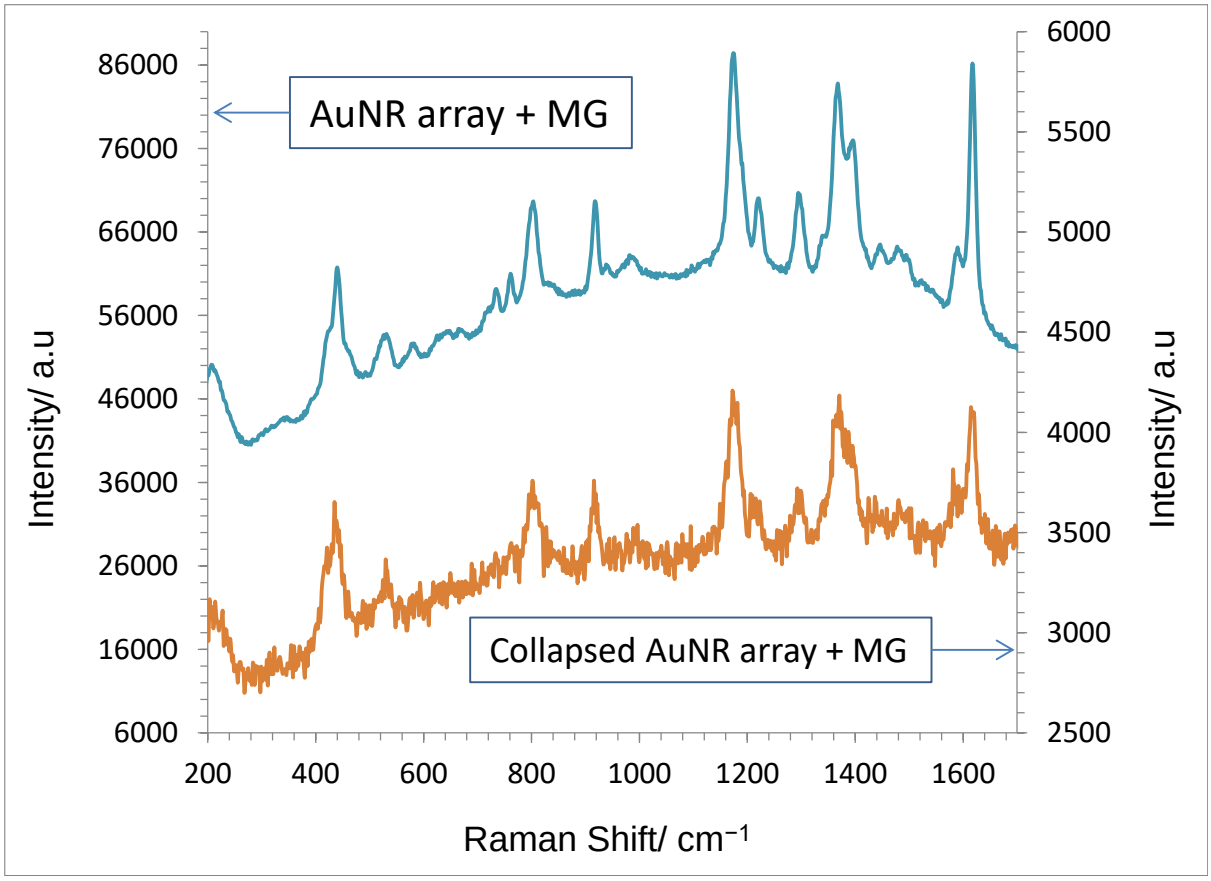

Figure 5.4 *Raman spectrum (top) obtained for an exposed AuNR sample covered in a monolayer of MG (blue) on the primary axis and underneath it the. (Bottom) Raman spectrum was obtained from an AuNR sample where the sample was over-etched and the rods have collapsed (orange) on the secondary axis,* λ_{ex}*= 633 nm in air with a 50 × objective and 1% laser power.*

In the case of an under-etched sample where the pores have been etched back and widened to the extent that the rods are on the cusp of full exposure, the SERRS signal sits on top of a high baseline to such an extent that the SERRS signal is partially out with the detection limits and the spectrum appears saturated with the tops of the peaks cut off. This occurred at 1% laser intensity and the data was not recorded. The samples were etched back more to fully expose the rods and the baseline lowered allowing the SERS signal to be viewed

5.3 Regeneration and repeatability of use of gold nanorod arrays

Regeneration of the AuNR surface and repeatability of use are desirable factors in the commercial success of a SER(R)S substrate. In an extension of the measurements discussed

earlier in Section 5.2, a study was performed to assess the repeated application and removal of a monolayer of MG. This was achieved by etching the SAM monolayer from the surface using oxygen plasma and then exposing the surface to a fresh solution of the dye. This cycle of etching and regeneration was performed five times over a period of several days. It was found that the monolayer was successfully removed and re-adsorbed without any significant loss in the SERS signal as shown in Figure 5.5.

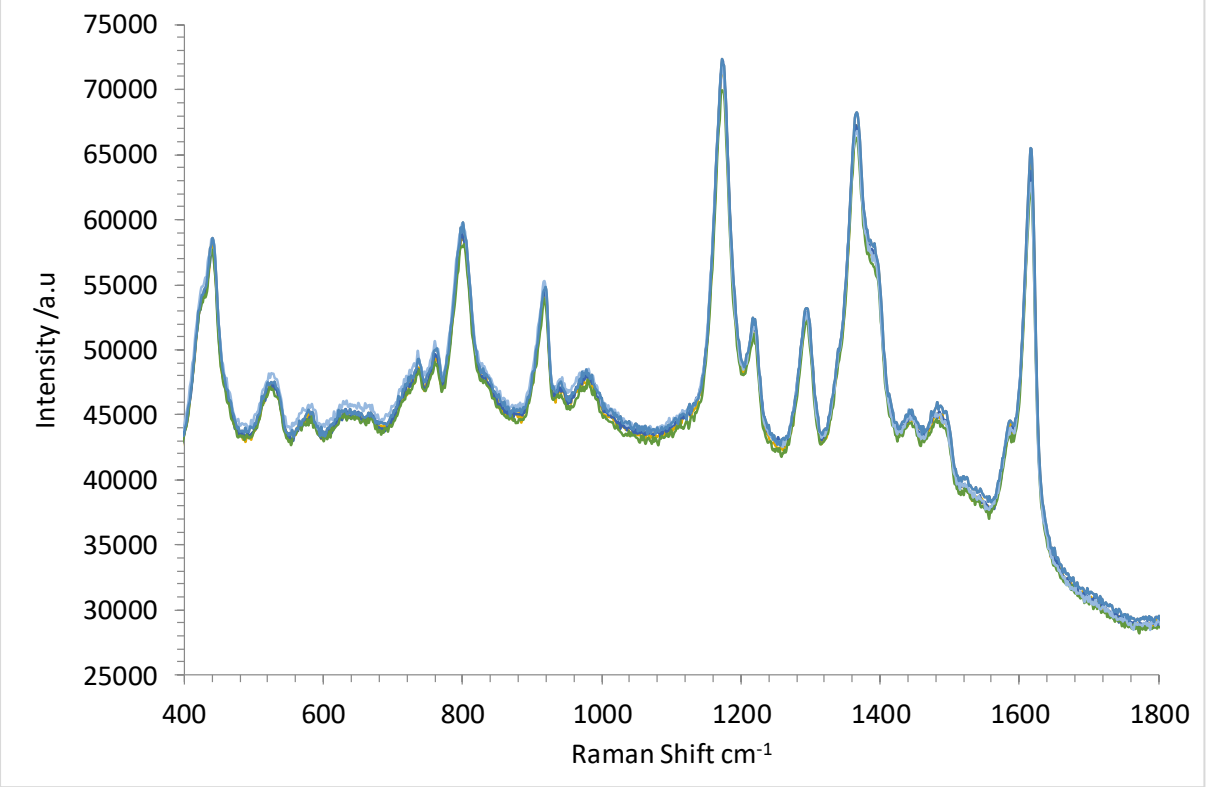

Figure 5.5 *Spectra obtained after repeated cycles of removal and MG monolayer reformation after the initial adsorption of MG on AuNR sample. Experiment performed five times over a period of several days.* λ_{ex} *= 633 nm in air with a 50 × objective and 1% laser power.*

The average SERS peak height obtained at 1618 cm^{-1}, measured from the rise in signal from a point on the baseline at 1677 cm^{-1}, was 31879 with a standard deviation of 1022 and RSD of 3.2% (n=6). This compares very well with the characterisation data in Section 5.2. Figure 5.3. While Figure 5.6 highlights the spectra in Figure 5.5 around the peak at 1618 cm^{-1}.

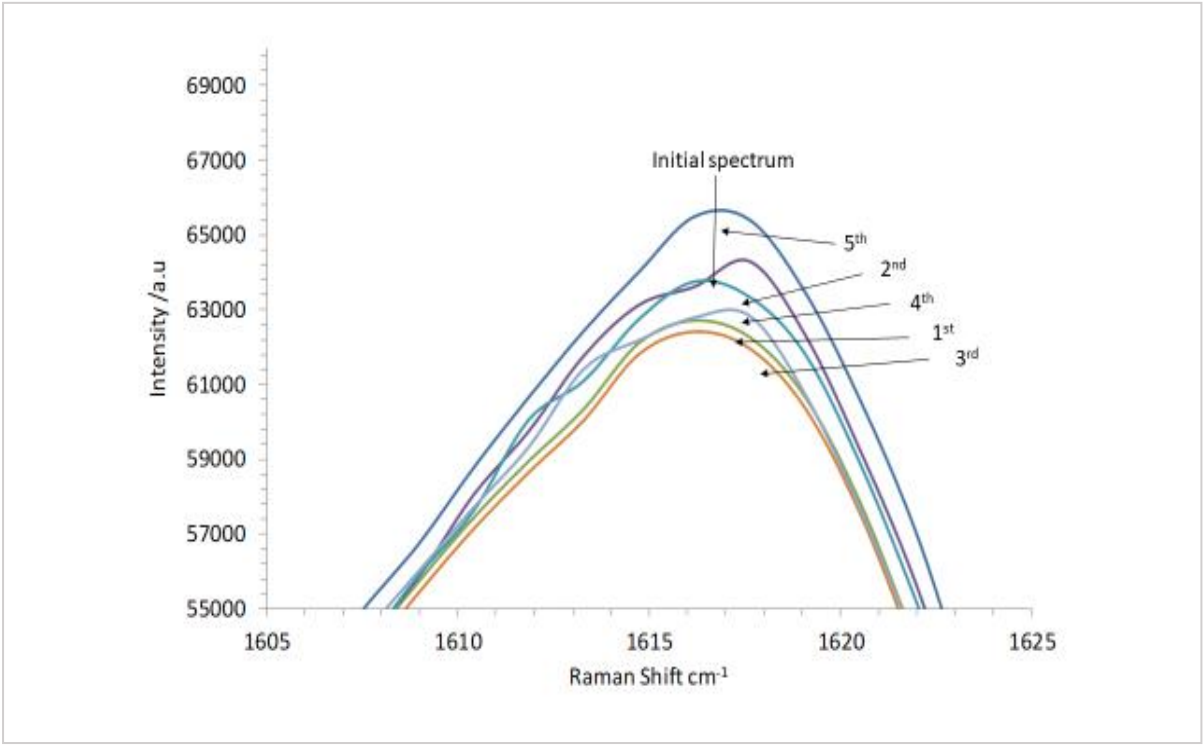

Figure 5.6 *Focuses on the spectra obtained in Figure 5.5 close to the peak at 1618 cm^{-1}. This shows the variation in peak height attained after each cycle of etch and regeneration with an overall RSD of 3.2% (n=6), λ_{ex}= 633 nm in air with a 50 × objective and 1% laser power.*

The actual number of regenerations possible before the AuNR performance deteriorates to an unacceptable level in order to determine the life span of the AuNR samples has yet to be established. However, recycling five times is a significant improvement with little in the literature even addressing this issue. The surface regeneration of AuNR in the presence other adsorbed molecules is addressed further in Section 6.4

5.4 Comparison of the performance of gold nanorod arrays compared to that of three alternative substrates.

In order to determine the viability of the AuNR as a suitable SERS substrate it was necessary to compare their performance with that of other available substrates. To this end the enhancement achieved by AuNR samples with a resonant and non-resonant reporter species were compared.

The additional substrates used for comparison were:

- NP - a monolayer of AuNP , 20 nm in diameter, on a glass slide;
- Klarite$^{TM\ 44}$ - a SERS substrate consisting of an array of gold coated inverted square pyramids patterned onto a silicon substrate which has become the industry standard over the last decade;
- Au film on glass slide.

Eight samples in total were prepared, two for each substrate as depicted in Figure 5.7. A monolayer of the non-resonant species MBA was adsorbed to the surface of and the second set of four were covered in a monolayer of the resonant species MG, excitation wavelength 633nm.

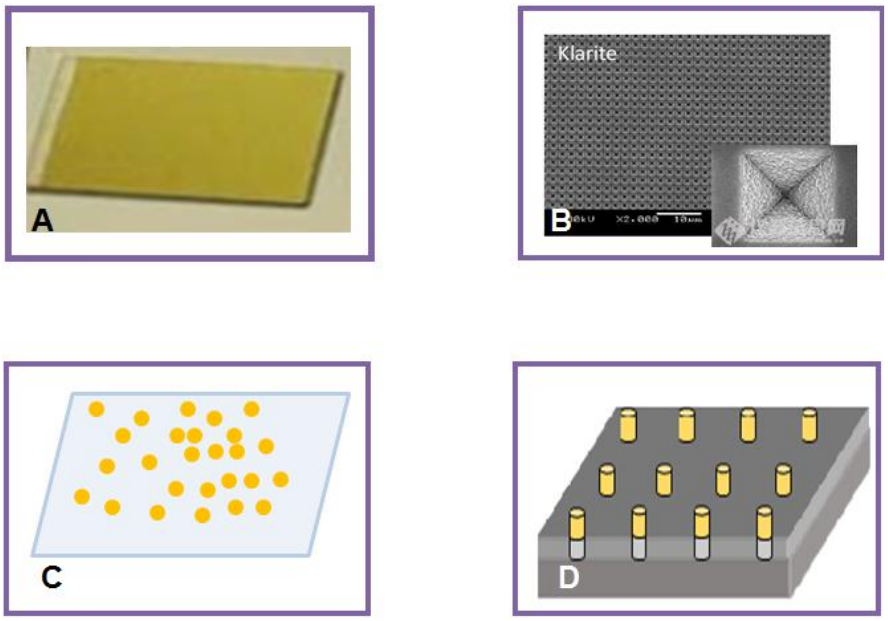

Figure 5.7 *Substrates used in the comparison top left A, gold film on glass slide, top right B, Klarite®, bottom left C, schematic of gold nanoparticles on a glass slide and bottom right D gold nanorod array/AAO sample.*

In order to reduce the possibility of variations in either instrumental or environmental conditions skewing results, side by side analysis was performed on all four substrates. Sample blanks were run prior to treatment to establish that no signals were obtained from any of the substrates. Indeed, Raman spectra of bare substrates were found to be, as expected, featureless with clean baselines containing no peaks. Thus, any peaks seen after the application of the SAMs could be attributed to the interaction of the SAM with the substrates alone. The different Raman reporter molecules were then adsorbed onto the surface of the AuNR. Good signal

enhancement was found for both the non-resonant MBA and resonant MG on all substrates apart from the gold film. All the spectra obtained gave the characteristic fingerprint associated with the adsorbed molecule.

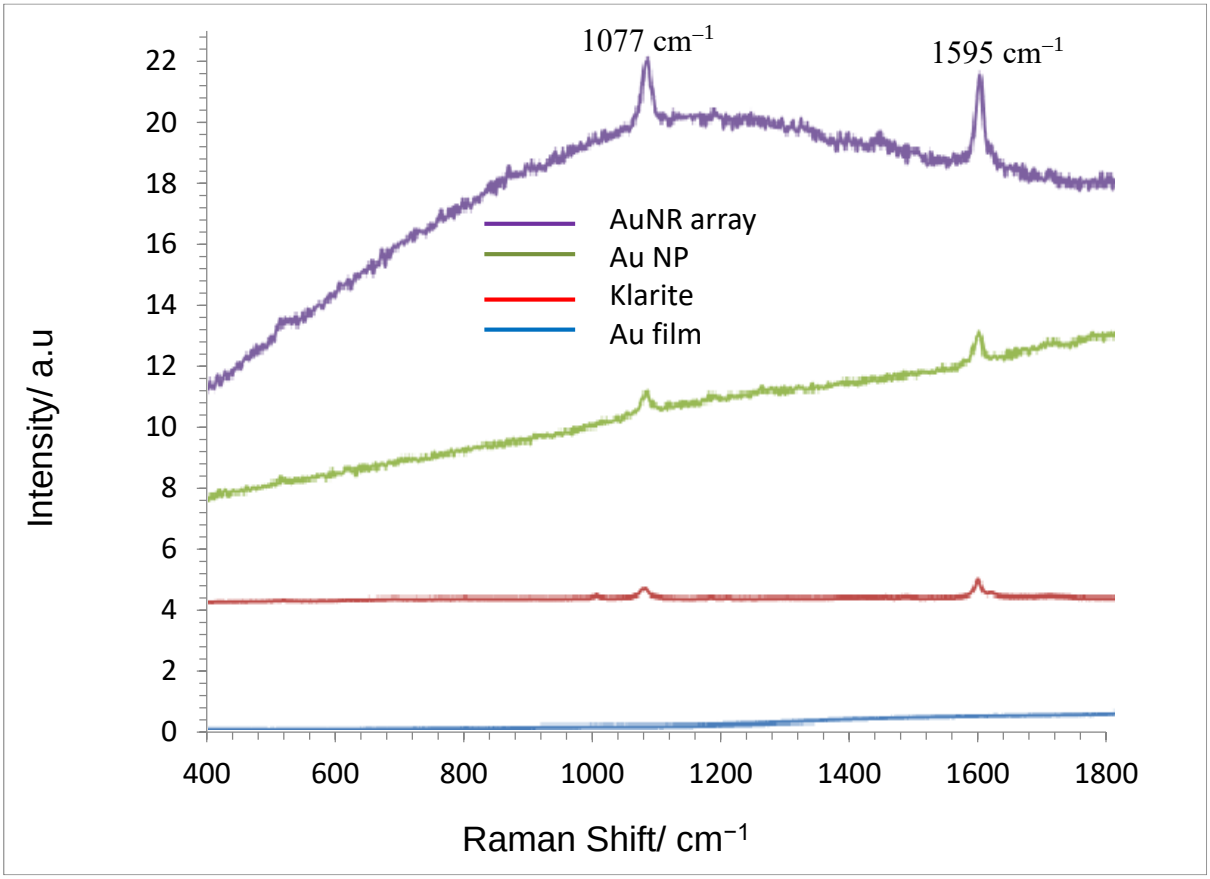

***Figure 5.8**: Comparison of MBA SERS signal obtained for gold film on glass, Klarite, AuNP and AuNR (all results were obtained using a 50× objective and have been normalised against a silicon wafer). λ_{ex} = 633 nm.*

Clear sharp peaks with a high signal-to-noise ratio were obtained. Not unsurprisingly, the signal intensity was found to be far stronger for the resonant MG species. The spectra obtained from AuNR, AuNP, Klarite (a commercially available substrate) and gold film with MBA and MG are shown in Figure 5.8 and Figure 5.9, respectively. The peak obtained for MBA at 1077 cm^{-1} is attributed to C–H in plane bending and the peak at 1595 cm^{-1} to C–C bond breathing.

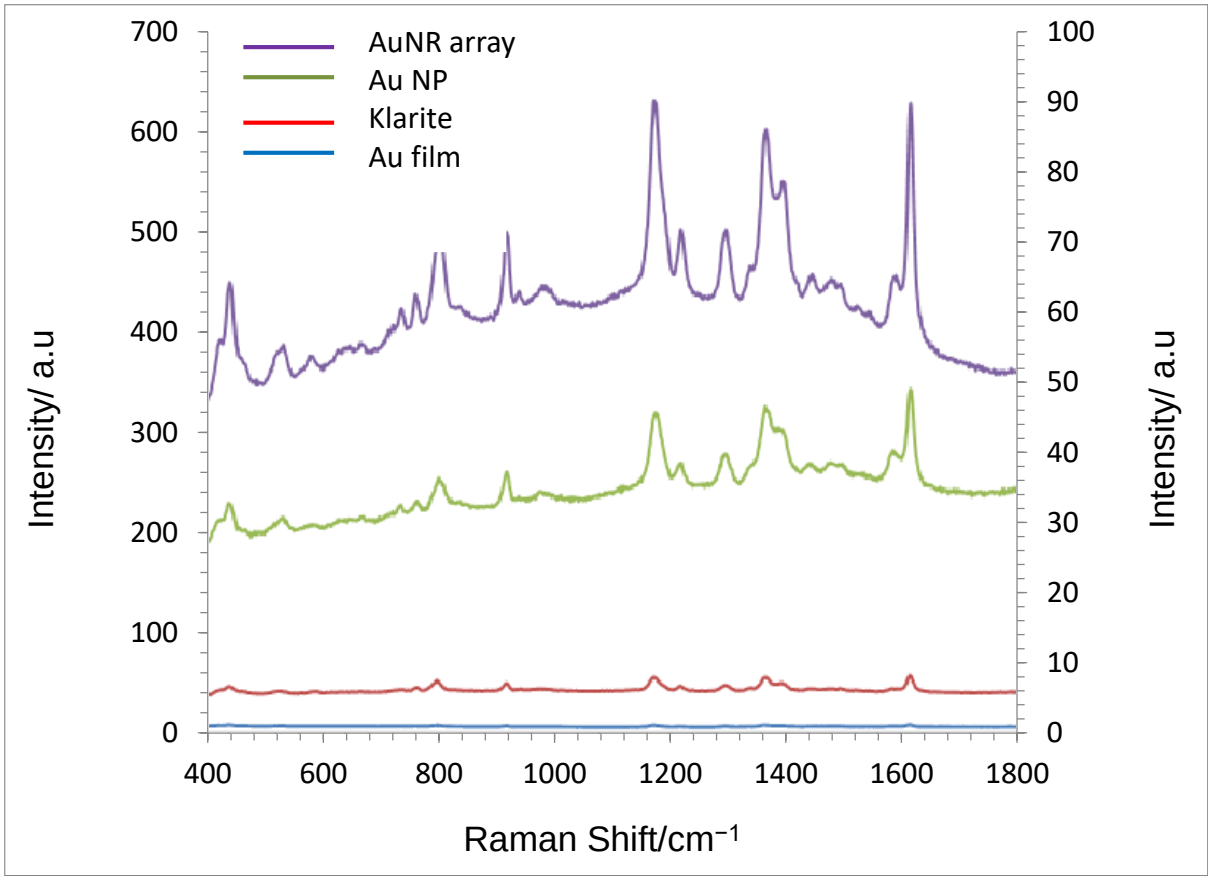

Figure 5.9 *Comparison of MG SERRS signal obtained for a gold film, Klarite ®, AuNP on the secondary axis) and AuNR on the primary axis (all results were obtained using a 50× objective and have been normalised against a silicon wafer)* λ_{ex} *= 633 nm.*

While for the MG comparison study the main peaks of interest are at 1618 cm^{-1} and 1370 cm^{-1}, which are attributed to the in plane stretching of the phenyl rings. For present purposes, analysis of only the first and largest peak at 1618 cm^{-1} for MG is employed. It can clearly be seen that the greatest signal enhancement was obtained using AuNR with a relative enhancement 18 times that of AuNP, 32 times that of Klarite and more than 1225 times that of the gold film.

All spectra were normalised against a silicon wafer in order to compare results at the different laser intensities. The variation in the peak height of the main peak for AuNR % RSD = 2.5. This was found to be comparable with instrumental variation, which was calculated to be RSD = 2.2 % (n=5) on the day of study and was found to be 3.29 % (n=25) when results taken over a five day period were calculated. The mean peak height at 1618 cm^{-1} for the AuNP sample gave results that varied widely from excellent to very poor, with a mean peak height of 11825,

standard deviation of 8477 and RSD of 72 % (n=5) on the pre normalised spectra. Thus, it can be seen that the AuNR samples performed well in the study with both resonant and non-resonant reporter molecules.

5.5.1 Dark-field Microscopy

Dark-field microscopy images were acquired of various AAO samples to monitor changes in the surface morphology. Figure 5.10 shows an image of a substrate in which gold had been deposited into specific areas highlights a clear distinction between areas of alumina alone and areas where nanorods were to be found. This was created by gold electrodeposition through a patterned array described in detail in Section 6.4. Intuitively, the brighter spots could be considered to originate from larger particles. However, a more probable explanation is that the variation in the reflectance is associated with the roughness of the surface. The alumina side of the image is generally brighter due to the higher reflectance of the polished surface at the base of the empty pores. Prior to analysis the samples were rinsed in methanol and dried in a nitrogen stream to remove dust prior to imaging. lt is worth pointing out that particle separation is too narrow to optically resolve individual rods. From the SEM images in Section 4.6 the etching process is uneven and may contribute to the variation in the dark-field images. Thus, dark-field was found to be useful in monitoring the exposure of the rods across the entire surface area as well as other factors such as the flatness of the substrate, and the uniformity of the etching process.

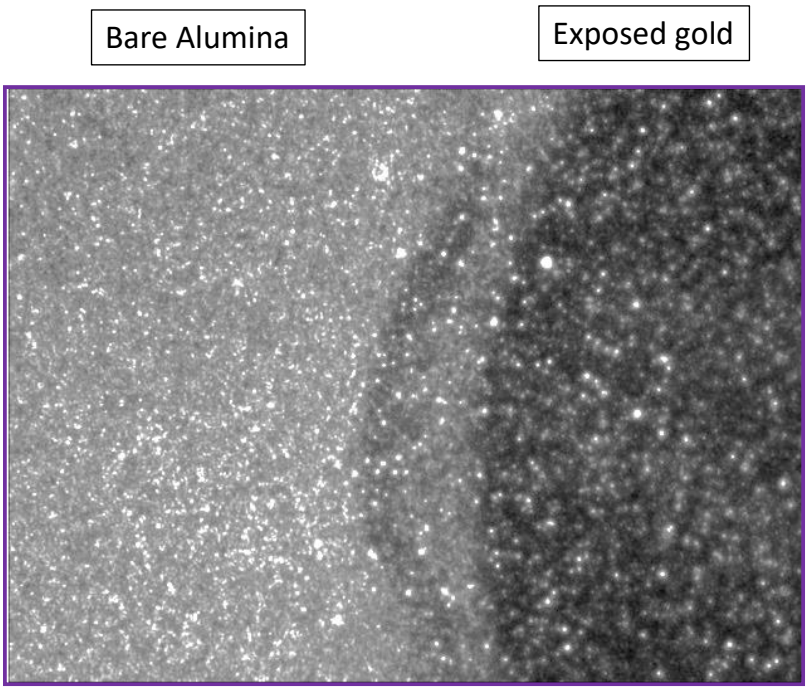

Figure 5.10 *Dark-field image of a sample where the interface between an area of gold deposition and that of bare alumina. Field of view: 174 μm × 130 μm with a 50× objective.*

5.5 Monitoring of changes in plasmonic properties of gold nanorod arrays

5.5.2 Monitoring Au nanoparticle adsorption onto AuNR

Another objective was to assess if it was possible to monitor the changes in the plasmonic properties of the Au NR arrays in response to an adsorption event. This was explored by the deposition of small 20 nm AuNP onto an exposed AuNR. The NP chosen to match the width of individual rods of which the AuNR is comprised. The extinction spectrum of the AuNP has been shown previously in section 1.2.4. Samples were initially viewed without additional preparation. Then after the deposition of small 20 nm AuNP onto the exposed AuNR surface coating the exposed AuNR with a monolayer of NP. This was achieved by, first cleaning the sample surface by oxygen plasma and then soaking the sample overnight in a solution of MBA in methanol, which was prepared by adding 4 mg of the acid to 15 ml of methanol. The sample was rinsed thoroughly in methanol and dried gently in nitrogen. It was then placed in a polydiallyldimethylammoniumchloride solution (PDADMAC) which was prepared by adding a 40 μl aliquot of PDADMAC into 1 mL of a 1 mM NaCl solution and left for 30 minutes. This was rinsed in DIW rinsed and gently dried in a nitrogen stream. This procedure positively

charges the sample surface, which helps the gold nanoparticles to attach to the surface [29]. Finally the sample surface was covered in the nanoparticles (*Tm* =520 nm) and left for two hours before being gently washed and dried.

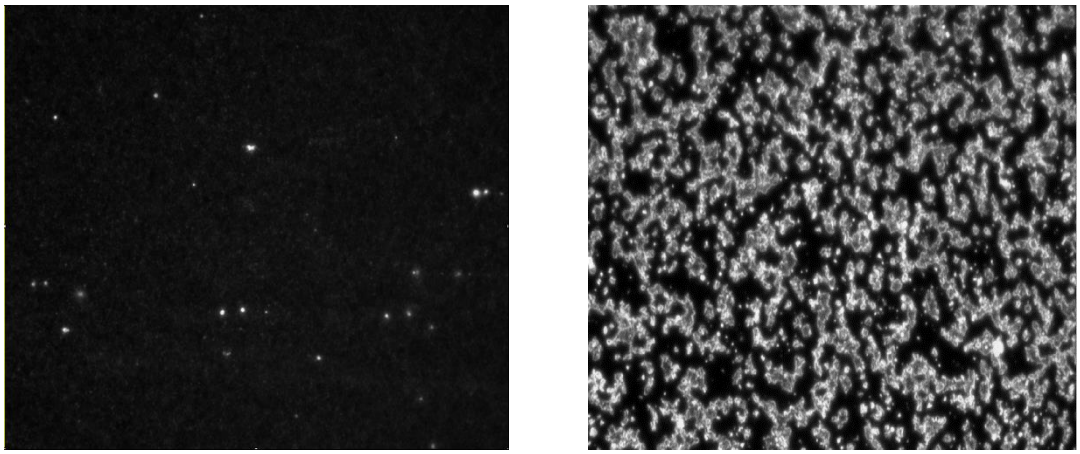

A **B**

Figure 5.11 *Dark-field image of bare AuNR before (**A**) and after (**B**) the adsorption of ~20 nm AuNP onto the surface of an AuNR sample. The nanoparticle deposits appear significantly lighter which is associated with higher scattering and can be seen to be unevenly distributed across the AuNR. Approximate image size is 60 μm × 60 μm.*

Firstly, the dark-field images in Figure 5.11 shows a significant difference between before and after exposure of the Au colloid to the partially etched AuNR surface. The areas of enhanced scattering suggest that the coating of Au spheres was not uniform, which may in part be due to drying-induced aggregation. The 'before' and 'after' specular reflectance spectra comparing the bare AuNR spectrum with that from the same AuNR sample once covered in a monolayer of NP. These are shown in Figure 5.12. The absorption feature seen at 520 nm for the reflectance spectra for the bare AuNR became less distinct and much broader in the presence of the Au colloid. This suggests that the specular reflectance is responsive to changes in refractive index around the exposed AuNR (this was not observed for molecular monolayers). Given the large aspect ratio of the electrodeposited rods, the reflectance spectrum is only the LSPR associated with the transverse mode, which is close to the LSPR of the AuNP. Further measurements comparing both exposed and enclosed AuNR are needed to further clarify the interaction between the colloid and exposed AuNR but this was not explored.

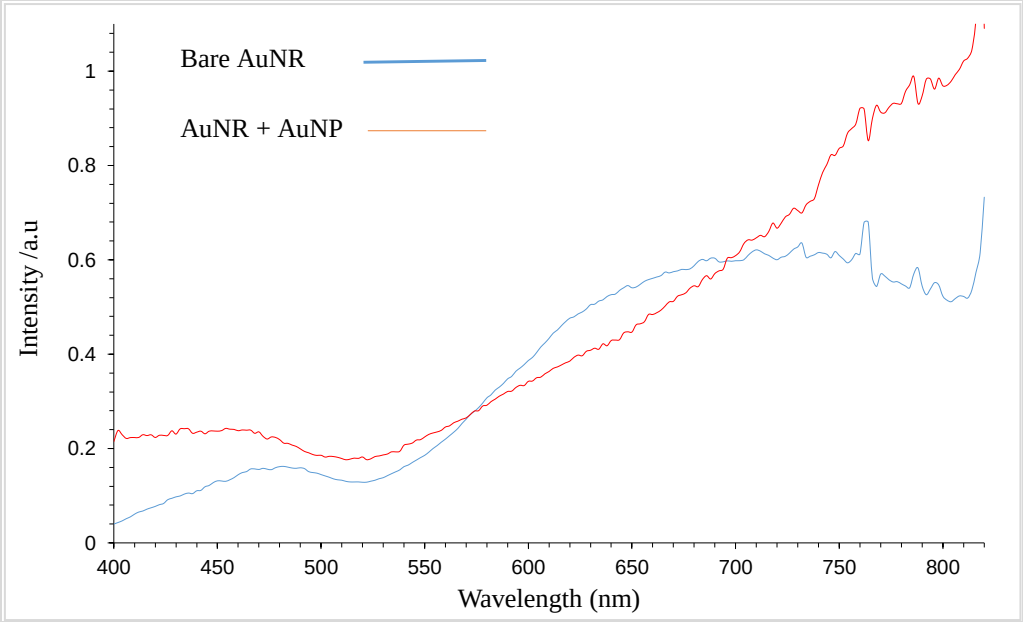

Figure 5.12 *Specular reflectance spectra (with p-polarised light) obtained from an AuNR sample (20 nm width) and from the same sample covered in AuNP (blue) at angle of incidence of 36°. The plasmon at 520 nm appears less pronounced for the AuNP (20 nm diameter covered sample than sample once covered in AuNP (20 nm diameter).*

5.6 In-situ potential dependence studies on vertical AuNR.

A clear advantage to having the etched AuNR remain within the confines of the alumina template is that it provides the opportunity to use the AuNR as a working electrode. This was demonstrated previously in section 4.7 thus enabling the of *in-situ* SERS measurements under an applied electrical field.

Experiments were carried out in order to investigate the effect of electrode potential on the fingerprint spectra obtained for a number of analytes. In this section the analytes discussed are MG, thiophene electropolymerised to polythiophene and 1,8-diaza-4,5-dithia-1,8-di(2-chloro-[1,4]-naphthoquinone-3-yl)octane (NQ), which was synthesised and kindly supplied by the Campbell group from the Department of Chemistry at The University of Edinburgh[38].These experiments were conducted using an electrochemical flow cell designed specifically to be used with the AuNR samples. A photograph and description of the cell can be found in Figure 6.13. A schematic diagram of the set up used with MG is shown in Figure 5.13 and the experimentation carried out using thiophene and NQ were also carried out in a similar fashion.

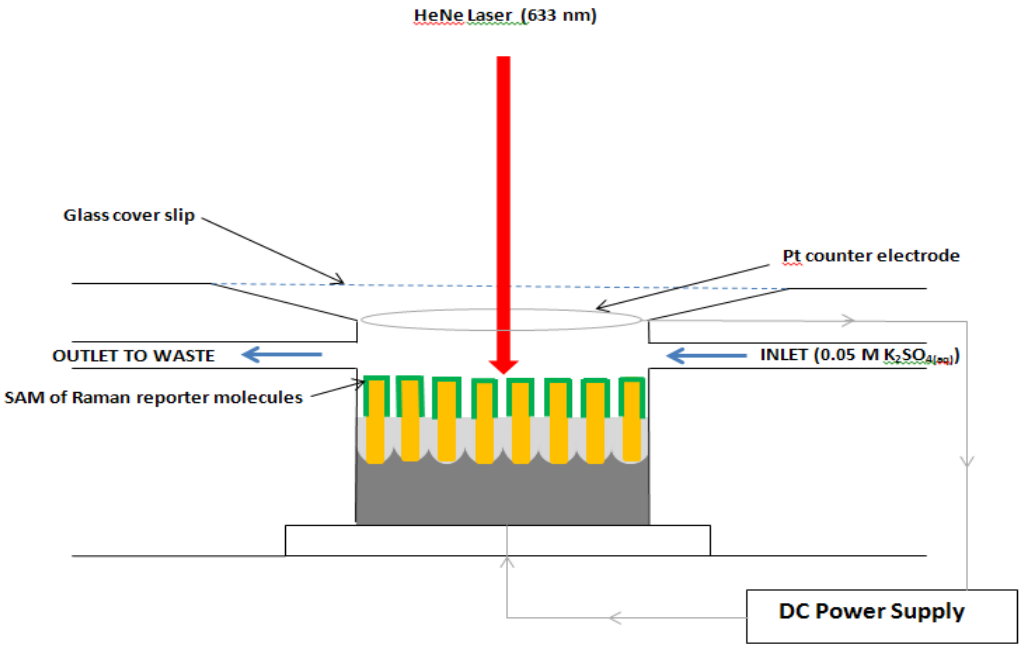

Figure 5.13 *Schematic representation of the flow cell set up for use with SE(R)RS under electrochemical control, with an AuNR sample covered with a monolayer of MG dye.*

5.6.1 Potential dependence of MG covered AuNR

The AuNR sample was covered in a MG self-assembled monolayer (SAM) and placed into the specially designed electrochemical flow cell. An inert electrolyte solution of 0.05 M K_2SO_4 was employed. The open circuit potential for this cell, using a platinum counter and pseudo reference electrode, was –885 mV. The potential range employed in this study was from –3.0 V to 3.0 V. This large potential range was possible in the aqueous medium because MG formed a blocking layer on the electrode surface and no Faradaic reaction was possible. The electrode therefore behaved as an ideally polarisable electrode, with virtually no electrolysis current flowing over this large voltage range.

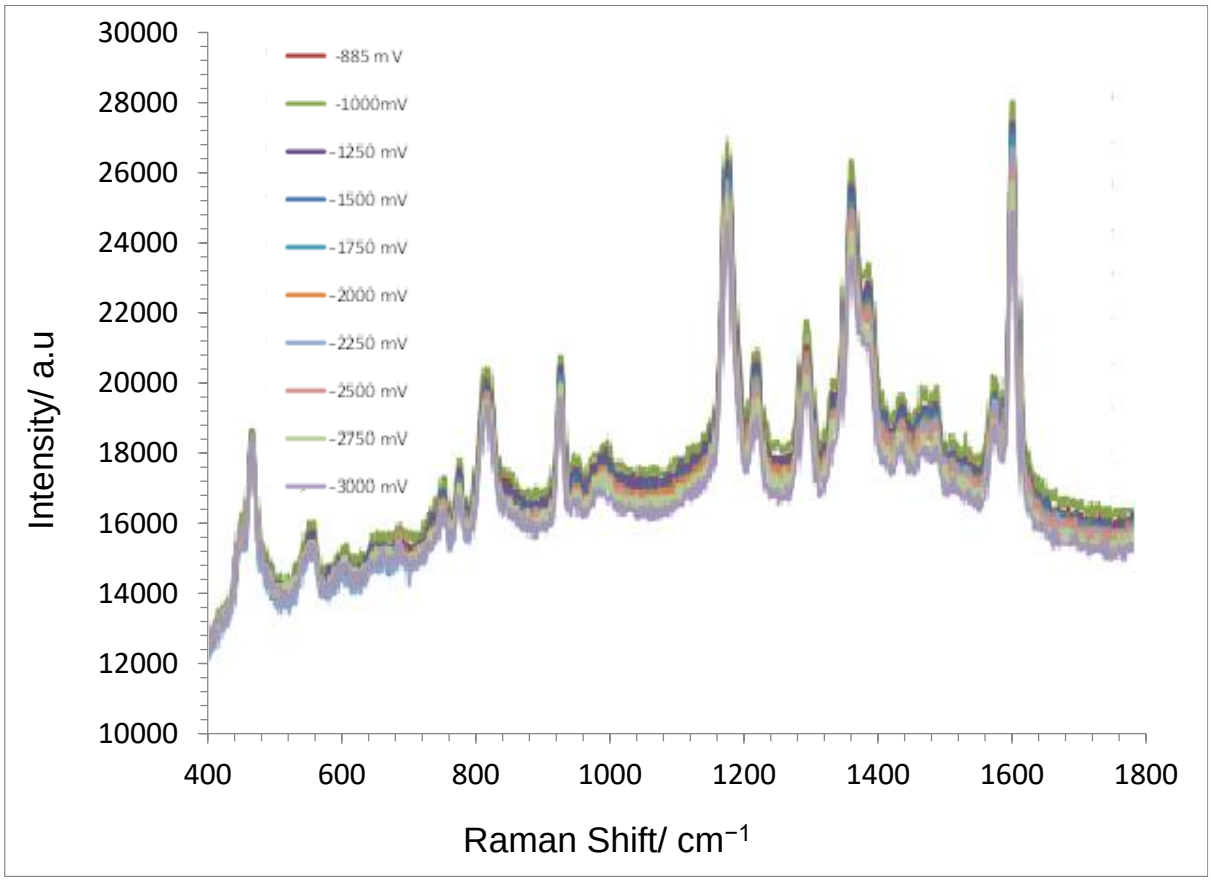

Figure 5.14 *SERRS spectra obtained from AuNR with adsorbed MG across the potential range of –0.885 V to –3.0 V in 0.05 M K_2SO_4. (λ_{ex}= 633 nm). For clarity, spectra to 3.0 V have been omitted.*

Not unsurprisingly therefore, there were no detectable changes in either peak height or position observed in the SERRS spectra for the MG as the potential was increased/decreased, in 250 mV steps, as shown in the Figure 5.14. This implied that the MG SAM was stable under these conditions, and most importantly was not removed from the surface or altered by cathodic polarisation up to –3000 mV.

5.6.2 Electrochemical polymer growth on AuNR

Polythiophene is a conducting polymer and also known as a "synthetic metal"[167,168]. Delocalised π electrons run along the polymer backbone and these are responsible for its

electrical conductivity. Optical properties such as colour shifts have been achieved by the distortion of this backbone[169, 170] through substitutions on the β position.

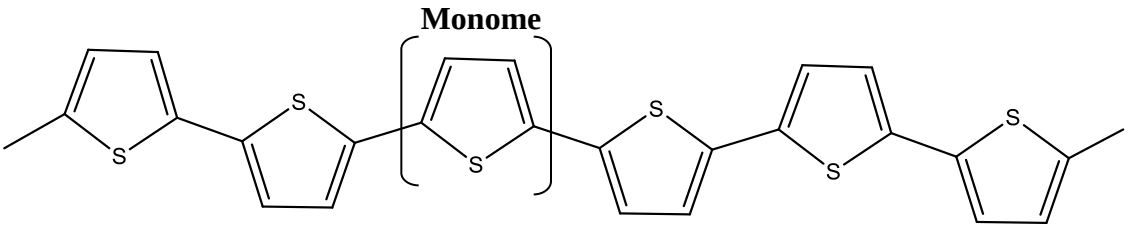

Figure 5.15 *Representation of polythiophene with the monomer repeat unit bracketed.*

To this end, the variation in the SERS spectrum obtained with adsorbed thiophene on the AuNR surface was compared to that of a layer of polythiophene, the structural formula of which is depicted in Figure 5.15, which was electrochemically grown on the AuNR surface[169,171,172]. The polymer is electroactive and can undergo oxidation of the backbone with corresponding insertion of anions or loss of cations on reduction, the latter leading to loss of conjugation and so a lowering in electrical conductivity.

Prior to polymer growth on the AuNR sample the SERS spectrum from the AuNR sample with an adsorbed layer of thiophene was obtained and is shown in Figure 5.16. The polythiophene film was then grown on top of the exposed AuNR by means of cyclic voltammetry in an aqueous solution containing 0.05 M thiophene in 0.1 M K_2SO_4 in a 60 vol% DIW: 40 vol% ethanol solution.

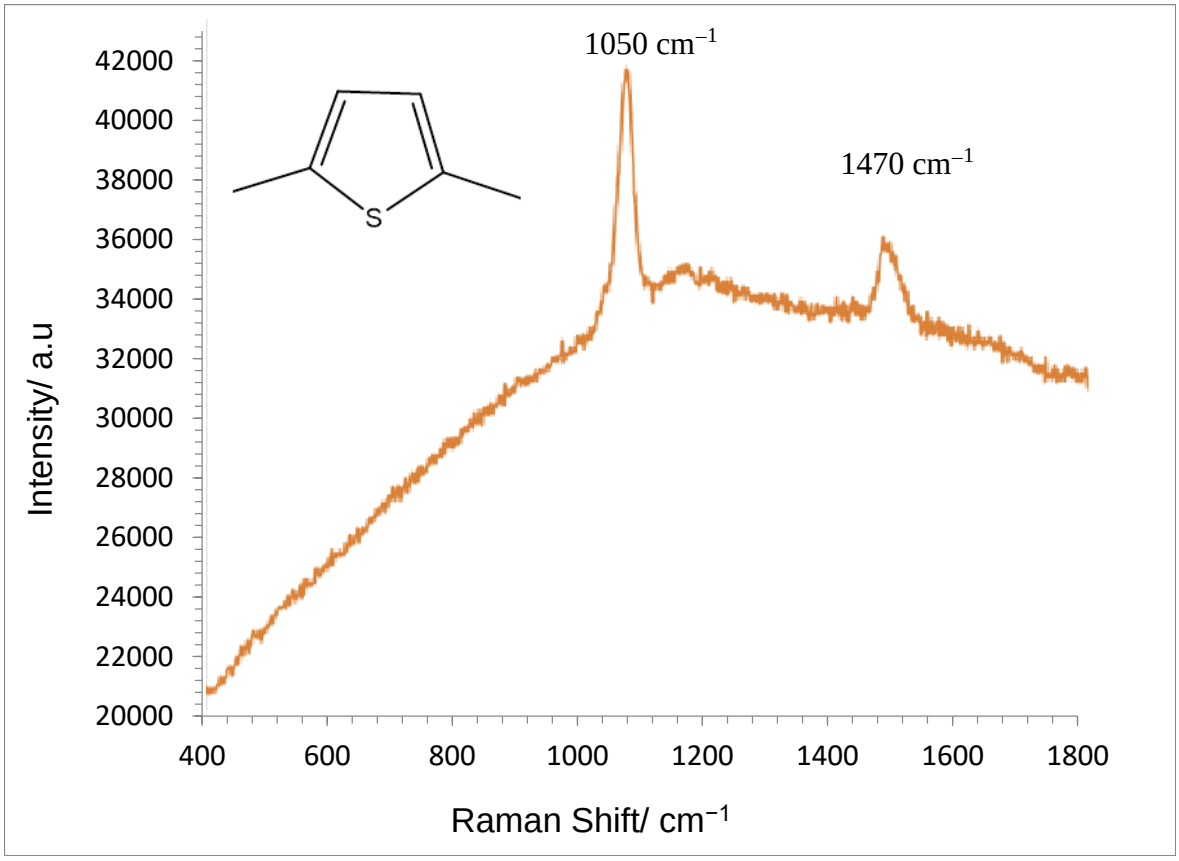

Figure 5.16 *SERS spectrum obtained from AuNR with an adsorbed monolayer of thiophene (λ_{ex}= 633 nm, with a 20× objective and 100% laser power).*

This involved repeated potential cycles between –0.7 V and 1.3 V vs SCE as shown in Figure 5.17. On the first cycle the anodic polymerisation process was initiated at a potential of ~ 0.9 V. As the cycling continued, a strong feature developed on the positive scan, showing as a peak at 0.8 V. As noted above, this is due to the oxidation of the polymer film and an associated increase in the electrical conductivity of the polymer. Whilst during the negative scan the electrical conductivity of the polymer is severely reduced due to the loss of conjugation in the backbone and so very low currents are recorded. Repeated potential cycling to grow electropolymers is a technique commonly employed in the literature[173] and the increase in the current response with cycling signifies that growth of the polymer on the AuNR surface was indeed occurring. Figure 5.17 shows the regions of electropolymer oxidation and reduction as well as that of polymer growth beyond 1.1 V

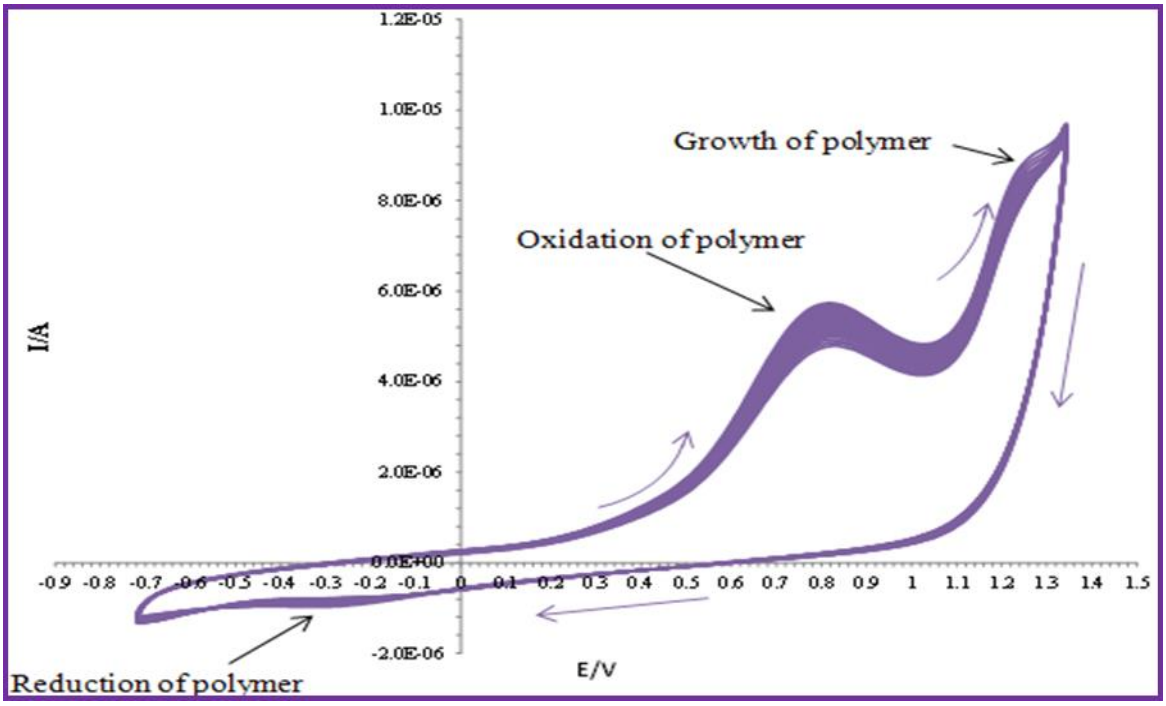

Figure 5.17 *Cyclic voltammogram of the growth of polythiophene on AuNR by repeated potential cycles between –0.7 V and 1.3 V vs SCE. by means of cyclic voltammetry in an aqueous solution containing 0.05 M thiophene in 0.1 M K_2SO_4 in a 60 vol% DIW: 40 vol% ethanol solution.*

.

The differences in the SERS spectrum obtained for an alumina/AuNR composite sample with an adsorbed layer of thiophene (Figure 5.16) compared to that obtained after growth of the polymer by cyclic voltammetry (Figure 5.18) can be ascribed to the formation of the polymer polythiophene on the surface of the exposed nanorod arrays. The SERS spectrum recorded for adsorbed thiophene on the AuNR surface revealed two peaks. The first at ~and the second at 1470 cm^{-1} correspond to symmetric vibrations of C=C and C–C, respectively. However, for the polythiophene SERS spectrum several more features can be observed. The peak at 1620 cm^{-1} is as a result of the ring C–C stretching vibrations. The double peak at ~ 1400 cm^{-1} is attributed to the C=C anti-symmetric stretching of the polymer while the 1200 cm^{-1} band arises from the inter-ring C–C stretch and the band at 1045 cm^{-1} is from the C–H in-plane bending. While the peak at 810 cm^{-1} was attributed to C–H out-of-plane bending.

The open circuit potential for this cell, using a platinum counter electrode and pseudo reference electrode, was – 490 mV. Subsequent variations of the applied voltage to the polythiophene-covered AuNR surface, over the potential range –1.5 V to 1.5V proved to have no effect on

either peak height or position. This would suggest that although during oxidation of the polythiophene film, anion insertion/cation removal (and the reverse during reduction) occurs, these changes did not register in the SERS spectra due to the thickness of the polymer film and the insensitivity of the technique to probe these processes.

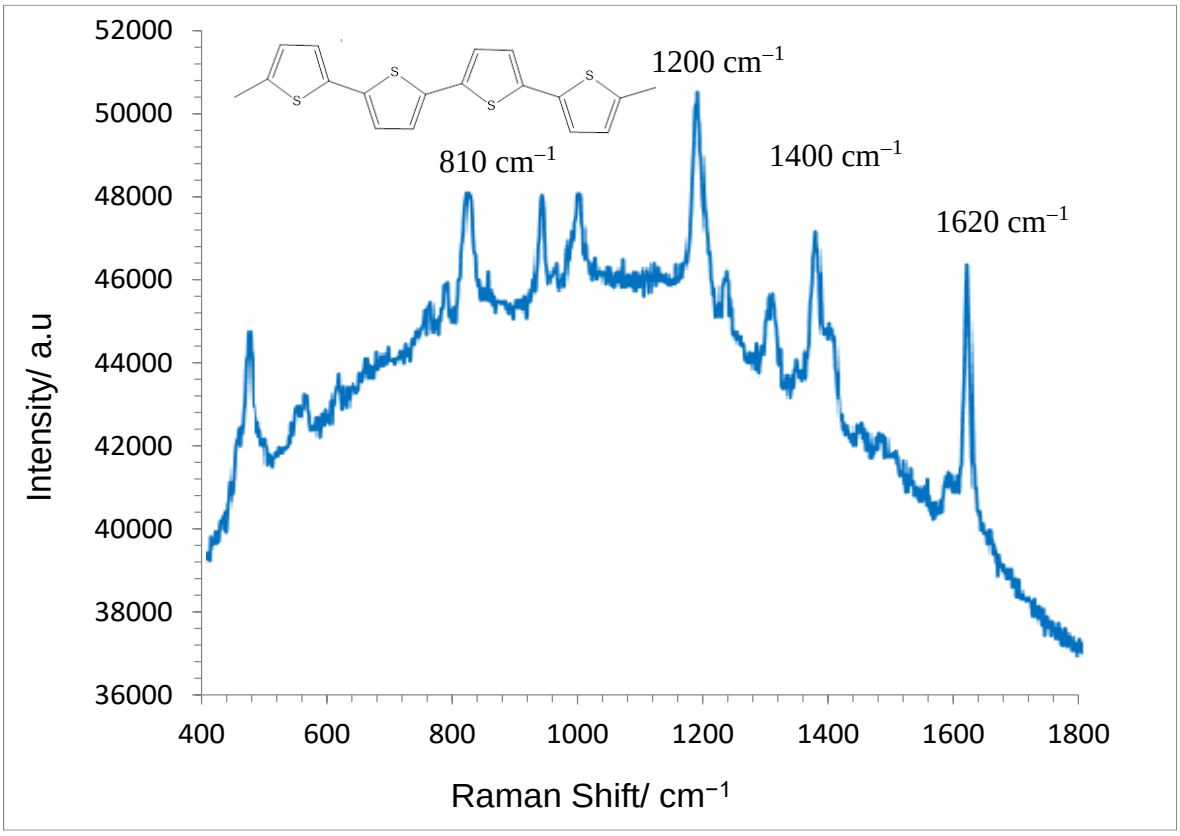

Figure 5.18 *SERS spectrum for polythiophene grown on AuNR (λ_{ex}= 633 nm) with a 20× objective and 100% laser power.*

5.6.3 The electroactive species NQ on a gold nanorrod array

A sample of the compound 1,8-diaza-4,5-dithia-1,8-di(2-chloro-[1,4]-naphthoquinone-3-yl)octane (NQ), shown in Figure 5.19 was synthesised and supplied by the Campbell group from The University of Edinburgh. Again, the strong sulfur gold affinity was utilised for attachment through chemisorption. The Campbell group have successfully performed reversible $2e^-$, $2H^+$ redox reactions using this compound that result in a change of structure and in the SERS fingerprint with varying potentials.

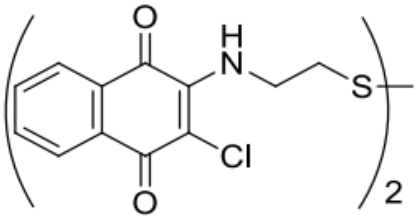

Figure 5.19 *1,8-diaza-4,5-dithia-1,8-di(2-chloro-[1,4]-naphthoquinone-3-yl)octane (NQ).*

However in this instance, as can be seen in Figure 5.20, the SERS spectra obtained was poor, at 100% laser intensity and a 20× objective, in comparison to that achieved by the Campbell group[38].

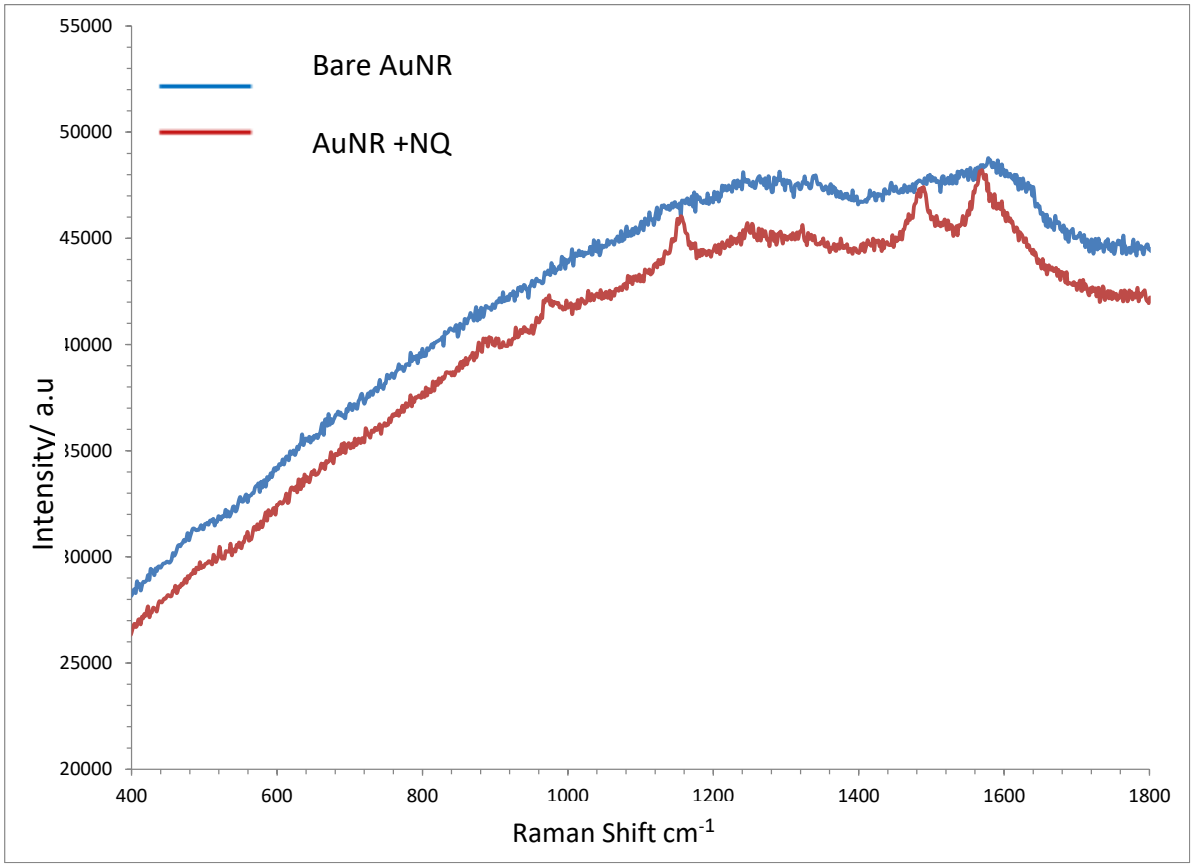

Figure 5.20 *SERS spectrum for 1, 8-diaza-4, 5-dithia-1, 8-di(2-chloro-[1,4]-naphthoquinone-3-yl)octane (NQ) on AuNR in 0.1 M K_2SO_4 solution (λ_{ex}= 633 nm, OCP = -814 mV, with a 20× objective and 100% laser intensity).*

Again utilising the purpose built flow with a 0.1 M K_2SO_4 solution cell the open circuit potential for this cell was found to be −814 mV. Subsequent variations of the applied voltage to the NQ covered AuNR surface, over the potential range −1.5 V to 1.5V proved to have no effect on either peak height or position. The signal obtained here had a low signal to noise ratio thus proving difficult in distinguishing of the faint features from the baseline. Not surprisingly therefore no change in fingerprint or intensity of signal was observed during variation in potential.

5.7 Chapter 5 Summary

The AuNR have been shown to be hydrophilic. Signal enhancement in the presence of a monolayer of the resonant dye MG is excellent with a high signal to noise ratio, evident by the clarity and sharpness of peaks obtained. The uniformity of signal across a single sample surface was found to be 2.2%. Comparison studies between AuNR and gold film on glass slide, klarite® and a monolayer of 20 nm nanoparticles on a glass slide covered in a monolayer of both MG and MBA. It showed that in both cases, the AuNR samples came top for signal enhancement and uniformity of signal.

AuNR samples have been regenerated five times, using a methanol wash and oxygen plasma cleaning, with an RSD of 3.2% on the height of the 1618 cm^{-1} thus showing no significant loss in signal with repeated use. Further studies are required to determine the actual life span of the samples with repeated application and cleaning of a monolayer of MG.

The three species selected for electrochemical experiments proved to be unsuccessful in this regard and further work in this area is required.

While it was not possible to quantify or control the length of nanorod exposed after etch-back. At present, it is only possible to confirm full exposure and so a study into the effect of the variation in length of exposed AuNR. Further utilisation of specular reflectance FTIR may prove to be beneficial in this quest.

6. Creating patterned gold nanorod arrays for multi analyte analysis

In this chapter, the development of a method to selectively deposit gold onto isolated regions of the alumina template and create separate AuNR regions on the same surface was investigated with the aim of detecting multiple analytes simultaneously on the same surface. The previous chapter demonstrates that AuNR samples can be prepared with strong SERS signal enhancement and good uniformity across the sample surface area. However, the total sample surface area available is much larger than that of the incident laser beam spot and indeed substantially more than that needed for the detection of a single analyte. Considering the time required preparing the samples, the benefits of multi-analyte analysis are substantial. Therefore further efforts were made to address these challenges. The method employed to produce patterned samples is described and the development of a procedure for the isolation and attachment of a number of different reporter molecules onto the patterned areas is discussed. Finally, additional methods for surface regeneration of the AuNR are explored.

6.1 NIR797 isothiocyanate

In addition to the reporter molecules introduced previously (MG and MBA) in Section 5.1 a third Raman reporter dye was used in this part of the work. NIR797 isothiocyanate **(**1,1′-Bis(4-sulfobutyl)-11-(4-isothiocyanatophenylthio)-3,3,3′,3′-tetramethyl-10,12-tri methyleneindotricarbocyanine monosodium salt) which is a NIR fluorescent cyanine dye primarily used for the labelling of proteins the absorbance spectrum is shown in Figure 6.1. It was selected due to its λ_{max} value of 795 nm, which closely matches the 785 nm excitation wavelength to be used in this section.

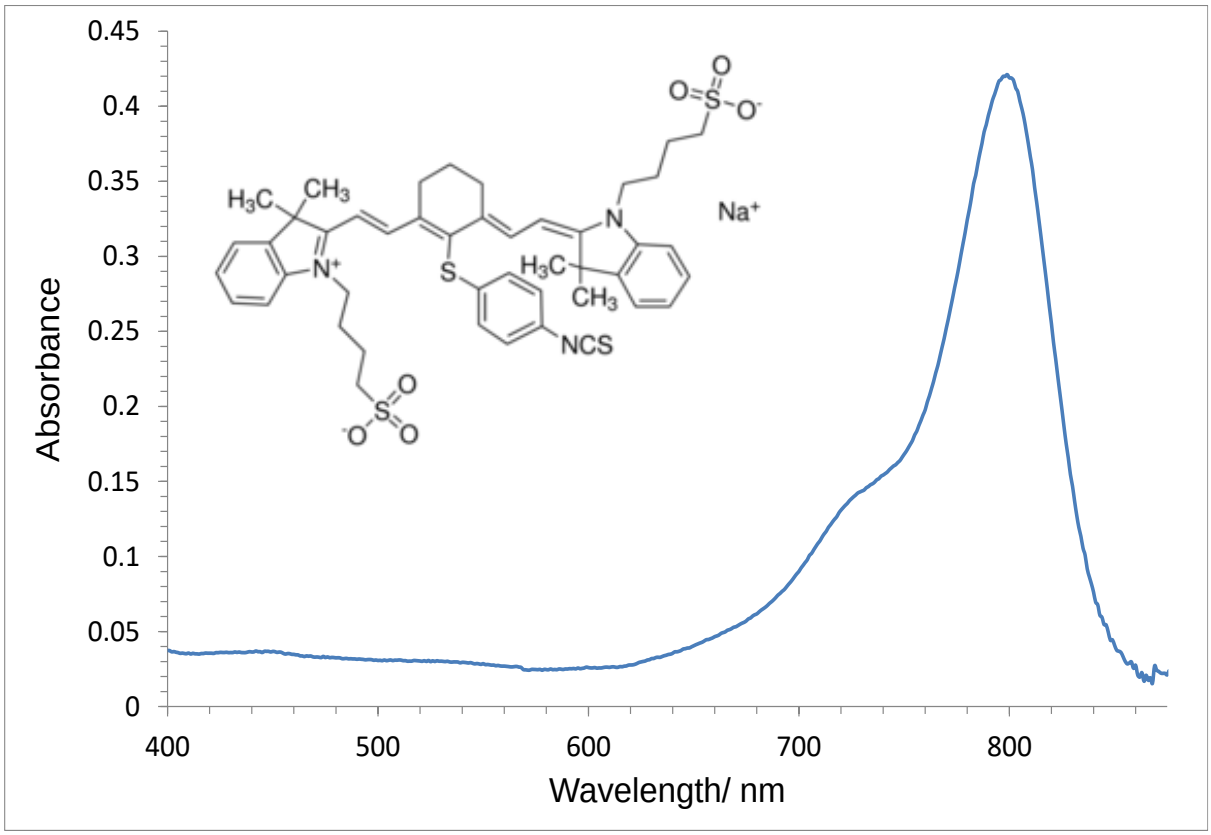

Figure 6.1 *Absorption spectrum of NIR 797 at a concentration of 10^{-5} M in MeOH (λ_{max} at 795 nm).*

6.2. Fabrication of patterned gold nanorod arrays

In order to facilitate the use of AuNR as multi-analyte substrates it was first necessary to devise a means by which to isolate specific areas within the template in which the gold could be deposited and also prevent the flow of current to the other areas of the template so that they remain gold free. For this purpose a PTFE mask was designed that allowed AuNR electrodeposition only on selected parts of the anodised alumina sample surface.

The schematic in Figure 6.2 shows how the different surface patterns were created. The size and shape of the pattern produced can be easily customised to suit the individual needs and requirements of the sensor. Each of the patterned samples shown in Figure 6.3 was prepared using the same conditions, gold deposition time and etch-back time that were established in the previous chapters for the non-patterned samples. In sample A four active areas were produced

together with a smaller alignment area used to aid the identification of each area 1 to 4; whereas in sample B, 9 active areas were formed in a square pattern and in sample C, 9 active areas in a circular pattern.

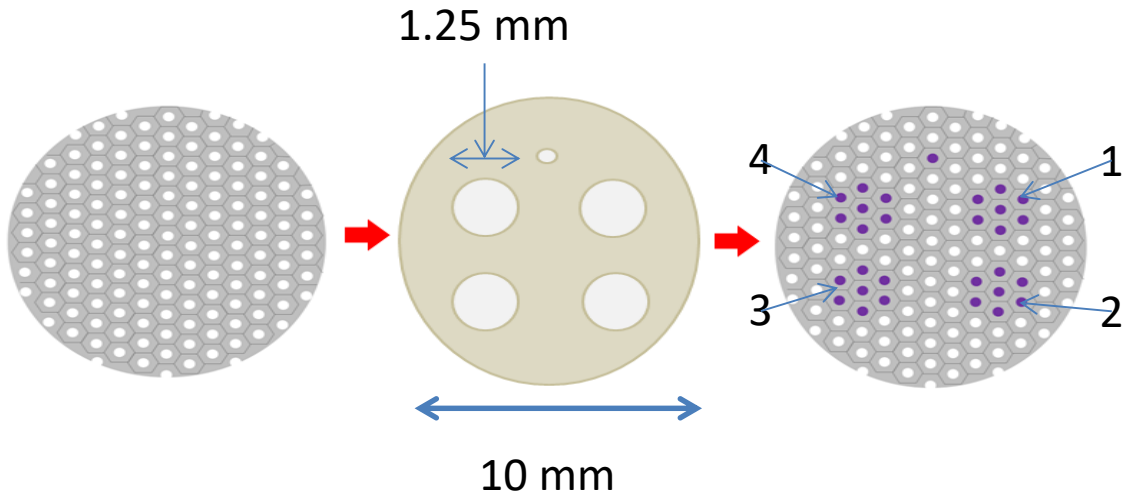

Figure 6.2 *Schematic representation of elective AuNR coverage achieved using a PTFE mask during the electrodeposition of gold into the pores of an AAO film in a 4-dot pattern. A smaller fifth dot is used as an alignment and marker in order to identify the dots that are numbered clockwise 1 to 4.*

Figure 6.3 *Examples of patterned AuNR samples produced using PTFE masks. Sample A – four 1.25 mm dots, sample B – nine 0.5 mm dots and sample C – nine 1 mm dots.*

In an initial characterisation analysis, the entire surface area of the patterned samples was covered in a monolayer of MG and the SERRS signals from each localised area were compared using an excitation wavelength of 633 nm. It was noted that no signal was obtained from the areas of bare alumina, thus confirming that signal achieved was only due to the interaction of the dye molecule with the AuNR. Samples A and C provided repeatable enhancement spectra

comparable to those previously achieved with the non-patterned sample discussed in Chapter 5. In both cases, each AuNR "dot" was 1.25 mm in diameter. However in Sample B, each individual dot measured ~0.5 mm in diameter and the signal enhancement was found to be approximately 25-30% less than seen with the larger dots of Samples A and C. This reduction in enhancement may be due to the difficulty in establishing that the laser beam was fully centred within the smaller AuNR dot region. This could result therefore in the laser beam focusing on the edge or out with the AuNR spot altogether. A much smaller active surface provides fewer opportunities for plasmonic enhancement. The calculated theoretical laser spot diameter at 633 nm was ~ 1545 nm. However, the actual laser spot size is likely to be larger than this.

6.2 SERS analysis of patterned AuNR

For the majority of this study, the four-dot sample (sample A) was selected for use to allow for comparison of the SERRS signal achieved to that from the non-patterned surface. The four-dot sample allowed three separate dots for reporter molecules, with the fourth dot kept free as "bare" AuNR in order to provide a control. In addition, the spatial design provided good separation between the dots to help facilitate their complete isolation when attaching the selected molecules and preventing cross contamination.

6.2.1 Signal enhancement across a four gold nanorod array dot sample

An initial experiment was performed to establish if the SERS signal intensity for each of the four dots were comparable to each other. Figure 6.4 shows SERS spectra obtained for a sample where the whole surface was covered in a monolayer of MG. The SERS spectra from each spot was, compared to each other by noting the Raman intensity of one of the largest peaks at 1618 cm^{-1} and subtracting the intensity on a nearby baseline point at 1618 cm^{-1}. The average intensity of the four peak heights was 36245 counts with a standard deviation of 1838 and % RSD of 5.1. This value is greater than that seen on the single sample surface in Section 5.2, but still compares favourably with the variation established earlier, whereby a % RSD of 2.2 was achieved across the entire sample surface. At only 1.8 % higher, the variation in the data for the four-dot sample can be considered satisfactory.

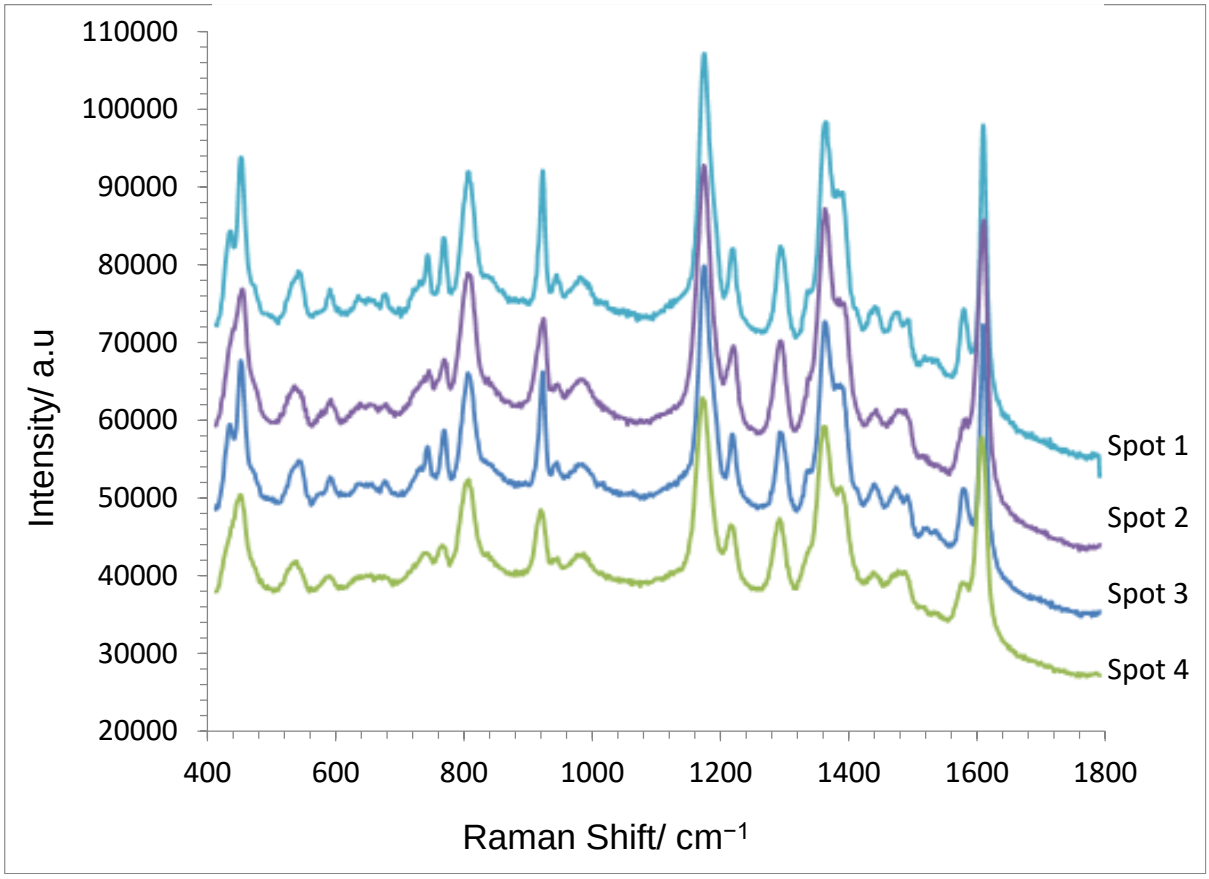

Figure 6.4 *Raman spectra obtained for a MG coated four dot patterned AuNR sample (prepared by a 5 minute second anodisation period with gold deposition carried out for 6 s at 6.5 V_{rms} and 25 minute etch-back to expose the nanorods). Raman spectra were acquired in air at λ_{ex}= 633 nm and an excitation time of 10 s. Spectra are vertically offset for clarity.*

6.2.2 Multi-analyte attachment onto patterned gold nanorod arrays

Having created a four-dot AuNR sample and with good uniformity of signal across each of the four-dot regions with a single analyte, the next step was to establish a method to attach different analytes to each individual dot. Securely isolating each dot proved problematic due to the hydrophilic nature of the substrate compounded by the natural lip created at the boundary between the alumina template and aluminium surrounding it during manufacture. While this proved advantageous during full sample surface coverage with a single analyte it resulted in difficulty establishing a good and secure seal in order to isolate patterned areas from each other. As a result each analyte leached out from the selected deposition area and contaminated the other dots. Therefore, a means by which each dot could be isolated from the others during the attachment of multiple analytes needed to be developed.

In order to facilitate the successful isolation and attachment of multiple analytes, a method was proposed whereby the reporter molecules were contained within a gel rather than an alcohol solution to prevent leaching and cross contamination. To this end, a sample of an undoped electroactive organo-gel produced by the Ulijn Group, then based at The University of Strathclyde, was used. The electroactive conducting gel used consists of one dimensional self-assembled nanofibers with a low-molecular-mass[343]. The gel was produced by the attachment and self-assembly of diphenylalanine amide derivative to *p*-type tetrathiafulvalene (TTF)−dipeptide bioconjugate (TTF-FF-NH2). With the addition of chloroform and ethyl acetate and mixing, a self-supporting organo-gel was formed. The addition of Tetracyanoquinodimethane (TCNQ) resulted in the formation of a two-component charge transfer gel[174].

The gel was mixed with the selected resonant and non-resonant dyes and two aliquots of each placed on top of the 4 AuNR dots. For the non-resonant gel spot no signal was obtained while for the resonant gel spot a faint signal was produced when the thickness of the gel was ~3 mm and it increased slightly when this was reduced to ~1 mm. However the signal reduced again with further thinning until no signal was obtained once the majority of gel had been removed. Whilst it proved a successful method in isolating the analytes on each dot from each other, it was entirely unsuccessful as a means of adhering reporter molecules to the dots or achieving an acceptably usable spectra.

In order to load the three different reporter molecules directly onto three separate spots containing the AuNR, a central perspex plug (thickness ~2.5 cm) as discussed in Chapter 3.9 with holes drilled through to match exactly the size and position of the dots on the sample surface was devised. The sample was secured in the original flow cell and the central plug inserted and secured. The solution wells, so created above each of the AuNR areas, were subsequently filled with solutions, each containing one of the three reporter molecules. Firstly MBA was attached to the AuNR dot electrochemically (see Section 6.3 for details). Immediately after, the second and third dots were coated via a 20 minute immersion period in 10^{-4} M MG solution and 0.2 µM NIR 797 solution respectively with the fourth well remaining free of solution to provide a control or blank spot.

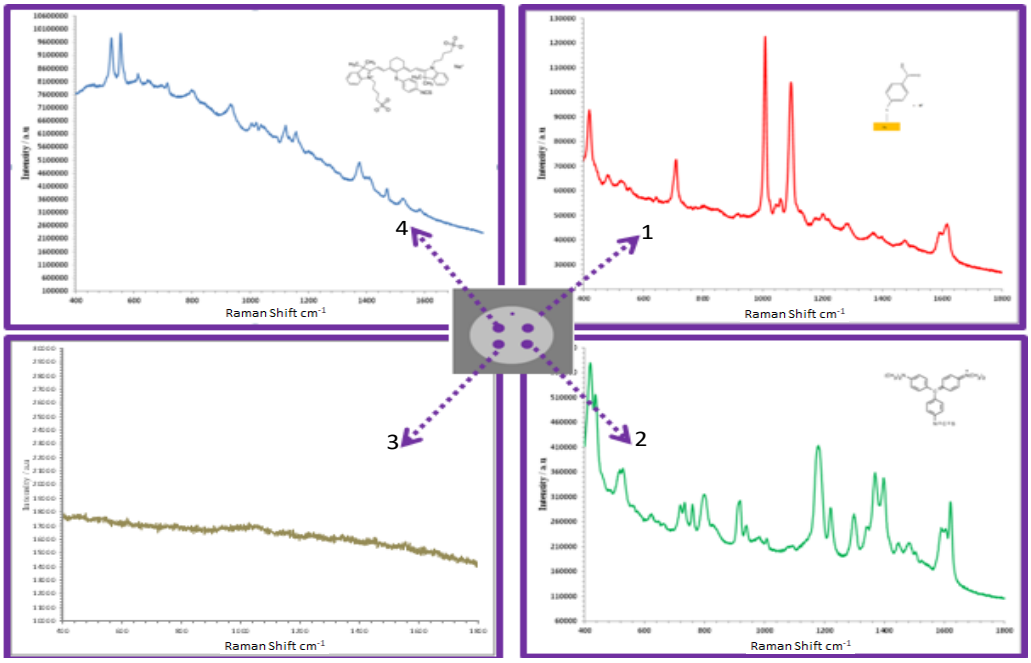

Figure 6.5 *SERS spectra from a multi-analyte AuNR 4-dot sample with, Spot 1-MG, Spot 2 - MBA, Spot 3 – blank and Spot - 4 NIR797 confined within their designated areas (20 x magnification with results adjusted to 100% laser intensity)* λ_{ex} *= 785 nm.*

Distinct spectra were obtained for the three different dyes with no evidence of cross-contamination as shown in Figure 6.5. Comparison of the spectra obtained from each spot at excitation wavelengths of 633 nm and 785 nm are given in Section 6.2.3. These results showed that the concept of a multi-analyte sensor on a single AuNR alumina composite sample was valid. While further refinement might be required to simplify and make the process of manufacture more straightforward with respect to eventually moving towards mass production, the method of the selective attachment of specific reporter molecules to specific areas had clearly been successful. No movement of the reporter molecules from their allocated well areas had occurred and the addition of a blank ensured that any results obtained are confidently attributed to the response obtained from interactions of the AuNR with the reporter molecule present at each of the three locations on the sample.

6.2.3 Comparison of the fingerprint spectra obtained at 633 nm and 785 nm wavelengths

The four-dot sample examined using a 633 nm excitation laser in addition to the 785 nm laser. This was to determine the enhancement attributable to the λ_{max} of the reporter molecules MG

and NIR 797 closely matching that of the respective laser excitation wavelength in addition to that of the non-resonant reporter molecule MBA. The calculated laser spot of diameter ~ 1915 nm for the 785 nm laser was ~ 24% larger than that of the 633 nm laser spot.

6.2.3.1 MG at 633 nm and 785 nm

The spectrum obtained for MG at 633 nm was compared to that obtained using a laser with an excitation wavelength of 785 nm and the results are shown in Figure 6.6. There are clear differences between the fingerprint of the two spectra obtained at resonant and non-resonant excitation wavelengths. The first and most obvious difference is the intensity of signal which saw a decrease in peak height measured (evaluated from 1677 cm^{-1} on the baseline to the peak height at 1618 cm^{-1}) of almost 90 %, from 32878 to 3556 counts. A similar; decrease in peak height at 1369 cm^{-1} relative to that of the peak at 1397 cm^{-1} can clearly be seen. In addition, the base line is shown to slope upwards towards the lower wavenumbers at λ_{ex} = 785 nm and an upwards slope towards the higher wavenumbers at λ_{ex} = 633 nm. This may be the result of the effect of the choice of excitation wavelength on the background luminescence from the alumina template substrate[175].

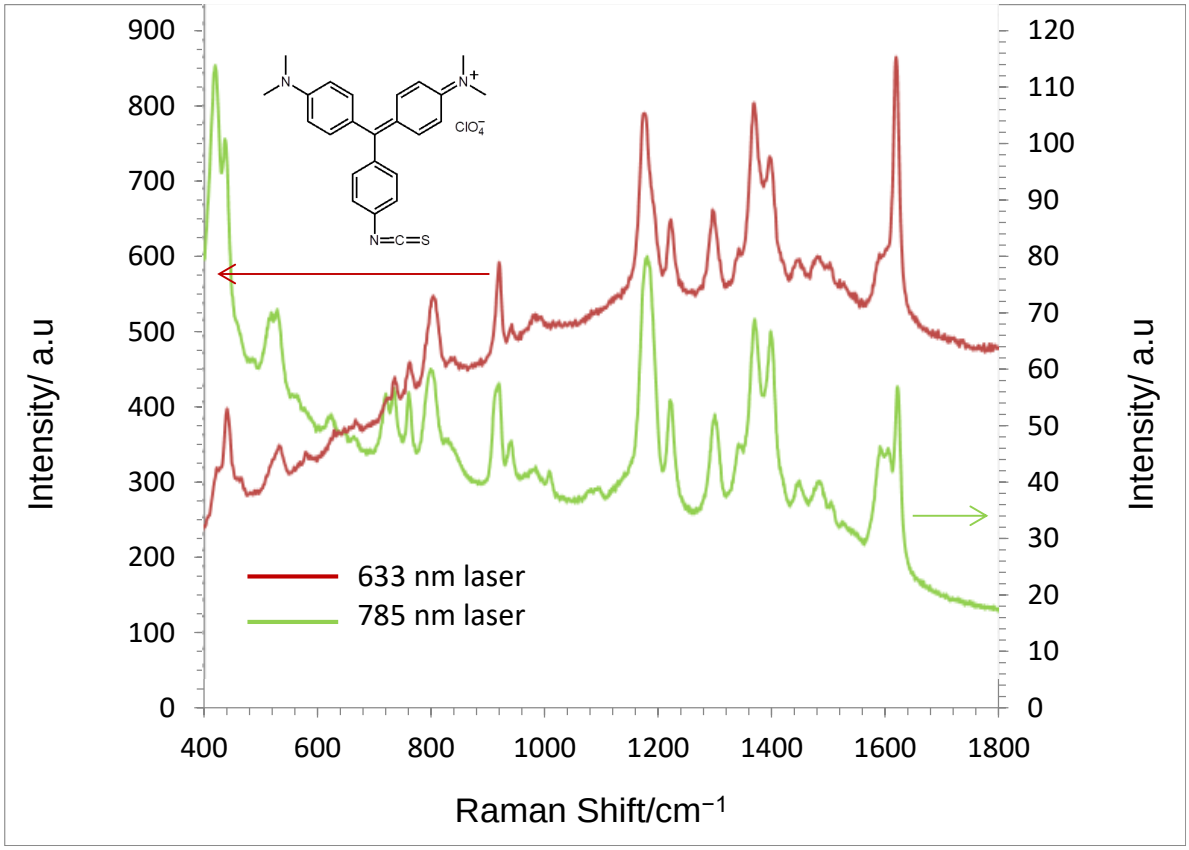

Figure 6.6 *SERRS spectra from MG obtained at λ_{ex}785nm (green) compared to that at λ_{ex} 633 nm (red) in air. Integration time of 10 seconds, a 50× objective and 1% laser intensity. The results have been normalised against a silicon wafer to enable comparison of the spectra obtained at different wavelengths.*

There are clear differences between the fingerprint of the two spectra obtained at resonant and non-resonant excitation wavelengths. The first and most obvious difference is the intensity of signal which saw a decrease in peak height measured (evaluated from 1677 cm^{-1} on the baseline to the peak height at 1618 cm^{-1}) of almost 90 %, from 32878 to 3556 counts. A similar; decrease in peak height at 1369 cm^{-1} relative to that of the peak at 1397 cm^{-1} can clearly be seen. In addition, the base line is shown to slope upwards towards the lower wavenumbers at λ_{ex} = 785 nm and an upwards slope towards the higher wavenumbers at λ_{ex} = 633 nm. This may be the result of the effect of the choice of excitation wavelength on the background luminescence from the alumina template substrate[175].

6.2.3.2 NIR 797 at 633 nm and 785 nm

The spectrum obtained for NIR 797 at 633 nm was compared to that obtained using a laser with an excitation wavelength of 785 nm with the results shown in Figure 6.7. Due to the high background signal it was necessary to reduce the laser power down from 1% to 0.5% when collecting data for NIR797 to be able to view the SERS spectra, as at higher laser powers the Raman detector was completely saturated. The fact that this was only partially successful can be seen as the spectrum obtained at λ_{ex} 633nm saturates at wavelengths below 860 cm^{-1}. Thus 633 nm should not be used as an excitation wavelength for this dye unless the laser power an be dropped further.

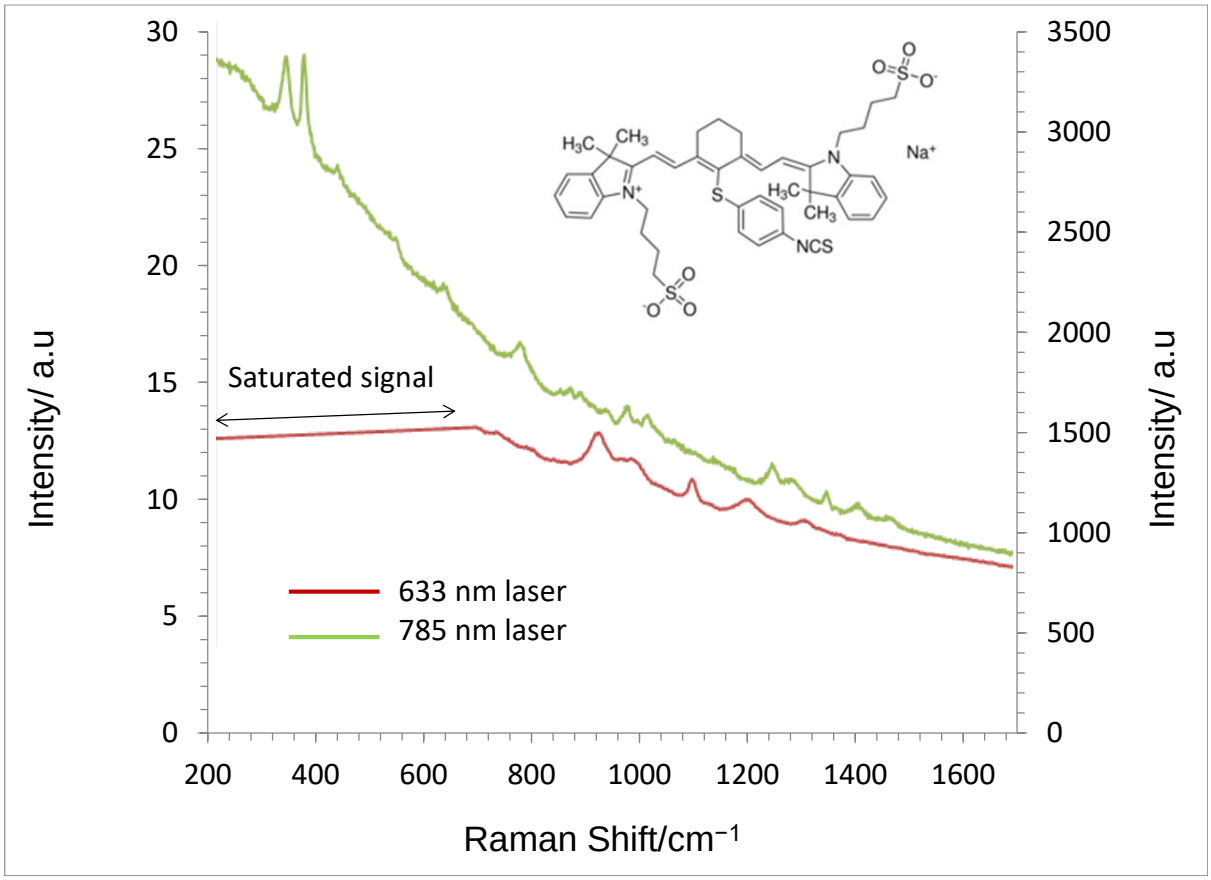

Figure 6.7 *SERS spectra from spectra NIR797 (0.2μM in EtOH) obtained at λ_{ex}785nm (green) compared to that at λ_{ex} 633 nm (red) in air. Both integration time of 10 seconds and a 20× objective and at 0.5% laser intensity. The results have been normalised against a silicon wafer to enable comparison of the spectra obtained at different wavelengths.*

There is also significant disparity in the intensity of SERS signal at both excitation wavelengths. In Figure 6.6, the largest signal enhancement for MG adsorbed on AuNR was obtained at the excitation wavelength of 633 nm, while for NIR967 the largest signal enhancement was at the excitation wavelength that most closely matches that of the λ_{max} of the NIR 797 dye at 795 nm. The spectra obtained for NIR 797 at both excitation wavelengths can be seen to slope sharply upwards towards the left. This is due to the fluorescence background signal decreasing in intensity at higher wavelengths and is why the signal saturates with the lower excitation wavelength of 633 nm even though the Raman signal itself is significantly weaker than that obtained with an excitation wavelength of 785 nm[164,176].

6.2.3.3 MBA at 633 nm and 785 nm

The spectrum obtained for MBA at 633 nm was compared to that obtained using a laser with an excitation wavelength of 785 nm and the results are shown in Figure 6.8. The spectra obtained at each of the two excitation wavelengths are of similar intensity, which is to be expected as MBA is a non-resonant molecule. There are clear differences between the two spectra where slightly more baseline noise is evident at 633 nm, with more features visible at 785 nm. The peaks at 1006 cm^{-1} are of similar intensity at both wavelengths. However, the height of the peak at 1096 cm^{-1} with 633 nm is approximately half the size of that seen at 785 nm. The peak at 1200 cm^{-1} is also much more pronounced at 633 nm than at 785 nm while the peaks at 710 cm^{-1} and 420 cm^{-1} are larger at 785 nm than at 633 nm. The peak at 1612 cm^{-1} with 633 nm is blue shifted to 1620 cm^{-1} at 785 nm.

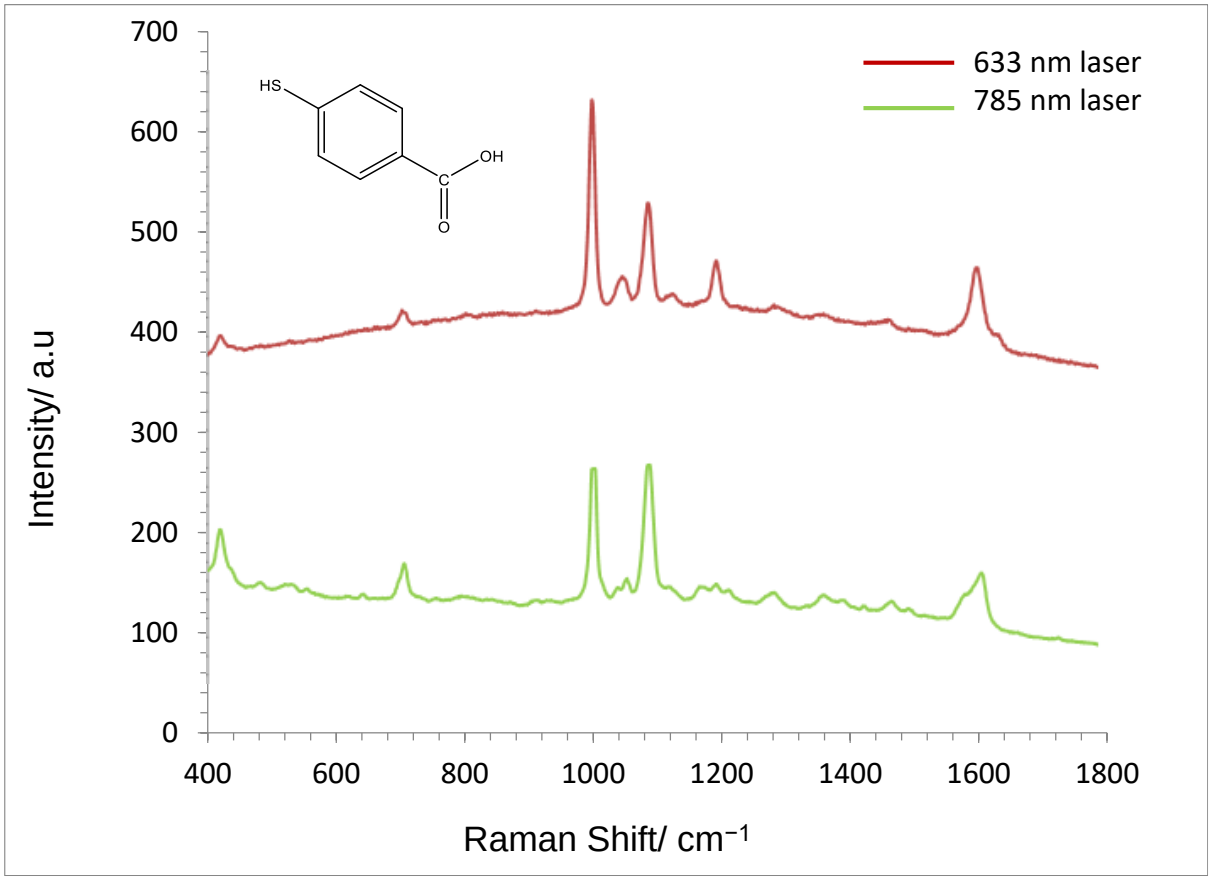

Figure 6.8 *SERS spectra for MBA obtained at λ_{ex}785nm (green) compared to that at λ_{ex} 633 nm (red) in air. Both integration times 10 seconds and a 50× objective and 25% laser intensity. (Spectra have been vertically offset for clarity). The results have been normalised against a silicon wafer to enable comparison of the spectra obtained at different wavelengths.*

6.3 Irreversible binding of MBA to gold nanorod array surface

The initial method whereby a SAM of MBA was adsorbed onto the surface of the AuNR involved overnight immersion of the AuNR sample in a 10 mM MBA solution. However, this method was found to be ineffective in achieving a SERS response when using the patterned samples. The length of time required for adsorption increased substantially to three to four days. As noted above, the need to isolate each dot from the others to avoid cross contamination of the reporter molecules involved constructing individual solution wells able to contain a maximum volume of 3.5 mm^3 around each dot. Therefore the volume of solution able to be put into the wells was so small that the adsorption efficiency was drastically reduced. In part, this problem was solved by the use of a saturated MBA solution although the reduced volume and

the need to leave it longer than overnight caused problems through evaporation of the solution. As the other two reporter molecules used with the four dot sample only required 20 minutes for full monolayer coverage, it was therefore necessary to devise a means by which the process of 'locking' the MBA onto the AuNR surface could be expedited or the use of MBA with the patterned sample would be impractical. Thus, a method was developed to electrochemical bind the MBA onto the AuNR by oxidation in order to facilitate a stronger bond formation, following the schematic in Figure 6.9.

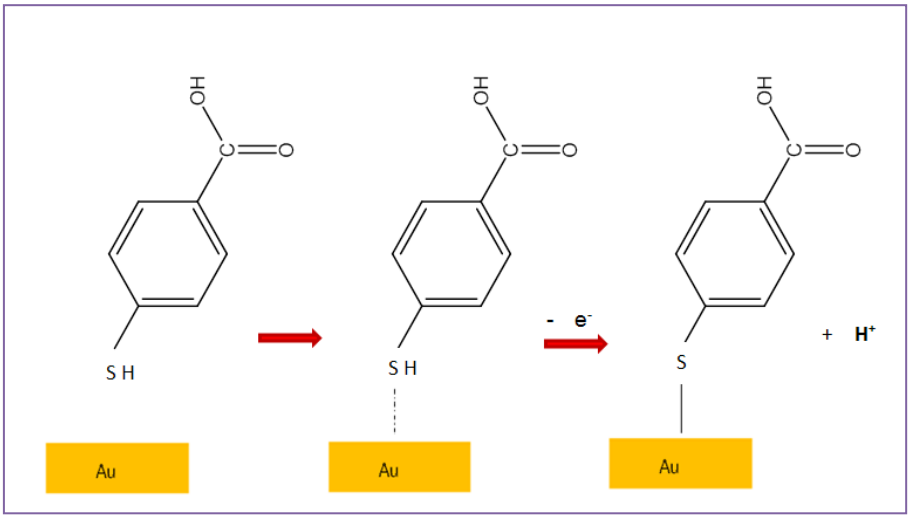

Figure 6.9 *Schematic representation of the electrochemical oxidation of MBA at a gold electrode.*

Initial cyclic voltammetry measurements were first performed on a gold disk electrode. From Figure 6.10, it can be seen that the attachment of the MBA was carried out by repeated cycling between –0.5 V and 1.5 V in a 40 vol% ethanol/H_2O solution containing 1.0×10^{-3} M MBA Two peaks at 0.6 V and 1.4 V are present on the first oxidation cycle but on the second cycle the height of first peak reduced by ~50% and shifted towards a lower potential while the second peak showed little change. The third cycle saw the first peak disappear altogether with the current dropping to virtually zero, possibly indicating full surface coverage by the MBA. Subsequent cycles saw no further significant change in the CV shape, although the second peak current can be seen to drop slightly with each subsequent cycle. The first peak at 0.6 V is attributed to the oxidation of the MBA and the second at 1.4 V, to the surface oxide formation on or dissolution of the gold. Clearly, the latter process is to be avoided with the AuNR samples

and so, the upper potential limit was set to 0.5 V *vs* the platinum counter/pseudo-reference electrode.

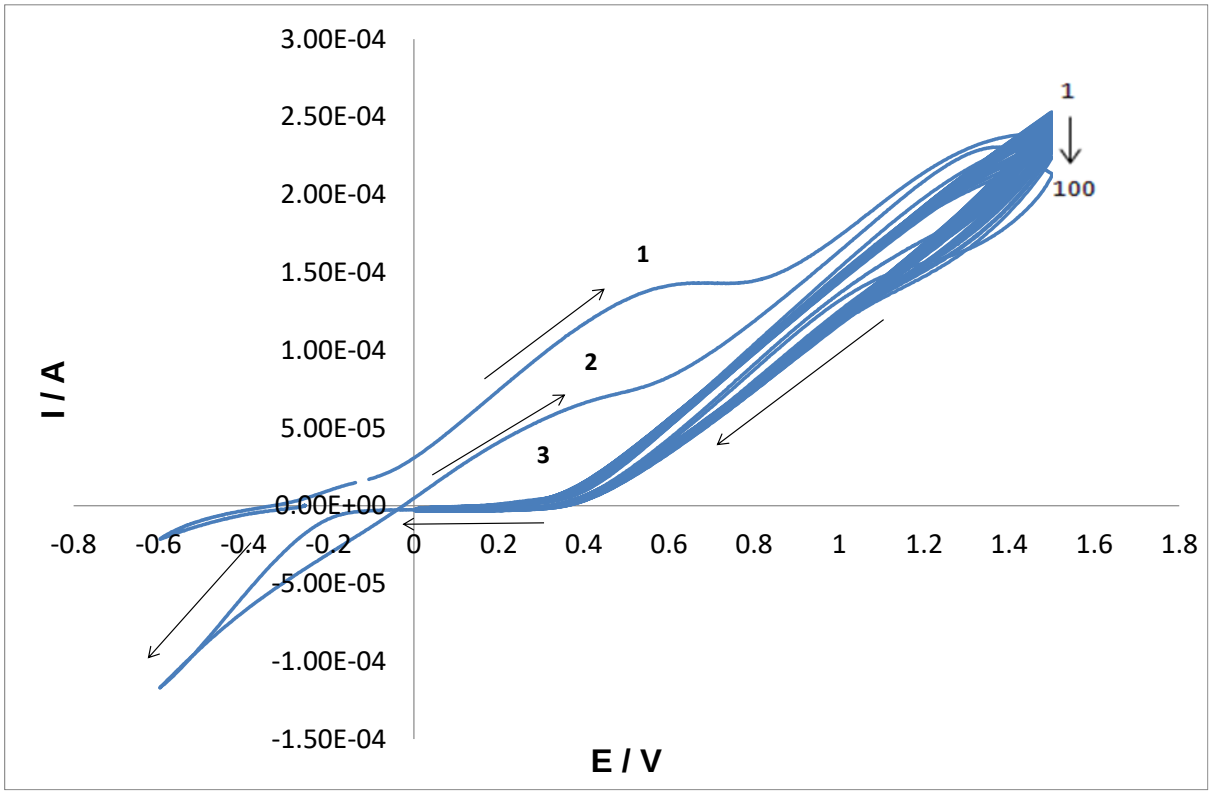

Figure 6.10 *CV of MBA growth on a gold disk electrode 7 mm in diameter. Solution composition: 0.001M MBA in 60 vol% water: 40 vol% EtOH. (Scan rate = 50 mV* s^{-1}*).*

Figure 6.11 shows the corresponding CVs obtained during the growth of MBA on the AuNR electrode. The first cycle was very similar to that of the gold disk electrode. However for the AuNR electrode, with each subsequent cycle the current recorded during the voltage scans decreased until it 'flatlined' after the eighth scan, indicating no further electrochemical response from the sample, signifying a blocking layer present on the AuNR surfaces.

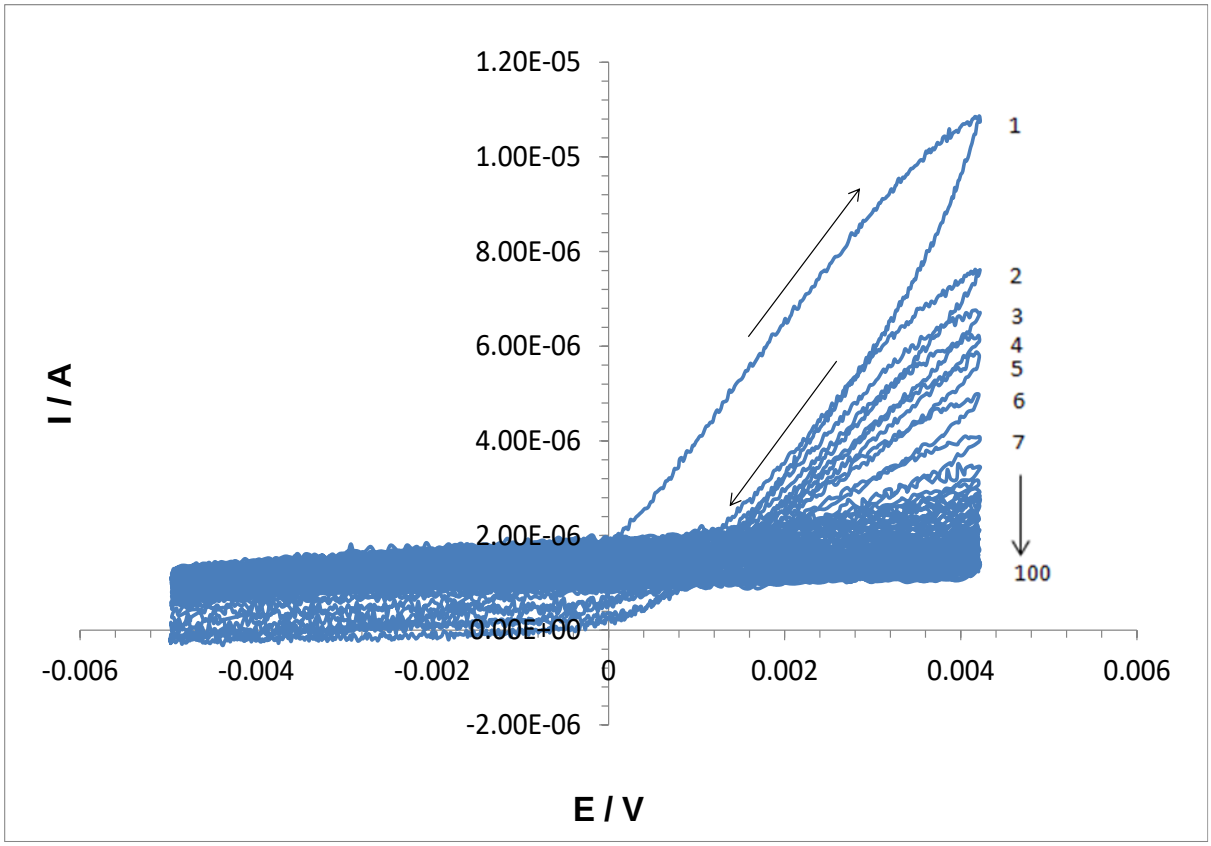

Figure 6.11 *CVs of MBA growth on AuNR electrode from a solution containing 0.001 M MBA in a 60% water: 40% ethanol solution. Scan rate = 50 mV* s^{-1}.

The SERS spectra obtained from the AuNR-MBA sample prepared in this fashion is shown in Figure 6.12. There is a marked difference between the fingerprints obtained for MBA on the AuNR surface formed by electrochemical oxidation to that by adsorption alone as seen in Figure 5.8. While the two main peaks seen at 1077 cm^{-1} and 1585 cm^{-1} are still present, they are dwarfed by the two new adjacent peaks at 1098 cm^{-1} and 1612 cm^{-1} respectively.

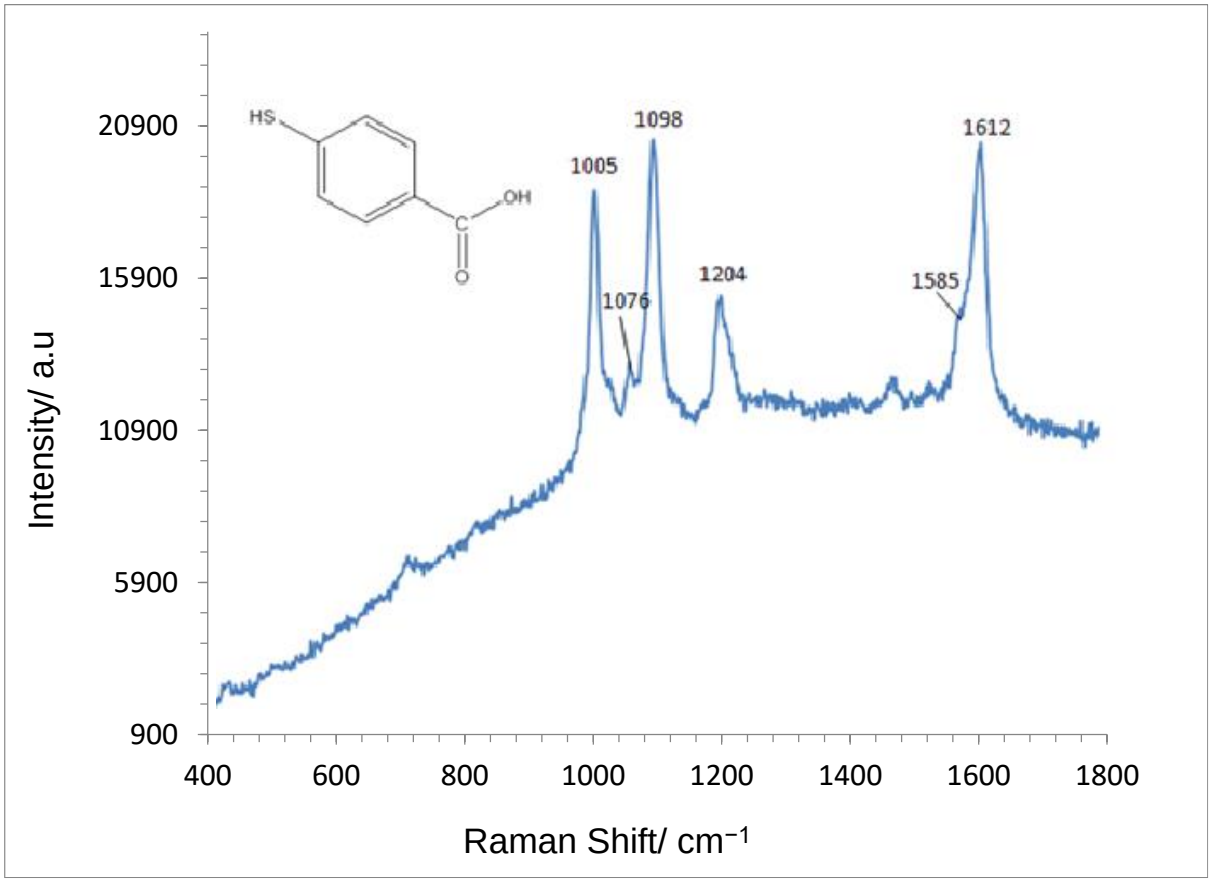

Figure 6.12 *SERS signal obtained after electrochemical oxidation of MBA on AuNR electrode (λ_{ex} = 633 nm).*

The strong attraction between gold and sulfur molecules is known to occur spontaneously, with underpotential SAM formation on the gold surface. Wen-qiang Ma *et al*[177] found MBA molecules adsorb at an oblique angle between the plane of the benzene ring and the surface. It would appear that the forced electro-oxidation at positive potentials resulted in irreversible covalent bonding of these 'adlayers' resulting in an increased surface coverage. This would naturally alter the angle at which the molecules lie relative to the plane thus increasing the distance of the carboxyl group from the sample surface [178]. In addition, Gao *et al*.[179] found the sulfur 'adlayer' underwent 'substantial structural modification as the overall anodic oxidation proceeds. Quijada *et al*[180] have also reported that the respective SERS peak for deprotonated sulfur–gold bond to shift to a higher wavenumbers than that for adsorbed sulfur on gold.

It appears then that the two main peaks have experienced a slight blue shift from 1076 cm^{-1} to 1098 cm^{-1} and from 1585 cm^{-1} to 1612 cm^{-1}. The strength in the intensity of the peaks is believed to be a result of the combination of an increased surface coverage, Au-S bond strength

and modification of the angle at which the MBA molecules lie relative to the surface. The strength of the Au–S bond is further verified in that after electrochemical formation of the MBA SAM on the AuNR substrate, removal of the SAM proved to be very difficult. The original cleaning method using oxygen plasma failed to remove the MBA, and this was verified by no loss in the SERS signal strength after each attempt at cleaning.

6.4 Surface regeneration of gold nanorod arrays

A desirable quality in a SERS substrate is that the surface can be regenerated to enable the substrate to be used multiple times without loss of performance. There are a number of well-established methods for the removal of SAM from gold substrates in order to make them reusable[60,163,181,182]. Due to the alumina base matrix, it was not possible to use oxidative acid solutions such as piranha for this purpose. The method employed and found to be effective to this point was photo-oxidative plasma cleaning which was used to clean samples prior to SAM growth and also to remove MG as discussed in Section 5.3. While this method proved to be effective in the preparation of the AuNR for the adsorption of MG and its subsequent removal, the technique did not prove effective in the complete removal of MBA. There was always some evidence, albeit, substantially reduced in intensity, of the MBA SERS spectrum present. The subsequent reapplication of MBA gave a similar signal intensity to that obtained prior to initiating the cleaning procedure.

Another method tried was that of immersion in piranha solution, a strong oxidising agent that is commonly used to remove organic molecules from gold substrates. However when attempted, this resulted in the destruction of the AuNR sample. It was therefore decided to explore electrochemical cleaning in order to attempt to totally remove the MBA from the AuNR surface and allow for the application of a different analyte.

Electrochemical cleaning was employed to reductively remove adsorbed species from AuNR using a 0.5 M HNO_3 electrolyte. Here the clear advantage of the use of the flow cell for this purpose is seen as *in-situ* monitoring with SE(R)RS could be carried out to follow the process. The flow cell was thus used to enable surface regeneration and the subsequent re-application of the chosen analytes. A picture of the 4-dot AuNR sample that acted as the working electrode,

attached to the base of the flow cell with silver conducting paint, is shown in Figure 6.13 and a schematic representation of which was shown in Figure 5.13.

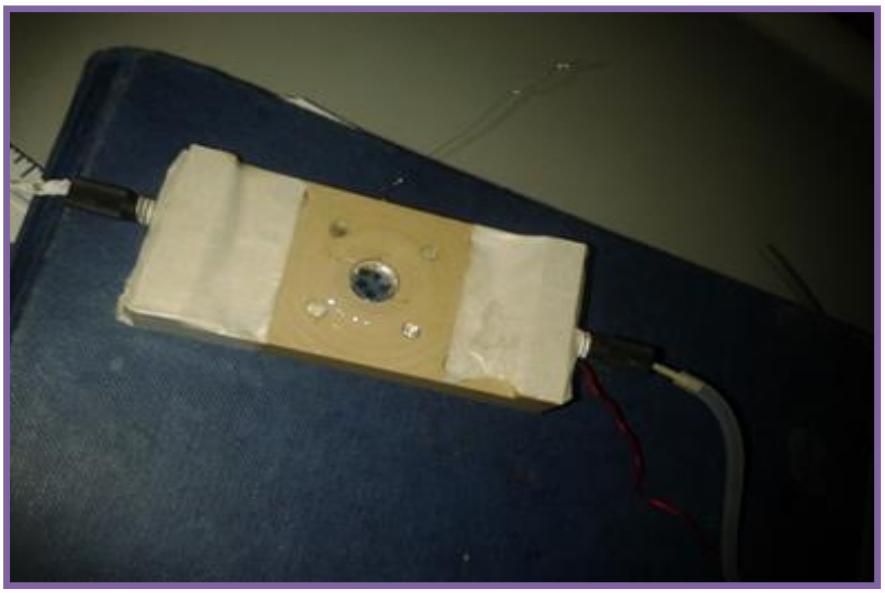

Figure 6.13 *The specially designed flow cell for use with the AuNR samples in this instance with the 4-dot sample and set up for data acquisition.*

The solution was pumped into the main body of the cell (volume 1 mL) using a peristaltic pump. Electrical connections to the nanorod array working electrode and to the Pt wire counter/ pseudo-reference electrode allowed electrochemical polarisation of the nanorods to be carried out during SE(R)RS measurements using a potentiostat. The flow cell and tubing were cleaned prior to use by pumping through either a 10 vol% HNO_3 solution or 20 vol% *aqua regia* solution. The resultant SERRS signal from the MG adsorbed onto the AuNR surface could be removed by the application of a voltage of – 0.5 V in an aqueous solution of 0.5 M HNO_3. As Figure 6.14 shows, the signal intensity decreased with increasing duration of the applied voltage and was virtually gone after 15 minutes. More importantly though, it showed that the process did not damage the functionality of the AuNR surface with the subsequent re-adsorption of MG again giving a strong SERRS response.

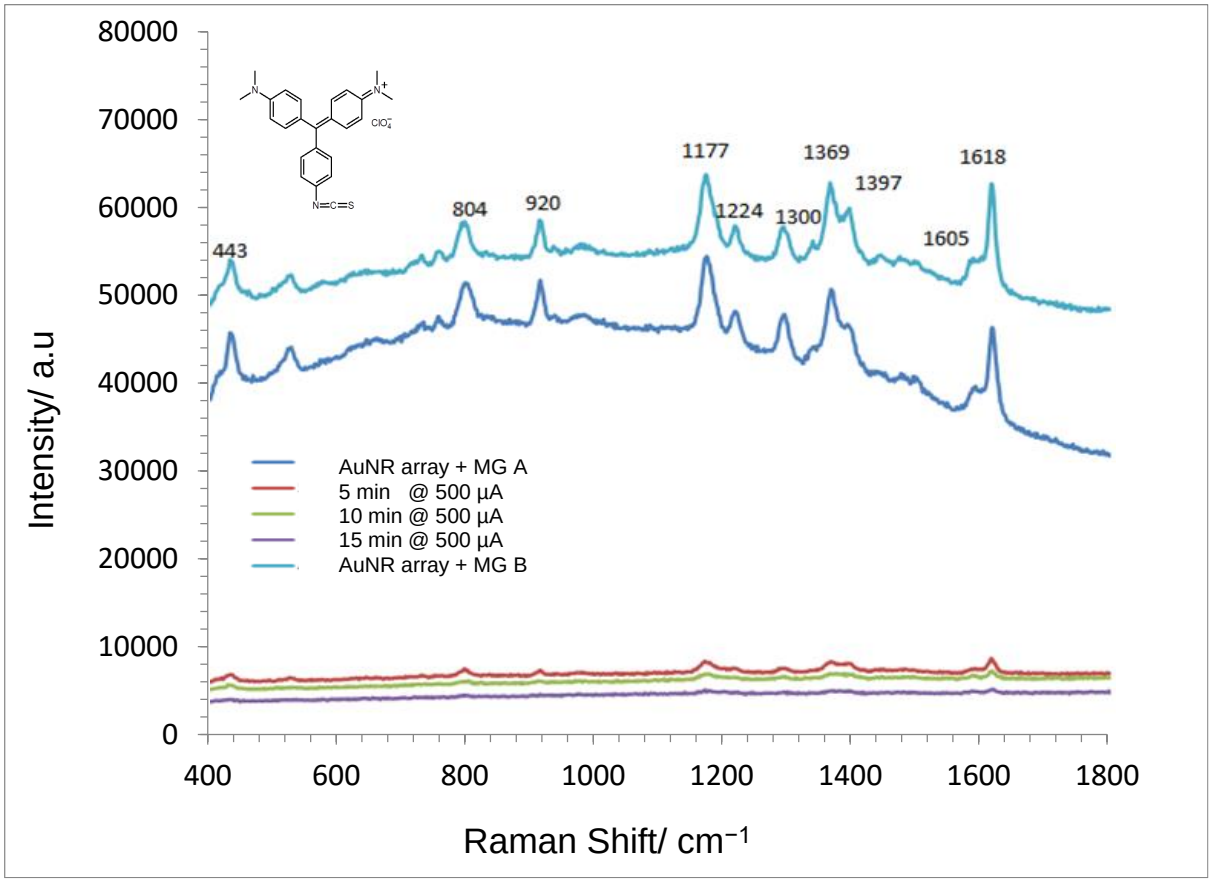

Figure 6.14 *In-situ SERRS spectra recorded after the application of an applied current of 500 µA at ocp for 5, 10 and 15 minute duration. Where* ***A*** *is spectra obtained from the original surface and* ***B*** *is for the spectra of MG re-adsorbed after surface cleaning (spectra vertically offset for clarity).*

A series of SE(R)RS spectra depicting measurements carried out on a multianalyte surface are shown in Figure 6.15. The sample contained four AuNR regions: one containing adsorbed MG, another with MBA and the remaining two being blank, as control. The measurements were carried out first with the adsorbed selected molecules, and then again after applying the cleaning procedure. The cleaning procedure entailed using a cathodic current of 1 mA for 10 min to the sample in the flow cell.

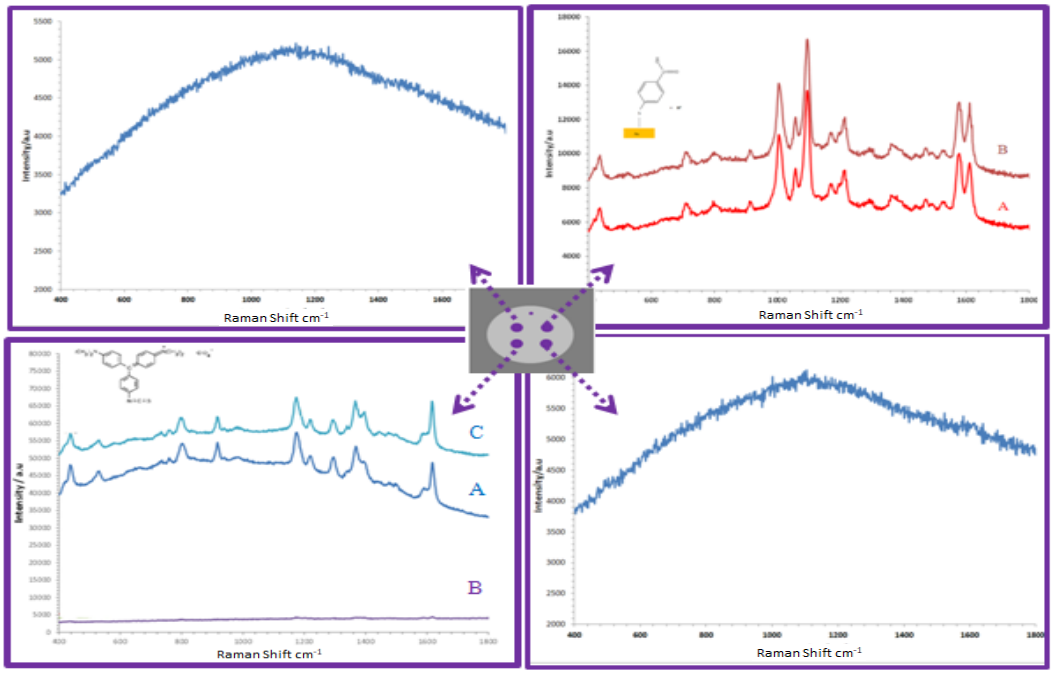

Figure 6.15 *SE(R)RS spectra from a 4-dot sample. Dot 1- MBA, Dot 2- Blank, Dot 3- MG, Dot 4- Blank. Where A = initial adsorbed species spectrum, B = spectrum obtained after an applied current of –1.0 mA for 10 minutes. C = spectrum for readsorbed species, (λ_{ex}= 633 nm, spectra have been vertically offset on B and C. N.B. Electrochemically bonded MBA was unable to be removed and the signal remains unaltered thoughout).*

As noted above, in the case of MG, the removal and subsequent reformation of the self-assembled monolayer (SAM) of MG could be successfully carried out, with no loss in the SE(R)RS signal when solution containing the MG was introduced back onto the AuNR surface. Thus, the electrochemical method was effective for MG removal and furthermore does not appear to damage the AuNR. However electrochemically bonded MBA could not be removed and the signal in this section of the sample remained undiminished. Although this was at first viewed as inconvenient, the resilience of MBA from electrochemical removal and persistence of the signal strength throughout could instead be viewed as advantageous by making MBA suitable for use as a reference marker in a multi-analyte sensors. Subsequently, it was found that soaking the samples in a 0.5 M sodium borohydride ($NaBH_4$) for 20 minutes was effective in removing MBA attached in the conventional way from the AuNR samples.

6.5 Chapter 6 Summary

In this chapter the production of patterned samples has been achieved with good uniformity in the SE(R)RS signal obtained within the patterned AuNR surface. This signifies that the patterned area was large enough to encompass the full laser spot directed at the sample surface. A methodology to selectively deposit different molecules onto the surface of a 4-dot AuNR sample was developed and successfully implemented. No cross-contamination between the various analytes tested was observed and reproducible SE(R)RS data were obtained. An electrochemical method was developed by which MBA was attached to the AuNR. This enabled a substantial reduction in the required period for attachment from several hours to several minutes. The resulting sulfur-to-gold bond formed provided a stronger signal to that of the conventional means of attachment. Several conventional cleaning methods employed to regenerate the substrates have been shown to be compatible for use with the AuNR samples.

7. Conclusions and Future Work

The aim of this work was to produce and utilise porous anodic aluminium oxide (AAO) templates with which to develop electroactive SERS substrates for use as multi targeted sensors.

This study has seen the development of such a substrate, gold nanorod arrays (AuNR) in a porous alumina film. Initially, interest was focussed on optimisation of the sample preparation in order to produce a substrate that gives signal enhancement consistently and repeatedly larger than currently obtained with alternative substrates. The AuNR were produced by *a.c.* electrodeposition of gold into the pores of a hexagonally ordered alumina film grown on an aluminium substrate using a two-stage anodisation process in oxalic acid followed by barrier layer thinning. Specular reflectance FTIR provided a new and rapid method of determining the porous film thickness. Rather than removing the rods from the template, as is common practice, here the template remained in place and was instead etched-back only as far as to expose the rods. Thus the template itself helped to support the rods which were several hundred nm in length. Keeping the aluminium base in place allowed for ease of handling whilst affording a degree of protection to the sample. In addition the aluminium base facilitated their use as an electrode in a liquid environment and so enabling electrochemical polarisation studies to be performed. For this purpose a specially designed flow cell was produced.

In terms of the sample preparation, the use of a mechanical polisher helped produced flatter, smoother sample surfaces which in turn helped to encourage parallel pore growth. Bubble formation on the sample surface which can result in pitting and affect ordered pore formation was reduced during the electropolishing procedure through the use of RDE to control the convective flow to the electropolishing surface. The alumina porous film thickness was determined by the duration of the second anodisation period and this was verified by both ellipsometry and FTIR. The film thickness was accurately determined by modelling the ellipsometric data of the second anodisation period. It was also determined that FTIR instrumentation could be used as a quick method to determine film thickness using the bayerite peak at 955 cm^{-1}. *In-situ* monitoring of the barrier layer thinning process by ellipsometry revealed that film growth continued at a substantial rate even as the applied cell voltage was

reduced from 40 V to 24 V. However below the latter voltage, film growth slowed dramatically with little further growth observed between 24 V and 6.5 V.

FE-SEM imaging showed that the surface of the individual nanorods to be rough and sharp edged which should prove to be beneficial with regards to increasing SERS enhancement. The width of the rods was found to be ~20 nm with the distance between each ~40 nm. However, it was not possible to determine the length of the rods since they remained anchored to the bottom of the pores. Consequently, it was not possible to calculate the aspect ratio of the rods. This problem must be resolved in future work as the aspect ratio together with the spacing between the rods is key to the properties and behaviour exhibited by the gold nanorod arrays.

The attachment of reporter molecules to the rods revealed them to be ideal substrates for SE(R)RS analysis as these adsorbed molecular species, under illumination by an excitation laser beam, were subjected to an intense electric field brought about by localised surface plasmon resonance (LSPR). The excellent enhancement obtained for SERRS using MG at 1% laser intensity has proved very encouraging. Polymer growth onto the gold nanorod arrays by cyclic voltammetry was also successful. However, the SERS results obtained for polythiophene indicated that this was an area that required a great deal more work in order to be able to utilise this technique to follow the changes in the polythiophene layer as it underwent redox cycling.

The production of patterned samples has been achieved with good uniformity of SE(R)RS signal obtained within the patterned AuNR surface. Selective deposition of different molecules onto the surface of a 4-dot AuNR sample was achieved and with no evidence of cross-contamination between the various analytes tested. Again here, reproducible SE(R)RS data was obtained.

An electrochemical method was developed by which MBA was attached to the AuNR. This enabled a substantial reduction in the required period for attachment from several hours of exposure to the MBA solution to just minutes. Finally, several conventional cleaning methods have been found to be suitable for use in analyte removal and surface regeneration.

In terms of the future direction of this research, a number of paths are available to be explored. The major priority would be to extend the examination of more electro-active species combined with *in-situ* monitoring and really highlight the advantages of the developed platform. Being

able to monitor molecular reactions in real-time under an applied electrochemical field has potential applications in a variety of systems e.g. catalysis, enegy *etc* where a highly controlled surface morphology is desirable.

Advanced studies could also be achieved by the controlled electrodeposition of other polymer and metal species. This could be performed on top of the AuNR's or create an entirely different substrate. For example, co-depositing platinum or palladium may be interesting for SERS and catalysis studies. Also, semiconductor (SC) nanostructures or hybrid plasmonic/SC systems are also of increasing interest. Further optical characterisation of the AuNR at much longer wavelengths in the IR is also desirable to investigate the longitudinal plasmon resonances that potentially exist as the studies in this thesis were mostly restricted to the transverse mode as the electrodeposition method prevents suitably short length rods to be created.

Improvements could also be carried out in the AAO template process such as reducing the time required to produce the template, focusing for example on the purity of the electrolyte, in particular, the absence of Cl^- and the pH of the solution. Also, the nanorod array template can be applied to other optical techniques in addition to SERS. For example, another area which has not yet been touched on is that of surface enhanced fluorescence (SEF) involving controlled spacing between chromophores and the metal surface. The SERS background signals did suggest a certain amount of intrinsic fluorescence from the AuNR/AAO template and this needs to be understood better alongside exploring different excitation wavelengths and surface chemistries for chromophore attachment.

Finally, *in-situ* studies should certainly make greater use of the purpose-built flow cell that a lot of effort was spent in designing. This approach could also be combined with other optical techniques such as dark-field and SEF simultaneously on the same electrode surface.

Appendix 1

Chemical reagent list

Chemical reagent	Details	Supplier
Aluminium sheeting	99.999%	Goodfellow
20 nm Gold Nanoparticles in citrate buffer	HAuCl:NaCit I mM: 353 mM	University of Strathclyde
Oxalic acid	$C_2H_2O_4$ ≥ 99+ % purity MW= 126.07 g mol^{-1}	Sigma Aldrich
Oxalic acid	$C_2H_2O_4$ ≥ 99.999 % purity MW= 126.07 g mol^{-1}	Sigma Aldrich
Chromium (VI) oxide	CrO_3 ≥ 98 % purity MW= 99.99 g mol^{-1}	Sigma Aldrich
Gold (I) potassium cyanide	$AuK(CN)_2$ ≥ 99.99 % purity MW= 288.1 g mol^{-1}	Alfa Aesar
Thiophene	C_4H_4S ≥ 99% MW= 84.14 g mol^{-1}	Sigma-Aldrich.
Malachite green isothiocyanate	$C_{24}H_{24}ClN_3O_4S$ ≥ 95% MW= 485.98 g mol^{-1}	Invitrogen
Ortho-phosphoric Acid	H_3PO_4 ≥ MW= 98 g mol^{-1}	Fisher Chemicals
Tartaric acid	CHOH COOH ≥ 99.5 % purity MW= 150.09	Sigma-Aldrich
Hydrochloric Acid	HCl 36.5% MW= 36.46 g mol^{-1}	Sigma Aldrich
Nitric Acid	HNO_3 MW= .01 g mol^{-1}	Sigma Aldrich
Sulfuric Acid	H_2SO_4 MW= 98.08 g mol^{-1}	Sigma Aldrich
Hydrogen Peroxide	H_2O_2 30 % MW= 34.01 g mol^{-1}	Sigma aldrich
Methanol	CH_4O ≥ 99.7 % MW= 32.04 g mol^{-1}	Sigma-Aldrich.
Iso-Propanol (2-Propanol)	C_3H_8O ≥ 99.5 % purity MW= 60.03	Sigma-Aldrich.

Acetone	C_3H_6O ≥ 99 % purity MW= 58.03 g mol^{-1}	Sigma-Aldrich.
Deionised water	Resistivity 18.2 MΩ cm	Milli-Q
Ethanol	C_2H_6O ≥ 99.8 % MW= 46.07 g mol^{-1}	Sigma-Aldrich.
Alumina polishing powder	1.0 μm & 0.3 μm Al_2O_3	Buehler
Polishing cloth	10’ microcloth PSA ≥ 99.99 % purity	Buehler
Sodium borohydride	$NaBH_4$ ≥ 98% purity MW= 37.83 g mol^{-1}	Sigma Aldrich
Tetrabutylammonium hexafluorophosphate	$(CH_3CH_2CH_2CH_2)_4N(PF_6)$ ≥ 99.0% purity MW= 387.43 g mol^{-1}	Sigma Aldrich
Poly(diallyldimethylammonium chloride) solution	$(C_8H_{16}NCl)_n$ MW= 174.26 g mol^{-1}≥ 99.99 % purity	Sigma Aldrich
Potassium Sulphate	K_2SO_4 MW= 174.26 g mol^{-1} 99.99 % purity	Sigma Aldrich
Sodium Chloride	NaCl MW=58.44 g mol^{-1} ≥ 98 % purity	Sigma Aldrich
Ammonium Solution	NH_3 MW=17.037 N in MeOH	Sigma Aldrich
Copper Nitrate	$Cu(NO_3)_2 \cdot xH_2O$ MW =187.56 g mol^{-1} ≥ 99.99 % purity	Sigma Aldrich
NIR797 isothiocyanate	$C_{45}H_{50}N_3NaO_6S_4$ MW 880.14 g ≥70% (coupling to amines)	Sigma Aldrich
NQ	Campbell Group	University of Edinburgh

References

1 D. Decoster and J. Harari, *Optoelectronic Sensors*, ISTE, London, UK, 2009.
2 J. R. Stetter, W. R. Penrose and S. Yao, *J. Electrochem. Soc.*, 2003, **150**, 11–16.
3 A. Hulanicki, S. Glab and F. Ingman, *Pure Appl. Chem.*, 1991, **63**, 1247–1250.
4 C. Gnoth and S. Johnson, *Geburtshilfe Frauenheilkd.*, 2014, **74**, 661–669.
5 A. Melesse, Q. Weng, S. Prasad and G. Senay, *Sensors*, 2007, **7**, 3209–3241.
6 D. D. Lee, *IEEE Sens. J.*, 2001, **1**, 214–224.
7 M. Bacci, C. Cucci, A. A. Mencaglia and A. G. Mignani, *Sensors*, 2008, **8**, 1984–2005.
8 L. Wang, W. Ma, L. Xu, W. Chen, Y. Zhu, C. Xu and N. A. Kotov, *Mater. Sci. Eng. R Reports*, 2010, **70**, 265–274.
9 K. W. Jones, *Sensors A Compr. Surv.*, 2008, **8**, 451–489.
10 W. a Alto, D. Meyer, J. Schneid, P. Bryson and J. Kindig, *J. Am. Board Fam. Pract.*, 1997, **15**, 1–6.
11 J. W. Severinghaus and P. B. Astrup, *J. Clin. Monit.*, 1986, 2, 125–139.
12 A. X. Wang and X. Kong, *Materials (Basel).*, 2015, 8, 3024–3052.
13 B. Sharma, R. R. Frontiera, A.-I. Henry, E. Ringe and R. P. Van Duyne, *Mater. Today*, 2012, **15**, 16–25.
14 K. R. Pirota, D. Navas, M. Hernández-Vélez, K. Nielsch and M. Vázquez, *J. Alloys Compd.*, 2004, **369**, 18–26.
15 Norio Taniguchi, *Nanotechnology*, Oxford University Press, 1996.
16 W. A. James F. Shackelford, *CRC Materials Science and Engineering Handbook eBook: James F. Shackelford, William Alexander: CRP Press, 4th Edition 2015:*, .
17 J. Zaanen, G. A. Sawatzky and J. W. Allen, *Phys. Rev. Lett.*, 1985, **55**, 418–421.
18 W. A. James F. Shackelford, *CRC Materials Science and Engineering Handbook*, Third Edition CRC Press LLC, 2001.
19 R. Levy, Principles of Solid State Physics, Elsevier 2014 pp 317-376
20 S. Kasap, *Optoelectronics and photonics : principles and practices*, Pearson, 2013.
21 S. B. Dugdale, *Phys. Scr.*, 2016, **91**, 053009.
22 F. Scholz, *Electroanalytical methods: Guide to experiments and applications*, 2010.
23 Turley. J, *Choice Rev. Online*, 2013, **38**, 38-3372-38–3372.
24 T. N. Corles, *Gold. The chemistry behind the precious metal: Gold's chemical properties (Facts, properties, and use of precious metals)*, 2017.
25 R. Sardar, A. M. Funston, P. Mulvaney and R. W. Murray, *Langmuir*, 2009, **25**, 13840–13851.
26 O. Benson, in *Elements of Nanophotonics*, 2009, pp. 208–239.
27 Z. Liang, J. Sun, Y. Jiang, L. Jiang and X. Chen, *Plasmonics*, 2014, 9, 859–866.
28 A. Magrez, J. W. Seo, R. Smajda, M. Mionić and L. Forró, *Materials (Basel).*, 2010, 3, 4871–4891.
29 L. Guo, J. A. Jackman, H. H. Yang, P. Chen, N. J. Cho and D. H. Kim, *Nano Today*, 2015, 10, 213–239.
30 A. Moores and F. Goettmann, *New J. Chem.*, 2006, 30, 1121–1132.
31 K. A. Willets and R. P. Van Duyne, *Annu. Rev. Phys. Chem.*, 2007, **58**, 267–297.
32 K. A. Willets and R. P. Van Duyne, *Annu. Rev. Phys. Chem.*, 2007, **58**, 267–297.
33 A. V. Zayats, I. I. Smolyaninov and A. A. Maradudin, *Phys. Rep.*, 2005, 408, 131–314.
34 P. J. Poole, D. Dalacu, J. Lefebvre and R. L. Williams, *Nanotechnology*, 2010, **21**, 295302.
35 J. Turkevich, P. C. Stevenson and J. Hillier, *Discuss. Faraday Soc.*, 1951, **11**, 55.
36 W. Haiss, N. T. K. Thanh, J. Aveyard and D. G. Fernig, *Anal. Chem.*, 2007, **79**, 4215–4221.
37 B. D. Chithrani, A. A. Ghazani and W. C. W. Chan, *Nano Lett.*, 2006, **6**, 662–668.
38 A. Gole and C. J. Murphy, *Chem. Mater.*, 2004, **16**, 3633–3640.
39 S. Cintra, M. E. Abdelsalam, P. N. Bartlett, J. J. Baumberg, T. A. Kelf, Y. Sugawara and A. E. Russell, *Faraday Discuss.*, 2006, **132**, 191–199.
40 C. F. Landes, S. Link, M. B. Mohamed, B. Nikoobakht and M. a. El-Sayed, *Pure Appl. Chem.*, 2002, **74**, 1675–1692.
41 L. Gou and C. J. Murphy, *Chem. Mater.*, 2005, **17**, 3668–3672.
42 S. K. Kang, S. Chah, C. Y. Yun and J. Yi, *Korean J. Chem. Eng.*, 2003, **20**, 1145–1148.
43 J. Becker, A. Trügler, A. Jakab, U. Hohenester and C. Sönnichsen, *Plasmonics*, 2010, **5**, 161–167.
44 F. Kim, J. H. Song and P. Yang, *J. Am. Chem. Soc.*, 2002, **124**, 14316–14317.
45 H. Chen, L. Shao, Q. Li and J. Wang, *Chem. Soc. Rev.*, 2013, **42**, 2679–2724.
46 B. S. Yin, Y. F. Huang, C. Y. Li and Z. Q. Tian, in *NEMS 2011 - 6th IEEE International Conference on*

Nano/Micro Engineered and Molecular Systems, 2011, pp. 868–872.
47 T. Pham, J. B. Jackson, N. J. Halas and T. R. Lee, *Langmuir*, 2002, **18**, 4915–4920.
48 D. Graham, K. Faulds, D. Thompson, F. McKenzie, R. Stokes, C. Dalton, R. Stevenson, J. Alexander, P. Garside and E. McFarlane, *Biochem. Soc. Trans.*, 2009, **37**, 697–701.
49 A. P. Herrera, O. Resto, J. G. Briano and C. Rinaldi, *Nanotechnology*, 2005, **16**, S618–S625.
50 A. D. Wiesner, L. E. Katz and C. C. Chen, *J. Colloid Interface Sci.*, , DOI:10.1016/j.jcis.2006.05.011.
51 T. H. Kim, J. A. I. Acapulco, S. Hong, S. Lee and S. Park, *Bull. Korean Chem. Soc.*, 2015, **36**, 815–821.
52 M. A. El-Sayed, *Acc. Chem. Res.*, 2001, **34**, 257–264.
53 T. Moore, *Robotica*, 1998, **16**, 703–703.
54 A. Smekal, *Naturwissenschaften*, 1923, **11**, 873–875.
55 C. V. Raman and J. R. Nielsen, *Science*, 1929, **69**, 267–275.
56 R. Singh, *Phys. perspect.*, 2002, **4**, 399–420.
57 W. L. Peticolas, *Annu. Rev. Phys. Chem.*, 1972, **23**, 93–116.
58 Y. Ozaki and S. Sasic, in *Pharmaceutical Applications of Raman Spectroscopy*, John Wiley & Sons, Inc., Hoboken, NJ, USA, 2007, pp. 1–28.
59 H. Herrmann and H. Bucksch, in *Dictionary Geotechnical Engineering/Wörterbuch GeoTechnik*, 2014.
60 X. Liu, in *Zeolite Chemistry and Catalysis*, Springer Netherlands, Dordrecht, 2009, pp. 197–222.
61 P. Bartlett, K. J. Voss, S. Sathyendranath and A. Vodacek, *Appl. Opt.*, 1998, **37**, 3324.
62 E. Smith and G. Dent, *Modern Raman Spectroscopy - A Practical Approach*, John Wiley & Sons, Ltd, Chichester, UK, 2004.
63 R. S. Das and Y. K. Agrawal, *Vib. Spectrosc.*, 2011, **57**, 163–176.
64 K. Kneipp, M. Moskovits and H. Kneipp, *Surface-enhanced raman scattering physics and applications*, 2006, vol. 103.
65 H. Ko, S. Singamaneni and V. V. Tsukruk, *Small*, 2008, 4, 1576–1599.
66 D. A. Watson, L. O. Brown, D. F. Gaskill, M. Naivar, S. W. Graves, S. K. Doorn and J. P. Nolan, *Cytom. Part A*, 2008, **73**, 119–128.
67 M. Moskovits, *Rev. Mod. Phys.*, 1985, **57**, 783–826.
68 B. Sharma, M. Fernanda Cardinal, S. L. Kleinman, N. G. Greeneltch, R. R. Frontiera, M. G. Blaber, G. C. Schatz and R. P. Van Duyne, *MRS Bull.*, 2013, **38**, 615–624.
69 J. He, H. Zhou, F. Wan, Y. Lu and G. Xue, *Vib. Spectrosc.*, 2003, **31**, 265–269.
70 E. C. Le Ru, E. Blackie, M. Meyer and P. G. Etchegoin, *J. Phys. Chem. C*, 2007, **111**, 13794–13803.
71 D. Wei, S. Chen and Q. Liu, *Appl. Spectrosc. Rev.*, 2015, **50**, 387–406.
72 G. McNay, D. Eustace, W. E. Smith, K. Faulds and D. Graham, *Appl. Spectrosc.*, 2011, 65, 825–837.
73 S.-R. Nie, S. and Emory, *Science (80-.).*, 1997, **275**, 1102–1106.
74 M. D. Morris and D. J. Wallan, *Anal. Chem.*, 1979, **51**, 182A-192A.
75 M.-R. Guo, H.-X. Cai, G. Chen, Y. Fan and X.-H. Zhang, *Guang Pu Xue Yu Guang Pu Fen Xi*, 2011, **31**, 1541–1544.
76 M. Fleischmann, P. J. Hendra and A. J. McQuillan, *Chem. Phys. Lett.*, 1974, **26**, 163–166.
77 X. P. Gao, Y. Zhang and M. J. Weaver, *Langmuir*, 1992, **8**, 668–672.
78 D. Myers, *Surfaces, Interfaces, and Colloids*, John Wiley & Sons, Inc., New York, USA, 1999, vol. 4.
79 R. MacKenzie, C. Fraschina, T. Sannomiya, V. Auzelyte and J. Vörös, *Sensors (Basel).*, 2010, **10**, 9808–9830.
80 K. M. Byun, S. J. Kim and D. Kim, *Appl. Opt.*, 2006, **45**, 3382–9.
81 J. F. Betz, W. W. Yu, Y. Cheng, I. M. White and G. W. Rubloff, *Phys. Chem. Chem. Phys.*, 2014, **16**, 2224–2239.
82 T. Härtling, Y. Alaverdyan, M. T. Wenzel, R. Kullock, M. Käll and L. M. Eng, *J. Phys. Chem. C*, 2008, **112**, 4920–4924.
83 L. J. Guo, *Adv. Mater.*, 2007, **19**, 495–513.
84 R. K. Watts, in *Very Large Scale Integration (VLSI)*, Springer Berlin Heidelberg, Berlin, Heidelberg, 1982, pp. 42–88.
85 S. M. Oja, Y. Fan, C. M. Armstrong, P. Defnet and B. Zhang, *Anal. Chem.*, 2016, 88, 414–430.
86 C. Eschenbaum, D. Großmann, K. Dopf, S. Kettlitz, T. Bocksrocker, S. Valouch and U. Lemmer, *Opt. Express*, 2013, **21**, 29921.
87 W. Zaghdoudi, A. Bardaoui, N. Khalifa and R. Chtourou, *Superlattices Microstruct.*, 2013, **53**, 204–212.
88 A. Heuberger, *Microelectron. Eng.*, 1986, **5**, 3–38.
89 C. D. Sheraw, L. Zhou, J. R. Huang, D. J. Gundlach, T. N. Jackson, M. G. Kane, I. G. Hill, M. S. Hammond, J. Campi, B. K. Greening, J. Francl and J. West, *Appl. Phys. Lett.*, 2002, **80**, 1088–1090.
90 M. Kahl, E. Voges and W. Hill, *Spectrosc. Eur.*, 1998, **10**, 8–13.

91 K. Gamo, *Nucl. Instruments Methods Phys. Res. Sect. B Beam Interact. with Mater. Atoms*, 1992, **65**, 40–49.
92 Z. Huang, G. Cao, Y. Sun, S. Du, Y. Li, S. Feng, J. Lin and J. Lei, *J. Nanomater.*, 2017, **2017**, 1–8.
93 N. Haberkorn, S. A. L. Weber, R. Berger and P. Theato, *ACS Appl. Mater. Interfaces*, 2010, **2**, 1573–1580.
94 H. Puliyalil and U. Cvelbar, *Nanomaterials*, 2016, **6**, 108.
95 F. Hua, J. Shi, Y. Lvov and T. Cui, *Nano Lett.*, 2002, **2**, 1219–1222.
96 W. M. Choi and O. O. Park, *Nanotechnology*, 2004, **15**, 1767–1770.
97 Y. Hu, Z. Lao, B. P. Cumming, D. Wu, J. Li, H. Liang, J. Chu, W. Huang and M. Gu, *Proc. Natl. Acad. Sci.*, 2015, **112**, 6876–6881.
98 T. Kim, K. Lee, M. S. Gong and S. W. Joo, *Langmuir*, 2005, **21**, 9524–9528.
99 E. Pensa, E. Cortés, G. Corthey, P. Carro, C. Vericat, M. H. Fonticelli, G. Benítez, A. A. Rubert and R. C. Salvarezza, *Acc. Chem. Res.*, 2012, **45**, 1183–1192.
100 M. Moskovits, *J. Raman Spectrosc.*, 2005, **36**, 485–496.
101 K. Raiber, A. Terfort, C. Benndorf, N. Krings and H. H. Strehblow, *Surf. Sci.*, 2005, **595**, 56–63.
102 A. Kamińska, I. Dzięcielewski, J. L. Weyher, J. Waluk, S. Gawinkowski, V. Sashuk, M. Fiałkowski, M. Sawicka, T. Suski, S. Porowski and R. Hołyst, *J. Mater. Chem.*, 2011, **21**, 8662.
103 E. Stern, G. Cheng, E. Cimpoiasu, R. Klie, S. Guthrie, J. Klemic, I. Kretzschmar, E. Steinlauf, D. Turner-Evans, E. Broomfield, J. Hyland, R. Koudelka, T. Boone, M. Young, a Sanders, R. Munden, T. Lee, D. Routenberg and M. a Reed, *Nanotechnology*, 2005, **16**, 2941–2953.
104 H. Masuda, T. Yanagishita, K. Yasui, K. Nishio, I. Yagi, T. N. Rao and A. Fujishima, *Adv. Mater.*, 2001, **13**, 247–249.
105 J. N. Anker, W. P. Hall, O. Lyandres, N. C. Shah, J. Zhao and R. P. Van Duyne, *Nat. Mater.*, 2008, **7**, 442–453.
106 A. W. Wark, R. J. Stokes, S. B. Darby, W. E. Smith and D. Graham, *J. Phys. Chem. C*, 2010, **114**, 18115–18120.
107 S. Śanchez-Cortés and J. V. Garcia-Ramos, *J. Raman Spectrosc.*, 1992, **23**, 61–66.
108 W. Li, X. Zhao, Z. Yi, A. M. Glushenkov and L. Kong, *Anal. Chim. Acta*, 2017, **984**, 19–41.
109 E. C. Le Ru and P. G. Etchegoin, in *Principles of Surface-Enhanced Raman Spectroscopy*, Elsevier, 2009, pp. 185–264.
110 Y. Yang, S. Matsubara, L. Xiong, T. Hayakawa and M. Nogami, *J. Phys. Chem. C*, 2007, **111**, 9095–9104.
111 H. Kim, K. M. Kosuda, R. P. Van Duyne and P. C. Stair, *Chem. Soc. Rev.*, 2010, **39**, 4820–44.
112 K. Kneipp, M. Moskovits and H. Kneipp, *Surface-Enhanced Raman Scattering*, 2006.
113 Y. Ozaki, K. Kneipp and R. Aroca, *Frontiers of surface-enhanced raman scattering : single-nanoparticles and single cells*, Wiley Blackwell , 2014.
114 V. Flauraud, M. Mastrangeli, G. D. Bernasconi, J. Butet, D. T. L. Alexander, E. Shahrabi, O. J. F. Martin and J. Brugger, *Nat. Nanotechnol.*, 2017, **12**, 73–80.
115 C. Vericat, M. E. Vela, G. Benitez, P. Carro and R. C. Salvarezza, *Chem. Soc. Rev.*, 2010, **39**, 1805.
116 C. J. Orendorff, A. Gole, T. K. Sau and C. J. Murphy, *Anal. Chem.*, 2005, **77**, 3261–3266.
117 I. Uechi and S. Yamada, *Anal. Bioanal. Chem.*, 2008, 391, 2411–2421.
118 X. Zhou, N. Zhang, K. Y. Liu, C. Tan and W. Knoll, *J. Nanoparticle Res.*, 2009, **11**, 2061–2069.
119 S. Habouti, M. Matefi-Tempfli, C.-H. Solterbeck, M. Es-Souni, S. Matefi-Tempfli and M. Es-Souni, *J. Mater. Chem.*, 2011, **21**, 6269–6273.
120 F. Zacharatos, V. Gianneta and A. G. Nassiopoulou, *Nanotechnology*, 2008, **19**, 495306.
121 C. A. R. Auchinvole, P. Richardson, C. McGuinnes, V. Mallikarjun, K. Donaldson, H. McNab and C. J. Campbell, *ACS Nano*, 2012, **6**, 888–896.
122 A. B. Taylor, P. Michaux, A. S. M. Mohsin and J. W. M. Chon, *Opt. Express*, 2014, **22**, 13234–43.
123 T. Ding, D. O. Sigle, L. O. Herrmann, D. Wolverson and J. J. Baumberg, *ACS Appl. Mater. Interfaces*, 2014, **6**, 17358–17363.
124 P. Candeloro, E. Iuele, G. Perozziello, M. L. Coluccio, F. Gentile, N. Malara, V. Mollace and E. Di Fabrizio, *Microelectron. Eng.*, 2017, **175**, 30–33.
125 Renishaw Diagnostics, Klarite SERS substrate from Renishaw Diagnostics helps EU Photosens project teamRenisg, https://www.renishaw.com, accessed 12-04-11 .
126 A.Gopinath, S.V Boriskina, B.M Reinhard, L. Dal Negro. Optics Express, 2009, **17**: 3741-3753.
127 B. G. McMillan, Ĺ. E. A. Berlouis, F. R. Cruickshank, D. Pugh and P. F. Brevet, *Appl. Phys. Lett.*, 2005, **86**, 1–3.
128 B. Ding, H. Wu, W. Xu, Z. Zhao, Y. Liu, H. Yu and H. Yan, *Nano Lett.*, 2010, **10**, 5065–5069.

129 J. D. Driskell, S. Shanmukh, Y. Liu, S. B. Chaney, X. J. Tang, Y. P. Zhao and R. A. Dluhy, *J. Phys. Chem. C*, 2008, **112**, 895–901.
130 W. W. Yu and I. M. White, *Anal. Chem.*, 2010, **82**, 9626–9630.
131 K. Jung, J. Hahn, S. In, Y. Bae, H. Lee, P. V. Pikhitsa, K. Ahn, K. Ha, J. K. Lee, N. Park and M. Choi, *Adv. Mater.*, 2014, **26**, 5924–5929.
132 M. S. Schmidt, J. Hübner and A. Boisen, *Adv. Mater.*, 2012, **24**, OP11–OP18.
133 Z. Q. Tian, *J. Raman Spectrosc.*, 2005, **36**, 466–470.
134 L. Cui, S. Mahajan, R. M. Cole, B. Soares, P. N. Bartlett, J. J. Baumberg, I. P. Hayward, B. Ren, a E. Russell and Z. Q. Tian, *Phys. Chem. Chem. Phys.*, 2009, **11**, 1023–6.
135 M. C. Kum, B. Y. Yoo, Y. W. Rheem, K. N. Bozhilov, W. Chen, A. Mulchandani and N. V Myung, *Nanotechnology*, 2008, **19**, 325711.
136 J. Lee, J. Choi, J. Lee, S. K. Choi and H. D. Chun, *Nanotechnology*, 2005, **16**, 1449–1453.
137 Z.-L. Yang, Q.-H. Li, B. Ren and Z.-Q. Tian, *Chem. Commun.*, 2011, **47**, 3909.
138 M. Schierhorn, S. J. Lee, S. W. Boettcher, G. D. Stucky and M. Moskovits, *Adv. Mater.*, 2006, **18**, 2829–2832.
139 J. Martin and J. Plain, *J. Phys. D. Appl. Phys.*, 2015, **48**, 184002.
140 E. Petryayeva and U. J. Krull, *Anal. Chim. Acta*, 2011, 706, 8–24.
141 W. Plieth, *Electrochemistry for Materials Science*, Elsevier, 2008.
142 X. Y. Zhang, L. D. Zhang, W. Chen, G. W. Meng, M. J. Zheng, L. X. Zhao and F. Phillipp, *Chem. Mater.*, 2001, **13**, 2511–2515.
143 X. M. Qian and S. M. Nie, *Chem. Soc. Rev.*, 2008, **37**, 912–920.
144 L. Meng, Q. Xu, S. Fan, C. R. Dick and X. Wang, *Appl. Phys. Lett.*, 2017, **111**, 183103.
145 K. Balasubramanian and M. Burghard, *Small*, 2005, **1**, 180–92.
146 G. S. Bumbrah and R. M. Sharma, *Egypt. J. Forensic Sci.*, 2016, **6**, 209–215.
147 P. Ghosh, G. Han, M. De, C. K. Kim and V. M. Rotello, *Adv. Drug Deliv. Rev.*, 2008, 60, 1307–1315.
148 E. Delamarche, B. Michel, H. A. Biebuyck and C. Gerber, *Adv. Mater. (Weinheim, Ger.*, 1996, **8**, 719–729.
149 D. L. Jeanmaire and R. P. Van Duyne, *J. Electroanal. Chem.*, 1977, **84**, 1–20.
150 Q. Hu, L.-L. Tay, M. Noestheden and J. P. Pezacki, *J. Am. Chem. Soc.*, 2007, **129**, 14–15.
151 S. A. Jadhav, *Cent. Eur. J. Chem.*, 2011, **9**, 369–378.
152 N. T. K. Thanh and L. A. W. Green, *Nano Today*, 2010, **5**, 213–230.
153 E. Pensa, E. Cortés, G. Corthey, P. Carro, C. Vericat, M. H. Fonticelli, G. Benítez, A. A. Rubert and R. C. Salvarezza, *Acc. Chem. Res.*, 2012, **45**, 1183–1192.
154 H. Häkkinen, *Nat. Chem.*, 2012, **4**, 443–455.
155 S. Nath, S. Praharaj, S. Panigrahi, S. Kundu, S. K. Ghosh, S. Basu and T. Pal, *Colloids Surfaces A Physicochem. Eng. Asp.*, 2006, **274**, 145–149.
156 H. Bönnemann, G. Braun, W. Brijoux, R. Brinkmann, A. S. Tilling, K. Seevogel and K. Siepen, *J. Organomet. Chem.*, 1996, **520**, 143–162.
157 W. E. Doering, M. E. Piotti, M. J. Natan and R. G. Freeman, *Adv. Mater.*, 2007, **19**, 3100–3108.
158 M. Oliverio, S. Perotto, G. C. Messina, L. Lovato and F. De Angelis, *ACS Appl. Mater. Interfaces*, 2017, **9**, 29394.
159 M. A. Bedics, H. Kearns, J. M. Cox, S. Mabbott, F. Ali, N. C. Shand, K. Faulds, J. B. Benedict, D. Graham and M. R. Detty, *Chem. Sci.*, 2015, **6**, 2302–2306.
160 C. L. Zavaleta, B. R. Smith, I. Walton, W. Doering, G. Davis, B. Shojaei, M. J. Natan and S. S. Gambhir, *Proc. Natl. Acad. Sci.*, 2009, **106**, 13511–13516.
161 S. Laing, K. Gracie and K. Faulds, *Chem. Soc. Rev.*, 2016, **45**, 1901–1918.
162 S. Schlücker, *ChemPhysChem*, 2009, 10, 1344–1354.
163 L. Rodriguez-Lorenzo, L. Fabris and R. A. Alvarez-Puebla, *Anal. Chim. Acta*, 2012, **745**, 10–23.
164 K. C. Bantz, A. F. Meyer, N. J. Wittenberg, H. Im, O. Kurtuluş, S. H. Lee, N. C. Lindquist, S.-H. Oh and C. L. Haynes, *Phys. Chem. Chem. Phys.*, 2011, **13**, 11551–67.
165 D. Cam, K. Keseroglu, M. Kahraman, F. Sahin and M. Culha, *J. Raman Spectrosc.*, 2009, **41**, 484–489.
166 J. Homola, H. Vaisocherová, J. Dostálek and M. Piliarik, *Methods*, 2005, 37, 26–36.
167 M. V Yigit and Z. Medarova, *Am J Nucl Med Mol Imaging*, 2012, **2**, 232–241.
168 M. Kalia, *Metabolism*, 2015, **64**, S16–S21.
169 K. Faulds, W. E. Smith and D. Graham, *Analyst*, 2005, **130**, 1125–31.
170 M. Yang, Y. Liu and X. Jiang, *Chem. Soc. Rev.*, 2019, **48**, 850–884.
171 T. Li, W. Hu and D. Zhu, *Adv. Mater.*, 2010, **22**, 286–300.
172 L. Qin, S. Park, L. Huang and C. A. Mirkin, *Science (80-.).*, 2005, **309**, 113–115.

173 F. Meng, Y.-M. Hervault, Q. Shao, B. Hu, L. Norel, S. Rigaut and X. Chen, *Nat. Commun.*, 2014, **5**, 3023.
174 B. Zhao, J. Shen, S. Chen, D. Wang, F. Li, S. Mathur, S. Song and C. Fan, *Chem. Sci.*, 2014, **5**, 4460–4466.
175 N. R. Champness, *Dalt. Trans.*, 2011, **40**, 10311.
176 M. Ricci, C. Lofrumento, E. Castellucci and M. Becucci, *J. Spectrosc.*, 2016, **2016**, 1–10.
177 V. Polshettiwar and T. Asefa, *Nanocatalysis Synthesis and Applications*, John Wiley & Sons, Inc., Hoboken, NJ, USA, 2013.
178 R. Awual, M. Hasan and A. Shahat, *Sensors Actuators B. Chem.*, 2014, **203**, 854–863.
179 S. Tajima, *Electrochim. Acta*, 1977, **22**, 995–1011.
180 J. Yang, M. Palla, F. G. Bosco, T. Rindzevicius, T. S. Alstrøm, M. S. Schmidt, A. Boisen, J. Ju and Q. Lin, *ACS Nano*, 2013, **7**, 5350–5359.
181 R. D. Piner, J. Zhu, F. Xu, S. Hong and C. A. Mirkin, *Science (80-.).*, 1999, **283**, 661–663.
182 A. El Eter, T. Grosjean, P. Viktorovitch, X. Letartre, T. Benyattou and F. I. Baida, *Opt. Express*, 2014, **22**, 14464.
183 J. Nelayah, M. Kociak, O. Stéphan, F. J. García de Abajo, M. Tencé, L. Henrard, D. Taverna, I. Pastoriza-Santos, L. M. Liz-Marzán and C. Colliex, *Nat. Phys.*, 2007, **3**, 348–353.
184 E. E. Bedford, J. Spadavecchia, C. M. Pradier and F. X. Gu, *Macromol. Biosci.*, 2012, 12, 724–739.
185 H. Im, H. Shao, Y. Il Park, V. M. Peterson, C. M. Castro, R. Weissleder and H. Lee, *Nat. Biotechnol.*, 2014, **32**, 490–495.
186 P. C. Lee and D. Meisel, *J.Phys.Chem.*, 1982, **86**, 3391–3395.
187 J. D. Joannopoulos, S. G. Johnson, J. N. Winn, R. D. Meade and C. J. Sjödahl, *Photonic crystals: molding the flow of light*, Princeton University Press, 2nd Editio., 2011.
188 B. Platschek, A. Keilbach and T. Bein, *Adv. Mater.*, 2011, 23, 2395–2412.
189 L. Ma, J. Li, S. Zou and Z. Zhang, *Sensors*, 2017, **17**, 1895.
190 L. L. Schramm, in *Encyclopedia of Polymer Science and Technology*, John Wiley & Sons, Inc., Hoboken, NJ, USA, 2004, vol. 9.
191 P. L. Stiles, J. a Dieringer, N. C. Shah and R. P. Van Duyne, *Annu. Rev. Anal. Chem. (Palo Alto. Calif).*, 2008, **1**, 601–626.
192 T. Sueoka, J. Inukai and M. Ito, *J. Electron Spectros. Relat. Phenomena*, 1993, **64**–**65**, 363–370.
193 E. C. Le Ru, E. Blackie, M. Meyer and P. G. Etchegoin, *J. Phys. Chem. C*, 2007, **111**, 13794–13803.
194 T. T. Chuong, A. Pallaoro, C. A. Chaves, Z. Li, J. Lee, M. Eisenstein, G. D. Stucky, M. Moskovits and H. T. Soh, *Proc. Natl. Acad. Sci. U. S. A.*, 2017, **114**, 9056–9061.
195 C. Gourier-Fréry and N. Fréry, *EMC - Toxicol.*, 2004, 1, 79–95.
196 F. King, *Hist. Metall.*, 1985, **19**, 39–43.
197 P. J. Karditsas and M.-J. Baptiste, *Therm. Struct. Prop. Fusion Relat. Mater.*2012, **4** (26), 2-4
198 G. Thompson, Y. Xu and P. Skeldon, *Philos. Mag. Part B*, 1987, **55**, 651–667.
199 T. Campbell, R. K. Kalia, A. Nakano, P. Vashishta, S. Ogata and S. Rodgers, *Phys. Rev. Lett.*, 1999, **82**, 4866–4869.
200 H. P. Boehm, *Discuss. Faraday Soc.*, 1971, **52**, 264.
201 J. P. O'Sullivan and G. C. Wood, *Proc. R. Soc. A Math. Phys. Eng. Sci.*, 1970, **317**, 511–543.
202 J. W. W. Willstrop and H. Sutton, *Trans. IMF*, 1939, **15**, 53–68.
203 L. J. Durney, *Electroplating engineering handbook.*, Chapman & Hall, 1996.
204 F. Keller, M. S. Hunter and D. L. Robinson, *J. Electrochem. Soc.*, 1953, **100**, 411.
205 G. E. Thompson, H. Habazaki, K. Shimizu, M. Sakairi, P. Skeldon, X. Zhou and G. C. Wood, *Aircr. Eng. Aerosp. Technol.*, 1999, 71, 228–238.
206 C. E. Caicedo-Martinez, E. V. Koroleva, G. E. Thompson, P. Skeldon, K. Shimizu, H. Habazaki and G. Hoellrigl, *Surf. Interface Anal.*, 2002, **34**, 405–408.
207 W. Lee and J.-C. Kim, *Nanotechnology*, 2010, **21**, 485304.
208 H. F. Church, *Proc. IEE - Part B Electron. Commun. Eng.*, 1962, **109**, 399–406.
209 A. M. Gañán-Calvo, L. Martín-Banderas, R. González-Prieto, A. Rodríguez-Gil, T. Berdún-Álvarez, A. Cebolla, S. Chávez and M. Flores-Mosquera, *Int. J. Pharm.*, 2006, **324**, 19–26.
210 S.-M. Moon and S.-I. Pyun, *J. Solid State Electrochem.*, 1998, **2**, 156–161.
211 F. Brown and W. D. Mackintosh, *J. Electrochem. Soc.*, 1973, **120**, 1096.
212 University of Bath, WP1.1D3, N.T.D. Report on Self-Ordered Porous Alumina Template Technology. Accessed 23-06-11.
213 H. Masuda, *J. Electrochem. Soc.*, 1997, **144**, L127.
214 A. P. Li, F. Müller, A. Birner, K. Nielsch and U. Gösele, *J. Appl. Phys.*, 1998, **84**, 6023–6026.
215 S.-M. Moon and S.-I. Pyun, *Electrochim. Acta*, 1999, **44**, 2445–2454.

216 Thompson, Wood, G. Thompson and G. Wood, *Nature*, 1981, **290**, 230–232.
217 Y. C. Sui, B. Z. Cui, L. Martínez, R. Perez and D. J. Sellmyer, *Thin Solid Films*, 2002, **406**, 64–69.
218 H. O. Ali and P. Neufeld, *Nat. (London), Phys. Sci.*, 1972, **240**, 14.
219 A. Orsi and D. Jason Riley, *J. Electrochem. Soc.*, 2013, **160**, D10–D12.
220 H. Masuda and K. Fukuda, *Science*, 1995, 268, 1466–1468.
221 W. Lee and S.-J. Park, *Chem. Rev.*, 2014, **114**, 7487–7556.
222 M. Sridar Ilango, A. Mutalikdesai and S. K. Ramasesha, *J. Chem. Sci*, 2016, **128**, 153–158.
223 J. Hong, K. Kim, J. Heo and I. Chung, *Thin Solid Films*, 2010, **518**, 4572–4577.
224 F. Zhou, D. J. LeClere, S. J. Garcia-Vergara, P. Skeldon, G. E. Thompson and H. Habazaki, *Surf. Interface Anal.*, 2010, **42**, 247–251.
225 A. A. Noyan, A. P. Leontiev, M. V. Yakovlev, I. V. Roslyakov, G. A. Tsirlina and K. S. Napolskii, *Electrochim. Acta*, 2017, **226**, 60–68.
226 N.-Q. Zhao, X.-X. Jiang, C.-S. Shi, J.-J. Li, Z.-G. Zhao and X.-W. Du, *J. Mater. Sci.*, 2007, **42**, 3878–3882.
227 Y. Yan, X. Guo, Y. Zhang and Y. Tang, *Catal. Sci. Technol.*, 2015, **5**, 772–785.
228 L. Zaraska, G. D. Sulka and M. Jaskula, *J. Solid State Electrochem.*, 2011, **15**, 2427–2436.
229 A. Yli-Pentti, in *Comprehensive Materials Processing*, 2014, pp. 277–306.
230 J. Hu, W. Li, J. Chen, X. Zhang and X. Zhao, *Surf. Coatings Technol.*, 2008, **202**, 2922–2926.
231 C. Ji and P. C. Searson, *Appl. Phys. Lett.*, 2002, **81**, 4437–4439.
232 F. . b Li and J. B. . Wiley, *J. Mater. Chem.*, 2008, **18**, 3977–3980.
233 S. J. H. Fathima, J. Paul and S. Valiyaveettil, *Small*, 2010, **6**, 2443–2447.
234 R. A. Lorenzo, A. M. Carro, C. Alvarez-Lorenzo and A. Concheiro, *Int. J. Mol. Sci.*, 2011, 12, 4327–4347.
235 S. Vallejos, T. Stoycheva, F. E. Annanouch, E. Llobet, P. Umek, E. Figueras, C. Canè, I. Gràcia and C. Blackman, *RSC Adv.*, 2014, **4**, 1489.
236 S. Vallejos, P. Umek, T. Stoycheva, F. Annanouch, E. Llobet, X. Correig, P. De Marco, C. Bittencourt and C. Blackman, *Adv. Funct. Mater.*, 2013, **23**, 1313–1322.
237 V. P. Menon and C. R. Martin, *Anal. Chem.*, 1995, **67**, 1920–1928.
238 R. A. Schoonheydt, *Chem. Soc. Rev.*, 2010, **39**, 5051–5066.
239 N. Soh, M. Sonezaki and T. Imato, *Electroanalysis*, 2003, **15**, 1281–1290.
240 F. Muench, S. Schaefer, L. Hagelüken, L. Molina-Luna, M. Duerrschnabel, H.-J. Kleebe, J. Brötz, A. Vaskevich, I. Rubinstein and W. Ensinger, *ACS Appl. Mater. Interfaces*, 2017, **9**, 31142–31152.
241 A. M. Nieto-Soto, D. K. Diaz-Maldonado and F. A. Rios Angarita, *J. Phys. Conf. Ser.*, 2017, **786**, 012001.
242 S. Dimitrijević, M. Rajčić-Vujasinović and V. Trujić, *Int. J. Electrochem. Sci.*, 2013, **8**, 6620–6646.
243 L. Bruschi, G. Fois, G. Mistura, K. Sklarek, R. Hillebrand, M. Steinhart and U. Gösele, *Langmuir*, 2008, **24**, 10936–10941.
244 X. Yu, C.-X. Zhang, L. Zhang, Y.-R. Xue, H.-W. Li and Y. Wu, *Sensors Actuators B Chem.*, 2018, **263**, 327–335.
245 G. D. Sulka, in *Nanostructured Materials in Electrochemistry*, Wiley-VCH Verlag GmbH & Co. KGaA, Weinheim, Germany, 2008, pp. 1–116.
246 Y. S. Kim, S. I. Pyun, S. M. Moon and J. D. Kim, *Corros. Sci.*, 1996, **38**, 329–336.
247 M. M. Crouse, A. E. Miller, D. T. Crouse and A. A. Ikram, *J. Electrochem. Soc.*, 2005, **152**, D167.
248 M. Lillo and D. Losic, *J. Memb. Sci.*, 2009, **327**, 11–17.
249 M. Shaban, H. Hamdy, F. Shahin, J. Park and S.-W. Ryu, *J. Nanosci. Nanotechnol.*, 2010, **10**, 3380–3384.
250 G. E. Possin, *Rev. Sci. Instrum.*, 1970, **41**, 772–774.
251 D. Mo, J. Liu, H.-J. Yao, J.-L. Duan, M.-D. Hou, Y.-M. Sun, Y.-F. Chen, Z.-H. Xue and L. Zhang, *Yuanzineng Kexue Jishu/Atomic Energy Sci. Technol.*
252 A. Alyamani and O. Lemine, 201 Superlattices and Microstructures, 2012 **52** (4), 793-799.
253 L. Zaraska, E. Kurowska, G. D. Sulka and M. Jaskuła, *J. Solid State Electrochem.*, 2012, **16**, 3611–3619.
254 Z. Huang, G. Meng, Q. Huang, B. Chen, C. Zhu and Z. Zhang, *J. Raman Spectrosc.*, 2013, **44**, 240–246.
255 W. J. Stępniowski and M. Salerno, *Manuf. nanostructures*, 2014, 321–357.
256 Y. Sun, *Nanoscale*, 2010, **2**, 1626–1642.
257 H. Schlörb, V. Haehnel, M. S. Khatri, A. Srivastav, A. Kumar, L. Schultz and S. Fähler, *Phys. status solidi*, 2010, **247**, 2364–2379.
258 A. Mohammadi, V. Sandoghdar and M. Agio, *J. Comput. Theor. Nanosci.*, 2009, **6**, 2024–2030.
259 H. J. Fan, R. Scholz, A. Dadgar, A. Krost and M. Zacharias, *Appl. Phys. A Mater. Sci. Process.*, 2005, **80**, 457–460.
260 Y. Fang, J. Liu, D. J. Yu, J. P. Wicksted, K. Kalkan, C. O. Topal, B. N. Flanders, J. Wu and J. Li, *J. Power*

Sources, 2010, **195**, 674–679.
261 L. Li, Y. Yang, X. Huang, G. Li and L. Zhang, *Nanotechnology*, 2006, **17**, 1706–1712.
262 G. Xiao and C. L. Chien, *J. Appl. Phys.*, 1987, **61**, 4061–4063.
263 K. H. Kim, Z. Jin, Y. Abe and M. Kawamura, *Superlattices Microstruct.*, 2014, **75**, 455–460.
264 A. Fert and L. Piraux, *J. Magn. Magn. Mater.*, 1999, **200**, 338–358.
265 M. T. Rahman, R. K. Dumas, N. Eibagi, N. N. Shams, Y.-C. Wu, K. Liu and C.-H. Lai, *Appl. Phys. Lett.*, 2009, **94**, 042507.
266 W. Lee, R. Scholz, K. Nielsch and U. Gösele, *Angew. Chemie Int. Ed.*, 2005, **44**, 6050–6054.
267 P. Ugo and L. M. Moretto, in *Handbook of Electrochemistry*, Elsevier, 2007, pp. 678–709.
268 R. O. Al-Kaysi, T. H. Ghaddar and G. Guirado, *J. Nanomater.*, 2009, **2009**, 1–14.
269 B. Fryczkowska, Z. Piprek, M. Sieradzka, R. Fryczkowski and J. Janicki, *Int. J. Polym. Sci.*, 2017, **2017**, 1–14.
270 M. Steinhart, *Science*, 2002, **296**, 1997–1997.
271 G. Song, X. She, Z. Fu and J. Li, *J. Mater. Res.*, 2004, **19**, 3324–3328.
272 C. Mijangos, R. Hernández and J. Martin, Progress in Polymer Science, 2016, 54, 148-182
273 E. Dervishi, F. Hategekimana, L. Boyer, F. Watanabe, T. Mustafa, A. Biswas, A. R. Biris and A. S. Biris, *Chem. Phys. Lett.*, 2013, **590**, 126–130.
274 J. Goldberger, R. Fan and P. Yang, *Acc. Chem. Res.*, 2006, **39**, 239–248.
275 M. Jung, J.-H. Kim and Y.-W. Choi, *J. Nanomater.*, 2018, **2018**, 1–9.
276 C. Zhao, Y. Zhu, L. Chen, S. Zhou, Y. Su, X. Ji, A. Chen, X. Gui, Z. Tang and Z. Liu, *Nanoscale*, 2018, **10**, 16278–16283.
277 J. Liang, H. Chik, A. Yin and J. Xu, *J. Appl. Phys.*, 2002, **91**, 2544–2546.
278 H. Masuda and M. Satoh, *Japanese J. Appl. Physics, Part 2 Lett.*, 1996, **35**, L126–L129.
279 H. Masuda, K. Yasui and K. Nishio, *Adv. Mater.*, 2000, **12**, 1031–1033.
280 K. Höflich, R. Bin Yang, A. Berger, G. Leuchs and S. Christiansen, *Adv. Mater.*, 2011, **23**, 2657–2661.
281 S.-H. Chang, S. K. Gray and G. C. Schatz, *Opt. Express*, 2005, **13**, 3150.
282 C. Zhou, T. Segal-Peretz, M. E. Oruc, H. S. Suh, G. Wu and P. F. Nealey, *Adv. Funct. Mater.*, 2017, **27**, 1701756.
283 A. Al-Haddad, Z. Zhan, C. Wang, S. Tarish, R. Vellacheria and Y. Lei, *ACS Nano*, 2015, **9**, 8584–8591.
284 N. Asai, T. Shimizu, S. Shingubara and T. Ito, *Sensors Actuators, B Chem.*, 2018, **276**, 534–539.
285 S. Ji, H. G. Seo, S. Lee, J. Seo, Y. Lee, W. H. Tanveer, S. W. Cha and W. Jung, *RSC Adv.*, 2017, **7**, 23600–23606.
286 K. Huang, Y. Li, Z. Wu, C. Li, H. Lai and J. Kang, *Opt. Express*, 2011, **19**, 1301–1309.
287 M. G. Banaee and K. B. Crozier, *Opt. Lett.*, 2010, **35**, 760–762.
288 G. Tian, D. Chen, J. Yao, Q. Luo, Z. Fan, M. Zeng, Z. Zhang, J. Dai, X. Gao and J.-M. Liu, *RSC Adv.*, 2017, **7**, 41210–41216.
289 E. Moyen, A. Hama, E. Ismailova, L. Assaud, G. Malliaras, M. Hanbücken and R. M. Owens, *Nanotechnology*, 2016, **27**, 074001.
290 N. Kwon, N. Kim, J. Yeon, G. Yeom and I. Chung, *J. Vac. Sci. Technol. B, Nanotechnol. Microelectron. Mater. Process. Meas. Phenom.*, 2011, **29**, 031805.
291 M. Havrdova, K. Polakova, J. Skopalik, M. Vujtek, A. Mokdad, M. Homolkova, J. Tucek, J. Nebesarova and R. Zboril, *Micron*, 2014, **67**, 149–154.
292 K. Takenaka, N. Togashi, N. Nishiyama and A. Inoue, *Intermetallics*, 2010, **18**, 1969–1972.
293 D. S. Abramkin, K. M. Rumynin, A. K. Bakarov, D. A. Kolotovkina, A. K. Gutakovskii and T. S. Shamirzaev, *JETP Lett.*, 2016, **103**, 692–698.
294 G. Das, N. Patra, A. Gopalakrishanan, R. Proietti Zaccaria, A. Toma, S. Thorat, E. Di Fabrizio, A. Diaspro and M. Salerno, *Microelectron. Eng.*, 2012, **97**, 383–386.
295 C.-Y. Lee, G.-W. Wu and W.-J. Hsieh, *Sensors Actuators A Phys.*, 2008, **147**, 173–176.
296 Y. Li, Y. Chen, M. Qiu, H. Yu, X. Zhang, X. W. Sun and R. Chen, *Sci. Rep.*, 2016, **6**, 20114.
297 H. Han, Z. Huang and W. Lee, *Nano Today*, 2014, **9**, 271–304.
298 Takashi Kyotani, A. Li-fu Tsai and A. Tomita, *Chem. Mater.*, 1996, **8**, 2109–2113.
299 Y. . Sui, B. . Cui, R. Guardián, D. . Acosta, L. Martínez and R. Perez, *Carbon N. Y.*, 2002, **40**, 1011–1016.
300 M. T. Saung, A. Sharei, V. A. Adalsteinsson, N. Cho, T. Kamath, C. Ruiz, J. Kirkpatrick, N. Patel, M. Mino-Kenudson, S. P. Thayer, R. Langer, K. F. Jensen, A. S. Liss and J. C. Love, *Small*, 2016, **12**, 5873–5881.
301 I. Lombardi, A. I. Hochbaum, P. Yang, C. Carraro and R. Maboudian, *Chem. Mater.*, 2006, **18**, 988–991.
302 T. Shimizu, T. Xie, J. Nishikawa, S. Shingubara, S. Senz and U. Gösele, *Adv. Mater.*, 2007, **19**, 917–920.
303 T. Gorisse, L. Dupré, P. Gentile, M. Martin, M. Zelsmann and D. Buttard, *Nanoscale Res. Lett.*, 2013, **8**,

287.
304 A. Sarkar and G. G. Khan, *Nanoscale*, 2019, **11**, 3414–3444.
305 J. Li, G. Lu, Y. Wang, Y. Guo and Y. Guo, *J. Colloid Interface Sci.*, 2012, **377**, 191–196.
306 F. Cheng, J. Zhao, W. Song, C. Li, H. Ma, J. Chen and P. Shen, *Inorg. Chem.*, 2006, **45**, 2038–2044.
307 G. Kwak, J. Hwang, J.-Y. Cheon, M. H. Woo, K.-W. Jun, J. Lee and K.-S. Ha, *J. Phys. Chem. C*, 2013, **117**, 1773–1779.
308 C. Vieu, F. Carcenac, A. Pepin, Y. Chen, M. Mejias, A. Lebib, L. Manin-Ferlazzo, L. Couraud and H. Launois, *Appl. Surf. Sci.*, 2000, **164**, 111–117.
309 S. Han, K. Sohn and T. Hyeon, *Chem. Mater.*, 2000, **12**, 3337–3341.
310 C. Cheng and H. J. Fan, *Nano Today*, 2012, 7, 327–343.
311 M. M. Arafat, B. Dinan, S. A. Akbar and A. S. M. A. Haseeb, *Sensors*, 2012, **12**, 7207–7258.
312 M. Sharma and B. K. Kuanr, in *Electroplating of Nanostructures*, InTech, 2015.
313 H. Baek, J. Ha, D. Zhang, B. Natarajan, J. P. Winterstein, R. Sharma, R. Hu, K. Wang, S. Ziemak, J. Paglione, Y. Kuk, N. B. Zhitenev and J. A. Stroscio, Physical Review B Condensed Matter , and Materials Physics, 2015 92 (9), 1-11 .
314 X. Wang, H. Chang, J. Xie, B. Zhao, B. Liu, S. Xu, W. Pei, N. Ren, L. Huang and W. Huang, *Coord. Chem. Rev.*, 2014, 273–274, 201–212.
315 F. Wang, G.-Q. Jin and X.-Y. Guo, *Mater. Lett.*, 2006, **60**, 330–333.
316 M. Prześniak-Welenc, M. Łapiński, T. Lewandowski, B. Kościelska, L. Wicikowski and W. Sadowski, *J. Nanomater.*, 2015, **2015**, 1–8.
317 A. R. Boccaccini, S. Keim, R. Ma, Y. Li and I. Zhitomirsky, *J. R. Soc. Interface*, , DOI:10.1098/rsif.2010.0156.focus.
318 B. Alberts and J. Lewis, in *Molecular Biology of the cell*, 2013.
319 X. Li, Y. He, T. Zhang and L. Que, *Opt. Express*, 2012, **20**, 21272.
320 K. Hotta, A. Yamaguchi and N. Teramae, *ACS Nano*, 2012, **6**, 1541–1547.
321 A. P. Vinogradov, A. V. Dorofeenko, A. A. Pukhov and A. A. Lisyansky, *Phys. Rev. B*, 2018, **97**, 235407.
322 U. Woggon, *Optical Properties of Semiconductor Quantum Dots*, Springer Berlin Heidelberg, 1997.
323 J. P. Reithmaier, G. Sęk, A. Löffler, C. Hofmann, S. Kuhn, S. Reitzenstein, L. V. Keldysh, V. D. Kulakovskii, T. L. Reinecke and A. Forchel, *Nature*, 2004, **432**, 197–200.
324 W.-L. Hsu, C.-H. Cheng, C.-L. Wu, Y.-H. Pai and G.-R. Lin, *IEEE J. Sel. Top. Quantum Electron.*, 2017, **23**, 1–7.
325 Y. Lai, in *IMID 2009*, 2009, pp. 1069–1072.
326 E. Hecht, *Opt. 4th Ed. by Eugene Hecht Read. MA AddisonWesley Publ. Co. 2001*, 2001, 1, 122.
327 M. Milosevic, *Intern. Reflect. ATR Spectrosc.*, 2012, 39–54.
328 J. Jung, J. Bork, T. Holmgaard and N. a. Kortbek, *Ellipsometry*, Aalborg University Projects, 2004 p132
329 D. Pristinski, V. Kozlovskaya and S. a Sukhishvili, *J. Opt. Soc. Am. A. Opt. Image Sci. Vis.*, 2006, **23**, 2639–2644.
330 C. Rosman, J. Prasad, A. Neiser, A. Henkel, J. Edgar and C. Sönnichsen, *Nano Lett.*, 2013, **13**, 3243–3247.
331 Z. Liu, L. Tian, S. Liu and L. Waller, *J. Biomed. Opt.*, 2014, **19**, 106002.
332 C. Berthomieu and R. Hienerwadel, *Photosynth. Res.*, 2009, 101, 157–170.
333 J. S. Gaffney, N. A. Marley and D. E. Jones, *Charact. Mater.*, 2012, 1104–1135.
334 A. J. Bard, L. R. Faulkner, N. York, W. Brisbane and S. E. Toronto, *Electrochemical Methods Fundamentals and Applications*, John Wiley & Sons Inc 1980
335 C. Lefrou, P. Fabry and J.-C. Poignet, *Electrochemistry*, Springer Berlin Heidelberg, Berlin, Heidelberg, 2012.
336 A. Inesi, *Bioelectrochemistry Bioenerg.*, 1986, **15**, 531.
337 P. T. Kissinger and W. R. Heineman, *J. Chem. Educ.*, 1983, **60**, 9242–5.
338 S. J. Lee, S. I. Pyun, S. K. Lee and S. J. L. Kang, *Isr. J. Chem.*, 2008, **48**, 215–228.
339 S. Van Gils, S. Holten, E. Stijns, M. Vancaldenhoven, H. Terryn and L. Mattsson, *Surf. Interface Anal.*, 2003, **35**, 121–127.
340 L. Young, *Anodic Oxide Films*, Academic Press Inc. (London) Ltd, London, UK, 1961.
341 D. Barriet, C. M. Yam, O. E. Shmakova, A. C. Jamison and T. R. Lee, *Langmuir*, 2007, **23**, 8866–8875.
342 W.-Q. Ma, Y. Fang, G.-L. Hao and W.-G. Wang, *Chin. J. Chem. Phys.*, 2010, **23**, 659–663.
343 S. K. rishna M. Nalluri, N. Shivarova, A. L. Kanibolotsky, M. Zelzer, S. Gupta, P. W. J. M. Frederix, P. J. Skabara, H. Gleskova and R. V. Ulijn, *Langmuir*, 2014, **30**, 12429–12437.